Study of Rejuvenation Heat Treatment for Life Extension of A-286 Gas Turbine Wheels

Girish Shejale
SAP ID: 500041348

DEPARTMENT OF MECHANICAL ENGINEERING

SCHOOL OF ENGINEERING STUDIES

Submitted

IN PARTIAL FULFILLMENT OF THE REQUIREMENT OF THE DEGREE OF DOCTOR OF PHILOSOPHY

To

UNIVERSITY OF PETROLEUM AND ENERGY STUDIES

DEHRADUN

NOVEMBER, 2018

Under the Guidance of

Dr. Rajnish Garg (Internal Guide)
Dr. Subrahmanyam V. Garimella (Internal Co-guide)
Dr. Alexander Schnell (External Guide)

ACKNOWLEDGEMENTS

The journey towards my research started in August 2014. Accomplishing this journey and a milestone in itself was not an easy task, but on this path there are several people who made my task easy, memorable and achievable.

A very sincere thanks and gratitude to my University Guide Professor, Dr. Rajnish Garg, without his support and guidance this research would have not been possible. His direction, academic support and guidance widened my research angles in different areas and have immensely helped in completion of this thesis and research work.

A sincere thanks to my University Co-Guide Professor, Dr. Garimella for motivating me and providing leads to valuable research papers.

I would like to extend a very special thanks to my External Guide, Dr. Alexander Schnell for being my guiding star on various technical issues and time to time motivation throughout the research journey.

I express my sincere gratitude and a trillion times thanks to Masaood John Brown, Dubai Management for providing me an opportunity to work on a current research project and providing financial support for all the research tests.

My sincere thanks to Brian Waddell (General Manager), Tommy Doyle (Workshop Production Manager), Ross Nicolson (Workshop Manager), Jim Adair (Rotor Workshop Manager), Khalid Bashir (Quality Manager) for the tremendous support and encouragement on the life extension research work of the A-286 turbine wheel. There are several personnel's in Masaood John Brown, Dubai whom I wish to thank for their timely support in various aspects. The list is endless, but without these persons my thesis would have been incomplete. The list of these persons is mentioned below along with the area of support.

- Vishal Suryawanshi, Darshan Ahire and Ashok Kandurkar for all the in-house laboratory preparation and testing.

- Shailesh Shetty for the turbine wheel sectioning work.

- Clarence Fernandez for the excel formatting and graphical charting.

- Showkath Ali, for the thesis file formatting.

- Greg Fernandez and Radha Krishnan for the guidance on the turbine wheel location.

- Wesley Anand for the schematic drawings of the turbine wheel.

- Hammad Amin for the formatting and binding of thesis.

The Masood John Brown, Dubai workshop team – Khalid Bashir, Clarence Fernandez, C. P. Babu, Rachel Padre, Showkath, Shailesh Shetty, A. P. Wesley, Shivanand Sampengi, Elmer and Sagar Bhandare have always motivated me to achieve my research goals.

I sincerely thank my friends Mahesh Pophale, Hemant Londhe, Rajeev Joshi, Charudutt Shringare, Chandarhas Jadhav, Vinayak Naiknaware for their motivational support to achieve my goals.

A deep bottom heart thanks to my Mother and Brothers for encouraging me throughout the PhD journey.

My daughter Ayushi and my son Abhang, were very patient and co-operative during the entire research work. A very sincere thanks to my lovely kids for sacrificing the family time and providing me time to be alone as and when required to complete my thesis.

Last but not the least; I would like to thank my wife Bhavana, for providing me continuous spiritual support and time to time motivation for completion of this thesis.

I am thankful to God for giving me an opportunity to work on this life extension research and for all the wonderful people around me who supported me for this research work.

Declaration by the Author

"I hereby declare that this submission is my own work and that, to the best of my knowledge and belief, it contains no material previously published or written by another person nor material which has been accepted for the award of any other degree or diploma of the university or other institute of higher learning, except where due acknowledgement has been made in the text".

Signature

29/10/18

Girish Shejale

UPES

www.upes.ac.in

THESIS COMPLETION CERTIFICATE

This is to certify that the thesis on **"Study of Rejuvenation Heat Treatment for Life Extension of A-286 Gas Turbine Wheels"** by **Girish Shejale, SAP ID 500041348** in Partial completion of the requirements for the award of the Degree of Doctor of Philosophy is an original work carried out by him under our joint supervision and guidance.

It is certified that the work has not been submitted anywhere else for the award of any other diploma or degree of this or any other University.

Internal Guide

Dr. Rajnish Garg

Place: Dehradun

Date: 31/10/2018

Internal Co-Guide

G.V. Subrahmanyam

Dr. Subrahmanyam V. Garimella

Place: Dehradun

Date: 31/10/2018

SCHNELL-Tech FZE
Independent Service Provider
Gas Turbines & Power Plants

THESIS COMPLETION CERTIFICATE

Date: 6th September 2018

Subject: THESIS COMPLETION CERTIFICATE

to whom it may concern

This is to certify that the thesis on "Study of Rejuvenation Heat Treatment for Life Extension of A-286 Gas Turbine Wheels" by Girish Shejale, SAP ID 500041348 in Partial completion of the requirements for the award of the Degree of Doctor of Philosophy is an original work carried out by him under our joint supervision and guidance.

It is certified that the work has not been submitted anywhere else for the award of any other diploma or degree of this or any other University.

External Guide

Dr. Alexander Schnell
General Manager
Schnell-Tech FZE
Dubai Marina Plaza
PO Box 112229
Dubai, U.A.E
Direct +971 50 917 37 57

Place: Dubai

SCHNELL-TECH FZE, Trad. Lic. 6593/2015
Dubai Marina, Level 27, Marina Plaza
PO Box. 112229, Dubai, UAE

Tel: +971 4 278 5189
info@schnell-tech.net
www.schnell-tech.net

Contents

Acknowledgments	i
Declaration by Author	iv
Thesis Completion Certificate	v
Contents	vii
Executive Summary	xii
List of Symbols	xv
List of Figures	xvi
List of Tables	xxiii

Chapter 1 – INTRODUCTION

1.1 Motivation 1

1.2 Research Need 5

1.3 Overview 6

1.3.1 Gas Turbine Working Principle 7

1.3.2 Construction 8

1.4 Importance of Life Extension 11

1.5 Research Objectives 15

1.6 Research Methodology 16

Chapter 2 – LITERATURE REVIEW

2.1 Combustion Turbine Damage Mechanisms and Need for Life Assessment 19

2.2 Life Assessment of Turbines 21

2.3 Rejuvenation Heat Treatments for Life Extension 27

2.4 Study of A-286 Alloy, Microstructure and Properties 32

2.5 Literature Review - Key Inferences 36

2.6 Literature Review- Identified Gaps 38

Chapter 3 – EXPERIMENTAL WORK

3.1 Chemical Composition 41

3.1.1 Optical Emission Spectrometer 42

3.1.2 X-Ray Fluorescence (XRF) 44
3.2 Finite Element Analysis (FEA) 46
3.2.1 Finite Element Analysis Methodology 46
3.2.2 Finite Element Analysis Procedure 47
3.3 Portable Hardness Testing 49
3.4 Microexamination (Optical and Scanning Electron Microscope) 50
3.4.1 Metallographic Preparation 51
3.4.2 Optical Microscopy 54
3.4.3 Scanning Electron Microscopy (SEM) 56
3.4.4 Energy Dispersive X-Ray Analysis (EDAX) 57
3.5 Microhardness Testing 59
3.6 Dimensional Measurement 60
3.7 Heat Treatments (Solution Annealing & Age Hardening) 63
3.7.1 Heat Treatment Equipment 63
3.7.2 Heat Treatment Cycles 65
3.8 Destructive Tests 78
3.8.1 Tensile Testing (Room Temperature and High Temperature) 79
3.8.2 Charpy Impact Test 82
3.8.3 Stress Rupture Test 84
3.9 Fractography Using Scanning Electron Microscope 86

Chapter 4 – RESULTS

4.1 Chemical Composition 87
4.2 Finite Element Analysis 88
4.3 Portable Hardness Testing 91

4.4 Microstructure Evaluation / Microexamination 93
4.4.1 Microstructures of New A-286 Bar, Serviced Turbine Wheel, Pilot & Planned Heat Treatments 93
4.4.2 Microstructure Observations New A-286 Bar and Serviced Turbine Wheel 104
4.5 Energy Dispersive Analysis of X-ray (EDAX) 107
4.6 Vickers Hardness Survey – Microhardness Testing 110
4.7 Tensile Test (Room temperature and High temperature) 112
4.8 Charpy Impact Test 116
4.9 Stress Rupture Test 118
4.10 Compiled Mechanical Test Results 120
4.11 Fracture Morphology 124
4.12 Laboratory Test Reports 172

Chapter 5 – DISCUSSION
5.1 Background of A-286 Turbine Wheel 173
5.2 Stress Mapping of the A-286 Turbine Wheel 176
5.3 Chemical Composition 177
5.4 Portable Hardness Survey 180
5.5 Microstructures of New A-286 Bar and Serviced Turbine Wheel 181
5.6 Heat Treatments and Role of Carbides 183
5.7 Mechanical Properties 188
5.7.1 Charpy Impact Test 192
5.7.2 Stress Rupture Test 194
5.7.3 Vickers Hardness Survey 195
5.8 Selection of Optimized Heat Treatment 196

Chapter 6 – CONCLUSION

6.1 Life Cycle Management of Turbine Wheels 206

6.2 Future Scope of Work 210

References 211

Appendix-1 239

Profile of the Scholar 247

Published Papers Related to this Work 249

Executive Summary

This research is on the feasibility of extending the life of A-286 gas turbine wheels beyond its designed life for further continuation in service by suitable heat treatment

Currently, the gas turbine users wish to run the A-286 turbine wheels even after 200K hours of service rather than replacing it with new wheel. The OEM recommends replacing the A-286 wheel after 200k hours of operation. The replacement cost of the A-286 turbine wheel is 120K USD, which is not economical for the gas turbine users. The end users look forward for a solution to run the turbine wheel in service even after 200K hours. The end users think that if the wheel has not experienced any issues till 200k hours of operation, then it should be continued in service.

This research addresses the concern of the end users and provides a solution to extend the life of serviced A-286 turbine wheel by rejuvenation heat treatment.
There are several gas turbines operating with A-286 turbine wheel material in the Middle East and various other locations. The concern of the gas turbine users to operate the A-286 turbine wheel safely after the designed life was a starting point for this specific research. Life extension by non-destructive testing is a general method practiced by the industry. Life extension of components by heat treatments is a rare approach followed by the industry. Literature survey indicates that the gas turbine blades are heat treated as a part of repair works for continuation in service, but there has been no attempt to heat treat the A-286 turbine wheel for life extension. The present research explores the possibility of extending the life of A-286 turbine wheels by heat treatment.

Over a period of time microstructural degradation occurs in A-286 turbine wheels as it approaches 200K hours. The extent of microstructural degradation may vary from case to case basis depending on the operating history of the turbine unit. Microstructural degradation of turbine wheels decreases the mechanical properties of the wheel. It is essential to rejuvenate the microstructure of the wheel to gain the required mechanical properties. The microstructure rejuvenation is possible by heat treatments. The microstructure of the turbine wheel can be altered by heat treatment and can be brought to as near to the microstructure of a new A-286 turbine wheel. Considering this aspect, the life of the turbine wheel may be increased until the next inspection period.

The present research work is purely an experimental research. Stress mapping was performed on the serviced A-286 turbine wheel to verify the different stress levels across the wheel. A section of serviced A-286 turbine wheel was obtained to study the microstructure and properties. A new A-286 forged bar was purchased to study the microstructure and its properties. Heat treatments were performed on the sections of the serviced A-286 turbine wheel with variation in temperature and time. Microstructure and properties were studied after each performed heat treatment. A comparison of microstructure and properties was done after each heat treatment and was compared with the new A-286 forged bar. The mechanical properties studied and compared were room temperature tensile strength, high temperature tensile strength, stress rupture, Vicker's hardness and Charpy impact strength. The best heat treatment was selected which imparted microstructure and properties as near to those of the new A-286 forged bar.

The research findings and conclusions mate the required objectives. From the experimental research, it is concluded that the microstructural degradation can be eliminated and microstructure can be rejuvenated to restore the mechanical properties close to new A-286 material after the heat treatment. Thus, the turbine wheel can be continued in service for next 48,000 hours.

A life cycle management plan for the life extension of A-286 wheels is proposed. This involves inspection of the turbine wheel by replica metallography after 200K hours of service. The turbine wheel life can be extended by heat treatment, if there is any microstructural degradation.

List of Symbols

Symbol	Legend
γ'	Gamma Prime
η	Eta Phase

List of Figures

Figure Number	Figure Caption	Page Number
1.1	Schematic diagram of a gas turbine	8
1.2	Different Sections of gas turbine	9
1.3	Various components of a gas turbine	9
1.4	A Frame 5002 rotor assembly	11
1.5	Outline of Research Methodology	18
3.1	Optical emission spectrometer used for chemical analysis	44
3.2	XRF analysis on a new A-286 bar	45
3.3	XRF analysis on a serviced turbine wheel section	46
3.4	Mesh of turbine wheel created for finite element analysis	48
3.5	Portable Equotip-3 hardness tester	50
3.6	The hot mounting press- Citopress	52
3.7	Prepared hot mounts	53
3.8	Polishing machine “Abraham”, used for metallographic polishing	53
3.9	Optical Microscope used for microscopic evaluation	55
3.10	The Scanning Electron Microscope	57
3.11	EDAX Detector on the SEM	58
3.12	Microhardness tester used for hardness measurements	60
3.13	Dissected portion of turbine wheel	61
3.14	Four different sections after further dissections	61
3.15	Section 10 near the dovetail area after further dissections	62
3.16	Vacuum furnace used for heat treatments	65
3.17	Vacuum furnace showing the internal chamber	65
3.18	Graphical representation of the pilot heat treatments	66
3.19	Schematic of the A-286 turbine wheel section showing the cut section and sample direction for mechanical tests	79
3.20	Instron 5582, room temperature tensile testing machine	80
3.21	Instron 8561, high temperature tensile testing machine	81

Figure Number	Figure Caption	Page Number
3.22	Satec Impact Testing Machine.	82
3.23	Schematic showing the principle of Charpy Impact Test	83
3.24	Stress Rupture Testing Machine	85
4.1	Boundary Conditions applied to Finite Element Model	89
4.2	Stress Distribution Pattern in the serviced A-286 turbine wheel	90
4.3	Portable hardness test locations on dissected section of A-286 test block	91
4.4	Micrograph of as new A-286 bar; transverse section showing the general microstructure; Etched; Original Magnification – 200x (GS:6-7)	94
4.5	SEM micrograph of as new A-286 bar, transverse section; Etched; Original Magnification – 500x	94
4.6	Micrograph of serviced turbine wheel; transverse section showing the general microstructure; Etched; Original Magnification – 200x (GS:4-5)	94
4.7	SEM micrograph of serviced turbine wheel; transverse section displays carbide network; Etched; Original Magnification – 500x	94
4.8	Micrograph of Transverse section after pilot HT (SA – 750 ^{0}C x 3hrs) showing the general microstructure; Etched; Original Magnification – 200x (GS:4-5)	95
4.9	SEM micrograph of Transverse section after pilot HT (SA – 750 ^{0}C x 3hrs) showing the general microstructure Etched; Original Magnification – 500x	95
4.10	Micrograph of Transverse section after pilot HT (SA – 950 ^{0}C x 3hrs) showing the general microstructure; Etched; Original Magnification – 200x (GS:5-6)	95
4.11	SEM micrograph of Transverse section after pilot HT (SA – 950 ^{0}C x 3hrs) showing the general microstructure; Etched; Original Magnification – 500x	95

Figure Number	Figure Caption	Page Number
4.12	Micrograph of Transverse section after pilot HT (SA – 1120 ^{0}C x 3hrs) showing the general microstructure; Etched; Original Magnification – 200x (GS:1-2)	96
4.13	SEM micrograph of Transverse section after pilot HT (SA – 1120 ^{0}C x 3hrs) showing the general microstructure; Etched; Original Magnification – 500x	96
4.14	Micrograph of Transverse section after HT (SA – 1120 ^{0}C x 2hrs & Age 720 ^{0}C x 16hrs) showing the general microstructure; Etched; Original Magnification – 200x (GS:1-2)	96
4.15	SEM micrograph of Transverse section after HT (SA – 1120 ^{0}C x 2hrs & Age 720 ^{0}C x 16hrs) showing the general microstructure; Etched; Original Magnification – 500x	96
4.16	Micrograph of Transverse section after HT (SA – 950 ^{0}C x 2hrs & Age 720 ^{0}C x 16hrs) showing the general microstructure; Etched; Original Magnification – 200x (GS:4-5)	97
4.17	SEM micrograph of Transverse section after HT (SA – 950 ^{0}C x 2hrs & Age 720 ^{0}C x 16hrs) showing the general microstructure; Etched; Original Magnification – 500x	97
4.18	Micrograph of Transverse section after HT (SA – 950 ^{0}C x 3hrs & Age 720 ^{0}C x 16hrs) showing the general microstructure; Etched; Original Magnification – 200x (GS:5-6)	97
4.19	SEM micrograph of Transverse section after HT (SA – 950 ^{0}C x 3hrs & Age 720 ^{0}C x 16hrs) showing the general microstructure;; Etched; Original Magnification – 500x	97
4.20	Micrograph of Transverse section after HT (SA – 1120 ^{0}C x 3hrs & Age 720 ^{0}C x 16hrs) showing the general microstructure; Etched; Original Magnification – 200x(GS:1-2)	98
4.21	SEM micrograph of Transverse section after HT (SA – 1120 ^{0}C x 3hrs & Age 720 ^{0}C x 16hrs) showing the general microstructure; Etched; Original Magnification – 500x	98
4.22	Micrograph of Transverse section after HT (SA – 950 ^{0}C x 3hrs & Age 600 ^{0}C x 4hrs) showing the general microstructure Etched; Original Magnification – 200x (GS:4-5)	98

Figure Number	Figure Caption	Page Number
4.23	SEM micrograph of Transverse section; after HT (SA – 950 ^{0}C x 3hrs & Age 600 ^{0}C x 4hrs) showing the general microstructure Etched; Original Magnification – 500x	98
4.24	Micrograph of Transverse section after HT (SA – 950 ^{0}C x 3hrs & Age 600 ^{0}C x 8hrs) showing the general microstructure; Etched; Original Magnification – 200x(GS:4-5)	99
4.25	SEM micrograph of Transverse section after HT (SA – 950 ^{0}C x 3hrs & Age 600 ^{0}C x 8hrs) showing the general microstructure Etched; Original Magnification – 500x	99
4.26	Micrograph of Transverse section after HT (SA – 950 ^{0}C x 3hrs & Age 600 ^{0}C x 12hrs) showing the general microstructure; Etched; Original Magnification – 200x (GS:5-6)	99
4.27	SEM micrograph of Transverse section after HT (SA – 950 ^{0}C x 3hrs & Age 600 ^{0}C x 12hrs) showing the general microstructure Etched; Original Magnification – 500x	99
4.28	Micrograph of Transverse section after HT (SA – 950 ^{0}C x 3hrs & Age 640 ^{0}C x 4hrs) showing the general microstructure; Etched; Original Magnification – 200x (GS:5-6)	100
4.29	SEM micrograph of Transverse section after HT (SA – 950 ^{0}C x 3hrs & Age 640 ^{0}C x 4hrs) showing the general microstructure Etched; Original Magnification – 500x	100
4.30	Micrograph of Transverse section after HT (SA – 950 ^{0}C x 3hrs & Age 640 ^{0}C x 8hrs) showing the general microstructure; Etched; Original Magnification – 200x (GS:5-6)	100
4.31	SEM micrograph of Transverse section after HT (SA – 950 ^{0}C x 3hrs & Age 640 ^{0}C x 8hrs) showing the general microstructure Etched; Original Magnification – 500x	100
4.32	Micrograph of Transverse section after HT (SA – 950 ^{0}C x 3hrs & Age 640 ^{0}C x 12hrs) showing the general microstructure; Etched; Original Magnification – 200x (GS:6-7)	101
4.33	SEM micrograph of Transverse section after HT (SA – 950 ^{0}C x 3hrs & Age 640 ^{0}C x 12hrs) showing the general microstructure Etched; Original Magnification – 500x	101

Figure Number	Figure Caption	Page Number
4.34	Micrograph of Transverse section after HT (SA – 1120 ^{0}C x 3hrs & Age 600 ^{0}C x 4hrs) showing the general microstructure; Etched; Original Magnification – 200x (GS:1-2)	101
4.35	SEM micrograph of Transverse section after HT (SA – 1120 ^{0}C x 3hrs & Age 600 ^{0}C x 4hrs) showing the general microstructure; Etched; Original Magnification – 500x	101
4.36	Micrograph of Transverse section after HT (SA – 1120 ^{0}C x 3hrs & Age 600 ^{0}C x 8hrs) showing the general microstructure; Etched; Original Magnification – 200x (GS:2-3)	102
4.37	SEM micrograph of Transverse section after HT (SA – 1120 ^{0}C x 3hrs & Age 600 ^{0}C x 8hrs) showing the general microstructure; Etched; Original Magnification – 500x	102
4.38	Micrograph of Transverse section after HT (SA – 1120 ^{0}C x 3hrs & Age 600 ^{0}C x 12hrs) showing the general microstructure; Etched; Original Magnification – 200x (GS:2-3)	102
4.39	SEM micrograph of Transverse section after HT (SA – 1120 ^{0}C x 3hrs & Age 600 ^{0}C x 12hrs) showing the general microstructure Etched; Original Magnification – 300x	102
4.40	Micrograph of Transverse section after HT (SA – 1120 ^{0}C x 3hrs & Age 640 ^{0}C x 4hrs) showing the general microstructure; Etched; Original Magnification – 200x (GS:1-2)	103
4.41	SEM micrograph of Transverse section after HT (SA – 1120 ^{0}C x 3hrs & Age 640 ^{0}C x 4hrs) showing the general microstructure; Etched; Original Magnification – 500x	103
4.42	Micrograph of Transverse section after HT (SA – 1120 ^{0}C x 3hrs & Age 640 ^{0}C x 8hrs) showing the general microstructure; Etched; Original Magnification – 200x (GS:2-3)	103
4.43	SEM micrograph of Transverse section after HT (SA – 1120 ^{0}C x 3hrs & Age 640 ^{0}C x 8hrs) showing the general microstructure; Etched; Original Magnification – 500x	103
4.44	Micrograph of Transverse section after HT (SA – 1120 ^{0}C x 3hrs & Age 640 ^{0}C x 12hrs) showing the general microstructure Etched; Original Magnification – 200x (GS:2-3)	104

Figure Number	Figure Caption	Page Number
4.45	SEM micrograph of Transverse section after HT (SA – 1120 ^{0}C x 3hrs & Age 640 ^{0}C x 12hrs) showing the general microstructure Etched; Original Magnification – 500x	104
4.46	EDAX Analysis of Carbides at Location-1 in serviced turbine wheel..	108
4.47	EDAX Analysis of Carbides at Location-2 in serviced turbine wheel	109
4.48	SEM micrograph of as new A-286 bar fractured tensile sample at 21^{0}C; Original Magnification – 500x	124
4.49	SEM micrograph of as new A-286 bar fractured tensile sample at 450^{0}C; Original Magnification – 500x	124
4.50	SEM micrograph of as new A-286 bar fractured Charpy sample; Original Magnification – 500x	124
4.51	SEM micrograph of serviced A-286 wheel fractured tensile sample at 21^{0}C; Original Magnification – 500x	124
4.52	SEM micrograph of serviced A-286 wheel fractured tensile sample at 450^{0}C; Original Magnification – 400x	125
4.53	SEM micrograph of serviced A-286 wheel fractured Charpy sample; Original Magnification – 400x	125
4.54	SEM micrograph of serviced A-286 wheel fractured stress rupture sample; Original Magnification – 50x	125
4.55	SEM micrograph of serviced A-286 wheel fractured stress rupture sample; Original Magnification – 1000x	125
4.56	SEM micrograph of fractured tensile sample at 21 ^{0}C, (SA - 1120 ^{0}C x 2 hrs + Age – 720 ^{0}C x 16 hrs); Original Magnification – 300x	126
4.57	SEM micrograph of fractured tensile sample at 450 ^{0}C, (SA - 1120 ^{0}C x 2 hrs + Age – 720 ^{0}C x 16 hrs); Original Magnification – 400x	126
4.58	SEM micrograph of fractured charpy sample (SA - 1120 ^{0}C x 2 hrs + Age – 720 ^{0}C x 16 hrs); Original Magnification – 400x	126
4.59	SEM micrograph of fractured tensile sample at 21 ^{0}C, (SA - 950 ^{0}C x 2 hrs + Age – 720 ^{0}C x 16 hrs); Original Magnification – 500x	127
4.60	SEM micrograph of fractured tensile sample at 450 0C, (SA - 950 ^{0}C x 2 hrs + Age – 720 ^{0}C x 16 hrs); Original Magnification – 500x	127

Figure Number	Figure Caption	Page Number
4.61	SEM micrograph of fractured charpy sample (SA - 950 ^{0}C x 2 hrs + Age – 720 ^{0}C x 16 hrs); Original Magnification – 500x	127
4.62	SEM micrograph of fractured tensile sample at 21 ^{0}C, (SA - 950 ^{0}C x 3 hrs + Age – 720 ^{0}C x 16 hrs); Original Magnification – 500x	128
4.63	SEM micrograph of fractured tensile sample at 450 ^{0}C, (SA - 950 ^{0}C x 3 hrs + Age – 720 ^{0}C x 16 hrs); Original Magnification – 500x	128
4.64	SEM micrograph of fractured charpy sample (SA - 950 ^{0}C x 3 hrs + Age – 720 ^{0}C x 16 hrs); Original Magnification – 500x	128
4.65	SEM micrograph of fractured tensile sample at 21 ^{0}C, (SA - 1120 ^{0}C x 3 hrs + Age – 720 ^{0}C x 16 hrs); Original Magnification – 400x	129
4.66	SEM micrograph of fractured tensile sample at 450 ^{0}C, (SA - 1120 ^{0}C x 3 hrs + Age – 720 ^{0}C x 16 hrs); Original Magnification – 500x	129
4.67	SEM micrograph of fractured charpy sample (SA - 1120 ^{0}C x 3 hrs + Age – 720 ^{0}C x 16 hrs); Original Magnification – 500x	129
4.68	SEM micrograph of fractured tensile sample at 21 ^{0}C, (SA - 950 ^{0}C x 3 hrs + Age – 600 ^{0}C x 4 hrs); Original Magnification – 33x	130
4.69	SEM micrograph of fractured tensile sample at 21 ^{0}C, (SA - 950 ^{0}C x 3 hrs + Age – 600 ^{0}C x 4 hrs); Original Magnification – 200x	130
4.70	SEM micrograph of fractured tensile sample at 21 ^{0}C, (SA - 950 ^{0}C x 3 hrs + Age – 600 ^{0}C x 4 hrs); Original Magnification – 1000x	130
4.71	SEM micrograph of fractured tensile sample at 21 ^{0}C, (SA - 950 ^{0}C x 3 hrs + Age – 600 ^{0}C x 4 hrs); Original Magnification – 2000x	130
4.72	– SEM micrograph of fractured tensile sample at 450 ^{0}C, (SA - 950 ^{0}C x 3 hrs + Age – 600 ^{0}C x 4 hrs); Original Magnification – 33x	131
4.73	SEM micrograph of fractured tensile sample at 450 ^{0}C, (SA - 950 ^{0}C x 3 hrs + Age – 600 ^{0}C x 4 hrs); Original Magnification – 200x	131
4.74	SEM micrograph of fractured tensile sample at 450 ^{0}C, (SA - 950 ^{0}C x 3 hrs + Age – 600 ^{0}C x 4 hrs); Original Magnification – 1000x	131
4.75	SEM micrograph of fractured tensile sample at 450 ^{0}C, (SA - 950 ^{0}C x 3 hrs + Age – 600 ^{0}C x 4 hrs); Original Magnification – 2000x	131

Figure Number	Figure Caption	Page Number
4.76	SEM micrograph of fractured charpy sample (SA - 950 ^{0}C x 3 hrs + Age – 600 ^{0}C x 4 hrs); Original Magnification – 50x	132
4.77	SEM micrograph of fractured charpy sample (SA - 950 ^{0}C x 3 hrs + Age – 600 ^{0}C x 4 hrs); Original Magnification – 200x	132
4.78	SEM micrograph of fractured charpy sample (SA - 950 ^{0}C x 3 hrs + Age – 600 ^{0}C x 4 hrs); Original Magnification – 1000x	132
4.79	SEM micrograph of fractured tensile sample at 21 ^{0}C, (SA - 950 ^{0}C x 3 hrs + Age – 600 ^{0}C x 8 hrs); Original Magnification – 33x	133
4.80	SEM micrograph of fractured tensile sample at 21 ^{0}C, (SA - 950 ^{0}C x 3 hrs + Age – 600 ^{0}C x 8 hrs); Original Magnification – 200x	133
4.81	SEM micrograph of fractured tensile sample at 21 ^{0}C, (SA - 950 ^{0}C x 3 hrs + Age – 600 ^{0}C x 8 hrs); Original Magnification – 1000x	133
4.82	SEM micrograph of fractured tensile sample at 21 ^{0}C, (SA - 950 ^{0}C x 3 hrs + Age – 600 ^{0}C x 8 hrs); Original Magnification – 2000x	133
4.83	SEM micrograph of fractured tensile sample at 450 ^{0}C (SA - 950 ^{0}C x 3 hrs + Age – 600 ^{0}C x 8 hrs); Original Magnification – 33x	134
4.84	SEM micrograph of fractured tensile sample at 450 ^{0}C (SA - 950 ^{0}C x 3 hrs + Age – 600 ^{0}C x 8 hrs); Original Magnification – 200x	134
4.85	SEM micrograph of fractured tensile sample at 450 ^{0}C (SA - 950 ^{0}C x 3 hrs + Age – 600 ^{0}C x 8 hrs); Original Magnification – 1000x	134
4.86	SEM micrograph of fractured tensile sample at 450 ^{0}C (SA - 950 ^{0}C x 3 hrs + Age – 600 ^{0}C x 8 hrs); Original Magnification – 2000x	134
4.87	SEM micrograph of fractured charpy sample (SA - 950 ^{0}C x 3 hrs + Age – 600 ^{0}C x 4 hrs); Original Magnification – 50x	135
4.88	SEM micrograph of fractured charpy sample (SA - 950 ^{0}C x 3 hrs + Age – 600 ^{0}C x 4 hrs); Original Magnification – 200x	135
4.89	SEM micrograph of fractured charpy sample (SA - 950 ^{0}C x 3 hrs + Age – 600 ^{0}C x 4 hrs); Original Magnification – 1000x	135
4.90	SEM micrograph of fractured tensile sample at 21 ^{0}C, (SA - 950 ^{0}C x 3 hrs + Age – 600 ^{0}C x 12 hrs); Original Magnification – 33x	136

Figure Number	Figure Caption	Page Number
4.91	SEM micrograph of fractured tensile sample at 21 ^{0}C, (SA - 950 ^{0}C x 3 hrs + Age – 600 ^{0}C x 12 hrs); Original Magnification – 500x	136
4.92	SEM micrograph of fractured tensile sample at 21 ^{0}C, (SA - 950 ^{0}C x 3 hrs + Age – 600 ^{0}C x 12 hrs); Original Magnification – 1000x	136
4.93	SEM micrograph of fractured tensile sample at 21 ^{0}C, (SA - 950 ^{0}C x 3 hrs + Age – 600 ^{0}C x 12 hrs); Original Magnification – 2000x	136
4.94	SEM micrograph of fractured tensile sample at 450 ^{0}C (SA - 950 ^{0}C x 3 hrs + Age – 600 ^{0}C x 12 hrs); Original Magnification – 33x	137
4.95	SEM micrograph of fractured tensile sample at 450 ^{0}C (SA - 950 ^{0}C x 3 hrs + Age – 600 ^{0}C x 12 hrs); Original Magnification – 500x	137
4.96	SEM micrograph of fractured tensile sample at 450 ^{0}C (SA - 950 ^{0}C x 3 hrs + Age – 600 ^{0}C x 12 hrs); Original Magnification – 1000x	137
4.97	SEM micrograph of fractured tensile sample at 450 ^{0}C (SA - 950 ^{0}C x 3 hrs + Age – 600 ^{0}C x 12 hrs); Original Magnification – 2000x	137
4.98	SEM micrograph of fractured charpy sample (SA - 950 ^{0}C x 3 hrs + Age – 600 ^{0}C x 12 hrs); Original Magnification – 50x	138
4.99	SEM micrograph of fractured charpy sample (SA - 950 ^{0}C x 3 hrs + Age – 600 ^{0}C x 12 hrs); Original Magnification – 500x	138
4.100	SEM micrograph of fractured charpy sample (SA - 950 ^{0}C x 3 hrs + Age – 600 ^{0}C x 12 hrs); Original Magnification – 1000x	138
4.101	SEM micrograph of fractured tensile sample at 21 ^{0}C, (SA - 950 ^{0}C x 3 hrs + Age – 640 ^{0}C x 4 hrs); Original Magnification – 33x	139
4.102	SEM micrograph of fractured tensile sample at 21 ^{0}C, (SA - 950 ^{0}C x 3 hrs + Age – 640 ^{0}C x 4 hrs); Original Magnification – 500x	139
4.103	SEM micrograph of fractured tensile sample at 21 ^{0}C, (SA - 950 ^{0}C x 3 hrs + Age – 640 ^{0}C x 4 hrs); Original Magnification – 1000x	139
4.104	SEM micrograph of fractured tensile sample at 21 ^{0}C, (SA - 950 ^{0}C x 3 hrs + Age – 640 ^{0}C x 4 hrs); Original Magnification – 2000x	139
4.105	SEM micrograph of fractured tensile sample at 450 ^{0}C (SA - 950 ^{0}C x 3 hrs + Age – 640 ^{0}C x 4 hrs); Original Magnification – 33x	140

Figure Number	Figure Caption	Page Number
4.106	SEM micrograph of fractured tensile sample at 450 ^{0}C (SA - 950 ^{0}C x 3 hrs + Age – 640 ^{0}C x 4 hrs); Original Magnification – 500x	140
4.107	SEM micrograph of fractured tensile sample at 450 ^{0}C (SA - 950 ^{0}C x 3 hrs + Age – 640 ^{0}C x 4 hrs); Original Magnification – 1000x	140
4.108	SEM micrograph of fractured tensile sample at 450 ^{0}C (SA - 950 ^{0}C x 3 hrs + Age – 640 ^{0}C x 4 hrs); Original Magnification – 2000x	140
4.109	SEM micrograph of fractured charpy sample (SA - 950 ^{0}C x 3 hrs + Age – 640 ^{0}C x 4 hrs); Original Magnification – 50x	141
4.110	SEM micrograph of fractured charpy sample (SA - 950 ^{0}C x 3 hrs + Age – 640 ^{0}C x 4 hrs); Original Magnification – 500x	141
4.111	SEM micrograph of fractured charpy sample (SA - 950 ^{0}C x 3 hrs + Age – 640 ^{0}C x 4 hrs); Original Magnification – 1000x	141
4.112	SEM micrograph of fractured tensile sample at 21 ^{0}C, (SA - 1120 ^{0}C x 3 hrs + Age – 640 ^{0}C x 8 hrs); Original Magnification – 33x	142
4.113	SEM micrograph of fractured tensile sample at 21 ^{0}C, (SA - 1120 ^{0}C x 3 hrs + Age – 640 ^{0}C x 8 hrs); Original Magnification – 500x	142
4.114	SEM micrograph of fractured tensile sample at 21 ^{0}C, (SA - 1120 ^{0}C x 3 hrs + Age – 640 ^{0}C x 8 hrs); Original Magnification – 1000x	142
4.115	SEM micrograph of fractured tensile sample at 21 ^{0}C, (SA - 1120 ^{0}C x 3 hrs + Age – 640 ^{0}C x 8 hrs); Original Magnification – 1500x	142
4.116	SEM micrograph of fractured tensile sample at 450 ^{0}C (SA - 1120 ^{0}C x 3 hrs + Age – 640 ^{0}C x 8 hrs); Original Magnification – 33x	143
4.117	SEM micrograph of fractured tensile sample at 450 ^{0}C (SA - 1120 ^{0}C x 3 hrs + Age – 640 ^{0}C x 8 hrs); Original Magnification – 500x	143
4.118	SEM micrograph of fractured tensile sample at 450 ^{0}C (SA - 1120 ^{0}C x 3 hrs + Age – 640 ^{0}C x 8 hrs); Original Magnification – 1000x	143
4.119	SEM micrograph of fractured tensile sample at 450 ^{0}C (SA - 1120 ^{0}C x 3 hrs + Age – 640 ^{0}C x 8 hrs); Original Magnification – 2000x	143

Figure Number	Figure Caption	Page Number
4.120	SEM micrograph of fractured charpy sample (SA - 1120 ^{0}C x 3 hrs + Age – 640 ^{0}C x 8 hrs); Original Magnification – 50x	144
4.121	SEM micrograph of fractured charpy sample (SA - 1120 ^{0}C x 3 hrs + Age – 640 ^{0}C x 8 hrs); Original Magnification – 500x	144
4.122	SEM micrograph of fractured charpy sample (SA - 1120 ^{0}C x 3 hrs + Age – 640 ^{0}C x 8 hrs); Original Magnification – 1000x	144
4.123	SEM micrograph of fractured tensile sample at 21 ^{0}C, (SA - 1120 ^{0}C x 3 hrs + Age – 640 ^{0}C x 12 hrs); Original Magnification – 30x	145
4.124	SEM micrograph of fractured tensile sample at 21 ^{0}C, (SA - 1120 ^{0}C x 3 hrs + Age – 640 ^{0}C x 12 hrs); Original Magnification – 500x	145
4.125	SEM micrograph of fractured tensile sample at 21 ^{0}C, (SA - 1120 ^{0}C x 3 hrs + Age – 640 ^{0}C x 12 hrs); Original Magnification – 1000x	145
4.126	SEM micrograph of fractured tensile sample at 21 ^{0}C, (SA - 1120 ^{0}C x 3 hrs + Age – 640 ^{0}C x 12 hrs); Original Magnification – 1500x	145
4.127	SEM micrograph of fractured tensile sample at 450 ^{0}C (SA - 1120 ^{0}C x 3 hrs + Age – 640 ^{0}C x 12 hrs); Original Magnification – 35x	146
4.128	SEM micrograph of fractured tensile sample at 450 ^{0}C (SA - 1120 ^{0}C x 3 hrs + Age – 640 ^{0}C x 12 hrs); Original Magnification – 1500x	146
4.129	SEM micrograph of fractured tensile sample at 450 ^{0}C (SA - 1120 ^{0}C x 3 hrs + Age – 640 ^{0}C x 12 hrs); Original Magnification – 1000x	146
4.130	SEM micrograph of fractured tensile sample at 450 ^{0}C (SA - 1120 ^{0}C x 3 hrs + Age – 640 ^{0}C x 12 hrs); Original Magnification – 2000x	146
4.131	SEM micrograph of fractured charpy sample (SA - 1120 ^{0}C x 3 hrs + Age – 640 ^{0}C x 12 hrs); Original Magnification – 50x	147
4.132	SEM micrograph of fractured charpy sample (SA - 1120 ^{0}C x 3 hrs + Age – 640 ^{0}C x 12 hrs); Original Magnification – 500x	147
4.133	SEM micrograph of fractured charpy sample (SA - 1120 ^{0}C x 3 hrs + Age – 640 ^{0}C x 12 hrs); Original Magnification – 1000x	147
4.134	SEM micrograph of fractured tensile sample at 21 ^{0}C, (SA - 1120 ^{0}C x 3 hrs + Age – 640 ^{0}C x 4 hrs); Original Magnification – 33x	148

Figure Number	Figure Caption	Page Number
4.135	SEM micrograph of fractured tensile sample at 21 ^{0}C, (SA - 1120 ^{0}C x 3 hrs + Age – 640 ^{0}C x 4 hrs); Original Magnification – 500x	148
4.136	SEM micrograph of fractured tensile sample at 21 ^{0}C, (SA - 1120 ^{0}C x 3 hrs + Age – 640 ^{0}C x 4 hrs); Original Magnification – 1000x	148
4.137	SEM micrograph of fractured tensile sample at 21 ^{0}C, (SA - 1120 ^{0}C x 3 hrs + Age – 640 ^{0}C x 4 hrs); Original Magnification – 2000x	148
4.138	SEM micrograph of fractured tensile sample at 450 ^{0}C (SA - 1120 ^{0}C x 3 hrs + Age – 640 ^{0}C x 4 hrs); Original Magnification – 35x	149
4.139	SEM micrograph of fractured tensile sample at 450 ^{0}C (SA - 1120 ^{0}C x 3 hrs + Age – 640 ^{0}C x 4 hrs); Original Magnification – 500x	149
4.140	SEM micrograph of fractured tensile sample at 450 ^{0}C (SA - 1120 ^{0}C x 3 hrs + Age – 640 ^{0}C x 4 hrs); Original Magnification – 1000x	149
4.141	SEM micrograph of fractured tensile sample at 450 ^{0}C (SA - 1120 ^{0}C x 3 hrs + Age – 640 ^{0}C x 4 hrs); Original Magnification – 2000x	149
4.142	SEM micrograph of fractured charpy sample (SA - 1120 ^{0}C x 3 hrs + Age – 640 ^{0}C x 4 hrs); Original Magnification – 50x	150
4.143	SEM micrograph of fractured charpy sample (SA - 1120 ^{0}C x 3 hrs + Age – 640 ^{0}C x 4 hrs); Original Magnification – 500x	150
4.144	SEM micrograph of fractured charpy sample (SA - 1120 ^{0}C x 3 hrs + Age – 640 ^{0}C x 4 hrs); Original Magnification – 1500x	150
4. 145	SEM micrograph of fractured tensile sample at 21 ^{0}C, (SA - 1120 ^{0}C x 3 hrs + Age – 600 ^{0}C x 8 hrs); Original Magnification – 33x	151
4.146	SEM micrograph of fractured tensile sample at 21 ^{0}C, (SA - 1120 ^{0}C x 3 hrs + Age – 600 ^{0}C x 8 hrs); Original Magnification – 500x	151
4.147	SEM micrograph of fractured tensile sample at 21 ^{0}C, (SA - 1120 ^{0}C x 3 hrs + Age – 600 ^{0}C x 8 hrs); Original Magnification – 1000x	151
4.148	SEM micrograph of fractured tensile sample at 21 ^{0}C, (SA - 1120 ^{0}C x 3 hrs + Age – 600 ^{0}C x 8 hrs); Original Magnification – 2000x	151
4.149	SEM micrograph of fractured tensile sample at 450 ^{0}C (SA - 1120 ^{0}C x 3 hrs + Age – 600 ^{0}C x 8 hrs); Original Magnification – 33x	152

Figure Number	Figure Caption	Page Number
4.150	SEM micrograph of fractured tensile sample at 450 ^{0}C (SA - 1120 ^{0}C x 3 hrs + Age – 600 ^{0}C x 8 hrs); Original Magnification – 400x	152
4.151	SEM micrograph of fractured tensile sample at 450 ^{0}C (SA - 1120 ^{0}C x 3 hrs + Age – 600 ^{0}C x 8 hrs); Original Magnification – 1000x	152
4.152	SEM micrograph of fractured tensile sample at 450 ^{0}C (SA - 1120 ^{0}C x 3 hrs + Age – 600 ^{0}C x 8 hrs); Original Magnification – 2000x	152
4.153	SEM micrograph of fractured charpy sample (SA - 1120 ^{0}C x 3 hrs + Age – 600 ^{0}C x 8 hrs); Original Magnification – 50x	153
4.154	SEM micrograph of fractured charpy sample (SA - 1120 ^{0}C x 3 hrs + Age – 600 ^{0}C x 8 hrs); Original Magnification – 500x	153
4.155	SEM micrograph of fractured charpy sample (SA - 1120 ^{0}C x 3 hrs + Age – 600 ^{0}C x 8 hrs); Original Magnification – 1000x	153
4.156	SEM micrograph of fractured stress rupture sample (SA - 1120 ^{0}C x 3 hrs + Age – 600 ^{0}C x 8 hrs); Original Magnification – 50x	154
4.157	SEM micrograph of fractured stress rupture sample (SA - 1120 ^{0}C x 3 hrs + Age – 600 ^{0}C x 8 hrs); Original Magnification – 500x	154
4.158	SEM micrograph of fractured stress rupture sample (SA - 1120 ^{0}C x 3 hrs + Age – 600 ^{0}C x 8 hrs); Original Magnification – 1000x	154
4.159	SEM micrograph of fractured stress rupture sample (SA - 1120 ^{0}C x 3 hrs + Age – 600 ^{0}C x 8 hrs); Original Magnification – 2000x	154
4.160	SEM micrograph of fractured tensile sample at 21 ^{0}C, (SA - 1120 ^{0}C x 3 hrs + Age – 600 ^{0}C x 12 hrs); Original Magnification – 33x	155
4.161	SEM micrograph of fractured tensile sample at 21 ^{0}C, (SA - 1120 ^{0}C x 3 hrs + Age – 600 ^{0}C x 12 hrs); Original Magnification – 500x	155
4.162	SEM micrograph of fractured tensile sample at 21 ^{0}C, (SA - 1120 ^{0}C x 3 hrs + Age – 600 ^{0}C x 12 hrs); Original Magnification – 1000x	155
4.163	SEM micrograph of fractured tensile sample at 21 ^{0}C, (SA - 1120 ^{0}C x 3 hrs + Age – 600 ^{0}C x 12 hrs); Original Magnification – 2000x	155

Figure Number	Figure Caption	Page Number
4.164	SEM micrograph of fractured tensile sample at 450 ^{0}C (SA - 1120 ^{0}C x 3 hrs + Age – 600 ^{0}C x 12 hrs); Original Magnification – 35x	156
4.165	SEM micrograph of fractured tensile sample at 450 ^{0}C (SA - 1120 ^{0}C x 3 hrs + Age – 600 ^{0}C x 12 hrs); Original Magnification – 500x	156
4.166	SEM micrograph of fractured tensile sample at 450 ^{0}C (SA - 1120 ^{0}C x 3 hrs + Age – 600 ^{0}C x 12 hrs); Original Magnification – 1000x	156
4.167	SEM micrograph of fractured tensile sample at 450 ^{0}C (SA - 1120 ^{0}C x 3 hrs + Age – 600 ^{0}C x 12 hrs); Original Magnification – 2000x	156
4.168	SEM micrograph of fractured charpy sample (SA - 1120 ^{0}C x 3 hrs + Age – 600 ^{0}C x 12 hrs); Original Magnification – 50x	157
4.169	SEM micrograph of fractured charpy sample (SA - 1120 ^{0}C x 3 hrs + Age – 600 ^{0}C x 12 hrs); Original Magnification – 500x	157
4.170	SEM micrograph of fractured charpy sample (SA - 1120 ^{0}C x 3 hrs + Age – 600 ^{0}C x 12 hrs); Original Magnification – 1500x	157
4.171	SEM micrograph of fractured stress rupture sample (SA - 1120 ^{0}C x 3 hrs + Age – 600 ^{0}C x 12 hrs); Original Magnification – 50x	158
4.172	SEM micrograph of fractured stress rupture sample (SA - 1120 ^{0}C x 3 hrs + Age – 600 ^{0}C x 12 hrs); Original Magnification – 400x	158
4.173	SEM micrograph of fractured stress rupture sample (SA - 1120 ^{0}C x 3 hrs + Age – 600 ^{0}C x 12 hrs); Original Magnification – 500x	158
4.174	SEM micrograph of fractured stress rupture sample (SA - 1120 ^{0}C x 3 hrs + Age – 600 ^{0}C x 12 hrs); Original Magnification – 1500x	158
4.175	SEM micrograph of fractured tensile sample at 21 ^{0}C, (SA - 1120 ^{0}C x 3 hrs + Age – 600 ^{0}C x 4 hrs); Original Magnification – 33x	159
4.176	SEM micrograph of fractured tensile sample at 21 ^{0}C, (SA - 1120 ^{0}C x 3 hrs + Age – 600 ^{0}C x 4 hrs); Original Magnification – 500x	159
4.177	SEM micrograph of fractured tensile sample at 21 ^{0}C, (SA - 1120 ^{0}C x 3 hrs + Age – 600 ^{0}C x 4 hrs); Original Magnification – 1000x	159
4.178	SEM micrograph of fractured tensile sample at 21 ^{0}C, (SA - 1120 ^{0}C x 3 hrs + Age – 600 ^{0}C x 4 hrs); Original Magnification – 2000x	159

Figure Number	Figure Caption	Page Number
4.179	SEM micrograph of fractured tensile sample at 450 ^{0}C, (SA - 1120 ^{0}C x 3 hrs + Age – 600 ^{0}C x 4 hrs); Original Magnification – 33x	160
4.180	SEM micrograph of fractured tensile sample at 450 ^{0}C, (SA - 1120 ^{0}C x 3 hrs + Age – 600 ^{0}C x 4 hrs); Original Magnification – 500x	160
4.181	SEM micrograph of fractured tensile sample at 450 ^{0}C, (SA - 1120 ^{0}C x 3 hrs + Age – 600 ^{0}C x 4 hrs); Original Magnification – 1000x	160
4.182	SEM micrograph of fractured tensile sample at 450 ^{0}C, (SA - 1120 ^{0}C x 3 hrs + Age – 600 ^{0}C x 4 hrs); Original Magnification – 2000x	160
4.183	SEM micrograph of fractured charpy sample (SA - 1120 ^{0}C x 3 hrs + Age – 600 ^{0}C x 4 hrs); Original Magnification – 50x	161
4.184	SEM micrograph of fractured charpy sample (SA - 1120 ^{0}C x 3 hrs + Age – 600 ^{0}C x 4 hrs); Original Magnification – 500x	161
4.185	SEM micrograph of fractured charpy sample (SA - 1120 ^{0}C x 3 hrs + Age – 600 ^{0}C x 4 hrs); Original Magnification – 1000x	161
4.186	SEM micrograph of fractured stress rupture sample (SA - 1120 ^{0}C x 3 hrs + Age – 600 ^{0}C x 4 hrs); Original Magnification – 50x	162
4.187	SEM micrograph of fractured stress rupture sample (SA - 1120 ^{0}C x 3 hrs + Age – 600 ^{0}C x 4 hrs); Original Magnification – 500x	162
4.188	SEM micrograph of fractured stress rupture sample (SA - 1120 ^{0}C x 3 hrs + Age – 600 ^{0}C x 4 hrs); Original Magnification – 1000x	162
4.189	SEM micrograph of fractured stress rupture sample (SA - 1120 ^{0}C x 3 hrs + Age – 600 ^{0}C x 4 hrs); Original Magnification – 2000x	162
4.190	SEM micrograph of fractured tensile sample at 21 ^{0}C, (SA - 950 ^{0}C x 3 hrs + Age – 640 ^{0}C x 8 hrs); Original Magnification – 33x	163
4.191	SEM micrograph of fractured tensile sample at 21 ^{0}C, (SA - 950 ^{0}C x 3 hrs + Age – 640 ^{0}C x 8 hrs); Original Magnification – 300x	163
4.192	SEM micrograph of fractured tensile sample at 21 ^{0}C, (SA - 950 ^{0}C x 3 hrs + Age – 640 ^{0}C x 8 hrs); Original Magnification – 500x	163
4.193	SEM micrograph of fractured tensile sample at 21 ^{0}C, (SA - 950 ^{0}C x 3 hrs + Age – 640 ^{0}C x 8 hrs); Original Magnification – 2000x	163

Figure Number	Figure Caption	Page Number
4.194	SEM micrograph of fractured tensile sample at 450 ^{0}C, (SA - 950 ^{0}C x 3 hrs + Age – 640 ^{0}C x 8 hrs); Original Magnification – 33x	164
4.195	SEM micrograph of fractured tensile sample at 450 ^{0}C, (SA - 950 ^{0}C x 3 hrs + Age – 640 ^{0}C x 8 hrs); Original Magnification – 500x	164
4.196	SEM micrograph of fractured tensile sample at 450 ^{0}C, (SA - 950 ^{0}C x 3 hrs + Age – 640 ^{0}C x 8 hrs); Original Magnification – 1000x	164
4.197	SEM micrograph of fractured tensile sample at 450 ^{0}C, (SA - 950 ^{0}C x 3 hrs + Age – 640 ^{0}C x 8 hrs); Original Magnification – 2000x	164
4.198	SEM micrograph of fractured charpy sample (SA - 950 ^{0}C x 3 hrs + Age – 640 ^{0}C x 8 hrs); Original Magnification – 50x	165
4.199	SEM micrograph of fractured charpy sample (SA - 950 ^{0}C x 3 hrs + Age – 640 ^{0}C x 8 hrs); Original Magnification – 500x	165
4.200	SEM micrograph of fractured charpy sample (SA - 950 ^{0}C x 3 hrs + Age – 640 ^{0}C x 8 hrs); Original Magnification – 1000x	165
4.201	SEM micrograph of fractured tensile sample at 21 ^{0}C, (SA - 950 ^{0}C x 3 hrs + Age – 640 ^{0}C x 12 hrs); Original Magnification – 30x	166
4.202	SEM micrograph of fractured tensile sample at 21 ^{0}C, (SA - 950 ^{0}C x 3 hrs + Age – 640 ^{0}C x 12 hrs); Original Magnification – 500x	166
4.203	SEM micrograph of fractured tensile sample at 21 ^{0}C, (SA - 950 ^{0}C x 3 hrs + Age – 640 ^{0}C x 12 hrs); Original Magnification – 1000x	166
4.204	SEM micrograph of fractured tensile sample at 21 ^{0}C, (SA - 950 ^{0}C x 3 hrs + Age – 640 ^{0}C x 12 hrs); Original Magnification – 2000x	166
4.205	SEM micrograph of fractured tensile sample at 450 ^{0}C, (SA - 950 ^{0}C x 3 hrs + Age – 640 ^{0}C x 12 hrs); Original Magnification – 33x	167
4.206	SEM micrograph of fractured tensile sample at 450 ^{0}C, (SA - 950 ^{0}C x 3 hrs + Age – 640 ^{0}C x 12 hrs); Original Magnification – 500x	167
4.207	SEM micrograph of fractured tensile sample at 450 ^{0}C, (SA - 950 ^{0}C x 3 hrs + Age – 640 ^{0}C x 12 hrs); Original Magnification – 1000x	167
4.208	SEM micrograph of fractured tensile sample at 450 ^{0}C, (SA - 950 ^{0}C x 3 hrs + Age – 640 ^{0}C x 12 hrs); Original Magnification – 2000x	167

Figure Number	Figure Caption	Page Number
4.209	SEM micrograph of fractured charpy sample (SA - 950 ^{0}C x 3 hrs + Age – 640 ^{0}C x 12 hrs); Original Magnification – 50x	168
4.210	SEM micrograph of fractured charpy sample (SA - 950 ^{0}C x 3 hrs + Age – 640 ^{0}C x 12 hrs); Original Magnification – 500x	168
4.211	SEM micrograph of fractured charpy sample (SA - 950 ^{0}C x 3 hrs + Age – 640 ^{0}C x 12 hrs); Original Magnification – 1000x	168
5.1	Replication Locations at Dove Tail areas shown by arrows	175
5.2	Replication Location at the Bore area shown by arrow	175
5.3	Micrograph of replica at bore area showing carbide precipitation; Original Magnification – 500x	176
5.4	SEM micrograph of replica at dove tail area showing significant carbide precipitation; Original Magnification – 1000x	176
5.5	Schaeffler diagram for A-286 alloy	181
5.6	Schematic showing the carbides and restoration of microstructure after rejuvenation heat treatment in A-286 alloy	185
6.1	Life Cycle Management of Turbine Wheel - Flow Chart	209

List of Tables

Table Number	Table Caption	Page Number
3.1	Dimensions of the individual sections obtained from the block	63
3.2	Pilot Solution Annealing Heat Treatments	67
3.3	Planned Solution Annealing (SA) and Ageing (Age) Heat Treatments	67
4.1	Chemical Composition by Optical Spectrometer	87
4.2	Chemical Composition by XRF	88
4.3	Portable hardness testing readings of the serviced turbine block	92
4.4	Microexamination Observations for as new A-286 bar, serviced turbine wheel, pilot heat treatments and conducted heat treatments	104
4.5	EDAX analysis of carbides of serviced turbine wheel	107
4.6	Microhardness Test Results	110
4.7	Results of Room Temperature and High Temperature Tensile Test	112
4.8	Results of Room Temperature Charpy Impact Test	116
4.9	Results of Stress Rupture Test	118
4.10	Compiled Results of Mechanical Tests	120
4.11	Fracture Morphology Details for Samples in as Received Condition and after Pilot Heat Treatments	169
4.12	Fracture Morphology Observations for Samples after Heat Treatments	170
5.1	Operating History of the A-286 Wheel	174

CHAPTER 1

INTRODUCTION

1.1 MOTIVATION

Gas turbine is the versatile item of turbomachinery as of today and has a widespread application in several industries. Prime industries such as power generation, oil and gas, process plants, aviation use gas turbines. The first successful gas turbine was built in 1903, which comprised of a three-cylinder, multistage compressor, a combustion chamber and an impulse turbine [1]. The largest gas turbines today are over 200 MW (megawatts). The smallest capacity of gas turbine is as low as 50 KW (kilowatts). The demand for gas turbines has been escalating since last few years. It is interesting to know the region-wise gas turbine spread across the globe. As per the data published in October 2017, the population of gas turbines in Asia-Pacific region is 40%, 25% in Europe, 15% in Middle East and Africa, 15% in North America and 5% in Latin America [2].

United States, gas turbine market share is anticipated to expand over 8% by 2024. The Europe, United Kingdom gas turbine market size for 2015 was valued over USD 180 million. The China gas turbine market is expected to exceed over 10% by 2024. The Indian gas turbine market is predicted to witness strong growth of over 12% by 2024. Saudi Arabia gas turbine market revenue was valued over USD 1 billion in 2015 [3]. Gas turbines are an essential part of distributed power

technologies, and the growth of distributed power systems will accelerate the demand for gas turbines in the coming years. The market research predicts the global gas turbine market trend is inclined to grow at a steady annual growth rate of 3% by 2020 [4].

The gas turbine operating principle is easy to understand. Gas turbine continuously draws fresh air in and the drawn air is compressed to higher pressure in the compressor section. The compressor consists of a rotor with various stages of compressor wheels. Each stage of compressor wheel has blades mounted on it, which are known as compressor blades. In the combustion zone, fuel is added to compressed air and burnt to release its energy. The high-pressure, high-temperature air is than directed to expansion turbine that converts gas energy to mechanical energy [5]. The turbine section consists of turbine wheels on which vanes are mounted. One of the most robust and heavy-duty gas turbines is the General Electric Frame 3002 and Frame 5002 models. The Frame 3002 and 5002 gas turbines have twin shaft rotors. The turbine wheel is made up of A-286 alloy, which is iron-based super alloy [6].

It is a routine practice in the gas turbine industry to carry out repairs on gas turbine components. The repairs include rejuvenation heat treatments on rotating gas turbine components such as vanes [7]. The vanes are mounted on the turbine wheels. Rejuvenation heat treatment is required as the microstructure of the vanes deteriorates after a long-term service (more than 48k hours of operation) leading to reduced mechanical and creep properties [8]. Thus, the rejuvenation heat treatment on the vanes recovers the original microstructure. On recovery of the

original microstructure, the vanes can then be again continued in service [9]. Therefore, concisely the rejuvenation heat treatment essentially prolongs the life of the vanes, and hence the term “life extension”. Moreover, the replacement of the vanes is not economical, hence rejuvenation heat treatment provides a viable solution for continuation of vanes in service.

Additionally, another industrial practice is to conduct condition assessment studies on gas turbine rotors [10]. Such studies comprise of non-destructive tests to assess the health of the rotor components [11]. Moreover, there have been demanding business challenges within the gas turbine industry. These challenges are as follows:

- As per the Original Equipment Manufacturers (OEM) specifications, the A-286 material gas turbine wheels are decommissioned or replaced from service after 200k hours of operation [12].
- Any unexpected outages due to any failures in gas turbine results in high costs for repair and replacement of the components. This reduces plant availability, eventually causing a loss in net revenue. Due to the forced outages, there is loss of man hours required to make the gas turbine available in service. The potential cost to return a gas turbine unit back to service due to a particular outage event can be estimated. It is the product of the maintenance cost per event times the probability of the event occurring for a designated time period. Similarly, the risk of lost revenue due to an event can be estimated as the product of the lost revenue per event times its probability. The overall probable cost associated with that

event is the sum of the cost to return the unit to service, plus the lost net revenue [13].

- The gas turbine users have been strongly seeking a viable approach to continue the A-286 wheels in service beyond the prescribed 200k hours of operation. This is because the replacement cost of each wheel is about 120K USD, which is not economical. The end users are interested to know, if these wheels could potentially be continued in service beyond 200k hours of operation. The basis of continuation in service could be a methodological inspection and rejuvenation heat treatments [14, 15].

In lieu of the above discussed daunting business and technical scenarios, it was thus hypothesized, that, the rejuvenation heat treatment approach might be applied to gas turbine wheels. If the rejuvenation heat treatment works for the gas turbine vanes, it should as well work for the turbine wheels. Thus, this rejuvenation heat treatment would not only aid in life extension, but also could potentially save over 300K dollars and man hours. This forms the basis and prime motivation for this research.

1.2 RESEARCH NEED

The current industrial scenario and as explained in the earlier section thus demands an extension of the life of the gas turbine wheels beyond the designed life [16, 17]. Frame 3002 and Frame 5002 gas turbines can be classified as two-shaft, heavy duty gas turbines which are designed for high operating efficiency to cover a broad range of speed and loading conditions [18]. The gas turbine wheels

for these machines are made of an A-286 material, which is an iron-based super alloy [19]. The chemical composition of A-286 alloy consists of Ni-26%, Cr-15%, Mo-1.3%, Ti-2%, Fe-54%, Mn-1.3%.

Another pertinent interest of the end users being "Will there be any necessity of replacing the A-286 wheels after 200k hours, if they were maintained properly?" There may not be a need to replace the wheel, if the condition of the wheel is assessed and found to be good [20, 21]. This is because there are often damages that primarily occur in the A-286 gas turbine wheel due to microstructural and/or metallurgical transformations. The detrimental microstructural transformations in the form of creep voids, micro-cracks, formation of titanium or chromium carbides on the grain boundaries and formation of cellular phase could be evaluated [22]. In this way, the condition of the turbine wheel can be assessed, to ascertain any service damages incurred. Such assessments are routinely performed and are known as life extension studies. These life extension studies comprise of performing various non-destructive tests such as visual inspection, finite stress analysis, dye penetrant testing, ultrasonic flaw detection, eddy current test, replica metallography, on the wheel to check for any damages. Presently, the industry adapts the rejuvenation heat treatment as one of the Non-Destructive Testing approach to extend the life of the gas turbine components such as nozzles, transition pieces, liners and vanes.

As hypothesized earlier, the microstructural properties of the wheel could be enhanced by heat treatments leading to the rejuvenation of the microstructures.

The rejuvenation heat treatments have been a standard practice in the gas turbine industry for repairing turbine vanes after the long-term service.

The life extension of the turbine wheels by rejuvenation heat treatment is still an unexplored area. This area needs to be explored considering the potential business advantages and technical challenges. A thorough research is required to understand the nature of microstructural degradations, and the possible effects of various heat treatments on the microstructural improvement.

The present research work focuses on the study of the rejuvenation heat treatment of the A-286 wheels after long-term service. Thus the research outcomes, if positive, will prove beneficial to the end users primarily in the regions mentioned, and elsewhere in the world as well.

1.3 OVERVIEW

The gas turbine industry is a diverse industry having around 300 gas turbines with A-286 wheels in the Middle East region primarily in the Saudi Arabia and the United Arab Emirates. The power/electricity, oil and gas, chemical and petrochemical, and aircraft industries employ gas turbines on a day-to-day basis. They are also used by small-scale industries primarily for in-house power generation. The Frame 3002 and Frame 5002 heavy-duty gas turbines in the Middle East region are primarily used for power generation. The Frame 3002 gas turbines in total accounts for approximately 245 MW of power generation and Frame 5002 gas turbines accounts for approximately 6,937 MW of power generation [23].

1.3.1 GAS TURBINE WORKING PRINCIPLE

Apropos to the earlier mentioned relevance, it is now important to understand the basics of a gas turbine. A gas turbine can be classified as an internal combustion engine. The operating principle of a gas turbine is based on the Brayton cycle. In this cycle, fuel and compressed air are mixed together at a constant pressure and combustion takes place. At the room temperature, the air enters through the compressor end. In the compressor section, the pressure and temperature of the air is increased. The increase in air pressure and temperature depends on the capacity of the gas turbine. Then the high-pressure air passes through the combustion chamber, wherein the combustion of the fuel occurs at a constant pressure. Then the combustion gases present at high temperatures and pressures enter the turbine section. The combustion gases then expand to working pressures and emit energy or the required work [24]. A schematic diagram of the gas turbine is shown in Figure 1.1., and the working principle is explained in the next section.

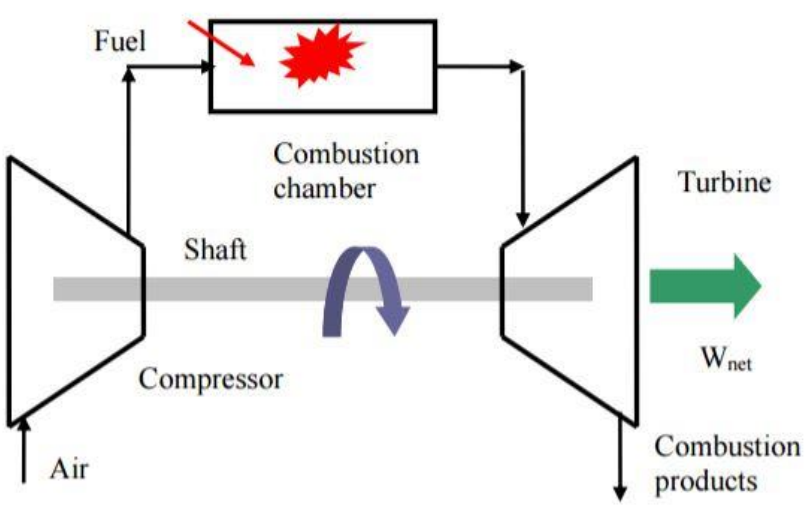

Figure 1.1: Schematic diagram of a gas turbine

1.3.2 CONSTRUCTION

The gas turbine primarily consists of a compressor section, combustion chamber, and a turbine section (Ref Fig 1.1). The gas turbine commonly comprises of a single shaft onto which the compressor and turbine are mounted. The rotor consists of a set of compressor wheels on which the compressor blades are mounted. This single shaft rotor normally rotates at 3,600-6,000 rpm [24]. Thus, a typical gas turbine consists of a generator, compressor, fuel injector, combustor, turbine and heat exchanger as shown in Figure 1.2.

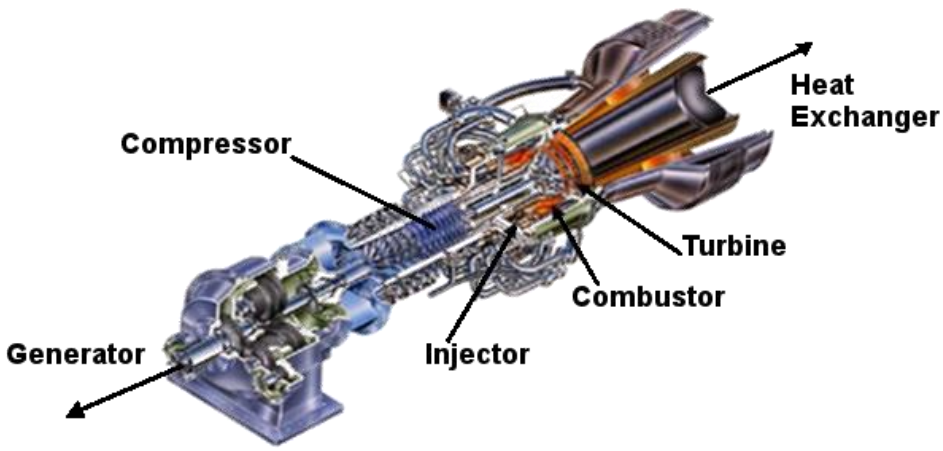

Figure 1.2: Different sections of gas turbine (Source: conservatoryhub.com)

Furthermore, the turbine section consists of a turbine wheel, on which the vanes are mounted as shown in Figure 1.3.

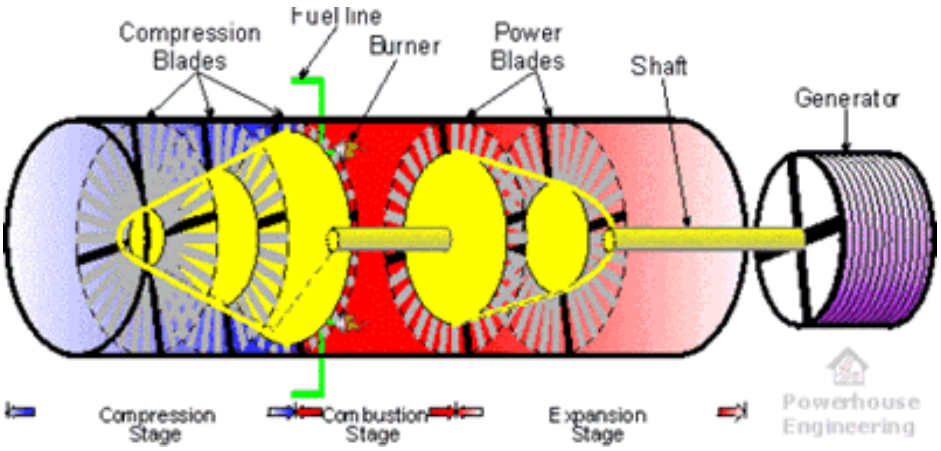

Figure 1.3: Various components of a gas turbine (Source: powerhousengineering.com)

During the compression stage, the air enters the compressor section and gets compressed by the compression blades of the first stage compressor wheel. The approximate compression is 25 times that of the original volume. This compressed air continuously propagates ahead to other stages and is further compressed to much lower volume (represented by dark blue in Figure 1.3). As the air is further compressed to reduce volume, it takes the shape of the turbine (shown as yellow cone in Figure 1.3). This compressor end is often referred to as the cold section.

While the compressor end forms the cold section, the hot section is the combustion area wherein the combustion takes place. The most common fuel used for combustion is the natural gas. The fuel burns in the combustion area/zone at a temperature in the range of 1000ºC to 1150ºC. The combustion gases are then allowed to expand and are directed towards the turbine vanes. A single shaft

connects both the compressor and the turbine sections. The energy that compressed the air in the compression section is actually the result of the force on the turbine section vanes. In most cases, the shaft on which the compressor and turbine are mounted is coupled to a generator for generating the electricity.

At this stage, it is important to understand the configuration of the turbine rotor assembly, as the focus of this research is the life extension of the A-286 gas turbine wheel. The turbine wheel is a part of the rotor assembly. The rotor consists of a compressor end and the turbine end. The compressor end consists of a rotor and has different stages. Each stage consists of a compressor wheel and there are in total 16 such stages. The compressor wheels are normally made of Cr-Mo steel or Ni-Cr-Mo steel. The compressor wheels have dove tail slots on which the compressor blades are mounted. The material of the compressor blades is SS 403 (12% Cr, 0.15% C, 1% Mn, 0.05% Si, Balance Fe). The turbine section comprises of a turbine wheel, and is made of A-286 (25% Ni, 15% Cr) or M152 (12% Cr, 2.5% Ni) material for Frame 3002 and Frame 5002 gas turbines. On the turbine wheel, vanes are mounted and that are made of GTD 111 or IN 738 (15% Cr, 9.5% Co, 3.85%W, Ni-balance) nickel based alloys. The Frame 5002 rotor assembly is shown in Figure 1.4.

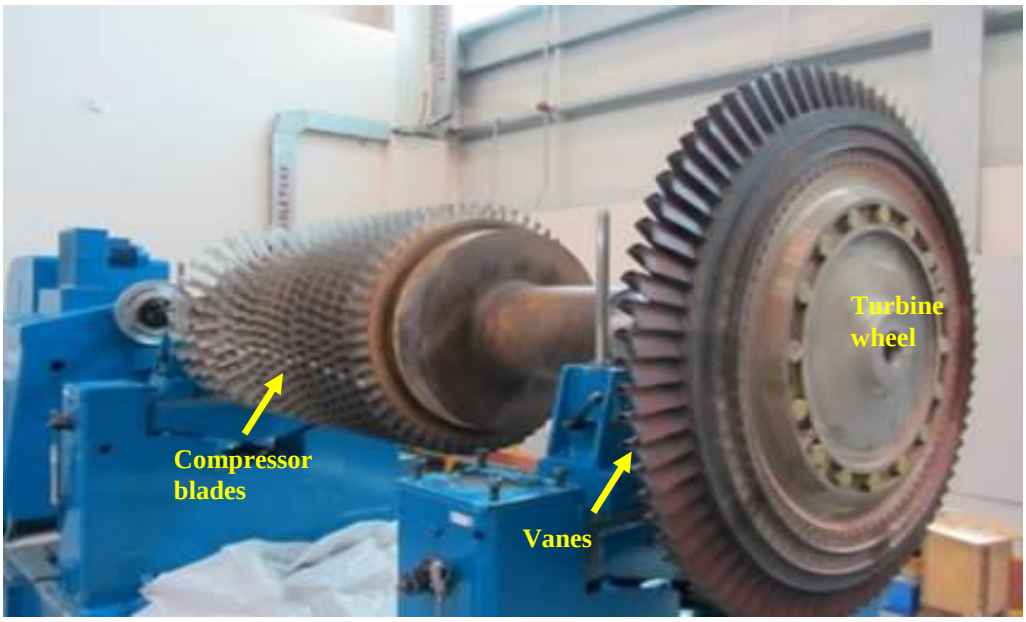

Figure 1.4: A Frame 5002 rotor assembly (Source: Masaood John Brown Rotor Workshop, Dubai)

1.4 IMPORTANCE OF LIFE EXTENSION

All over the world, many industries containing turbines have been in operation for more than 30 to 40 years. These plants have critical components and have been operating beyond their designated lifetimes. Currently, most of the combustion turbines use oil or natural gas as fuel. Some turbines also have the capability of using both oil and natural gas as fuel. Over the past and even today, combustion turbines have been an attractive source of power generation for various utilities. This is because of many factors such as its cost (relatively inexpensive) and the ease of installation. The utility users and owners look at these factors as an advantage against the high lead times in setting up the steam turbine plants and the uncertainties in the load growth projection. The efficiency of the combined cycle plants has increased considerably resulting in fuel cost savings. Combined-

cycle power plant uses steam and gas turbines together to generate 50 percent more electricity from the same fuel as compared to a simple-cycle plant [25]. There is an increasing trend towards the use of combustion turbines in combined-cycle plants. It is also projected that during the next decade the usage of combustion turbines would be growing significantly. The combined cycle plants and heat recovery system have critical components which have been in operation beyond their design life [26]. The critical components including gas turbines have aged and the plant owners and end users are significantly interested to run the critical components beyond their designed life. The replacement of components and purchase of critical components is not economical. Significant production losses are incurred due to the lead time of manufacturing and supply of new critical components. The plant owners therefore will be glad to continue with the critical plant components even after the designed life, with the life extension approach [27]. Life extension approach is focused on assessing the current condition of the critical components. Based on the inspection findings of the component, a decision is taken whether to continue, scrap or repair the component.

The life of the critical components could thus be extended beyond the designed life by condition assessment and life extension studies. Condition assessment and the remaining life analysis studies for rotating and stationary components of gas turbine comprise of non-destructive testing that are common in the industry [28]. A destructive test is recommended for a detail life assessment study, if there is a significant problem in the results of non-destructive testing.

There are many turbines in service, having exceeded 50k hours of operation, and are further expected to operate reliably even beyond the original designed life. Thus, a proper planned life assessment study and refurbishment can help in extending the life of such turbines by another 10 to 20 years, and whereby major capital expenditures can be avoided [29]. Again, instead of continuing the operation of the turbine just after the life assessment studies, it is also possible to restore the properties of the critical components to reasonable extent by heat treatment alone. Even if 50-60% of the original properties are restored it may result in huge cost savings, production times and man power to the plant owners [30].

In general, the decision on the replacement of the turbine components is based on the original equipment manufacturer's (OEM) recommendations. Many a times these recommendations are based on the OEM's past experiences, and are generally not confined to the actual machine. Thus, the decision of suggesting replacements is quite not clear to both the operators and users. However, the end users prefer to assess the aged components by a third party or experts other than the original manufacturer. This has become a concern for the plant users as it is not economical to replace the parts. Over a period of years, there has been substantial increase in cost of the parts. This is because the turbine components comprise of super alloys, and their cost alone is 15 to 20 % of the turbine's cost [26]. Besides this, the turbine operating practice also differs among the users and may tend to vary as compared with the manufacturers recommended practice. For example, operating the turbine at lower loads than the designed load is a common

practice. These cases of over and under design operations bear a detrimental effect on the critical components of the turbines. Additionally, the turbine users ought to have the inspection techniques to assess the excess life of critical components. From the assessments, it was concluded that the inspection schedules be increased to longer intervals to have major cost savings. Therefore, accurate planning of the inspection schedules will help to avoid any forced outages [31].

Considering the fact that the end user needs to ensure the availability and reliability of the turbines, precise and improved life-assessment techniques were emphasized. There is a common trend to increase the turbine inlet temperature or the firing temperature to increase the turbine efficiency. However, these high temperatures pave the way for creep mechanism on the components which is a time dependent phenomena [32]. Additionally, the turbine components also experience other damaging phenomenon such as fatigue, thermal-fatigue, creep-fatigue and high temperature erosion and corrosion. Components such as combustion liners, transition pieces, nozzle segments, vanes, and turbine wheels operate in the creep regime. These components are in the hot gas path and experience high temperature damages, such as hot corrosion, creep and creep-fatigue [7].

The safety of the plant components and the working personnel is of utmost importance [26]. This is because any failure of the turbine components will lead to severe consequential damage of other stationary and rotating parts resulting in catastrophic failure of the turbine. In this regard, there is a strong need to

understand the prior operating history of the components before commencing the life extension studies. Depending on the prior history of the components, appropriate non-destructive or destructive testing may be employed. Thus, an accurate life assessment can conclude whether a particular component is fit for further service or needs a replacement or refurbishment. The plant users then can accordingly take a remedial action [33].

1.5 RESEARCH OBJECTIVES

The primary objectives of this research are mentioned below:

1. To study the feasibility of extending the life of the A-286 gas turbine wheels beyond the Original Equipment Manufacturer (OEM) life.
2. To study the microstructures and properties of a new A-286 forged bar and an ex-service A-286 wheel, and define the degradation of the material involved.
3. To develop a rejuvenation heat treatment plan for an ex-service A-286 turbine wheel for continuation in service after 200k hours by comparing the microstructures and properties of new and heat-treated ex-service A-286 wheel material.
4. To establish microstructure-properties dependence and life cycle management plan for the turbine wheels.

1.6 RESEARCH METHODOLOY

This is primarily an experimental research, wherein the experiments shall be conducted on a laboratory scale to get an idea of the microstructural transformations occurring in the turbine wheel after various heat treatments.

Keeping in mind the research objectives, this research primarily consists of experiments in terms of carrying out rejuvenation heat treatments and studying the properties of the material after each heat treatment. This will be followed by a comparison of the data to select the best properties of the material. The detailed research methodology is explained as below:

- A new A-286 forged bar shall be purchased to study the microstructure and to evaluate the properties such as hardness, charpy impact strength, stress rupture test, room temperature and high temperature tensile strength. This bar would then serve as a representation of a new turbine wheel.
- A gas turbine wheel made of A-286 material with more than 200k operating hours will be identified. This shall be followed by sectioning/dissecting of a portion of this wheel for further experimental purposes.
- Finite element modeling shall be performed on the serviced turbine wheel, using the software, to map out the stresses at various zones.
- Portable hardness survey, using a portable hardness tester will be carried out on the sectioned portion of the serviced wheel to check for any variations in hardness.
- The dimensions of dissected/sectioned portions of the serviced wheel shall be measured. Marking will be done on the dissected portions for further sectioning. This is required to ensure that the samples meet the minimum length requirements of the laboratory for testing.

- Microstructural evaluation, hardness testing and Energy Dispersive X-ray Analysis (EDAX) shall be carried out on the serviced wheel section to study the transformations.
- Pilot heat treatments will be conducted on the serviced turbine wheel sections. The pilot heat treatments will comprise of solution annealing at 750ºC, 950ºC and 1120ºC respectively. Based on these results further heat treatments such as solution annealing and age hardening with variations in holding time shall be carried out.
- After each individual heat treatment, the specimens shall be taken for the various destructive testings.
- The results after each heat treatment will be compared with the new forged A-286 bar results. The heat treatment with the best rejuvenated microstructure and properties shall be selected, after comparison.
- The research methodology is outlined in Figure 1.5.

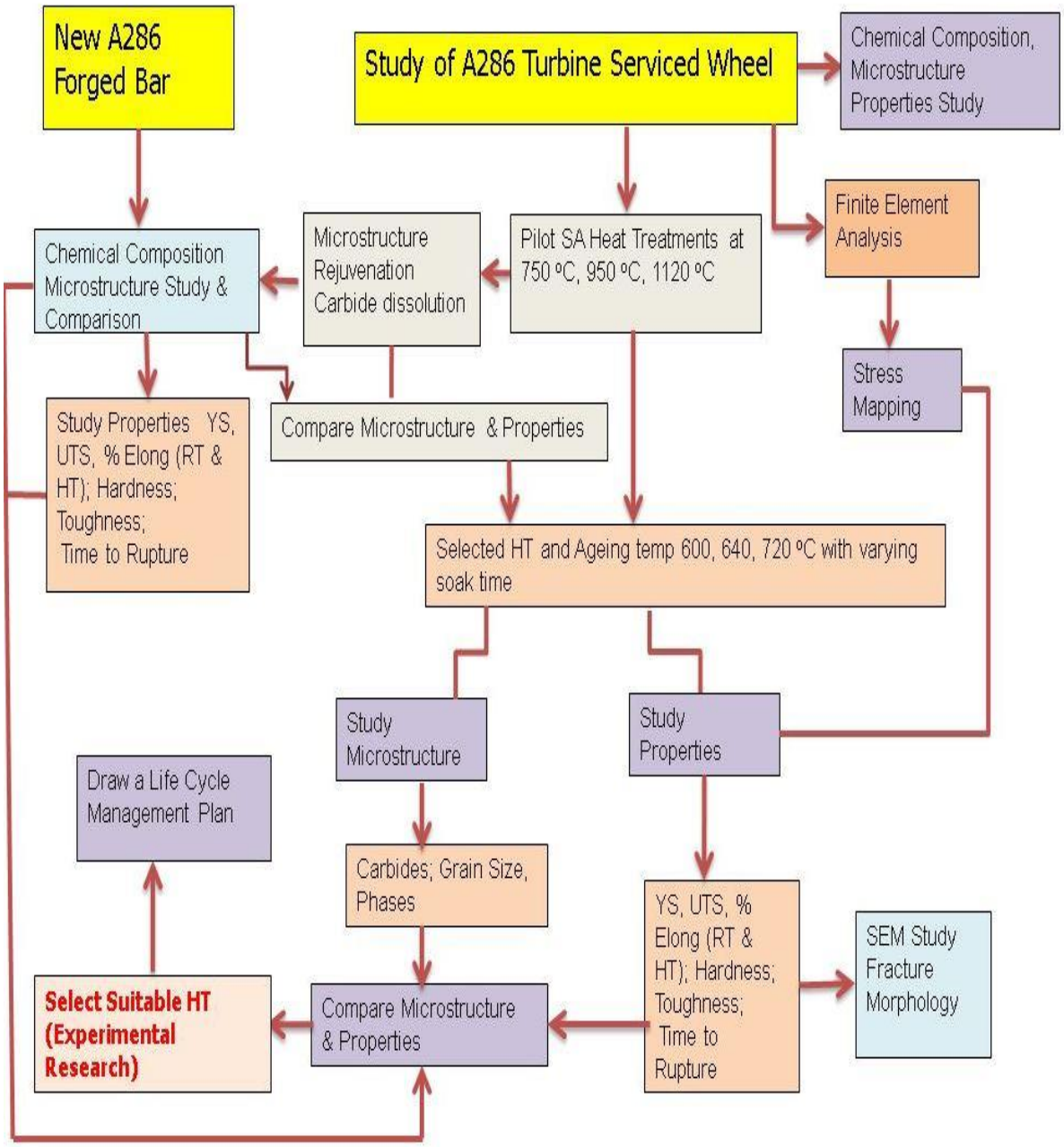

Figure 1.5: Outline of Research Methodology

CHAPTER 2

LITERATURE REVIEW

An extensive literature survey of the gas turbine components to enhance their life extensions was carried out. This survey containing various aspects and research gaps is classified into four segments and is explained below:

2.1 COMBUSTION TURBINE DAMAGE MECHANISMS AND THE NEED FOR LIFE ASSESSMENT

There are several combustion turbines having expensive components, and are in operation the world over. These turbines are used for generating electricity. During this generation, the utilities operate these turbines on base load continuously between the scheduled overhauls to meet the power supply demands. Many of these instances involve cyclic operation of the turbines to cope with the varying power load demands. There are however, many limiting factors during their operations such as rapid load fluctuations, start and shut downs resulting in thermal stresses and differential expansion of the components accompanied by vibrations of the rotor [34]. As mentioned in the introductory chapter, the turbine components made of super alloys are in the hot gas path and experience various damages [35]. Moreover, with cyclic loading these

components over a long-term usage are subjected to damaging mechanisms such as creep, thermal-fatigue, hot corrosion, oxidation. Several other studies suggested that the most common damaging mechanisms such as fatigue, creep, hot corrosion, alloy deformation, erosion, stress corrosion cracking, thermal and creep fatigues for turbine components result in the failure of the components [36]. Earlier studies indicated that the hot gas turbine path components should have better oxidation and hot corrosion resistance, high thermal and fatigue resistance, creep resistance and long-term microstructure stability [37]. Some other components such as nozzles, transition pieces, combustion liners have a thermal barrier coating (10 to 12 mils) for protecting the base metal. Eventually, the coating while in service may be damaged affecting the base material [38]. There is thus a strong need to assess the condition of these hot gas components for continuity in service even after their design lives. Proper understanding of the damage or degradation mechanisms in service of gas turbine component~~s~~ is one of the important aspects of life assessment studies [39]. Accurate life assessment techniques can help to conclude on the remaining life of the hot gas components. The life assessment techniques may include non-destructive and or destructive tests. The use of software for computing the remaining life can also be a valuable tool to extract more life from the aged components [40]. Proper modeling, laboratory studies and the study of turbine loading conditions as well aid in analyzing the remaining life of the hot gas components [41, 42].

The combustion turbines parts have a limited life due to the stresses experienced at varying temperatures. Stress corrosion and environment assisted cracking may

also occur due to combustion gases in the turbine. In addition, service life limitations occur due to the loading capability of the parts primarily exposed to high temperatures. Further, these components may fail within or before the anticipated designed life due to the manufacturing and service induced stresses. It was thus, concluded that periodic maintenance and inspections are required to avoid any un-excepted failure of the components [43-49].

The existing power plants are old and are ageing faster. As replacement of the components in these plants is a costly affair, the life assessment of power plants has thus become extremely significant. The degradation of the material during service and the current condition of the components can be assessed by non-destructive inspection techniques. This provides an opportunity to the end users to arrive at a conclusion whether a particular component is fit for further usage or needs replacement. The prime objective of life assessment studies is to extend the life of the components, beyond their designed life [50-52].

2.2 LIFE ASSESSMENT OF TURBINES

Based on the degradation mechanisms of the turbine components, many authors have studied the life assessment of the turbines using non-destructive testing and finite modeling methods.

Gas turbine rotor components such as turbine wheels, compressor wheels, distance piece shafts are in general designed for a safe operation of 200k hours. Taking into consideration that these components may fail prematurely, a margin of safety is provided by the design engineers [53-56]. In view of this, it was

recommended to replace these components at fixed intervals. However, considering the variations in operations based on the load demand, the components may undergo various stress levels inducing degradation in material properties. This may result in replacement of the components, even before their designed life or before the recommended replacement period. Operational factors primarily being the loading and other issues such as frequent start and stops, not envisaged during the original design thus, resulting in premature failure of the components should be taken in to consideration. The operational factors can lead to early failures on account of creep or thermal fatigue.

Life assessment programs can definitely prevent such premature failures and, thus can be useful in extending the life of the component even beyond its designed life. This will result in enormous cost cuttings. Various other non-destructive methods such as eddy current, ultrasonic examination and replica metallography were developed to assess the remaining life of the gas turbine units [57, 58].

An important parameter to assess the remaining useful life of the components is through microstructural evaluation. Many authors have concluded that the evaluation of microstructure of steam turbine components plays a prominent role in the determination of remaining useful life. This evaluation is usually done via replica metallography, wherein the microstructure is assessed without performing any sectioning. In this technique, the metallography polishing is performed on the component, and the microstructure is captured on a cellulose acetate tape known as replica. Replica microstructural studies have been conducted earlier on the turbine wheel and vanes, which have been in long-term service. The

microstructural evaluation concluded that the turbine wheel can be continued in service, but the microstructure needs to be monitored after four to five years of operation [59, 60].

In addition, there are life assessment studies such as hardness testing and creep models to evaluate and estimate the creep life prediction of the turbine wheels [61-63]. In this context, an interesting life assessment study was performed on a high-pressure rotor made of Cr-Mo-V steel to check for its material degradation. The rotor was in service for approximately 167,500 hours. The specimens of the rotor were collected from both the cold and hot sections. The results have shown the softening and temper embrittlement of the rotor material due to long-term service. Further, based on creep rupture data of the rotor material, it was concluded that the rotor material would not fail due to creep in future. This discrepancy was attributed to the uncertainties such as overheating, frequent starts and stops associated with the rotor operations. In view of these results, it was recommended that the rotor material's inspection and evaluation should be carried out after 10 years of operation [64].

Another group of authors worked on a power turbine wheel to determine its remaining life. The objective of this specific study was to study the initial or original design calculations with the current computing techniques. The authors concluded that stress distribution pattern within the turbine wheel material can be determined and co-related with the material properties. The operating temperatures of the turbine wheel are known and with the observed stress pattern distribution within the wheel, the remaining useful life of the turbine wheel can be

determined [65]. Pertinent to these computing techniques, many authors have proposed methodologies using Finite element Analysis (FEA) and Computational Fluid Dynamics (CFD) models for life assessment of turbine wheels. The investigation on the failure mechanisms was performed under the operational parameters of high rotational speed in high temperature environments. The turbine wheels usually operate in the temperature range of 450 ^{o}C to 550°C. The increase in operating temperature thereafter, poses a threat to the life of the turbine wheels. Previously, methodologies utilizing creep life and low cycle fatigue life were used for evaluating the life of the high temperature components. These methods were sufficient to predict the remaining service life.

In this particular case, the authors have demonstrated a practical methodology to predict remaining life of turbine wheels using a combination of (CFD, FEA and creep model). Based on the designs and operating conditions, a 3-dimensional CFD analysis was performed on the turbine wheel with the prime intention of capturing the thermal loads. The historical operating data plays a key role in determining the accuracy of this methodology [66, 67]. Further, FEA was performed on the turbine wheel, to unravel the stresses, which were then considered as inputs for the creep life modelling. It was concluded that this methodology is highly beneficial to calculate the remaining life analysis of the turbine wheels which were operating on high loads.

Various studies for life predictions are available on advanced computational models that take into account fatigue and creep damage. It is to be noted that the gas turbine components often fail by fatigue and creep or due to a combination of

both. Researchers have conducted fatigue testing on the gas turbine components. Considering the operating conditions, simulation models were developed to reflect the true service conditions for particular components that are prone to failure by fatigue and creep. These advanced simulation models are widely used, which can provide the probabilistic life of the particular gas turbine components [68-83].

A simulation model for the remaining life analysis of turbine wheel alloys such as GH4133 super alloy (Cr 22%, Ti 3%, and Ni– rest) was proposed. In this model cyclic hardening of the materials was taken in to account, and was developed on plastic strain energy density and energy based creep-fatigue parameter. Based on the plastic strain energy density, a generalized energy based fatigue-creep damage parameter was developed. The parameter accounted for the average strain or stress effects the creep damage in the low cycle fatigue region. It was found that this model predicts alloy's fatigue behavior better as compared to other models, which use the plastic strain energy density methods alone. The conclusion was that a more reliable life prediction of GH4133 is obtained under the average mean strain conditions of the material. Therefore, using similar models, which consider the stress-strain conditions of the material, life of other components such as turbine combustion liners and high temperature components can be assessed [84-86].

The gas turbines vanes are made of nickel-based alloys such as Inconel 738 (15% Cr, 9.5% Co, 3.85%W and Ni-rest), GTD 111(15% Cr, 9.5% Co, 3.85%W and Ni-rest) and Udimet 500 (19% Cr, 19% Co, 4% Mo, 3% Ti, 3% Al, 4 % Fe and

Ni-rest). The, strategies for life prediction of these vanes was based on modelling and taking into account creep and fatigue. It was notified that stress distribution pattern within the vane material is important and can help to understand the degradation mechanisms of the vane. Thus, by mapping the stresses within the vane material, it is possible to compute the remaining life. A finite element model was used to compute the stress distribution pattern and temperature profile of the first stage turbine vanes. Primarily, the effect of thermal transients and creep in allowing the re-distribution of the thermal stresses was considered. The application of the finite element model resulted in stress and temperature distribution patterns, which were used to estimate the damage accumulation in the material due to fatigue, creep and oxidation. Thus, the service damage mechanisms could be identified with the finite modelling. This model proves that the present damage in the vanes can be found, thus enabling to optimize the use of remaining vane life. The gas turbine users can thus be benefitted by saving the costs associated with the replacement of parts or refurbishment [87-91].

The literature review further suggests that there are quantitative type risk-based life assessment models for risk-based maintenance and for predicting the remaining life assessment of gas turbines. Such models primarily use the operational data of the gas turbines, which includes any pervious failures, previous repairs, starts and stops and operating hours in total. Based on the operating data, the time of failure is modelled using Weibull distribution, which is a continuous probability distribution. The Weibull distribution is widely used in reliability and life data analysis due to its versatility. Depending on the values of

the parameters, the Weibull distribution can be used to model the life behaviors of gas turbines.

It was concluded by the researchers that the risk estimation is possible considering the replacement, refurbishment, operating and the risk of failure of turbine as well after specific operation interval. Such models are effective tools to decide on maintenance strategy (repair or replacement) and for predicting the remaining life compared to the total accounted risk [92, 93]. Various computational models were developed by researchers to predict the remaining life of the coatings on the turbine vanes. The rotating components such as turbine vanes are coated with MCrAlY (M can be Nickel or Cobalt) or aluminide coatings. These coatings primarily protect the base material of the vanes from high temperature degradation. In the long-term service, the coatings degrade and affect the base material of the vanes. The models and software developed by the researchers can predict the remaining life of coatings, thus directly enhancing the life of the vanes [94].

2.3 REJUVENATION HEAT TREATMENTS FOR LIFE EXTENSION

Several research papers were reviewed on rejuvenation heat treatment of turbine components for repairs and further life extensions. The review concluded that the rejuvenation heat treatment has been successfully applied on gas turbine components such as vanes, nozzle segments, combustion liners and transition pieces for repairs and continuation in service [95-100].

Studies were conducted to evaluate the effect of re-heat treatment on serviced GTD 111 (15% Cr, 9.5% Co, 3.85% W and Ni-remaining) nickel based alloy used for turbine vanes. Various heat treatments were performed to investigate the microstructural transformations utilizing the scanning electron microscope and optical microscope. It was concluded that sustainable recovery is possible after a solution annealing and ageing heat treatment [101-102]. Precipitated carbides and the coarse carbides were dissolved in solid solution matrix during the solution annealing heat treatment. The age hardening heat treatment resulted in uniform dispersion of precipitated gamma prime particles. This was uniform as compared to those in the long-term exposed microstructure. The resulting microstructure after the heat treatments had an adequate grain size, which imparts better material properties for continuation of vane in service. Hot isostatic pressing was done when there was a significant amount of casting porosity. The hot isostatic pressing is a kind of pressurized heat treatment, which minimizes the porosity and the life of the vanes could be extended. Therefore, the vanes can safely be re-used after the heat treatment, which effectively extends the life span [103-109].

Elsewhere, studies were conducted on IN-738 vane alloy (15% Cr, 9.5% Co, 3.85%W and Ni-remaining) after different rejuvenation heat treatments for the evaluation of the gamma prime phase (γ') particles and the associated microstructural transformations [110]. The coarsening behavior of gamma prime particle after heat treatments at 900°C and 1000°C was studied through metallography. It was found that the gamma prime (γ') particles were coarsened after heat treatment as compared to the original conditions. It was also found that

solution annealing at a lower temperature resulted in a high rate of gamma prime coarsening whereas solution annealing at higher temperature resulted in low rate of gamma prime coarsening resulting in small size gamma prime particles [111]. Thus, these studies concluded that the microstructure of the serviced IN738 material vanes can be successfully rejuvenated by heat treatments [112-115].

Literature suggests that material degradation is a prime concern for the retirement of the gas turbine components, which are in the hot gas path. During long-term service, microstructural degradation is bound to occur under the normal operating conditions. The microstructural evaluation can be done by microscopic and stress rupture tests. It is essential to know the operating history, and microstructural phase transformations before heat treatment. The as received microstructure of serviced components shall form the basis of selecting the successful rejuvenation heat treatment [116-119].

Literature on the heat treatment of austenitic Fe-Ni alloy highlighted the concern on determination of the microstructure and the creep resistance. Considering this, experimental heat treatments comprising of solution annealing followed by single step and two-step ageing were performed. While, solution annealing was carried at 980°C, the ageing was performed at 715°C, 720°C and 650°C respectively. The heat-treated samples were found to have higher tensile and yield strength, especially the one which was heat-treated with a higher and lower temperature (two-stage) ageing process. Additionally, higher creep resistance was found in the sample with single stage ageing as compared with the two-stage ageing process. These authors have concluded that the Fe-Ni alloy with the rejuvenation heat

treatment of solution annealing and one stage ageing imparts much better properties to the material for continuation in service [120-124].

Several authors have studied the types of carbides in the nickel alloys and its degradation. A study on primary metal carbide (MC) degeneration in a long-term serviced nickel based alloy K452 (Cr 21%, Co 11%, W & Ti 3.5%, Al 2.5%, Ni-remaining) revealed that the degeneration was a diffusion-controlled process. The different transformed products were present in a sequence within the interfacial reaction, which occurs in service. It was concluded that the primary MC deterioration could lead to the formation of other chromium carbides such as $Cr_{23}C_{6.}$ Formation of such carbides along the grain boundaries can lead to cracking, while the material is in service [125-127].

Research has been done on the first stage gas turbine nozzle segment to study the microstructural degradation occurring at high temperatures (800°C to 1050°C) in the nozzle material after long-term service. The first stage nozzle material is FSX 414 (Cr 29%, Ni 10%, Co 52.5%, W 7.5% and Fe 1%), which is a cobalt based alloy. Investigations were performed to evaluate the effect of rejuvenation heat treatment on the microstructure and mechanical properties. The long term operated nozzle segment revealed precipitated carbides at the grain boundaries due to the microstructural phase transformations. The carbides found were of primary and secondary types such as M_6C and $M_{23}C_6$. Such precipitated carbides are detrimental to the life of nozzle segment as it reduces the toughness and ductility of the segment, which may serve as crack initiation sites while the nozzle segment is in service. It was concluded that the carbides transformation is

reversible and such precipitated carbides can be dissolved in the solid solution matrix by a rejuvenation heat treatment comprising of solution annealing and age hardening. In other cases where the trailing edge of the nozzle was damaged due to severe thinning, erosion, oxidation or deformation, a coupon replacement could be done [128-131]. The coupon replacement involves dissecting the entire trailing edge section and welding the new coupon on the nozzle.

Researchers have studied the microstructural degradations occurring in turbine vanes such as grain coarsening, carbide precipitation, grain boundary carbide precipitation, gamma prime coarsening and creep voids. In the long-term service, the vanes undergo decomposition of primary carbides and form detrimental chromium carbides. Due to the formation of these chromium carbides, the grain boundaries become brittle and may crack. The authors concluded that such type of microstructural degradation can be reversed by a rejuvenation heat treatment. The rejuvenated microstructure after the heat treatment can be as close to the microstructure of the new vane. The damages such as creep voids can not be totally recovered with a heat treatment alone, and hence the rejuvenation includes a combination of both; the hot isostatic pressing and the heat treatment. The rejuvenation heat treatment aids in dissolving the precipitated carbides in solid solution matrix, and imparts a uniform gamma prime distribution, thus enhancing the mechanical properties of the vane material [132].

Apropos to the earlier mentioned studies, there are component and maintenance programs which continuously monitor the operation of gas turbines for reliability

and efficiency. Such programs serve as efficient tools to track any component failures and also, to plan scheduled outages [133].

2.4 STUDY OF A-286 ALLOY, MICROSTRUCTURE AND PROPERTIES

The A-286 is an iron-based super alloy, and is used where high strength and corrosion resistance is required. The A-286 alloy can be used for temperature applications in the range of 480°C to 704°C, where a ductile and non-magnetic high strength material is required. The A-286 alloy is commercially available as plate, sheet, strip and rod forms and is normally produced by argon oxygen decarburization refining or vacuum induction melting. The A-286 alloy has a Nickel content of 24 to 27% and Chromium content in the range of 13.5 to 16%. These A-286 alloys have diverse applications in the gas turbine and aircraft industries [134-136]. The A-286 alloy exhibits better mechanical properties after solution annealing and age hardening, hence the gas turbine and aircraft industries use the A-286 alloy in the solution annealed and age hardened condition [137].

An A-286 super alloy ingot was studied for microstructural heterogeneities by metallographic evaluation. It was shown, that the A-286 ingot contains heterogeneities and impurities such as segregation, laves and cellular phases. These heterogeneities have a detrimental impact on the properties of the A-286 alloy. A series of experiments conducted by authors revealed that low Si and Ti contents are favorable for reducing the above-mentioned phases, which are normally observed in the inter-dendrites [138, 139].

Authors have studied and presented a model for steady state deformation of A-286 alloy at high temperature. This model is based on the theory of thermally activate glide of dislocations within the material. Experiments were conducted to know the parameters such as free energy, threshold stress required, and the volume rate, all primarily to control the movement of dislocations. Creep tests were conducted on the A-286 alloy at stress levels in the range of 180-750 MPa and in the temperature range of 600°C to 700°C. The gamma prime size and average distance between the gamma prime (γ') particles were determined using transmission electron microscopy. The study concluded that a relationship exists between the gamma prime (γ') particles and creep strength. The coarse gamma prime (γ') particles can reduce the creep strength of the A-286 material [140, 141].

The microstructure and mechanical properties of an A-286 alloy were studied after different ageing treatments. The effect of age hardening treatment was examined on the creep behavior of the alloy at 640°C. The A-286 material was evaluated in the as –received state using micro-hardness test. It was concluded that the precipitation of the stable eta (η) phase degrades the mechanical properties of the A-286 alloy. This is supported by the creep rupture time, which could be further reduced by variation in the ageing temperature. The microstructures exhibited different precipitate morphology with variation in the ageing temperature and soaking period. The creep samples failed in an intergranular fashion. A Larson–Miller parameter was used to provide a correlation between the stresses, temperature and rupture times. Further, it was

suggested that extrapolations to service conditions using this method must be considered with caution [142-147].

The microstructural characteristics of the A-286 alloy second stage vanes were evaluated and the effect of re-heat treatment was studied. The studies revealed that the A-286 alloy is more or less similar to the austenitic stainless steel. The high temperature properties of the A-286 alloy are notably due to γ' precipitates and uniform distribution of alloy carbides such as MC, M_6C and $M_{23}C_6$ and the solid solution strengthening. Over a period in service, this alloy undergoes microstructural degradation in the form of carbide precipitation and η-phase formation. The presence of precipitated carbides and a large number of η-phases can have detrimental effect on the stress rupture properties of the material. The A-286 alloy should have good creep resistance and dimensional stability at elevated temperatures to survive in the long-term gas turbine operations. The formation of the FCC γ' precipitates imparts significant amount of high temperature strength to the A-286 vanes. It was observed that addition of aluminum and titanium play a key role in formation of the γ' precipitates. The formation of detrimental η-phase results in depletion of γ' particles. The study involved re-using the A-286 gas turbine components after extending the life beyond the covered warranty by suitable heat treatments. The rejuvenation heat treatment comprising of solution annealing and age hardening can restore back the microstructure to as manufactured condition, thus enhancing the properties and life of the material component [148-153].

Studies are available on the A-286 alloy to evaluate the effect of solution annealing and ageing heat treatments. A study was performed in which a commercial A-286 alloy was solution annealed and age hardened at 715°C with a soaking period ranging from 0.5 to 450 hours, including the peak strength age hardening for around 16 hours. The microstructural evaluation indicated that the eta η phase was formed at grain boundaries after six hours of ageing and the fraction of eta η phase increased as the duration of ageing was increased. The tensile tests performed after ageing revealed ductile type fracture by micro-void coalescence. It was also observed that the ductile fracture path changes with ageing time variations, and becomes intergranular after an ageing time of 50 hours. It was noted that the presence of hydrogen decreased the ductility for samples, which were aged beyond 4 hours. The loss of ductility was almost constant beyond 4 hours of ageing and was independent of the fracture path. The fracture nucleation by carbide inclusion with gamma prime particles was evident for samples aged from 4 to 16 hours. Fracture nucleation by grain boundary eta phase was observed for samples aged beyond 50 hours [154].

Studies on the fatigue-crack propagation in A-286 alloy were conducted by comparison of crack growth rates. Depending on the cyclic stresses, the long and short crack growth rates were measured. It was concluded that microstructural phase transformations are responsible for crack growth within the material [155-160].

Interesting experiments were conducted to study the stress corrosion cracking behavior of the age hardenable Ni-Fe-Cr alloys such as X-750, IN 718 and A-286

alloy in flowing water reactor with pressure. It was concluded that A-286 alloy has a good stress corrosion cracking resistance in the age-hardened condition. The precipitates at the grain boundary have detrimental effect on fatigue and creep. The low cycle fatigue properties were enhanced with the improvised microstructure for A-286 alloy after age hardening heat treatment [161-164].

There are studies on precipitated hardened A-286 alloy to verify the influence of eta (η) phase and γ' phase on the corrosion behavior of A-286 alloys, particularly utilizing the electrochemical potentio-kinetic reactivation and double loop electrochemical potentio-kinetic reactivation techniques. It was observed that with a given ageing temperature, the gamma prime (γ') precipitates tend to form discontinuities in the passive layer, thus increasing the susceptibility to localized corrosion attack [165].

2.5 LITERATURE REVIEW – KEY INFERENCES

A detailed review of the literature spanning turbine damaging mechanisms, life assessment of turbines, rejuvenation heat treatments for life assessment, review of A-286 super alloy lead to key inferences. The key inferences being:

- The turbine components operating at high temperatures are subjected to various kinds of damaging mechanisms such as wear, erosion, hot corrosion, stress corrosion cracking, thermal fatigue, creep, and creep-fatigue [166]. Thus, the turbine components could experience premature failure in service due to any of the damaging mechanisms and can lead to heavy production, and subsequent economic losses. The life of gas turbine

components can be extended beyond the designed life for safe operation by condition assessment and remaining life analysis studies [167].

- The life extension studies can assess the current condition of a particular component to conclude whether the component can be further continued. There are various methodologies for life assessment, which include non-destructive testing such as replica metallography, portable hardness testing, ultrasonic flaw detection, eddy current testing, magnetic particle testing, dye penetrant testing, boroscopic inspection and visual testing [168]. The life assessment testing also includes finite element modelling, and concluding on life by high-end software. The use of software methodology for life assessment needs realistic inputs on the operational data and operating parameters [169, 170]. After such non-destructive/destructive tests, and modelling approaches for life assessment, a decision can be taken on whether to replace or continue the component in service. Such an approach helps the end users to plan an appropriate maintenance/inspection schedule outages as required with considerable amount of cost savings [171].
- The gas turbine components such as combustion liners, transition pieces, nozzle segments, shrouds are either refurbished or repaired after stipulated running hours. The primary objective is to assess the health of the components and decide if the components can be repaired or retired. The components after a certain period of operation undergo microstructural degradation, which reduces the mechanical properties [172]. The

microstructural degradation can be corrected by heat treatment. Through solution annealing and ageing heat treatment, the microstructure can be restored to as manufactured condition [173-176]. The rejuvenation heat treatments on gas turbine components such as vanes is possible, and is successful in enhancing the mechanical properties of the component. This approach is regularly followed by the gas turbine repair industry. The vanes are heat treated by solution annealing followed by ageing and the microstructure is evaluated [177-179]. The observed microstructure determines the suitability of vanes and other components for continuation in service.

2.6 LITERATURE REVIEW – IDENTIFIED GAPS

The literature review leads to identification of the gaps, which are as follows:

- There are life assessment methodologies, which consider the approach of non-destructive testing, finite modelling and destructive testing to assess the life of turbine wheels. The heat treatment approach to rejuvenate the turbine wheel material for continuation in service is not considered. The heat treatment approach for life extension is practiced for the gas turbine components such as nozzle segments, combustion liners, transition pieces and vanes and has proven successful. In particular, the rejuvenation heat treatment for gas turbine wheels is not attempted to extend the life span.
- Heat treatments comprising of solution annealing and age hardening have not been considered as an approach to extend the life of A-286 gas turbine

wheels after 200k hours of service. The microstructure of gas turbine wheel experiences degradation in terms of carbide precipitation in the continuous service operation. The microstructure of the A-286 can be rejuvenated after 200k hours of service but not considered, primarily for life extension. There are approaches such as non-destructive techniques and fracture mechanics for life extension but enhancing the properties and extending life of the A-286 gas turbine wheel by heat treatments is not explored.

- Microstructure and properties of A-286 gas turbine wheel after 200k hours of service have not been studied in depth and the effects of the degraded microstructure on the properties of the wheel material are not mapped. The microstructure of serviced gas turbine wheel consists of precipitated carbides and other phase. The mapping of the transformed microstructural constituents is not explored and in particular, the effect of the carbide transformation on the material properties has not been investigated. The effect of microstructural transformations on properties such as toughness, stress-rupture, hardness, high and low temperature tensile test properties have not been widely covered. This is primarily for the A-286 alloy wheel material, which has been in service for more than 200k hours.
- A recent study on a serviced gas turbine A-286 wheel was conducted by group of authors. The turbine wheel had accumulated more than 200,000 service hours. It was essential to know the condition of this wheel for fitness for service. The condition of this particular wheel was assessed by

microstructural study using replica metallography, which is a non-destructive method. The microstructural findings revealed excessive carbide precipitation along the grain boundaries and the authors concluded that the wheel should be retired from service.

- Earlier, in this section it was mentioned for the gas turbine vanes that with the rejuvenation heat treatment it is possible to restore the microstructure to as manufactured state. With this, if a rejuvenation heat treatment is performed on this particular A-286 wheel, it would have been possible to continue the wheel in service instead of retiring it from service. This would have been certainly beneficial for the end users.

CHAPTER 3

EXPERIMENTAL AND THEORETICAL WORK

This research is a combination of both experimental and theoretical work. This chapter describes the various tests performed, applicable standards, instrumentation along with the principles and procedures involved. The experiments and tests were carried out at the following organizations and laboratories:

- Masaood John Brown, Dubai, United Arab Emirates.
- Lonestar Technical Services, Dubai, United Arab Emirates.
- Incotest Laboratory, A Division of Special Metals, Wiggin Limited, Hereford, England.
- Westmoreland Mechanical Testing & Research, Limited, Banbury, United Kingdom.

3.1 CHEMICAL COMPOSITION

A forged A-286 bar (henceforth referred to new or as purchased) was procured as a part of the research requirements mentioned in the preceding sections. The chemical composition of this new A-286 bar was analyzed to compare with the composition of serviced turbine wheel. The chemical composition was

analyzed at Lonestar Technical Services in Dubai, which is a UKAS accredited laboratory and approved by Dubai Accreditation Centre. The chemical composition was determined using an Optical Emission Spectrometer (OES) and X-Ray Fluorescence Hand Held Gun.

3.1.1 OPTICAL EMISSION SPECTROMETER

The OES is an analytical instrument used for elemental analysis of solid metallic samples. The OES operates on the principles of Inductively Coupled Plasma (ICP) as the excitation source, and is also known as ICP optical emission spectrometry [180]. The OES utilizes application of electrical energy, which is in the form of a spark. This method is primarily called as arc spark OES. The arc is generated between an electrode and the metal sample to be analyzed. The sample is vaporized at temperatures in the range of 4500oC to 6000oC by the arc spark discharge. The generated atomic vapor containing atoms and ions are further excited to emit radiations. The emitted radiations are propagated into the spectrometer through a bundle of optical fibres and then dispersed into the spectral components. Each element has its own spectrum and a certain wavelength, and this element spectrum is measured by a device known as charge-coupled device (CCD). The intensity of the radiation is proportional to the concentration of element in the sample. This is then internally re-calculated from the calibrated curves stored in the library and is directly displayed as elemental concentration in percentage [181, 182].

An OES, Make-HILGER Analytical, United Kingdom (Model Polyvac E982) was used. The calibration of the OES was done using the chromium and cobalt element blocks. A small piece (3 inch x 3 inch) from the new A-286 bar and the serviced turbine wheel was analyzed under OES in accordance to ASTM E1019 "Standard Test Method for Determination of Carbon, Sulfur, Nitrogen, and Oxygen in Steel, Iron, Nickel, and Cobalt Alloys by Various Combustion and Inert Gas Fusion Techniques" and ASTM E353 "Standard Test Method for Chemical Analysis of Stainless, Heat-Resisting, Maraging, and Other Similar Chromium-Nickel-Iron Alloys". On each piece, 3 sparks were taken and the average percentage of element was reported. The OES used to determine the chemical composition of the A-286 new bar, and the serviced turbine wheel is shown in Figure 3.1.

Figure 3.1: Optical emission spectrometer used for chemical analysis

3.1.2 X-RAY FLUORESCENCE (XRF)

The chemical composition of the new A-286 bar and the serviced turbine wheel was also determined by a hand held XRF gun. An XRF hand held gun has two major components: an X-ray tube and a detector. The primary X-rays are generated by the source and are directed at the sample to be analyzed. These primary X-rays pass through a filter so that the X-ray beam is modified to a straight path. This beam then strikes the sample, and the secondary X-rays are emitted and collected for further processing by a detector. This is followed by the generation of a spectrum, which displays the X-ray intensity peak (Y-axis) against

the energy (X-axis) of a particular element. The elements present are then identified by the peak energy, which provides an indication of the amount of the element. This information is further used by the analyzer to calculate the element composition. The chemical composition of the sample (metal) is displayed on the screen after pressing the XRF gun trigger [183, 184].

The XRF gun used is Oxford make, X-Met 3000+. Prior to testing of the specimens, the XRF gun was calibrated with the test block of SS 304 (Cr 18%, Ni 8 %). Total 3 sets of readings were taken on the samples of these materials and the average was reported. The photographs of the XRF analysis on the new A-286 bar and serviced wheel section are shown in Figures 3.2 and 3.3.

Figure 3.2: XRF analysis on a new A-286 bar

Figure 3.3: XRF analysis on a serviced turbine wheel section

3.2 FINITE ELEMENT ANALYSIS (FEA)

Finite element analysis was carried out on the serviced turbine wheel. The aim was to verify and map the stress distribution patterns throughout the wheel. The finite element analysis was conducted in collaboration with PCI company, United Kingdom, which are experts in this field. Stress distribution patterns were mapped using high-end software, which is proprietary.

3.2.1 FINITE ELEMENT ANALYSIS METHODOLOGY

Most of the engineering problems in the industry are real-time and there are no readymade solutions available. This is because of the fact that they are of complex nature involving mathematical equations, and or the problems that arise with the boundary and initial conditions. These problems can only be solved with simulations and numerical equations. Numerical solutions tend to approximate equivalent or exact solutions primarily at the discrete points to map the stress [185, 186]. These discrete points are called nodes. The basis of FEA Method is

the principle of minimization of energy. This means that when a particular boundary condition is applied on a component, it can result in several different boundary configurations. Out of these several different boundary configurations, only one particular boundary configuration is possible based on the numerical methods. The first step of the numerical methods is discretization. In this method, the component to be mapped is divided into several sub-regions and nodes. The two most commonly used numerical methods being Finite Difference Method and Finite Element Method [187].

Finite element analysis is a computational method that involves modelling, to predict real-time simulations to check for the component's behavior while in service. This is done using a general purpose finite method software such as ANSYS [188]. In general, FEA modelling is used to predict how an individual component reacts in operation at a particular service condition through software simulations. The simulation is normally done to check the actual effects of stresses, forces, fluid flow, vibration and any other physical effects. Finally, FEA analysis utilizes numerical techniques and has applications in a variety of fields.

3.2.2 FINITE ELEMENT ANALYSIS PROCEDURE

The dimensions for the finite element model were primarily based on the measurements taken from the dissected section of the A-286 serviced turbine wheel. Considering the fact that the turbine wheel is aged in service, the wheel dimensions were adjusted with the nearest imperial dimensions to that of the wheel in as manufactured stage.

The basic material properties were based on the consensus values for alloy A-286: Density = 7940 kg/m^3, Young's Modulus = 201 GPa, Poisson's Ratio = 0.3. The boundary conditions were applied as a lateral restraint in the axial direction considering the A-286 alloy data. The 2-Dimensional axisymmetric mesh was created using the ABAQUS pre-processor by taking linear quadrilateral elements (ABAQUS type CAX4R). This mesh was created to cover the entire area of the dissected wheel material as shown in Figure 3.4.

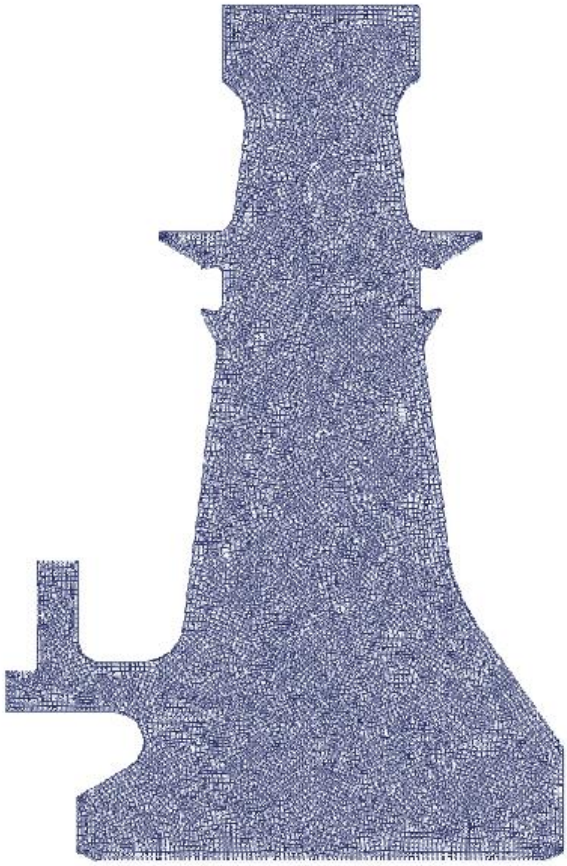

Figure 3.4: Mesh of a turbine wheel created for finite element analysis

The boundary conditions were applied as a lateral restraint in the axial direction. The rotational speed of 4670 rpm was based on the normal operating speed value as supplied. The initial elastic analysis was run assuming no temperature gradient and thermal effects to inform the creep test conditions and identify the peak stress locations.

3.3 PORTABLE HARDNESS TESTING

The operating principle of portable hardness tester is based on the impact device. An impact device releases an impact body containing a permanent magnet and a hard indenter on the material to be tested. Impact body is released by the application of spring force on the test area/sample. The hard indenter deforms the test material elastically and plastically. Once the impact body comes to halt, elastic recovery of the test sample and impact body occurs, which causes the impact body to rebound. The velocity of the impact body is recorded, and is converted to the hardness value. The hardness reading thus measured in the selected mode is displayed on the screen [189].

The hardness survey was performed on the dissected turbine wheel to check for any hardness variations within the material from bore to dove tail areas. The hardness tester was calibrated using the calibration block and Surface preparation, in the form of grinding with a 400-grit silicon carbide wheel was done prior to portable hardness testing. Portable hardness test was carried out in accordance with ASTM A956 “Standard Test Method for Leeb Hardness Testing of Steel Products”. Starting from bore to dove tail area, hardness readings were taken at

every 1-inch interval. At every location, 3 readings were taken and the average reading has been reported. The hardness survey was performed using an Equotip-3 portable hardness tester from Proceq, Switzerland. A photograph of the Equotip-3, hardness tester is shown in Figure 3.5.

Figure 3.5: Portable Equotip-3 hardness tester

3.4 MICRO EXAMINATION (OPTICAL & SCANNING ELECTRON MICROSCOPE)

Micro-examination was performed on the as new A-286 bar, serviced turbine wheel and the different specimens after heat treatments. The metallographic preparation was done in accordance with ASTM E3 – "Standard Guide for

Preparation of Metallographic Specimens". The preparation techniques may vary to some extent for the super alloys for desirable results.

The micro-examination was carried out using a standard metallurgical microscope and scanning electron microscope.

3.4.1 METALLOGRAPHY PREPARATION

Metallography samples with longitudinal and transverse sections were taken from new A-286 bar, serviced turbine wheel material before and after different heat treatments. The samples dissected for metallography were of 0.5" x 0.5" x 0.4" size. For identification purposes, the specimens were given the laboratory sample numbers such as 1, 2, 3, 4. This identification was primarily to trace the samples at any given moment of time.

The dissected samples were cleaned in an ultrasonic bath for 30 minutes for hot mounting. The hot mounting is a process where the samples to be metallographically polished are embedded in the resin, to obtain a mold of 25mm diameter for ease of polishing. After the ultrasonic cleaning, the samples were placed on a hot mounting stage. The hot mounting press used was Citopress from Struers, Denmark as shown in Figure 3.6.

Figure 3.6: The hot mounting press - Citopress

Two specimens, one with longitudinal section and other with transverse section were placed on the hot mounting stage. Multifast resin (from Struers, Denmark) was poured (around 2 spoons) over the sample stage. The mounting stage was then lowered and the start key on the machine was pressed. The Citopress was programmed for 2 minutes cycle (heating and cooling) for preparation of the mounts. On completion of the cycle, the alarm signal was displayed on the Citopress screen. The mounted sample was then again cleaned using acetone and water to get rid of any loose resin powder deposits. The representative hot mounts after mounting process are shown in Figure 3.7.

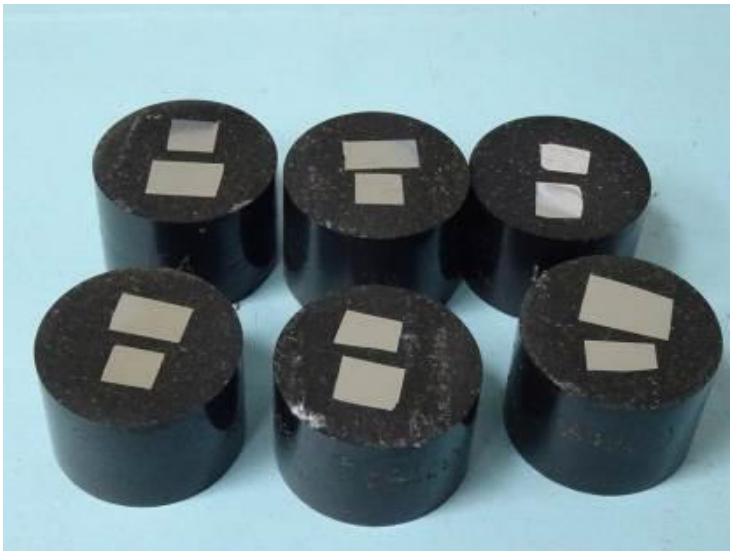

Figure 3.7: Prepared hot mounts

After mounting, the metallographic polishing was required in order to acquire the desired finish, so that the samples could be readily observed under the microscope. The metallographic polishing was done using Struers Polishing Machine – Abraham, Denmark that is shown in Figure 3.8.

Figure 3.8: Polishing machine “Abraham”, used for metallographic polishing

The samples for polishing were inserted in the fixture and placed on the polishing unit. The timer for polishing cycle was set for 2 minutes for each step. The polishing was done using silicon carbide grit papers of 220, 320, 500 and 1000. Fine polishing was done over a micro-cloth using 6 micron and 1 micron diamond suspensions. The final polishing was done using colloidal silica on a velvet cloth. After the final polishing, the mounts were cleansed with water and acetone, and were dried-up with a hot gun dryer, manufactured by Struers, Denmark. The specimens were observed in the un-etched and etched conditions. The etching was done using Aqua Regia for about 30 seconds to reveal the microstructure. The etching solution was prepared by mixing of concentrated hydrochloric acid and concentrated nitric acid (HCl: HNO_3) with ratio of 3:1. This entire etching process was done under a fume hood.

3.4.2 OPTICAL MICROSCOPY

An optical microscope also known as a light microscope, primarily utilizes the visible light and a system of lenses to magnify the images of the samples to be inspected [190]. The major parts of an optical microscope are the objective, eyepiece, focus knob, stage, condenser and light source. The magnified image of the sample is formed with the help of an objective lens and eyepiece by magnifying it, to observe the image with naked eyes through the eyepiece. The primary image (magnified image) of inverted real image is formed with an objective lens. The objective lens is a very high-powered magnifying glass having a very short focal length [191]. This was brought close to the sample under

examination, so that the light from the specimen comes to a focus of about 160 mm inside the microscope tube. This creates an enlarged image of the sample subject. After focusing the bright-lighted sample, a highly enlarged image could be seen. It is the image viewed by the eyepiece lens that provides further enlargement. The eyepiece was arranged in such a way that the primary image was located closer to the eyepiece than the anterior focal point to form an enlarged virtual image [192].

The mounted specimens were examined under the optical microscope in the un-etched and etched conditions. The as polished and etched sections were examined at magnifications of 50x, 100x and 200x. A CCD camera was attached on to the microscope to obtain the image on the computer screen. The images were captured using the PAXIT software. An Optical Microscope, Upright, Model-Axioskop, Carl Zeiss, Germany was used and is shown in Figure 3.9.

Figure 3.9: Optical Microscope used for microscopic evaluation

3.4.3 SCANNING ELECTRON MICROSCOPE (SEM)

The mounted specimens were also observed under the Scanning Electron Microscope (SEM). The principle of SEM involves that the electrons are produced at the top of the column, accelerated down and passed through a combination of lenses and apertures to produce a focused beam of electrons, which strikes the surface of the sample. The sample was mounted on the stage in the chamber area and both the column and the chamber are evacuated by a diffusion pump. The level of the vacuum achieved was of 10^{-3} Pa. The position of the electron beam on the sample was controlled by scan coils situated above the objective lens [193-195]. These coils allow the beam to be scanned over the surface of the sample. This beam rastering or scanning, as the name of the microscope suggests, enables information about a defined area on the sample to be collected. Due to electron-sample interaction, signals are generated and then detected by the appropriate detectors. The SEM produces images by scanning the sample with a high-energy beam of electrons. As the electrons interact with the sample, they produce secondary electrons, backscattered electrons and characteristic X-rays. These signals were collected by one or more detectors to generate images, which were then displayed on the computer screen. When the electron beam strikes the surface of the sample, it penetrates the sample to a depth of a few microns, depending on the accelerating voltage and the density of the sample. As a result of this interaction, secondary electrons, back scattered electrons, and X-rays are produced [196-198].

The etched samples were examined under the SEM at magnifications varying from 500x to 2000x. The mounted samples were made conductive by wounding copper tapes before placing on to the SEM stage. A Scanning Electron Microscope, Model-JSM 6010LV, JEOL, Japan was used and is shown in Figure 3.10.

Figure 3.10: The Scanning Electron Microscope

3.4.4 ENERGY DISPERSIVE X-RAY ANALYSIS (EDAX)

During EDAX analysis, two different types of X-rays are produced depending on the interaction of the electron beam on the sample surface [199]. The atoms are ionized by the primary electron beam leading to holes generated on the core shells; following the ionization, the electrons from outer shells fill the holes and cause the emission of X-ray fluorescence lines [200-202]. The silicon-based

detector utilizes the energy of the incoming X-ray, which is dissipated by the creation of a series of electron-hole pairs located in the semiconductor crystal. A high bias voltage was applied across the crystal which causes electrons and holes to move towards the electrodes on the opposite sides of the crystal, producing a charge signal which is passed on to the pulse processor. By measuring the amount of current produced by each X-ray photon, the original energy of the X-ray can be calculated [203]. An EDAX spectrum is essentially a histogram of the number of X-rays measured at each energy. The EDAX spectrum displayed the elements present in the sample or phase analyzed [204].

The SEM was also equipped with an Energy Dispersive Analysis of X-Ray (EDAX) from Oxford, England. The EDAX was used for the elemental analysis of a particular phase or bulk of the sample. The carbide mapping on the serviced wheel sections was done using the EDAX. The EDAX detector on the SEM is shown in Figure 3.11.

Figure 3.11 – EDAX Detector on the SEM

3.5 MICROHARDNESS TESTING

Microhardness testing is extremely useful to determine the hardness of a particular phase, carbides, and case or core hardness [205, 206]. The principle of any hardness tester lies in indenting the sample surface followed by measuring dimensions of the indentation (depth or actual surface area of the indentation). A diamond indenter is used which creates a square type pyramid shape on the sample. The diagonal lengths of the pyramid are measured using the micrometer on the hardness tester. The measured lengths are converted to the Vickers hardness number using the conversion table at that respective load. The Vickers hardness is calculated by using the formula F/A, where F is force applied on the indent in kgf, and A is the surface area of the indent in mm^2 [207, 208].

The micro-hardness testing was performed on all the prepared metallographic samples. The micro-hardness testing procedure was in accordance with the ASTM E-384, EN ISO 6507, and ASTM E-92 standard specifications. The etched mounts were placed on the micro-hardness tester stage. A load of 300 gm was applied for a short period. The diagonal lengths of the pyramid were measured using the micrometer on the hardness tester by viewing through the eyepiece at a magnification of 500x. On each mounted section, 5 hardness readings were taken and average was reported. The Vickers Microhardness tester used to measure the hardness of the prepared samples was of Mitutoyo, Japan, and is shown in Figure 3.12.

Figure 3.12: Microhardness tester used for hardness measurements

3.6 DIMENSIONAL MEASUREMENT

The portion available from the serviced A-286 turbine wheel for testing was 510 mm in length and 125 mm in thickness. The dimensional measurements were taken on the dissected block in order to plan for the individual sections for heat treatments and to cover the sample availability for destructive tests. The dimensions were mapped with a measuring tape. The turbine block section along with dimensions is shown in Figure 3.13.

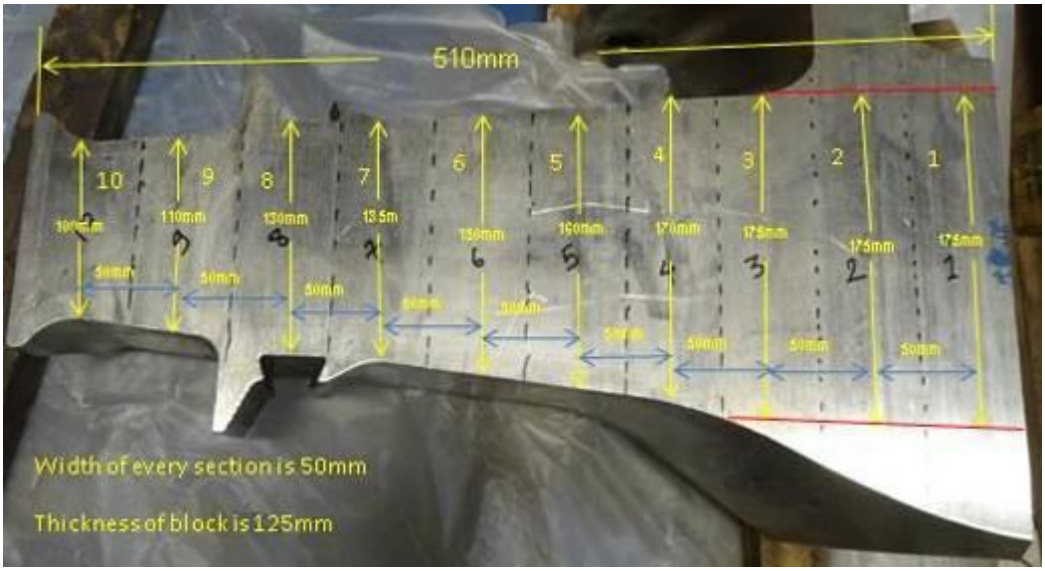

Figure 3.13: Dissected portion of turbine wheel

The representative photographs of the dissected sections after wire cutting is shown in Figures 3.14 and 3.15.

Figure 3.14 – Four different sections after further dissections

Figure 3.15: Section 10 near the dovetail area after further dissections

Overall, 10 different sections were marked and obtained from the original turbine block. The individual sectioning was done using Wire cutting method for taking out different sections from the dissected wheel portion. Some of the sections were further dissected into two halves for pilot runs. These sections were denoted with A, B, C and D. For example, if sections were taken from primary section 9, these were marked as 9A and 9B.

The detailed dimensions of the dissected sections are given in Table 3.1.

Table 3.1- Dimensions of the Individual Sections Obtained from the Block

Section No.	Length, mm	Width, mm	Height, mm
1	175	50	125
2	175	50	125
3	175	50	125
4	170	50	125
5	160	50	125
6	150	50	125
7	135	50	125
8	130	50	125
9	110	50	125
10	100	50	125

3.7 HEAT TREATMENTS (SOLUTION ANNEALING & AGE HARDENING)

Heat treatment experiments were conducted on the various dissected sections of the serviced turbine wheel.

3.7.1 HEAT TREATMENT EQUIPMENT

All the heat treatments were carried out in a vacuum furnace 'TAV, Vacuum Furnace Engineering Limited, United Kingdom. Model TPH 1200 S/N – 571' at Masaood John Brown workshop in Dubai. A vacuum furnace enables to perform heat treatments in vacuum. Heat treatments for gas turbine components require vacuum, primarily to prevent any oxidation effect. The vacuum furnace is also used to carry out the brazing operation [209].

The primary objective of vacuum heat treatment was to eliminate air and its reactive elements within the furnace zone. This was achieved by evacuating a tightly sealed heat-treating chamber by a vacuum pumping system. . An oil diffusion pump was incorporated along with the mechanical pumping system. The function of the diffusion pump was to remove the left out air in the heating chamber, thus providing a very clean atmosphere during the heat treatment process [210]. The bake-out cycle involves heating the empty furnace to a temperature of atleast 1000°C higher than its normal operating temperature and holding at that temperature for a period of up to 30 minutes [211]. The heat treatment cycle runs with a single push button. On completion of the heat treatment cycle, the buzzer goes on. The entire heat treatment program steps such as heating rate, cooling rate and the holding period are governed by the software (2010) provided by TAV, United Kingdom.

The maximum working temperature of furnace is 1300°C, and the hot working zone dimensions are 1200 mm width x 1200 mm height x 1200 mm depth. The final vacuum attained by furnace was of 10^{-5} / 10^{-6} millibar. The furnace was equipped with an argon gas fan for rapid quenching/cooling. All the samples to be heat treated were placed on the fixture inside the furnace.

The vacuum furnace used is shown in Figures 3.16 and 3.17.

Figure 3.16 – Vacuum furnace used for heat treatments

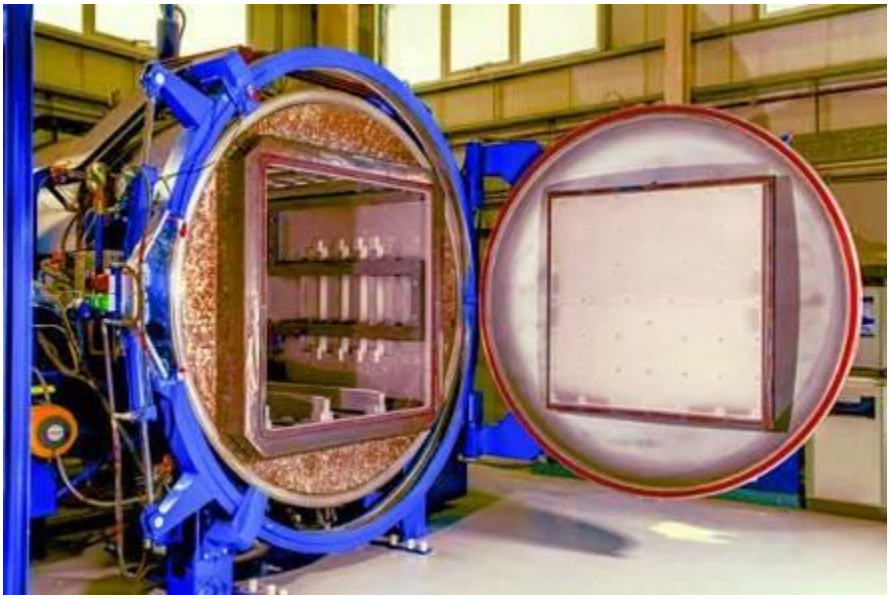

Figure 3.17 – Vacuum furnace showing the internal chamber

3.7.2 HEAT TREATMENT CYCLES

Initially the pilot heat treatments were carried out on the sections to include the lower and higher solution annealing temperatures as listed below:

- Solution annealing at 750°C for 3 hours
- Solution annealing at 950°C for 3 hours
- Solution annealing at 1120°C for 3 hours

Solution annealing heat treatment involved holding the wheel sections in furnace for the above specified temperature and time followed by rapid cooling. The graphical representation of pilot heat treatments is given in Figure 3.18.

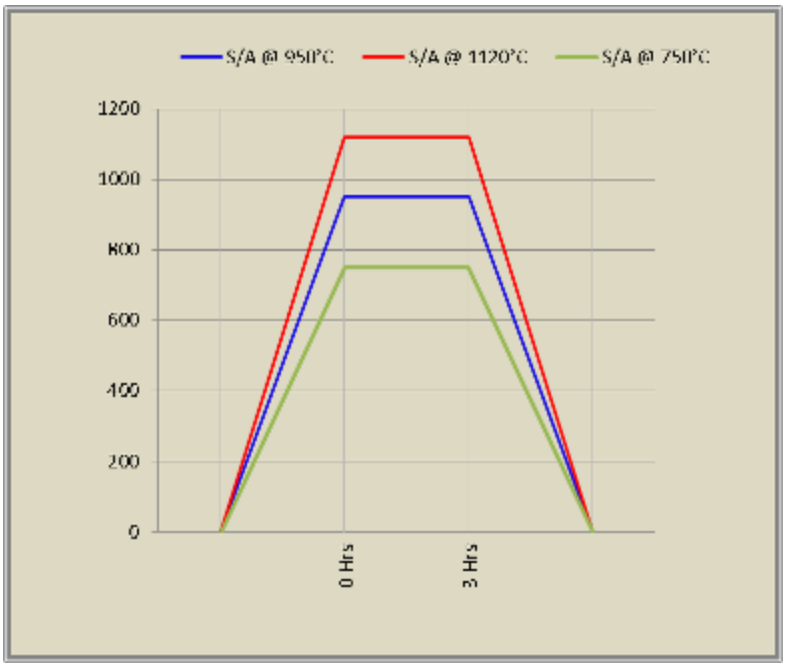

Figure 3.18 – Graphical representation of the pilot heat treatments

The microstructure was evaluated after the pilot solution annealing heat treatments. Based on the observations of the pilot heat treatments, the remaining heat treatments were formulated/planned.

The heat treatments performed on various sections of the serviced wheel are given in Table 3.2 and Table 3.3.

Table 3.2- Pilot Solution Annealing Heat Treatments

Section	Pilot Solution Annealing Heat Treatment
Section 9C	750°C x 3 hrs
Section 9A	950°C x 3 hrs
Section 9B	1120°C x 3 hrs

Table 3.3- Planned Solution Annealing (SA) and Ageing (Age) Heat Treatments

Section	Heat Treatment Cycle
Section 10	SA - 1120°C x 2 hrs + Age - 720°C x 16 hrs
Section 2	SA - 950°C x 2 hrs + Age - 720°C x 16 hrs
Section 9A	SA - 950°C x 3 hrs + Age - 720°C x 16 hrs
Section 9B	SA – 1120°C x 3 hrs + Age - 720°C x 16 hrs
Section 8C-1	SA – 950°C x 3 hrs + Age - 600°C x 4 hrs
Section 8C-2	SA – 950°C x 3 hrs + Age - 600°C x 8 hrs
Section 8D-1	SA – 950 ^{o}C x 3 hrs + Age - 600 ^{o}C x 12 hrs
Section 8D-2	SA – 950°C x 3 hrs + Age - 640°C x 4 hrs
Section 7.1	SA – 950°C x 3 hrs + Age - 640°C x 8 hrs
Section 7.2	SA – 950°C x 3 hrs + Age - 640°C x 12 hrs
Section 6	SA – 1120°C x 3 hrs + Age - 600°C x 4 hrs
Section 5.1	SA – 1120°C x 3 hrs + Age - 600°C x 8 hrs
Section 5.2	SA – 1120°C x 3 hrs + Age - 600°C x 12 hrs

Section	Heat Treatment Cycle
Section 4	SA – 1120°C x 3 hrs + Age - 640°C x 4 hrs
Section 3.1	SA – 1120°C x 3 hrs + Age - 640°C x 8 hrs
Section 7.2	SA – 1120°C x 3 hrs + Age - 640°C x 12 hrs

There was a need to program each heat treatment cycle and feed in the vacuum furnace operating system software, provided by TAV, United Kingdom, as, these heat treatment cycles were not available in the software. For this reason, individual heat treatment plots were drawn out as planned. The graphical plots for all the heat treatments performed are provided below:

1. **Pilot Heat Treatment Cycle – 1 (Section 9C) – Solution Annealing**

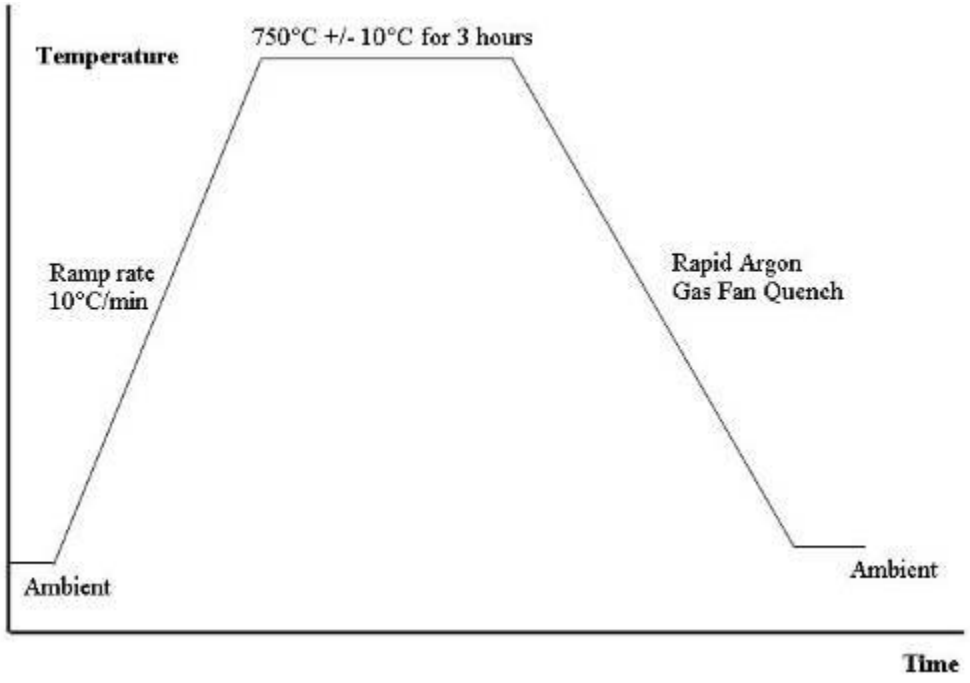

2. Pilot Heat Treatment Cycle – 2 (Section 9A) – Solution Annealing

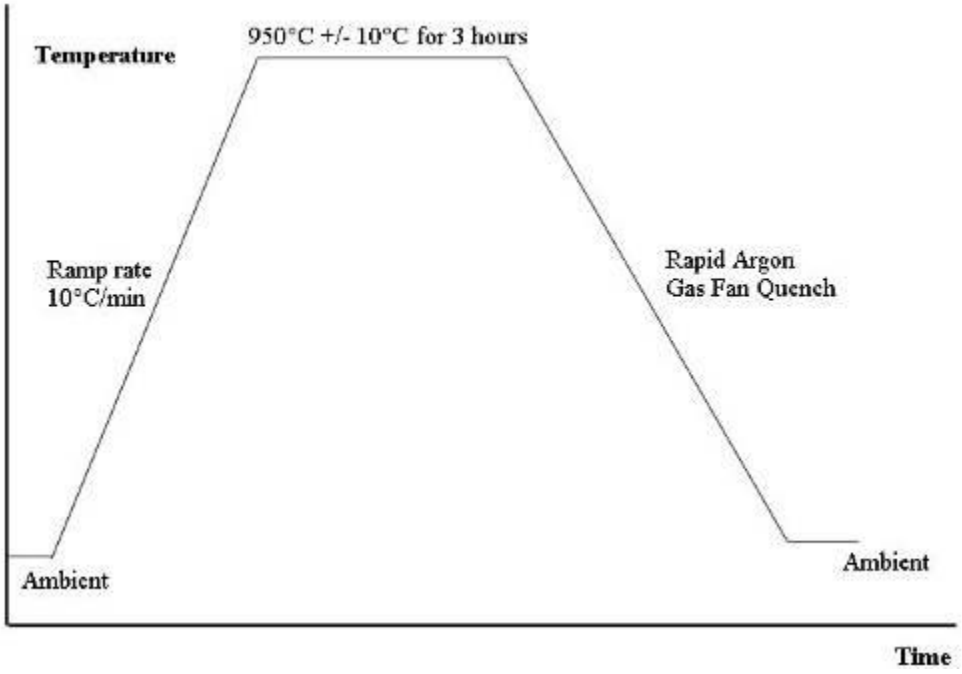

3. Pilot Heat Treatment Cycle – 3 (Section 9B) – Solution Annealing

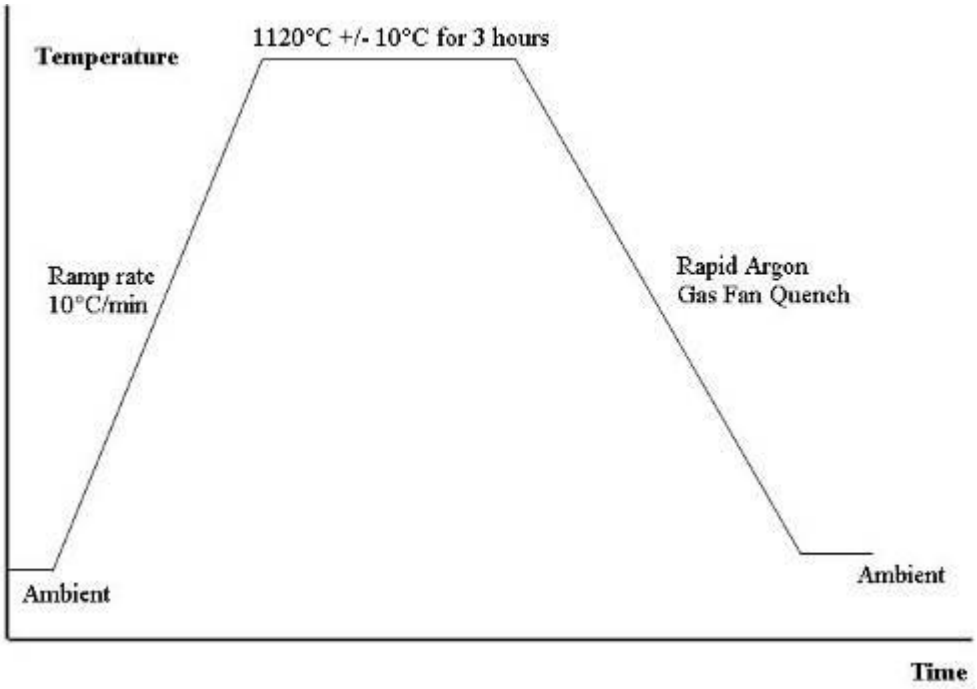

4. Heat Treatment Cycle – 4 (Section 10) – Solution Annealing + Ageing

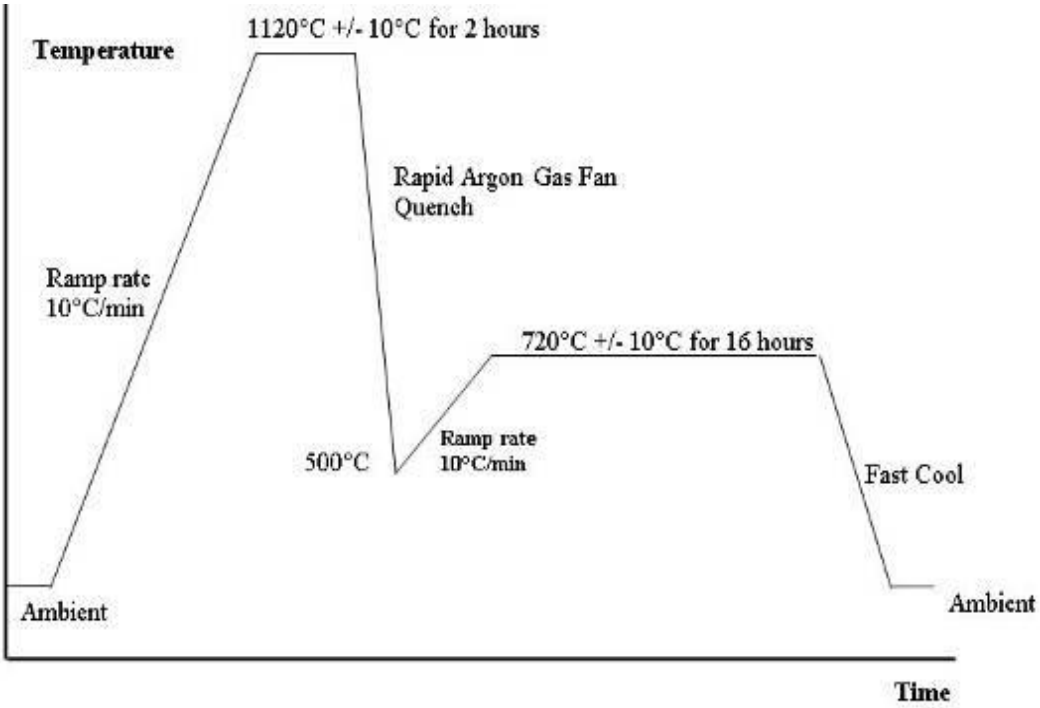

5. Heat Treatment Cycle – 5 (Section 2) - Solution Annealing + Ageing

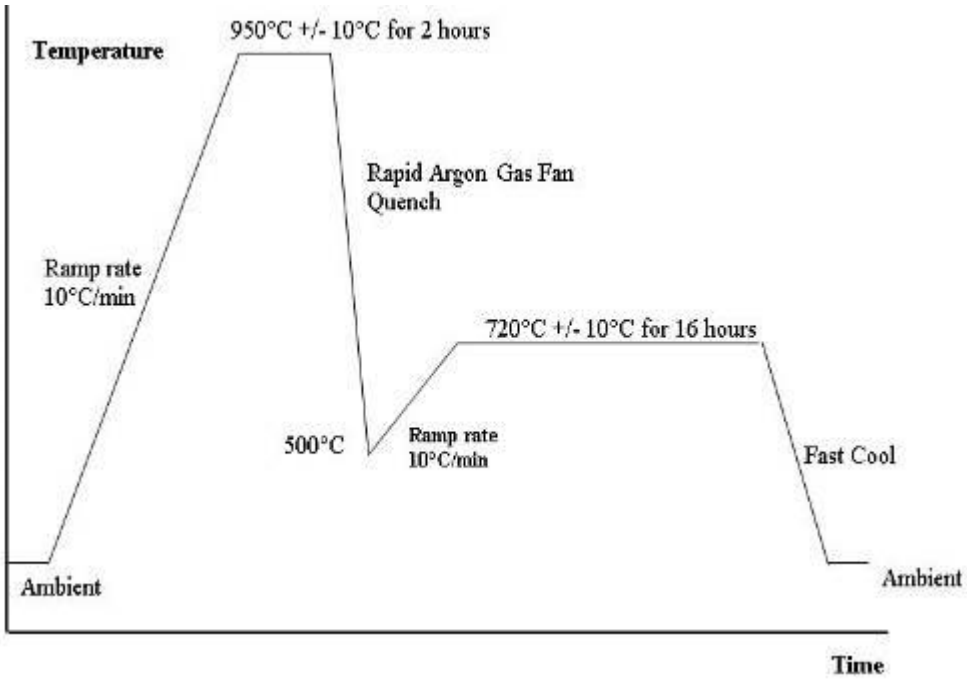

6. Heat Treatment Cycle – 6 (Section 9A) - Solution Annealing + Ageing

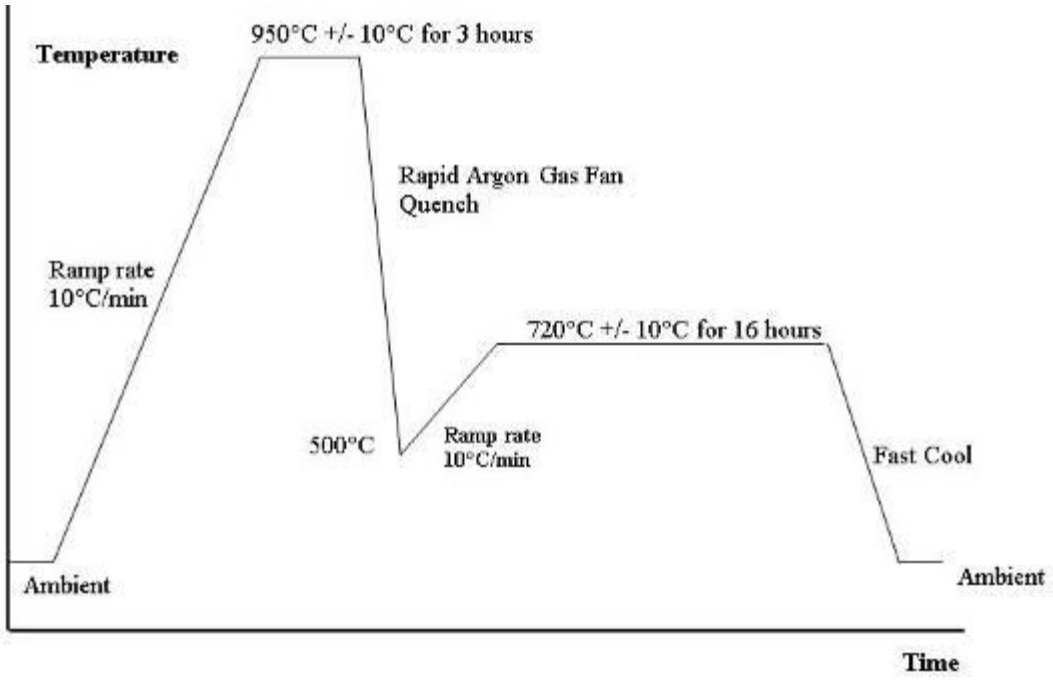

7. Heat Treatment Cycle – 7 (Section 9B) - Solution Annealing + Ageing

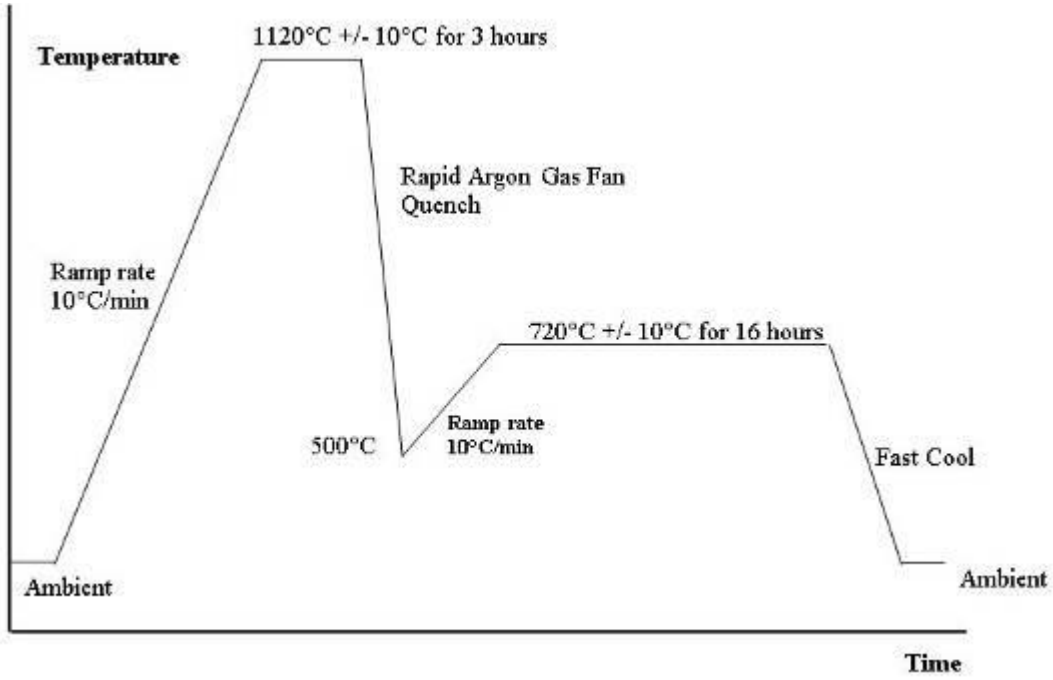

8. Heat Treatment Cycle – 8 (Section 8C-1) – SA + Age

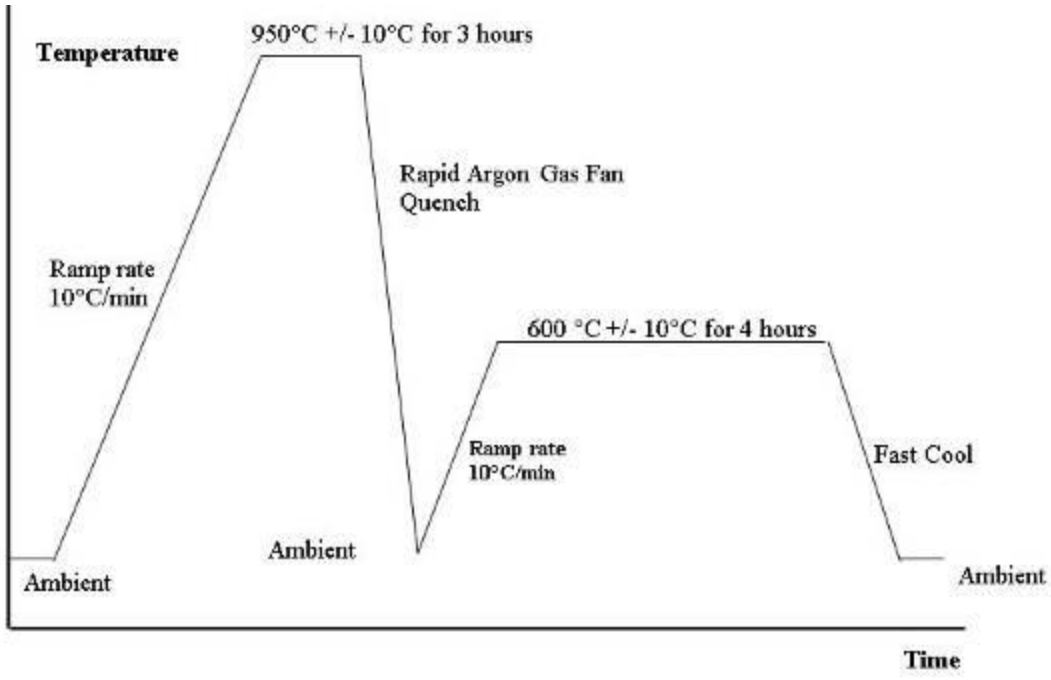

9. Heat Treatment Cycle – 9 (Section 8C-2) – SA + Age

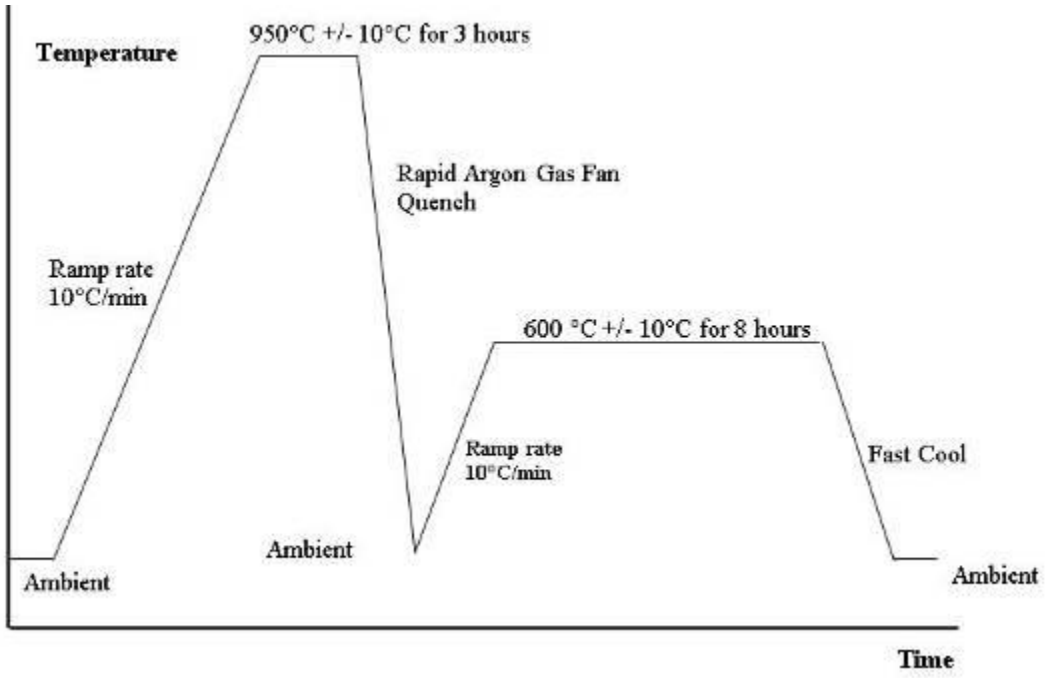

10. Heat Treatment Cycle – 10 (Section 8D-1) – SA + Age

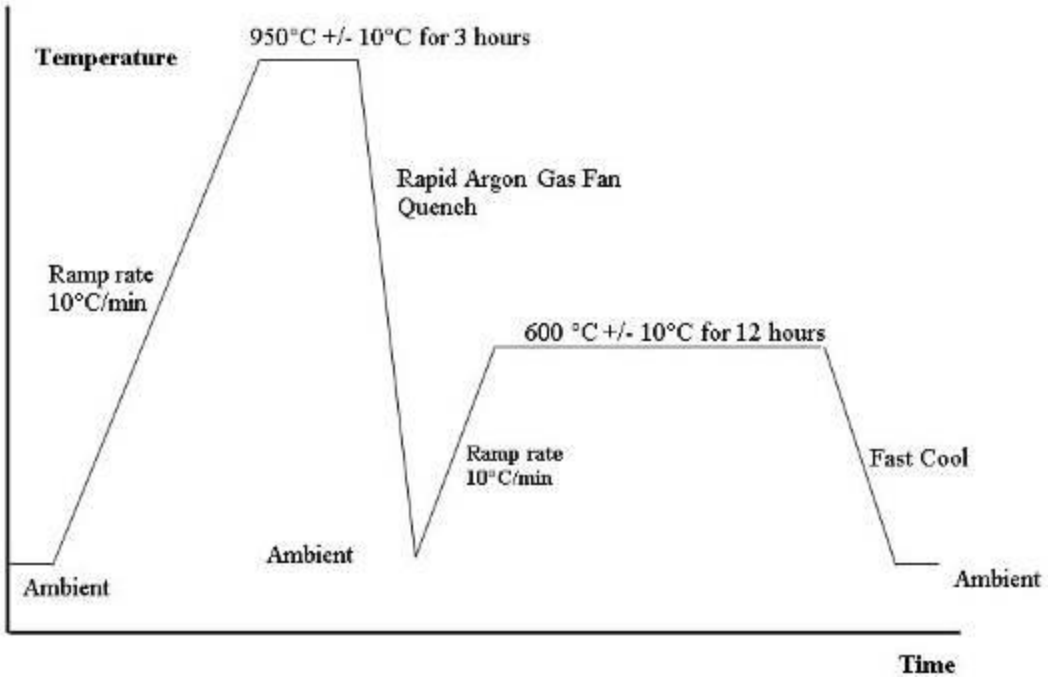

11. Heat Treatment Cycle – 11 (Section 8D-2) – SA + Age

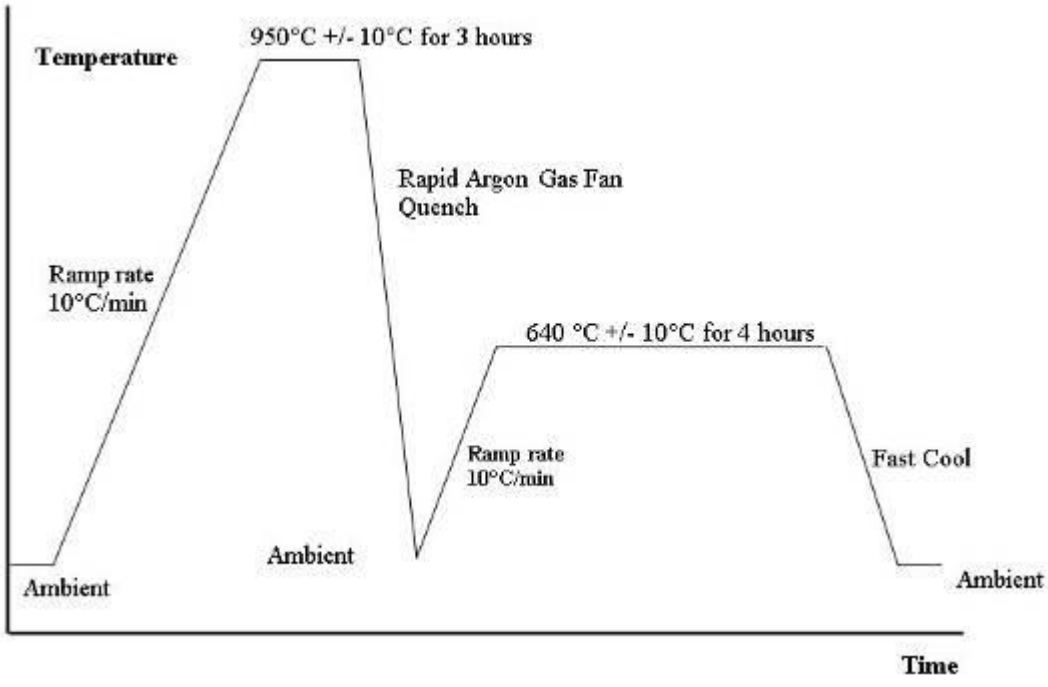

12. Heat Treatment Cycle – 12 (Section 7.1) – SA + Age

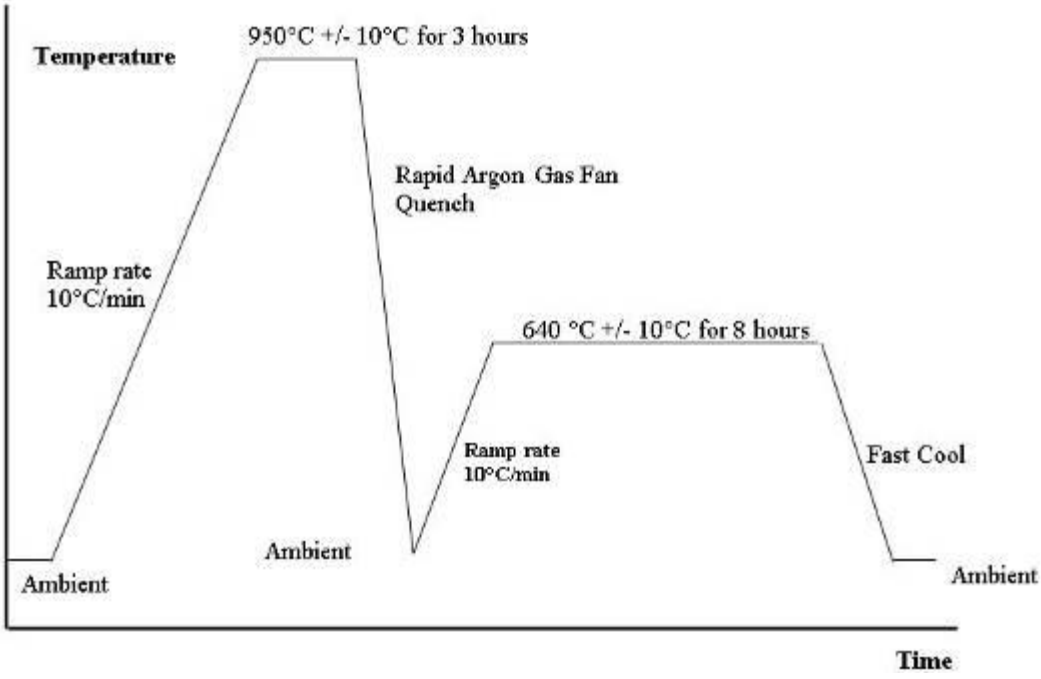

13. Heat Treatment Cycle – 13 (Section 7.2) – SA + Age

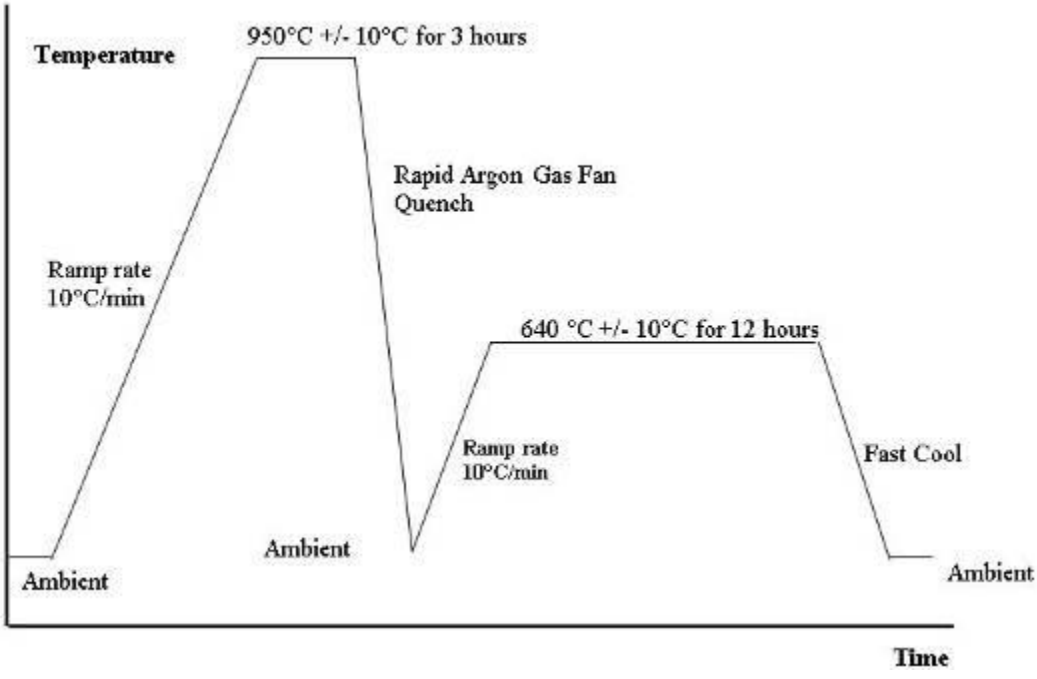

14. Heat Treatment Cycle – 14 (Section 6) – SA + Age

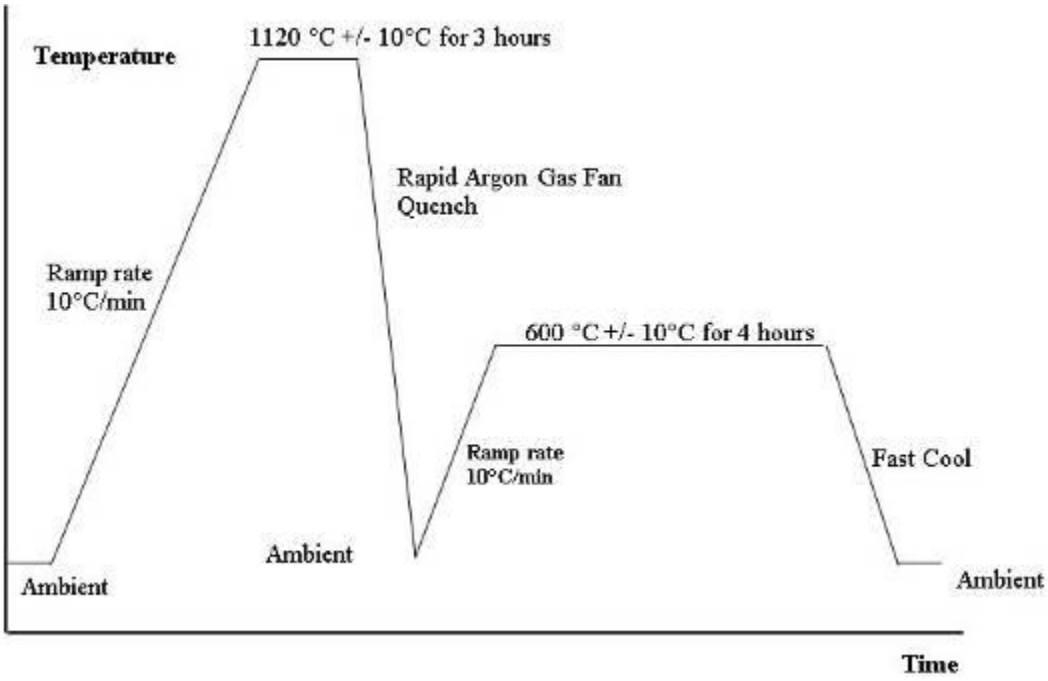

15. Heat Treatment Cycle – 15 (Section 5.1) – SA + Age

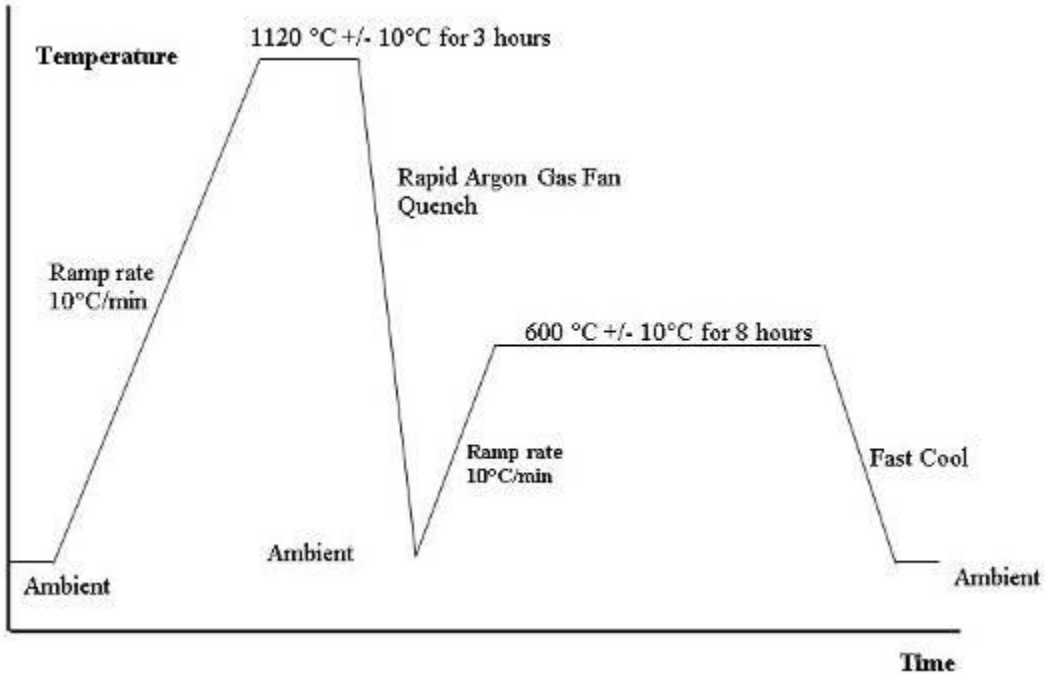

16. Heat Treatment Cycle – 16 (Section 5.2) – SA + Age

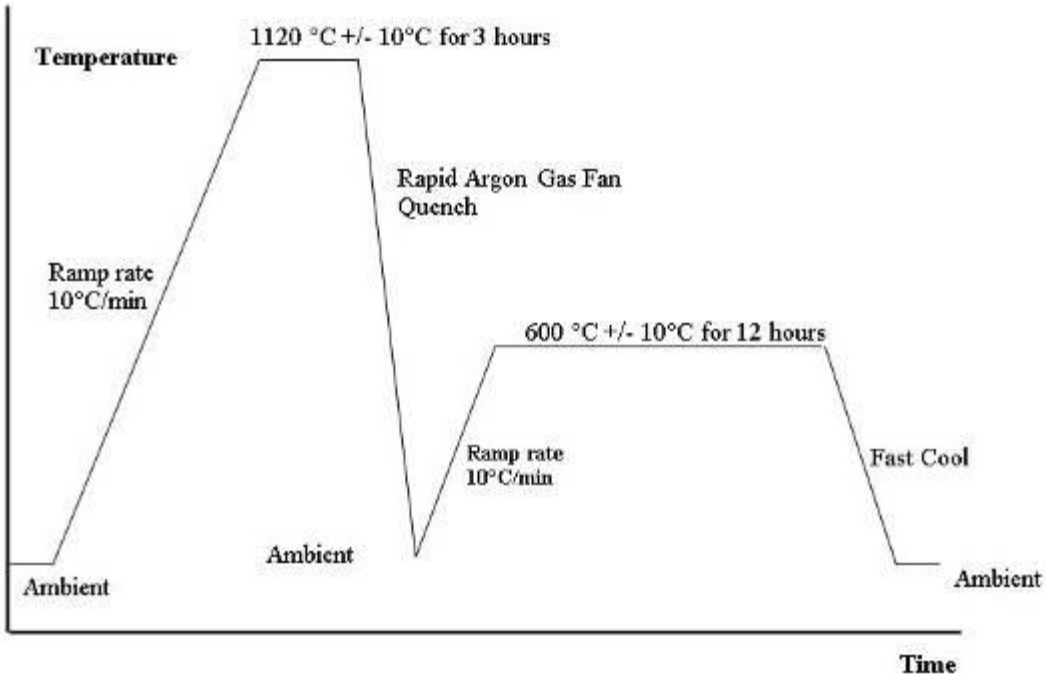

17. Heat Treatment Cycle – 17 (Section 4) – SA + Age

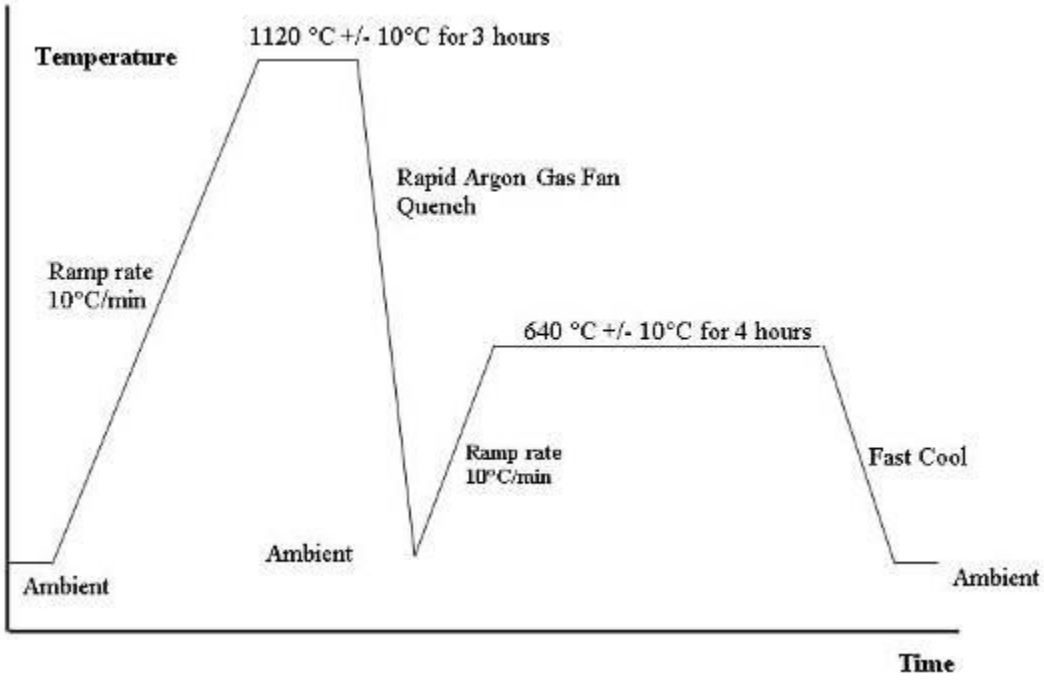

18. Heat Treatment Cycle – 18 (Section 3.1) – SA + Age

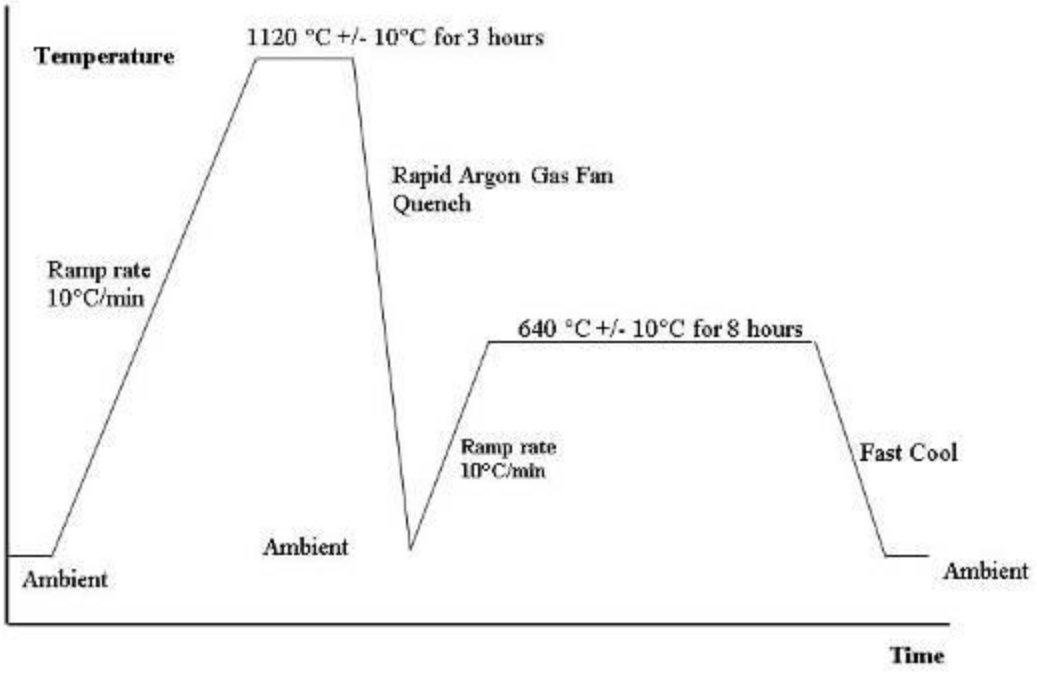

19. Heat Treatment Cycle – 19 (Section 7) – SA + Age

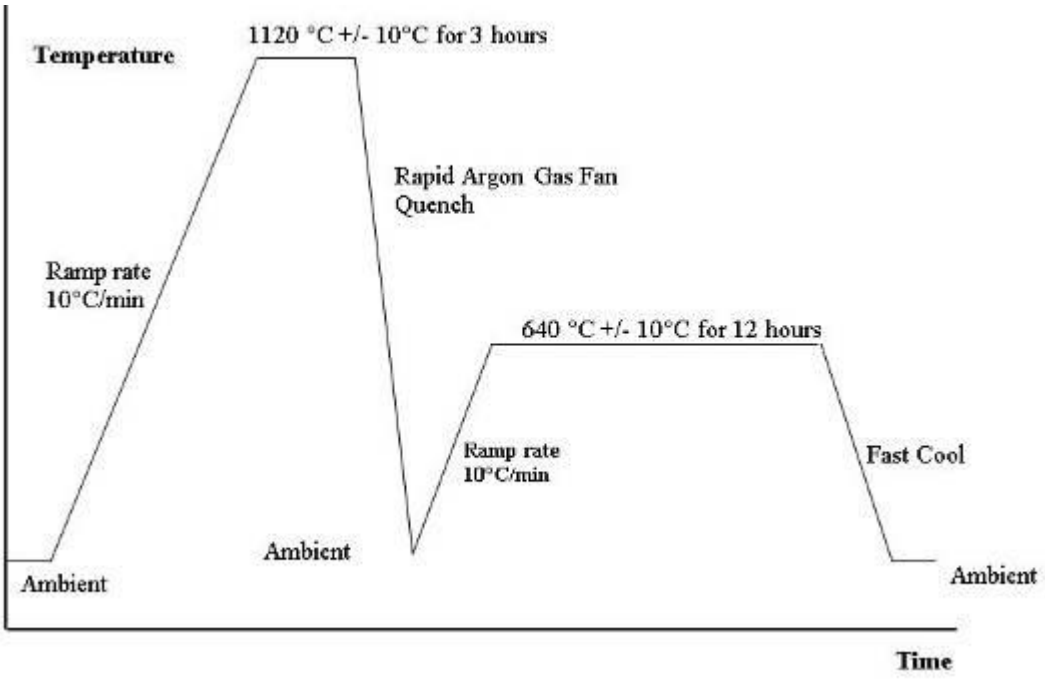

After each heat treatment, furnace charts/graphs were examined to check if the temperature and the soaking period were accurate. Each heat treatment cycle was named in accordance with the identified dissected section.

3.8 DESTRUCTIVE TESTS

Destructive tests were performed on each section after the heat treatment, and on the serviced turbine wheel. The destructive tests performed are listed below:

- Room Temperature Tensile Test
- High Temperature Tensile Test
- Stress Rupture Test
- Charpy Impact Test

The destructive tests were carried out at the laboratories in the United Kingdom.

The specimens for testing were along the thickness of the turbine wheel, as the maximum stresses are in this direction. The destructive mechanical testing direction for the sample on the test blocks is shown in Figure 3.19.

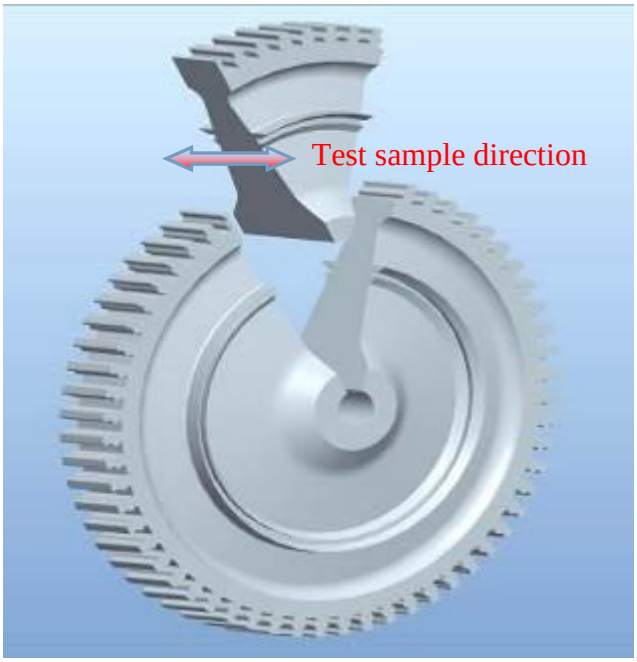

Figure 3.19: Schematic of the A-286 turbine wheel section showing the dissected section and sample direction for mechanical tests

3.8.1 TENSILE TESTING (ROOM TEMPERTAURE AND HIGH TEMPERATURE)

Tensile tests were performed on the new A-286 bar and the serviced turbine wheel sections. Tensile tests were also performed on the sections after various heat treatments. Two samples were tested and the average readings were reported. These tests were performed at both the room and high temperatures of (450°C), primarily to assess the tensile properties after various heat treatments. The room temperature tensile test was in accordance with ASTM E8 – "Standard Test Method for Tension Testing of Metallic Materials". The high temperature tensile test was in accordance with ASTM E21 – "Standard Test Methods for Elevated Temperature Tension Test of Metallic Materials". The tensile testing was carried

out at Incotest and Westmoreland laboratories, United Kingdom. The tensile testing machine used were Instron 5582 (room temperature) and Instron 8561 (high temperature) both of 100 kN capacity. The machines used for room temperature and high temperature tensile testing are shown in Figures 3.20 and 3.21.

Figure 3.20: Instron 5582, room temperature tensile testing machine

Figure 3.21: Instron 8561, high temperature tensile testing machine

All the samples for tensile testing were machined to nominal diameter 4.0 mm and parallel length 25.0 mm respectively. They were marked with a 4D gauge length for determination of plastic elongation. The samples were gripped with a single channel extensometer and tested at room temperature and 450 ^{o}C (Heating time approximately 60 mins and soak time 30 mins approximately) respectively. The samples were tested with a controlled strain rate beyond the yield point of the material with the help of an extensometer. All the tensile calculations were done by Instron software. The stress strain plots are also generated by the software.

3.8.2 CHARPY IMPACT TEST

The Charpy test is used to measure the impact energy required to break a material under certain impact load, normally at a predetermined temperature. Charpy impact tests were performed on the new A-286 bar and the serviced turbine wheel section before and after various heat treatments, in accordance with the ASTM E23 – "Standard Test Methods for Notched Bar Impact Testing of Metallic Materials". The charpy impact testing was carried out at Incotest and Westmoreland laboratories in the United Kingdom on Satec Systems Impact Testing Machine, Capacity: 240 ft-lbs. The Charpy testing machine used in the present study is shown in Figure 3.22.

Figure 3.22: Satec Impact Testing Machine

The Charpy impact test is primarily applied to know the material toughness or to determine whether the material is ductile or brittle [212]. On impact of the striking pendulum, the specimen absorbs energy until it yields. The specimen then starts to undergo plastic deformation at the notch. With the absorption of energy, the plastic zone at the notch work hardens. During this process and at a certain stage, the specimen would not be in a position to absorb any more energy, following which fracture occurs. The impact energy was then calculated based on the height to which the striker would have risen, if no test specimen was in place, and is compared with the height to which the striker actually rises [213]. Tough materials absorb a lot of energy, while brittle materials absorb very little energy prior to fracture. Fracture toughness can be evaluated by examining and studying the fracture surfaces [214]. The schematic in Figure 3.23 explains the mechanism of impact on the specimen.

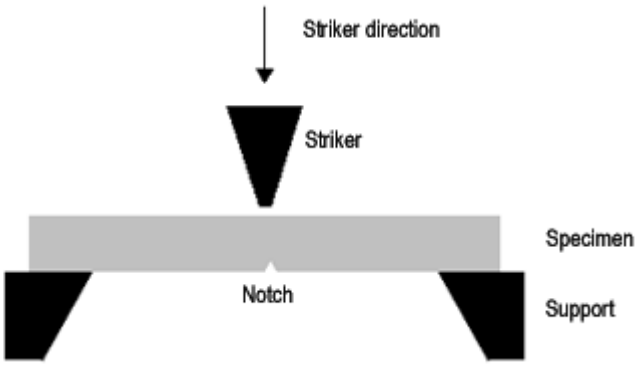

Figure 3.23: Schematic showing the principle of Charpy impact test

The samples were machined for testing as per ASTM E23 at room temperature. The specimen dimensions were 55 x 10 x 10 mm having a V notch. The V notch

is 2mm deep, with 45° angle and 0.25 mm radius at base of notch. The notch in the specimen is a zone of stress concentration. Three specimens were tested and the average value was reported.

3.8.3 STRESS RUPTURE TEST

The stress rupture test is primarily conducted to determine the time required for rupture of the material specimen at constant load and constant temperature. In general, the stress rupture test measures the time to rupture and the effect of temperature on long-time load-bearing characteristics. Stress rupture testing is similar to creep testing, except the stresses are higher [215].

Stress rupture and creep is initiated by three principal deformation processes at elevated temperature:

- Deformation by slip - More slip systems operate at high temperature, slip bands are coarser and widely spaced
- Sub-grain Formation: Creep deformation produces in-homogeneity especially around grain boundaries, allowing dislocations to arrange themselves into a low-angle grain boundary. This becomes easier for metals with high stacking false energy
- Grain boundary sliding: This is produced by shear process and promoted by increasing temperature/or decreasing strain rate. This results in grain boundary folding or grain boundary migration [216, 217].

Stress rupture testing was performed on the as new A-286 bar and the serviced turbine wheel section. Stress rupture tests were also performed on the sections

after various heat treatments, in accordance to ASTM E139 – "Standard Test Methods for Conducting Creep, Creep-Rupture, and Stress-Rupture Tests of Metallic Materials". Stress rupture testing was performed on one sample per section at two different set of parameters as mentioned below:

520 MPa stress and 550°C temperature

385 MPa stress and 650°C temperature

These parameters were finalized after discussion with Masood John Brown, Engineering Department. The parameters were so chosen that the design and actual operating conditions of the turbine wheel were covered. Stress rupture samples were machined to 6.34 mm diameter for 25.4 mm gauge length to apply a static stress at a specific temperature for 100 hours. The stress rupture tests were carried out on Qualicreep testing machine of 100 kN Capacity at Incotest and Westmoreland laboratories, United Kingdom. Stress rupture testing machine used is shown in Figure 3.24.

Figure 3.24: Stress Rupture Testing Machine

3.9 FRACTOGRAPHY USING SCANNING ELECTRON MICROSCOPE

The study of fractures is known as fractography. The study of fracture surface of a material enables to determine the nature and type of failure. Fractography or fracture analysis is important as it provides details on the nature and morphology of fracture including the origin of failure. Fracture morphology reveals important information whether the fracture is ductile or brittle by the modes such as dimple or cleavage. It can also provide valuable information such as breakage mechanism, direction of crack propagation and location of origin.

The fractured samples of the tensile tests, Charpy tests and the stress rupture testes were examined under SEM to study the fracture morphology. The fracture samples were dissected and cut just below the fracture surface. The dissected samples were cleaned in an ultrasonic bath for 30 minutes and then mounted on the SEM holder after making conductive with copper tapes. Fracture modes were observed by varying the magnifications from 1000x to 5000x. This was followed by capturing the images of the fractured specimens. The fracture morphology was co-related with the test performed.

CHAPTER 4

RESULTS

This chapter consists of results from chemical analysis, finite element modelling, portable hardness test, microstructural analysis, micro-hardness testing, room temperature and high temperature tensile test, stress rupture test and charpy impact test.

4.1 CHEMICAL COMPOSITION

The chemical composition of new A-286 bar and the serviced turbine wheel as analyzed on the optical spectrometer is given in Table 4.1.

Table 4.1- Chemical Composition by Optical Spectrometer

Weight %	C	Mn	Cr	Ni	Mo	Ti	V	Al	Si
New A-286 Bar	0.036	1.2	14.9	25.1	1.2	2.4	0.4	0.23	0.17
Serviced A-286 Turbine Wheel	0.039	1.2	14.8	25.1	1.3	2.4	0.39	0.23	0.17
A-286 Alloy Limits	0.08 max	2 max	13.5-16	24-27	1-1.5	1.9-2.35	0.1-0.5	0.35 max	1 max

The chemical composition of the as new A-286 bar and the serviced turbine wheel as analyzed by X-ray Fluorescence (XRF) is given in Table 4.2.

Table 4.2- Chemical Composition by XRF

Weight %	**C**	**Mn**	**Cr**	**Ni**	**Mo**	**Ti**	**V**	**Al**	**Si**
As New A-286 Bar	-	1.2	14.9	25.1	1.2	2.4	0.4	0.23	0.17
Serviced A-286 Turbine Wheel	-	1.2	14.8	25.1	1.3	2.4	0.39	0.23	0.17
A-286 Alloy Limits	0.08 max	2 max	13.5-16	24-27	1-1.5	1.9-2.35	0.1-0.5	0.35 max	1 max

The alloying elements of the as new A-286 bar and the serviced turbine wheel as analyzed on spectrometer and by XRF gun are consistent with the compositional limit of A-286 alloy.

4.2 FINITE ELEMENT ANALYSIS

Finite element analysis was performed on the serviced A-286 turbine wheel. The dimensions for the Finite Element model were primarily based on the measurements taken from the dissected section of the A-286 turbine wheel. The boundary conditions were applied as a lateral restraint in the axial direction, as shown in Figure 4.1.

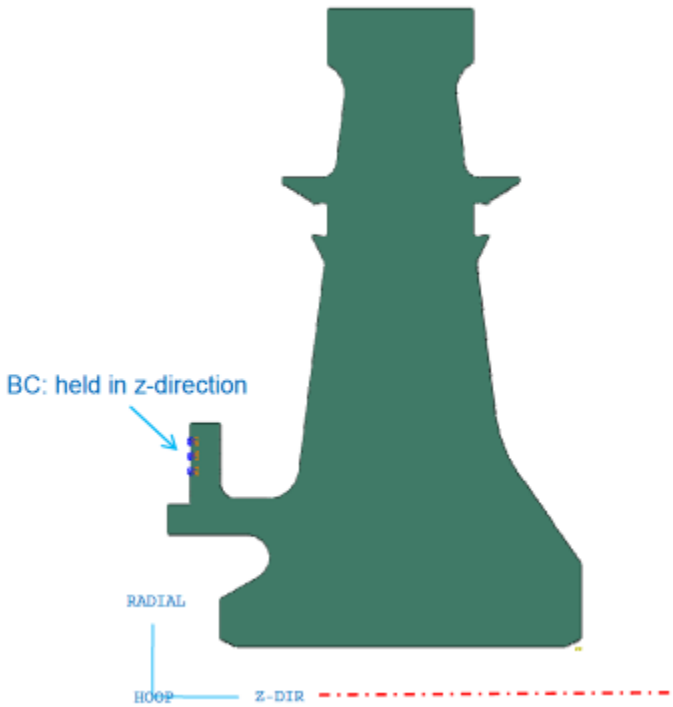

Figure 4.1: Boundary Conditions applied to Finite Element Model

The peak hoop stress occurs in the bore as would be expected. The radial stress distribution is more complex with stress concentrations occurring over a number of locations. The stress across the wheel was in the range of 300-450 MPa. While the locations are expected, the values are more dependent upon the geometry, boundary conditions and applied (blade) load. Obviously, the 2-D axisymmetric model does not include the dovetail slots; and hence the stress distribution shown near the rim is not representative of the real component. The stress distribution pattern on the serviced A-286 turbine wheel is shown in Figure 4.2.

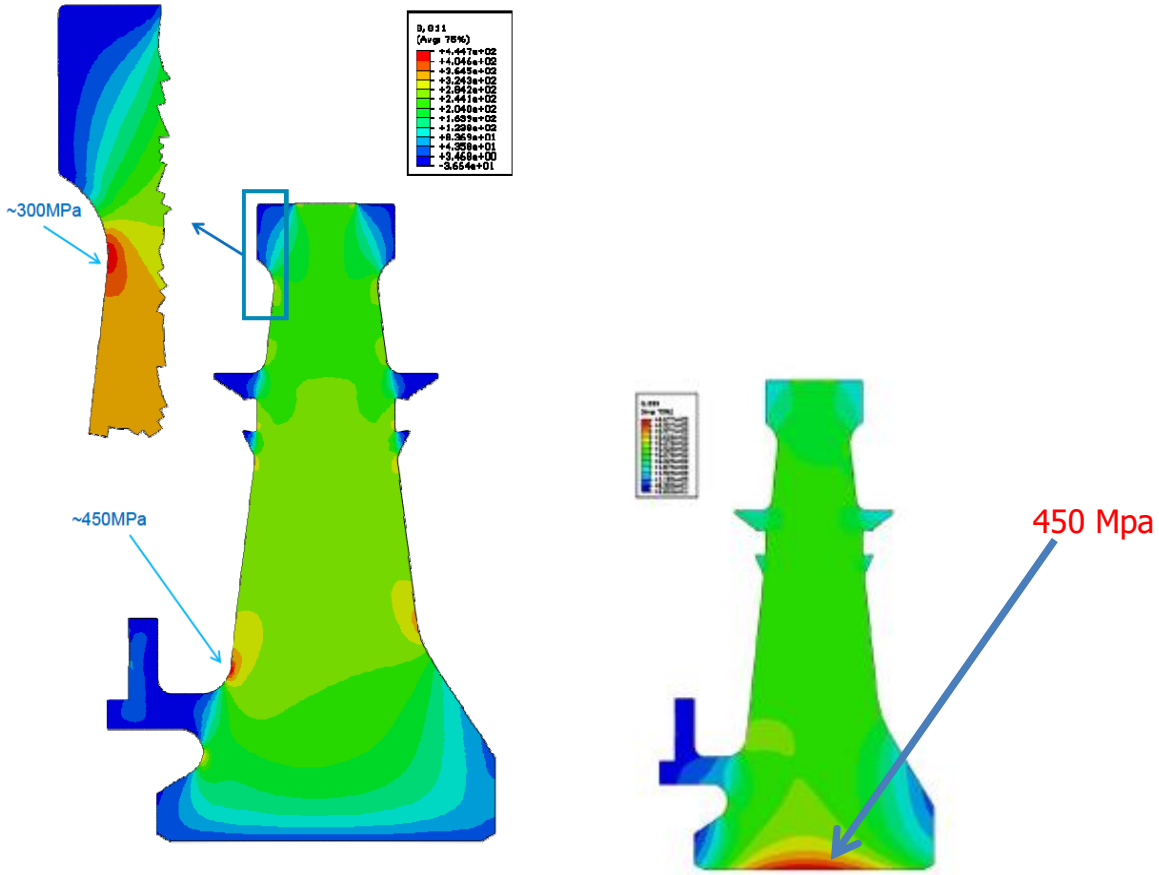

Figure 4.2: Stress Distribution Pattern in the serviced A-286 turbine wheel

4.3 PORTABLE HARDNESS TESTING

The portable hardness testing was conducted on the dissected section of the A-286 serviced wheel. The hardness measurement locations are shown in Figure 4.3.

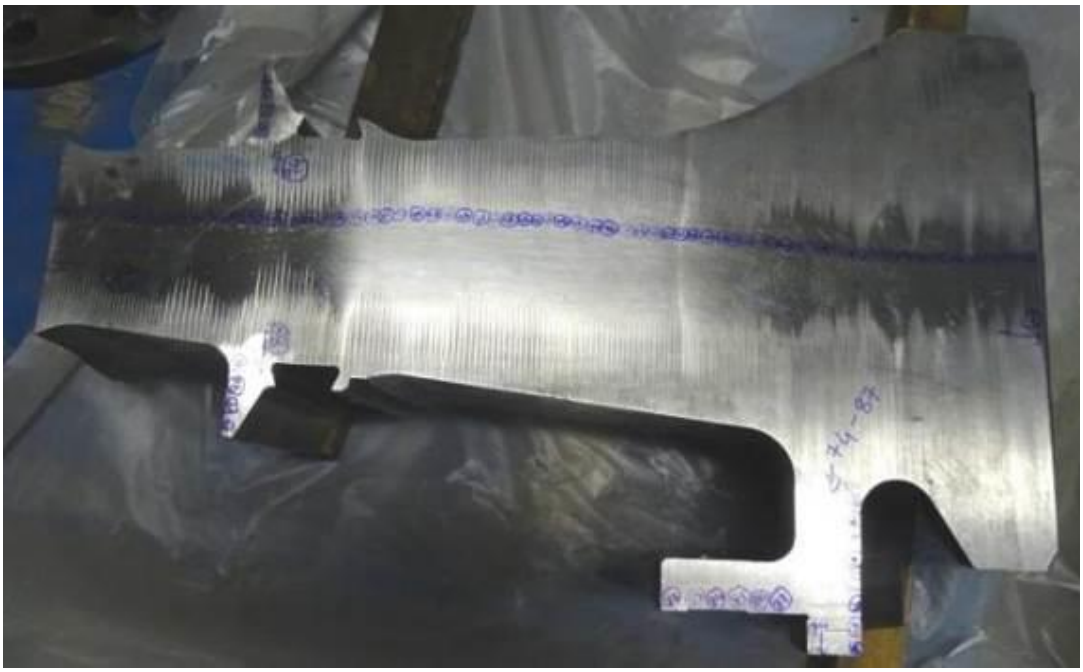

Figure 4.3: Portable hardness test locations on dissected section of A-286 test block

The portable hardness readings are given in Table 4.3.

Table 4.3- Portable hardness testing readings of the serviced turbine block.

Location	Hardness HV	Average HV	Location	Hardness HV	Average HV
1	319, 321, 325	322	49	323, 322, 324	323
2	323, 318, 316	319	50	325, 328, 329	327
3	320, 315, 312	316	51	332, 329, 331	331
4	313, 315, 318	315	52	333, 331, 335	333
5	319, 318, 321	319	53	321, 324, 326	324
6	317, 318, 316	317	54	324, 328, 329	327
7	312, 318, 319	316	55	328, 330, 323	327
8	318, 320, 322	320	56	326, 327, 324	326
9	319, 320, 316	318	57	332, 331, 328	330
10	316, 319, 320	318	58	322, 324, 327	325
11	324, 323, 327	325	59	321, 322, 324	322
12	322, 324, 320	322	60	319, 320, 323	321
13	321, 323, 325	323	61	321, 324, 325	323
14	322, 323, 325	323	62	322, 324, 320	322
15	324, 322, 325	324	63	327, 325, 321	324
16	326, 321, 328	325	64	323, 324, 327	325
17	320, 324, 322	322	65	325, 323, 324	324
18	327, 326, 325	326	66	321, 324, 326	324
19	326, 324, 323	324	67	324, 325, 321	323
20	325, 327, 326	326	68	326, 324, 325	325
21	324, 323, 325	324	69	322, 326, 324	324
22	329, 326, 327	327	70	331, 337, 334	334
23	324, 328, 326	326	71	328, 329, 331	329
24	329, 328, 325	327	72	325, 327, 329	327
25	334, 327, 332	331	73	324, 328, 329	327
26	330, 328, 329	329	74	330, 333, 334	332
27	330, 327, 329	329	75	329, 330, 334	331
28	330, 335, 333	333	76	329, 331, 333	331
29	333, 329, 328	330	77	329, 333, 334	332
30	335, 332, 327	331	78	329, 330, 333	331
31	332, 331, 336	333	79	331, 329, 330	330
32	335, 334, 333	334	80	324, 322, 329	325
33	331, 330, 335	332	81	330, 325, 324	326
34	333, 330, 332	332	82	303, 294, 306	301

Location	Hardness HV	Average HV
35	331, 335, 333	333
36	332, 329, 331	331
37	331, 330, 332	331
38	331, 332, 333	332
39	330, 331, 329	330
40	330, 331, 336	332
41	333, 334, 337	335
42	333, 331, 334	333
43	332, 334, 335	334
44	331, 334, 333	333
45	337, 332, 333	334
46	331, 335, 332	333
47	328, 327, 326	327
48	323, 321, 327	324

Location	Hardness HV	Average HV
83	311, 305, 306	307
84	317, 315, 312	315
85	318, 319, 316	318
86	323, 324, 321	323
87	321, 319, 316	319
88	314, 317, 311	314
89	327, 326, 319	324
90	326, 327, 328	327
91	326, 323, 324	324
92	323, 322, 321	322
93	321, 323, 326	323
94	330, 324, 328	327
95	329, 326, 325	327

It could be noted that there is no significant variation in the hardness. The hardness varies in the range of 314 to 344 HV.

4.4 MICROSTRUCTURE EVALUATION/ MICROEXAMINATION

The microstructures were examined for the new A-286 bar, serviced turbine wheel and on the wheel sections after different heat treatments. This section documents the observations of the microstructural evaluation.

4.4.1 MICROSTRUCTURES OF NEW A-286 BAR, SERVICED TURBINE WHEEL, PILOT AND PLANNED HEAT TREATMENTS

The micrographs of the as new A-286 bar and serviced turbine wheel are presented in Figures 4.4 to Figure 4.7.

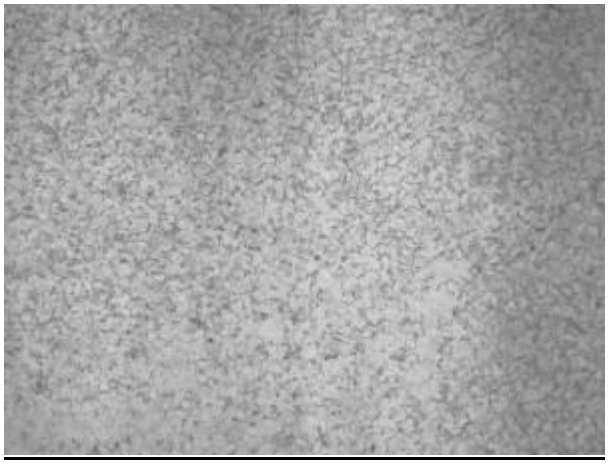

T

Figure 4.4: Micrograph of as new A-286 bar; transverse section showing the general microstructure; Etched; Original Magnification – 200x (GS:6-7)

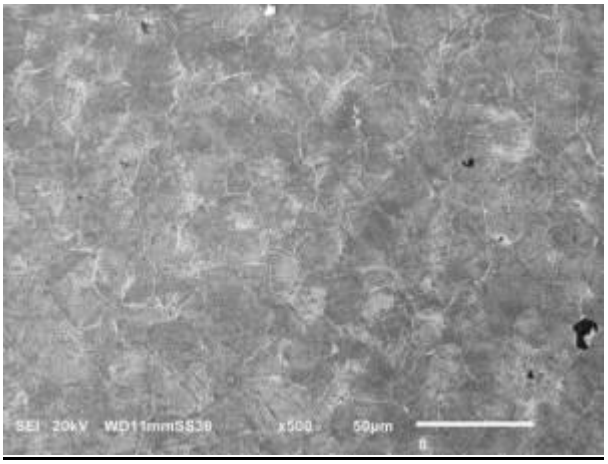

Figure 4.5: SEM micrograph of as new A-286 bar, transverse section; Etched; Original Magnification – 500x

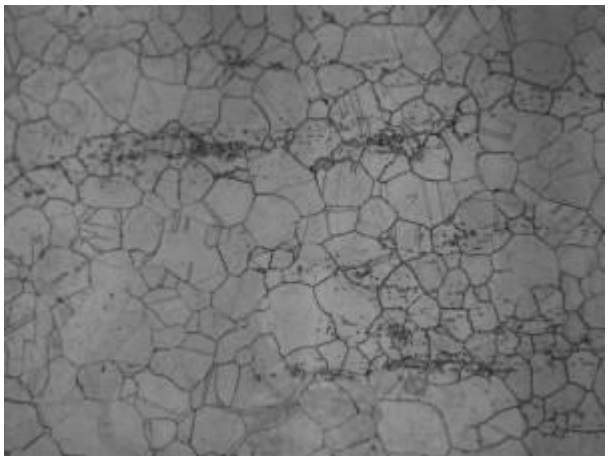

Figure 4.6: Micrograph of serviced turbine wheel; transverse section showing the general microstructure; Etched; Original Magnification – 200x (GS:4-5)

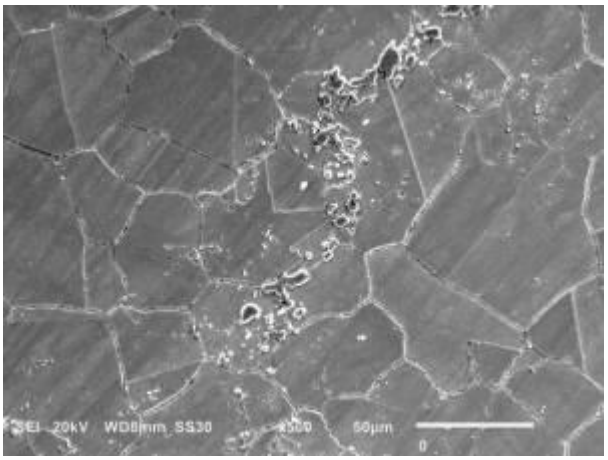

Figure 4.7: SEM micrograph of serviced turbine wheel; transverse section displays carbide network; Etched; Original Magnification – 500x

The micrographs of the pilot solution annealing heat treatments are presented in Figures 4.8 to Figure 4.13.

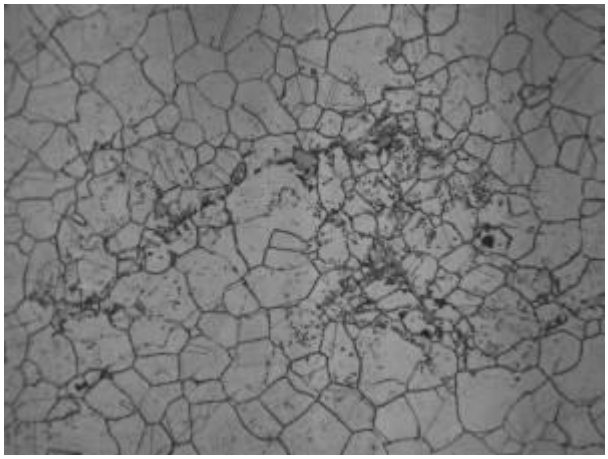

Figure 4.8: Micrograph of Transverse section after pilot HT (SA – 750 ^{0}C x 3hrs) showing the general microstructure; Etched; Original Magnification – 200x (GS:4-5)

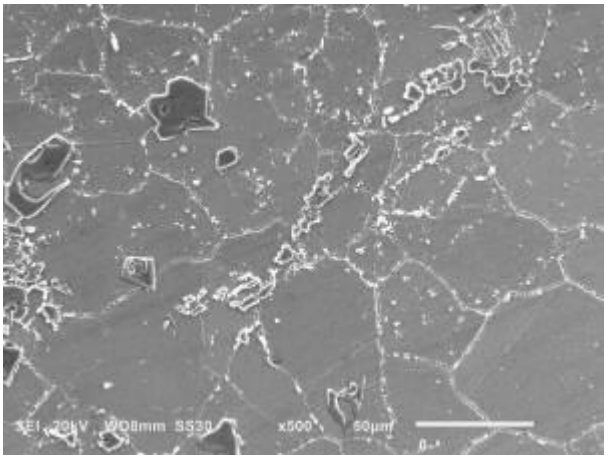

Figure 4.9: SEM micrograph of Transverse section after pilot HT (SA – 750 ^{0}C x 3hrs) showing the general microstructure Etched; Original Magnification – 500x

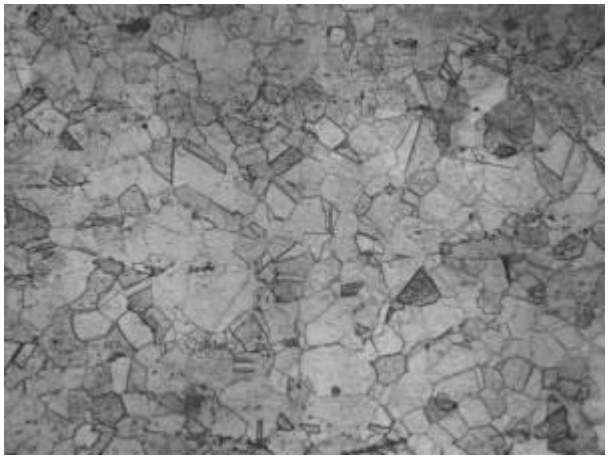

Figure 4.10: Micrograph of Transverse section after pilot HT (SA – 950 ^{0}C x 3hrs) showing the general microstructure; Etched; Original Magnification – 200x (GS:5-6)

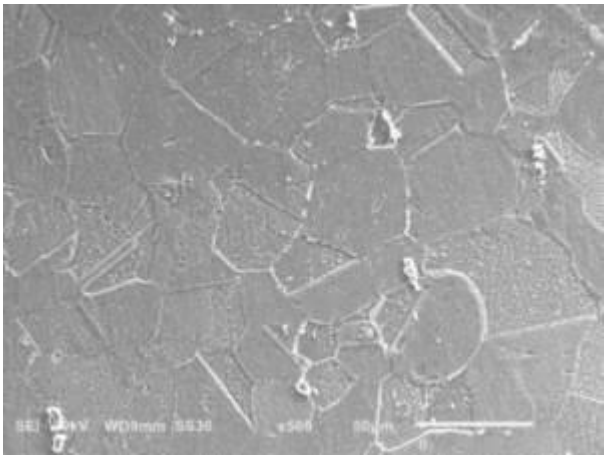

Figure 4.11: SEM micrograph of Transverse section after pilot HT (SA – 950 ^{0}C x 3hrs) showing the general microstructure; Etched; Original Magnification – 500x

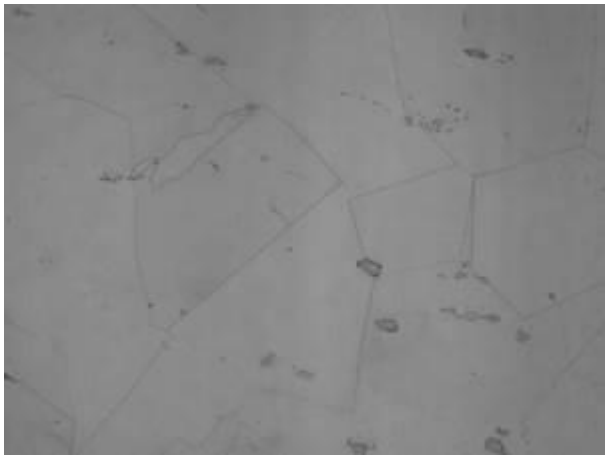

Figure 4.12: Micrograph of Transverse section after pilot HT (SA – 1120 ^{0}C x 3hrs) showing the general microstructure; Etched; Original Magnification – 200x (GS:1-2)

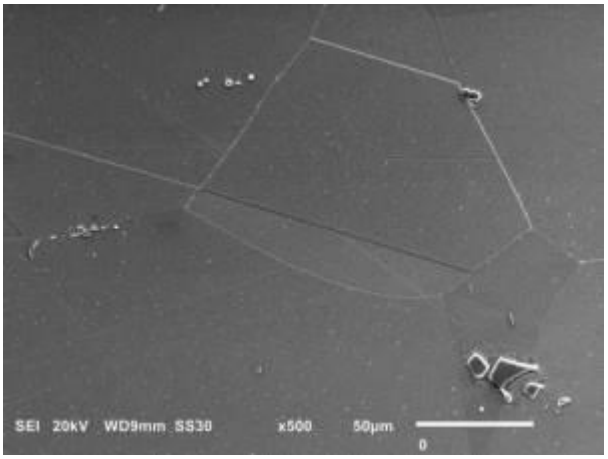

Figure 4.13: SEM micrograph of Transverse section after pilot HT (SA – 1120 ^{0}C x 3hrs) showing the general microstructure; Etched; Original Magnification – 500x

The micrographs of the conducted heat treatments (solution annealing + ageing) are presented in Figures 4.14 to Figure 4.45.

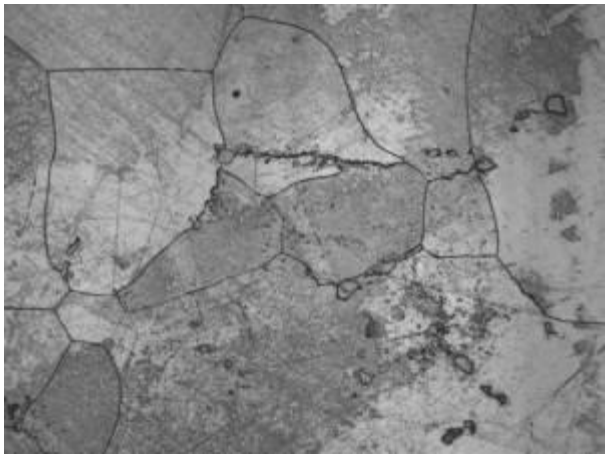

Figure 4.14: Micrograph of Transverse section after HT (SA – 1120 ^{0}C x 2hrs & Age 720 ^{0}C x 16hrs) showing the general microstructure; Etched; Original Magnification – 200x (GS:1-2)

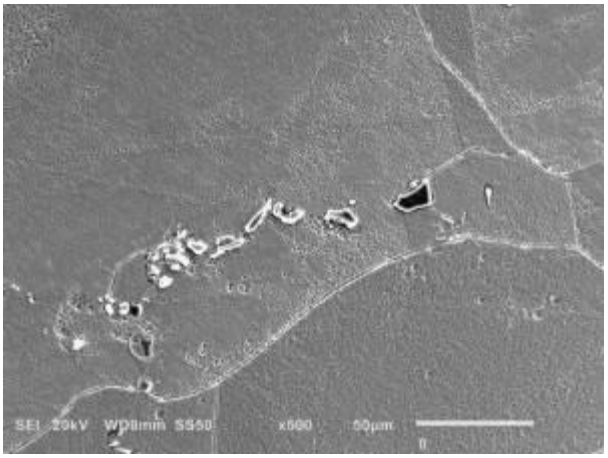

Figure 4.15: SEM micrograph of Transverse section after HT (SA – 1120 ^{0}C x 2hrs & Age 720 ^{0}C x 16hrs) showing the general microstructure; Etched; Original Magnification – 500x

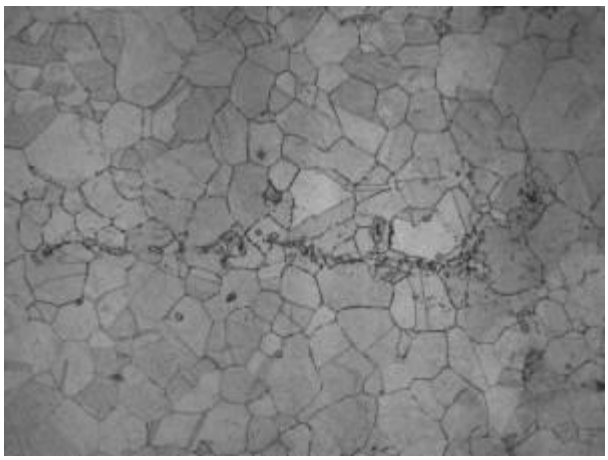

Figure 4.16: Micrograph of Transverse section after HT (SA – 950 ^{0}C x 2hrs & Age 720 ^{0}C x 16hrs) showing the general microstructure; Etched; Original Magnification – 200x (GS:4-5)

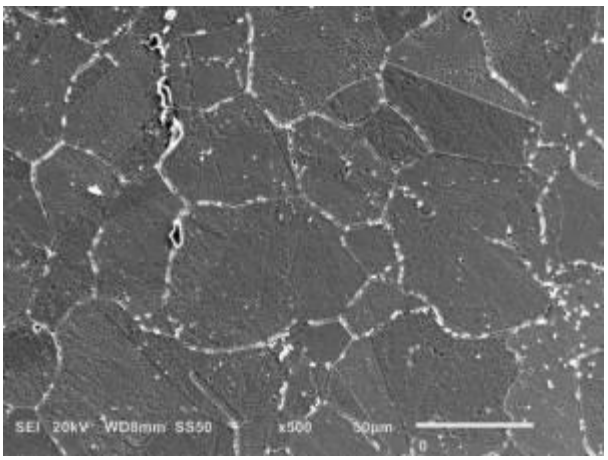

Figure 4.17: SEM micrograph of Transverse section after HT (SA – 950 ^{0}C x 2hrs & Age 720 ^{0}C x 16hrs) showing the general microstructure; Etched; Original Magnification – 500x

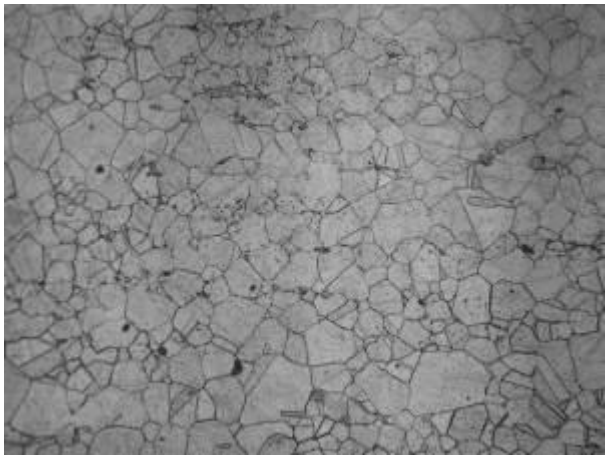

Figure 4.18: Micrograph of Transverse section after HT (SA – 950 ^{0}C x 3hrs & Age 720 ^{0}C x 16hrs) showing the general microstructure; Etched; Original Magnification – 200x (GS:5-6)

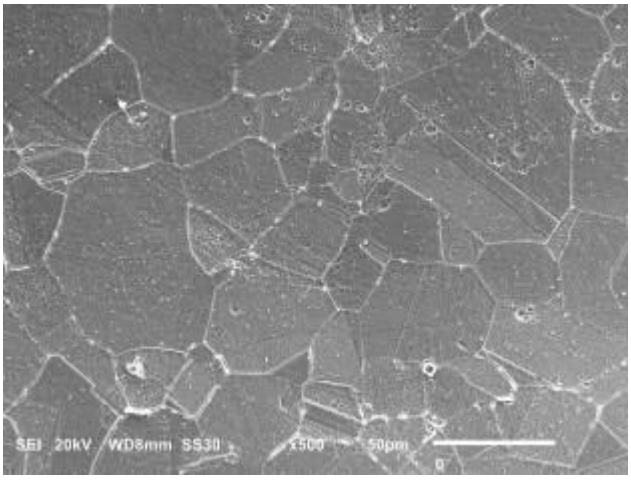

Figure 4.19: SEM micrograph of Transverse section after HT (SA – 950 ^{0}C x 3hrs & Age 720 ^{0}C x 16hrs) showing the general microstructure;; Etched; Original Magnification – 500x

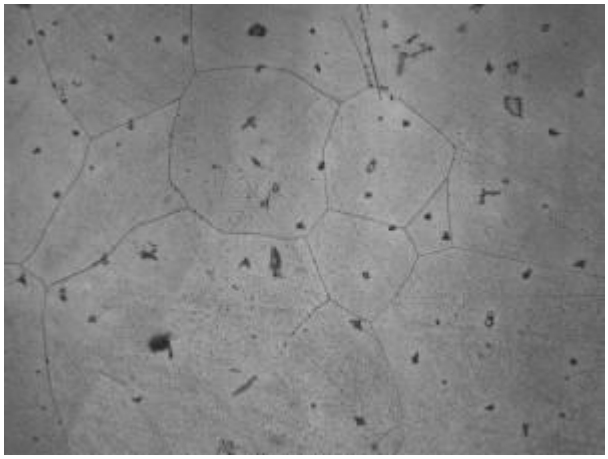

Figure 4.20: Micrograph of Transverse section after HT (SA – 1120 ^{0}C x 3hrs & Age 720 ^{0}C x 16hrs) showing the general microstructure; Etched; Original Magnification – 200x(GS:1-2)

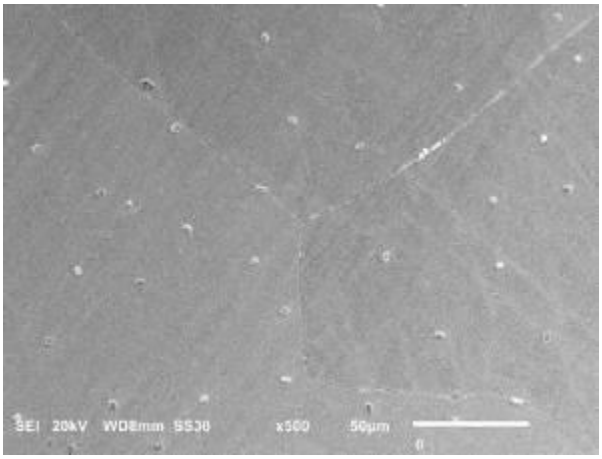

Figure 4.21: SEM micrograph of Transverse section after HT (SA – 1120 ^{0}C x 3hrs & Age 720 ^{0}C x 16hrs) showing the general microstructure; Etched; Original Magnification – 500x

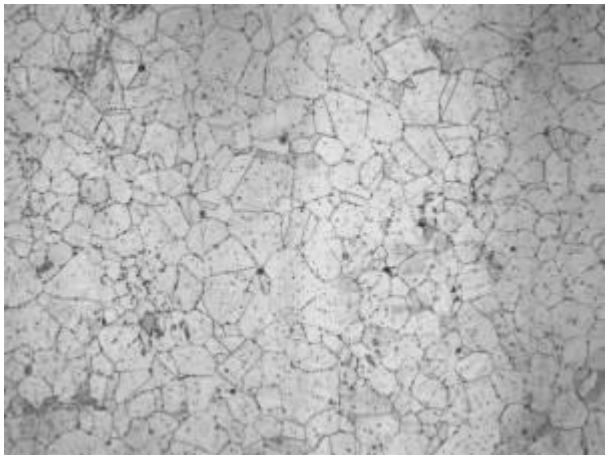

Figure 4.22: Micrograph of Transverse section after HT (SA – 950 ^{0}C x 3hrs & Age 600 ^{0}C x 4hrs) showing the general microstructure Etched; Original Magnification – 200x (GS:4-5)

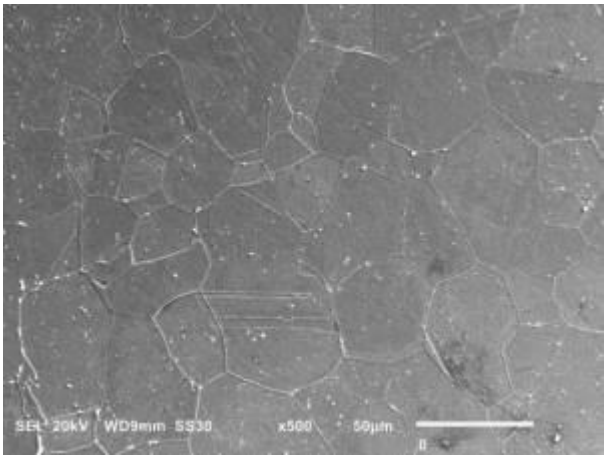

Figure 4.23: SEM micrograph of Transverse section; after HT (SA – 950 ^{0}C x 3hrs & Age 600 ^{0}C x 4hrs) showing the general microstructure Etched; Original Magnification – 500x

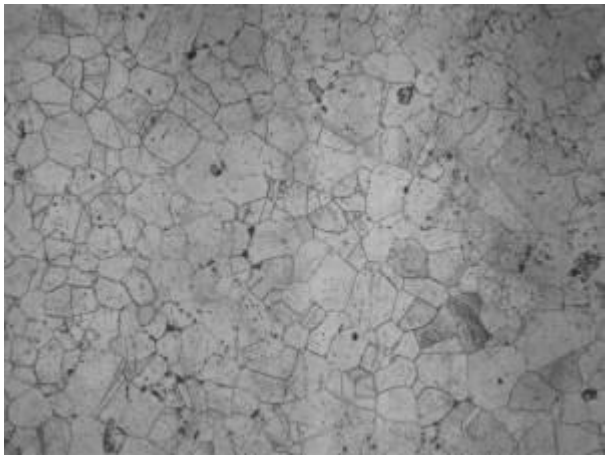

Figure 4.24: Micrograph of Transverse section after HT (SA – 950 ^{0}C x 3hrs & Age 600 ^{0}C x 8hrs) showing the general microstructure; Etched; Original Magnification – 200x(GS:4-5)

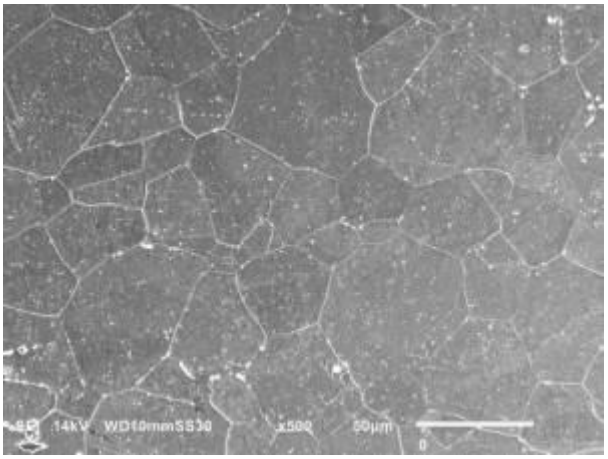

Figure 4.25: SEM micrograph of Transverse section after HT (SA – 950 ^{0}C x 3hrs & Age 600 ^{0}C x 8hrs) showing the general microstructure Etched; Original Magnification – 500x

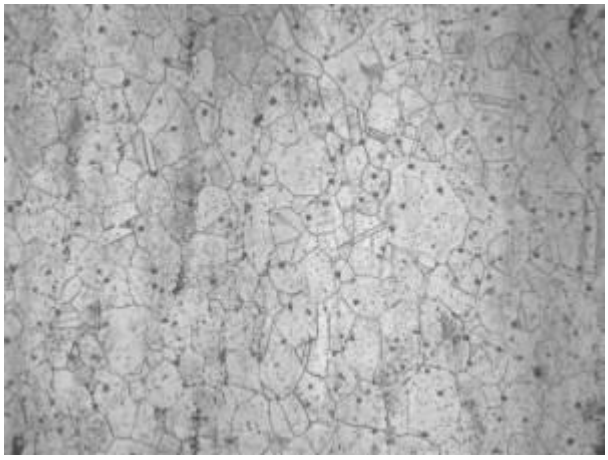

Figure 4.26: Micrograph of Transverse section after HT (SA – 950 ^{0}C x 3hrs & Age 600 ^{0}C x 12hrs) showing the general microstructure; Etched; Original Magnification – 200x (GS:5-6)

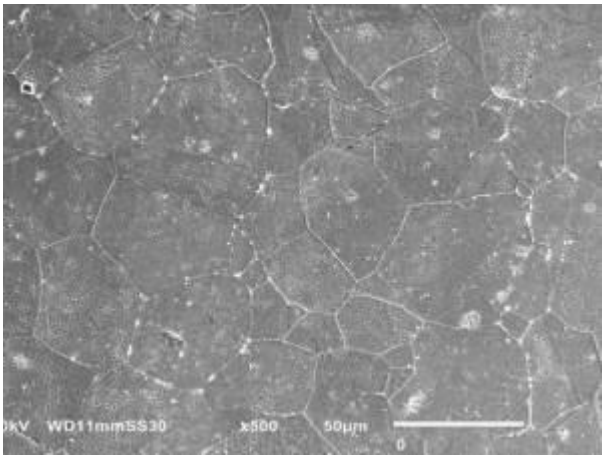

Figure 4.27: SEM micrograph of Transverse section after HT (SA – 950 ^{0}C x 3hrs & Age 600 ^{0}C x 12hrs) showing the general microstructure Etched; Original Magnification – 500x

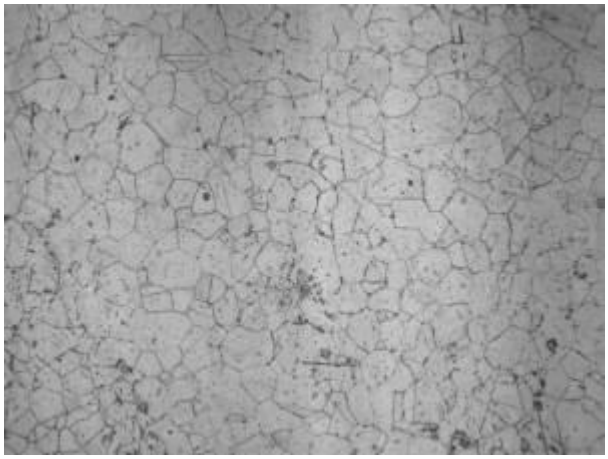

Figure 4.28: Micrograph of Transverse section after HT (SA – 950 ^{0}C x 3hrs & Age 640 ^{0}C x 4hrs) showing the general microstructure; Etched; Original Magnification – 200x (GS:5-6)

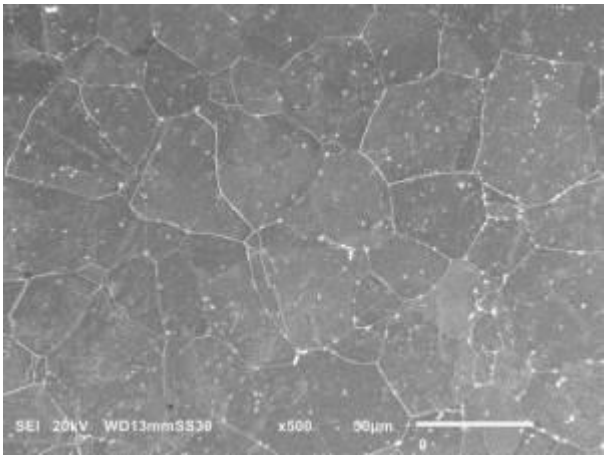

Figure 4.29: SEM micrograph of Transverse section after HT (SA – 950 ^{0}C x 3hrs & Age 640 ^{0}C x 4hrs) showing the general microstructure Etched; Original Magnification – 500x

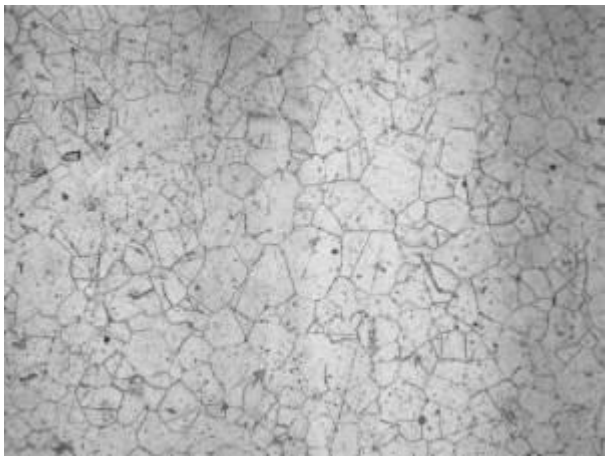

Figure 4.30: Micrograph of Transverse section after HT (SA – 950 ^{0}C x 3hrs & Age 640 ^{0}C x 8hrs) showing the general microstructure; Etched; Original Magnification – 200x (GS:5-6)

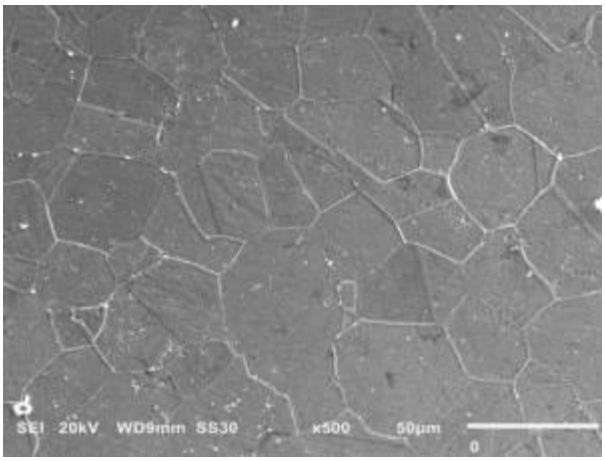

Figure 4.31: SEM micrograph of Transverse section after HT (SA – 950 ^{0}C x 3hrs & Age 640 ^{0}C x 8hrs) showing the general microstructure Etched; Original Magnification – 500x

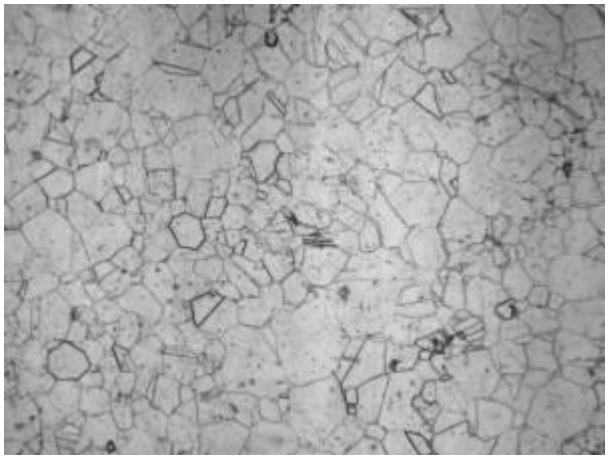

Figure 4.32: Micrograph of Transverse section after HT (SA – 950 ^{0}C x 3hrs & Age 640 ^{0}C x 12hrs) showing the general microstructure; Etched; Original Magnification – 200x (GS:6-7)

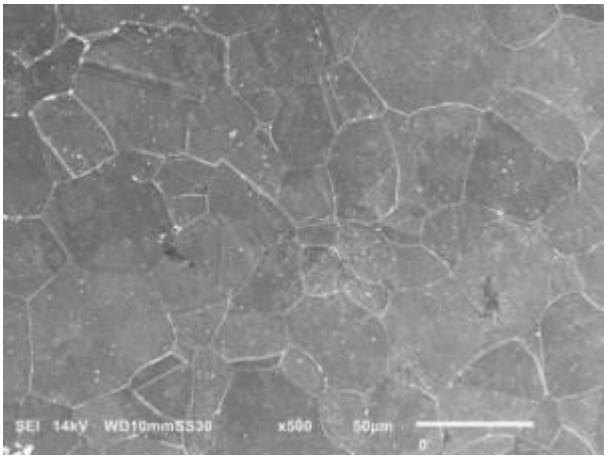

Figure 4.33: SEM micrograph of Transverse section after HT (SA – 950 ^{0}C x 3hrs & Age 640 ^{0}C x 12hrs) showing the general microstructure Etched; Original Magnification – 500x

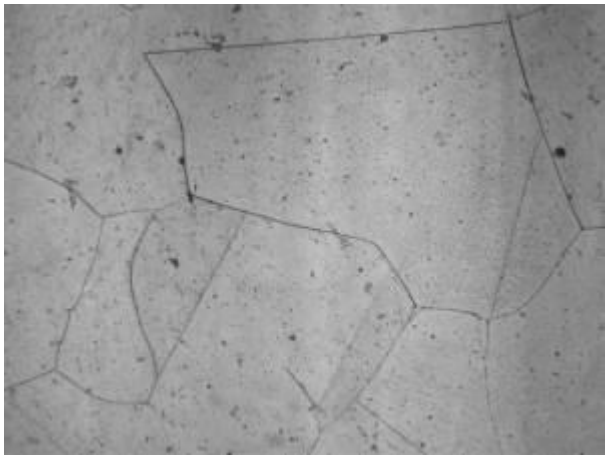

Figure 4.34: Micrograph of Transverse section after HT (SA – 1120 ^{0}C x 3hrs & Age 600 ^{0}C x 4hrs) showing the general microstructure; Etched; Original Magnification – 200x (GS:1-2)

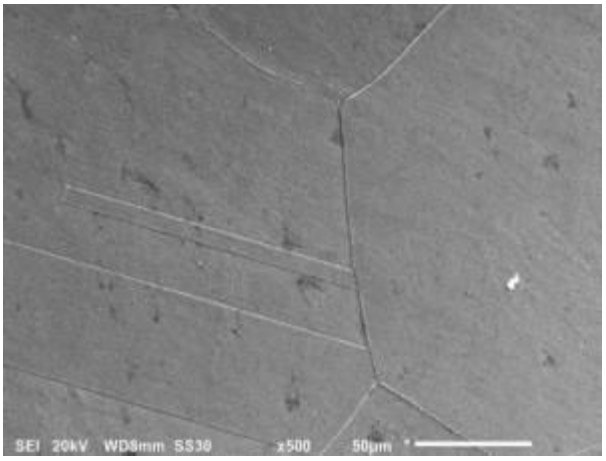

Figure 4.35: SEM micrograph of Transverse section after HT (SA – 1120 ^{0}C x 3hrs & Age 600 ^{0}C x 4hrs) showing the general microstructure; Etched; Original Magnification – 500x

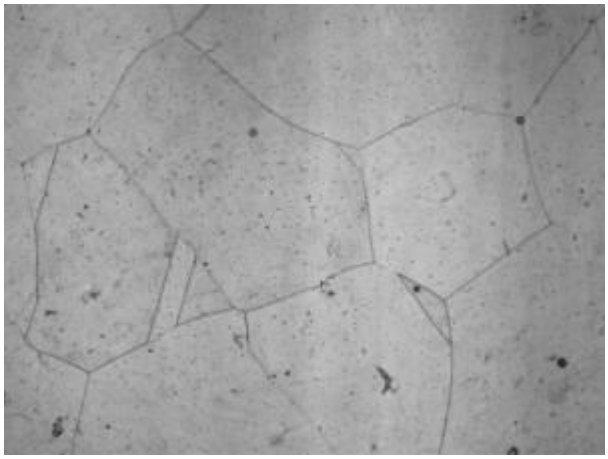

Figure 4.36: Micrograph of Transverse section after HT (SA – 1120 ^{0}C x 3hrs & Age 600 ^{0}C x 8hrs) showing the general microstructure; Etched; Original Magnification – 200x (GS:2-3)

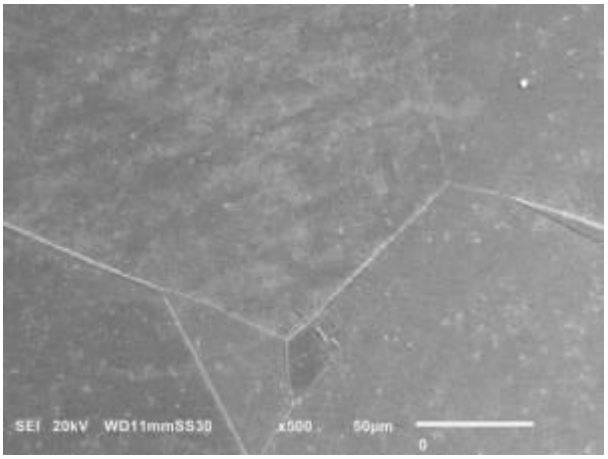

Figure 4.37: SEM micrograph of Transverse section after HT (SA – 1120 ^{0}C x 3hrs & Age 600 ^{0}C x 8hrs) showing the general microstructure; Etched; Original Magnification – 500x

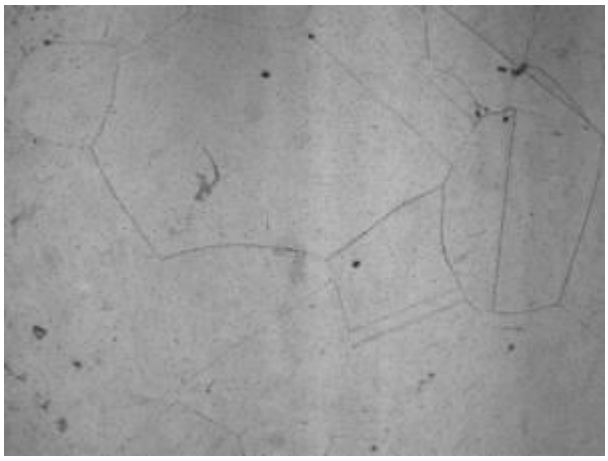

Figure 4.38: Micrograph of Transverse section after HT (SA – 1120 ^{0}C x 3hrs & Age 600 ^{0}C x 12hrs) showing the general microstructure; Etched; Original Magnification – 200x (GS:2-3)

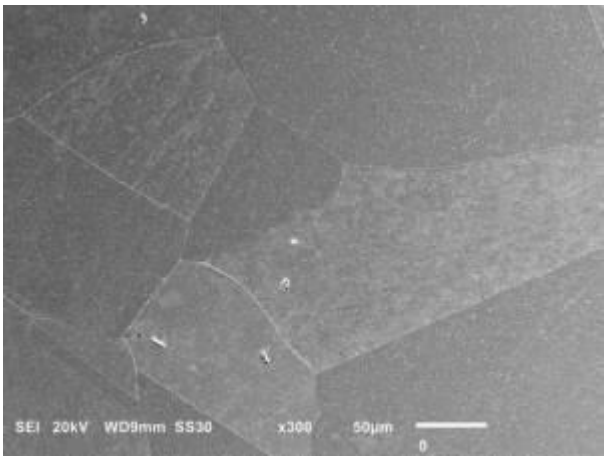

Figure 4.39: SEM micrograph of Transverse section after HT (SA – 1120 ^{0}C x 3hrs & Age 600 ^{0}C x 12hrs) showing the general microstructure Etched; Original Magnification – 500x

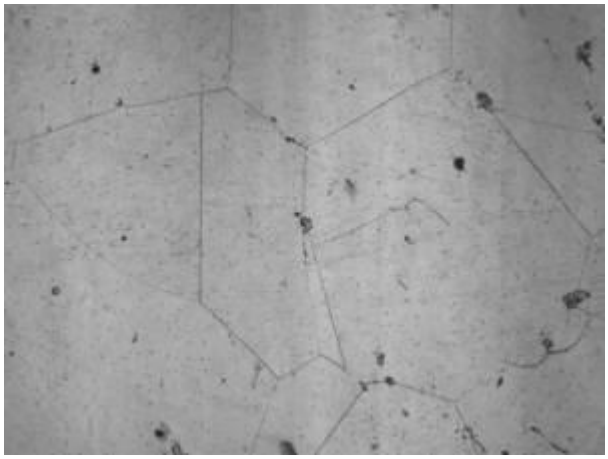

Figure 4.40: Micrograph of Transverse section after HT (SA – 1120 ^{0}C x 3hrs & Age 640 ^{0}C x 4hrs) showing the general microstructure; Etched; Original Magnification – 200x (GS:1-2)

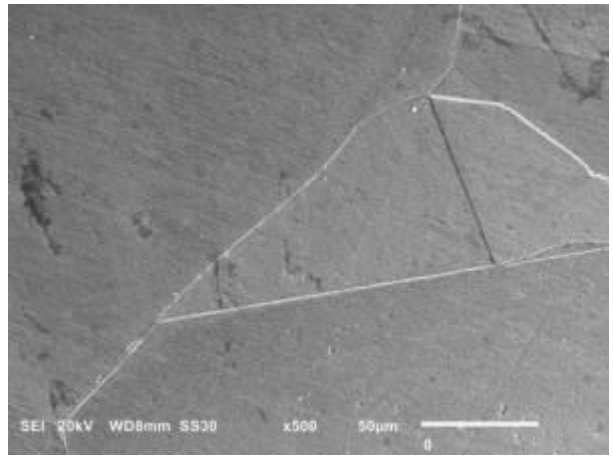

Figure 4.41: SEM micrograph of Transverse section after HT (SA – 1120 ^{0}C x 3hrs & Age 640 ^{0}C x 4hrs) showing the general microstructure; Etched; Original Magnification – 500x

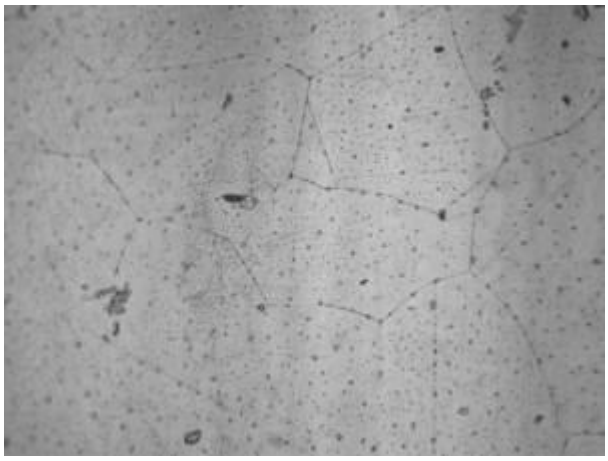

Figure 4.42: Micrograph of Transverse section after HT (SA – 1120 ^{0}C x 3hrs & Age 640 ^{0}C x 8hrs) showing the general microstructure; Etched; Original Magnification – 200x (GS:2-3)

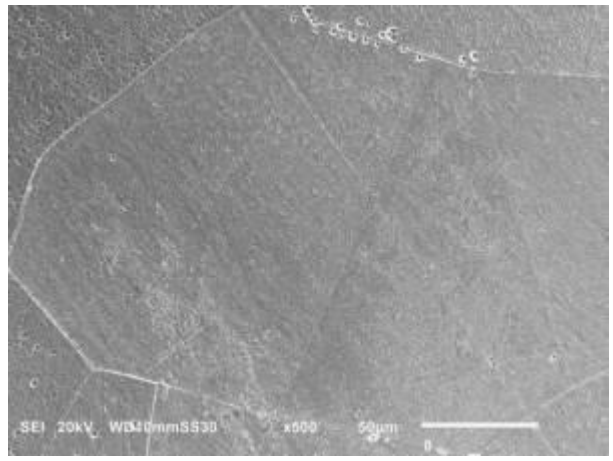

Figure 4.43: SEM micrograph of Transverse section after HT (SA – 1120 ^{0}C x 3hrs & Age 640 ^{0}C x 8hrs) showing the general microstructure; Etched; Original Magnification – 500x

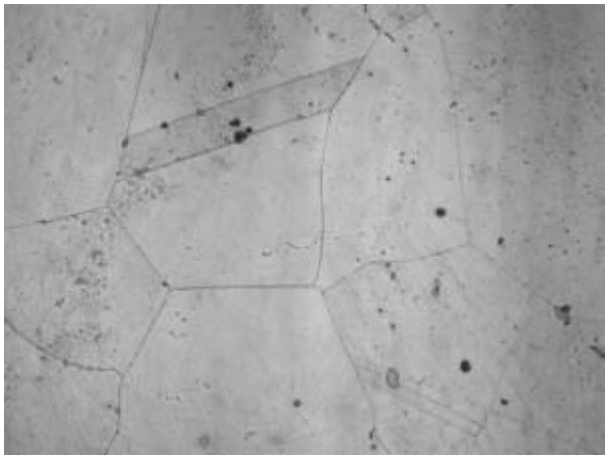

Figure 4.44: Micrograph of Transverse section after HT (SA – 1120 ^{0}C x 3hrs & Age 640 ^{0}C x 12hrs) showing the general microstructure Etched; Original Magnification – 200x (GS:2-3)

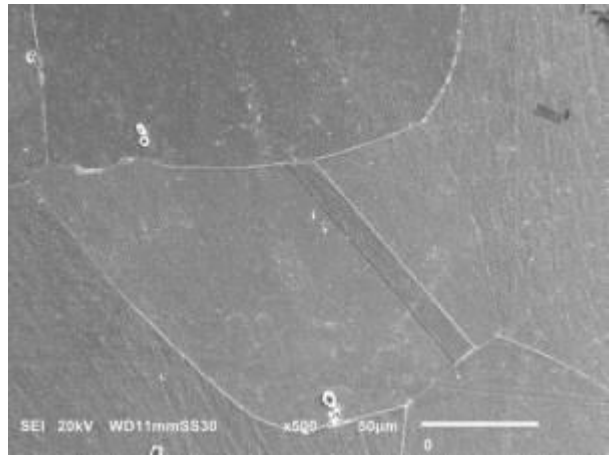

Figure 4.45: SEM micrograph of Transverse section after HT (SA – 1120 ^{0}C x 3hrs & Age 640 ^{0}C x 12hrs) showing the general microstructure Etched; Original Magnification – 500x

4.4.2 MICROSTRUCTURE OBSERVATIONS NEW A-286 BAR AND SERVICED TURBINE WHEEL

The microexamination observations for the as new A-286 bar and serviced turbine wheel is given in Table 4.4.

Table 4.4- Microexamination Observations for as new A-286 bar, serviced turbine wheel, pilot heat treatments and conducted heat treatments

Section	Microstructure Observations	ASTM Grain Size
New A-286 Bar	Uniform austenite grains with no carbides	6 - 7
Serviced Turbine Wheel	Austenite grains with severe carbide precipitation along and within the grain boundaries	4 - 5

Section	Microstructure Observations	ASTM Grain Size
PILOT SOLUTION ANNEALING (SA) HEAT TREATMENTS		
SA – 750°C x 3hrs	Uniform austenite grains. Carbides have not dissolved	6 - 7
SA - 950°C x 3hrs	Uniform austenite grains. Carbide dissolution is evident	5 - 6
SA - 1120°C x 3hrs	Coarse austenite grains. Carbide dissolution is evident	1 - 2
CONDUCTED HEAT TREATMENTS (SOLUTION ANNEALING + AGEING)		
SA 1120°C x 2hrs + Age 720°C x16hrs	Coarse austenite grains. Carbides observed	1 - 2
SA 950°C x 2hrs + Age 720°C x 16hrs	Uniform austenite grains. Carbides observed	4 - 5
SA 950°C x 3hrs + Age 720°C x 16hrs	Uniform austenite grains. Carbide dissolution is evident	5 - 6
SA 1120°C x 3hrs + Age 720°C x 16hrs	Coarse austenite grains. Carbide dissolution is evident	1 - 2
SA 950°C x 3hrs + Age 600°C x 4hrs	Uniform austenite grains. Carbide dissolution is evident. Re-precipitated carbides observed	4 - 5
SA 950°C x 3hrs + Age 600°C x 8hrs	Uniform austenite grains. Carbide dissolution is evident. Re-precipitated carbides observed	4 - 5
SA 950°C x 3hrs + Age 600°C x 12hrs	Uniform austenite grains. Carbide dissolution is evident. Re-precipitated carbides observed	5 – 6
SA 950°C x 3hrs + Age 640°C x 4hrs	Uniform austenite grains. Carbide dissolution is evident. Re-precipitated carbides observed	5 - 6
SA 950°C x 3hrs + Age 640°C x 8hrs	Uniform austenite grains. Carbide dissolution is evident. Re-precipitated carbides observed	5 - 6

Section	Microstructure Observations	ASTM Grain Size
CONDUCTED HEAT TREATMENTS (SOLUTION ANNEALING + AGEING)		
SA 950°C x 3hrs + Age 640°C x 12hrs	Uniform austenite grains. Carbide dissolution is evident. Re-precipitated carbides observed	6 - 7
SA 1120°C x 3hrs + Age 600°C x 4hrs	Coarse austenite grains. Carbide dissolution is evident. Re-precipitated carbides observed to some extent	1 - 2
SA 1120°C x 3hrs + Age 600°C x 8hrs	Coarse austenite grains. Carbide dissolution is evident. Re-precipitated carbides observed to some extent	2 - 3
SA 1120°C x 3hrs + Age 600°C x12hrs	Coarse austenite grains. Carbide dissolution is evident. Re-precipitated carbides observed to some extent	2 - 3
SA 1120°C x 3hrs + Age 640°C x 4hrs	Coarse austenite grains. Carbide dissolution is evident. Re-precipitated carbides observed to some extent	1 - 2
SA 1120°C x 3hrs + Age 640°C x 8hrs	Coarse austenite grains. Carbide dissolution is evident. Re-precipitated carbides observed to some extent	2 - 3
SA 1120°C x 3hrs + Age 640°C x 12hrs	Coarse austenite grains. Carbide dissolution is evident. Re-precipitated carbides observed to some extent	2 - 3

4.5 ENERGY DISPERSIVE ANALYSIS OF X-RAY (EDAX)

The EDAX mapping was performed on the microsections of the serviced wheel to determine the type of carbides. The results of the grain boundary carbides are given in Table 4.5.

Table 4.5 - EDAX analysis of carbides of serviced turbine wheel

Element %	C	Si	Ti	Cr	Mn	Fe	Ni	Mo
Serviced Turbine Wheel Location 1	4.83	1.10	2.37	13.97	1.33	50.51	25.80	-
Serviced Turbine Wheel Location 2	20.81	0.71	63.97	1.55	-	3.71	2.96	6.50

The EDAX mapping of carbides along with the spectrum is shown in Figures 4.46 and 4.47.

It is observed that the carbides along the grain boundaries are rich in chromium and titanium. The carbides primarily mapped by EDAX are a combination of $M_{23}C_6$; M_6C; and MC type carbides.

Spectrum processing :
Peak possibly omitted : 2.299 keV

Processing option : All elements analyzed (Normalised)
Number of iterations = 2

Standard :
C CaCO3 1-Jun-1999 12:00 AM
Si SiO2 1-Jun-1999 12:00 AM
Ti Ti 1-Jun-1999 12:00 AM
Cr Cr 1-Jun-1999 12:00 AM
Mn Mn 1-Jun-1999 12:00 AM
Fe Fe 1-Jun-1999 12:00 AM
Ni Ni 1-Jun-1999 12:00 AM

Elem	Weight%	Atomic%
C K	4.93	19.21
Si K	1.10	1.83
Ti K	2.37	2.32
Cr K	13.97	12.58
Mn K	1.33	1.13
Fe K	50.51	42.35
Ni K	25.80	20.58
Totals	100.00	

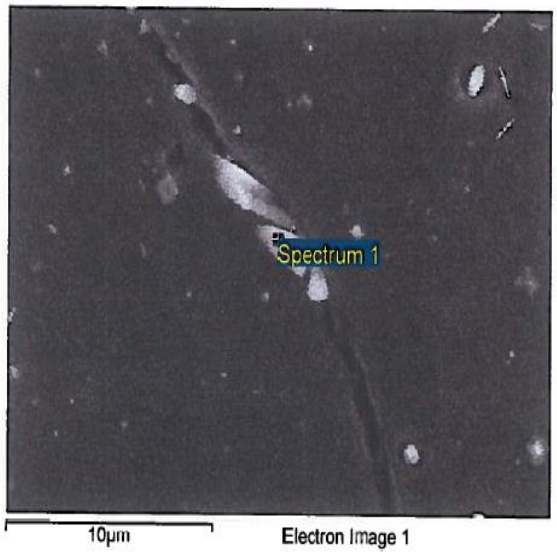

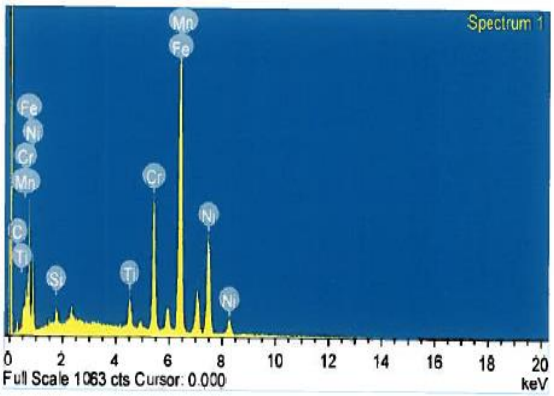

Comment: sample 4A- GB carbide

Figure 4.46: EDAX Analysis of carbides at location-1 in serviced turbine wheel

Spectrum processing :
No peaks omitted

Processing option : All elements analyzed (Normalised)
Number of iterations = 3

Standard :
C CaCO3 1-Jun-1999 12:00 AM
Si SiO2 1-Jun-1999 12:00 AM
Ti Ti 1-Jun-1999 12:00 AM
Cr Cr 1-Jun-1999 12:00 AM
Fe Fe 1-Jun-1999 12:00 AM
Ni Ni 1-Jun-1999 12:00 AM
Mo Mo 1-Jun-1999 12:00 AM

Elem...	Weight%	Atomic%
C K	20.61	52.14
Si K	0.71	0.77
Ti K	63.97	40.59
Cr K	1.55	0.90
Fe K	3.71	2.02
Ni K	2.96	1.53
Mo L	6.50	2.06
Totals	100.00	

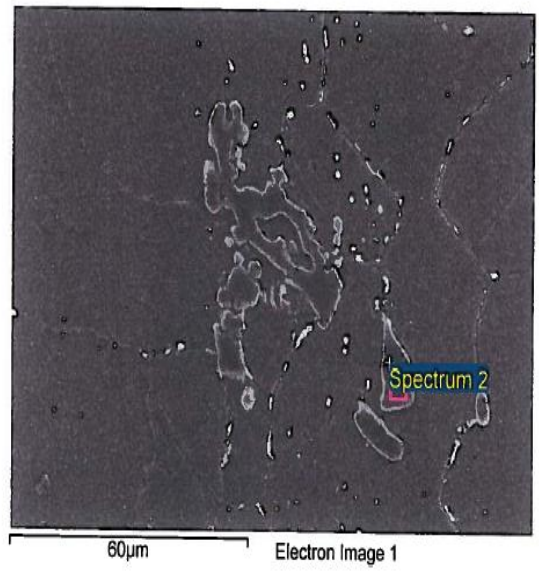

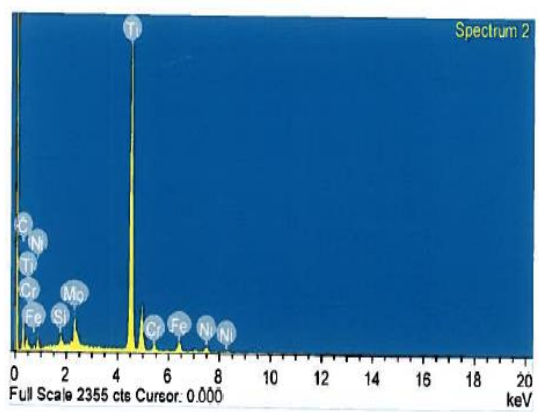

Comment: sample 4A- GB Carbide 1

Figure 4.47: EDAX Analysis of carbides at location-2 in serviced turbine wheel

4.6 VICKERS HARDNESS SURVEY – MICROHARDNESS TESTING

The hardness survey was performed on the microsections of the as new A-286 bar, serviced turbine wheel, micro-sections after pilot heat treatments and the micro-sections after various heat treatments. The results are given in Table 4.6.

Table 4.6- Microhardness Test Results

Section	Hardness Readings, Vickers (HV)	Average Hardness Vickers (HV)
As New A-286 Bar	366, 363, 382, 388, 386, 390, 381, 373, 366	378
Serviced Turbine Wheel	350, 356, 340, 322, 342, 337,334, 331, 339, 346	340
Pilot Heat Treatments		
SA – 750°C x 3 hrs	182, 190, 186, 179, 176, 184, 194, 191, 180, 185	185
SA - 950°C x 3 hrs	177, 172, 167, 169, 159, 166, 171, 174, 165, 172	169
SA - 1120°C x 3 hrs	158, 157, 159, 162, 165, 169, 170, 177, 157, 160	163
Conducted Heat Treatments		
SA 1120°C x 2hrs + Age 720°C x16hrs	351, 334, 333, 346, 356, 350, 348, 358, 361, 355	349
SA 950°C x 2hrs + Age 720°C x 16hrs	356, 333, 343, 345, 342, 358, 351, 350, 355, 340	347
SA 950°C x 3hrs + Age 720°C x 16hrs	361, 363, 366, 359, 351, 343, 334, 340, 350, 368	354
SA 1120°C x 3hrs + Age 720°C x 16hrs	363, 366, 373, 336, 340, 356, 359, 351, 361, 366	377
SA 950°C x 3hrs + Age 600°C x 4hrs	213, 216, 207, 218, 203, 226, 208, 223, 221, 215	215
SA 950°C x 3hrs + Age 600°C x 8hrs	234, 226, 232, 227, 224, 230, 237, 243, 226, 237	232

Section	Hardness Readings, HV	Average Hardness Reading, HV
Conducted Heat Treatments		
SA 950°C x 3hrs + Age 600°C x 12hrs	263, 268, 267, 264, 272, 269, 271, 275, 270, 266	269
SA 950°C x 3hrs + Age 640°C x 4hrs	234, 249, 243, 254, 250, 241, 235, 244, 247, 242	244
SA 950°C x 3hrs + Age 640°C x 8hrs	250, 263, 257, 264, 253, 238, 244, 256, 262, 264	255
SA 950°C x 3hrs + Age 640°C x 12hrs	288, 303, 293, 283, 281, 277, 311, 275, 294, 283	289
SA 1120°C x 3hrs + Age 600°C x 4hrs	207, 206, 201, 208, 202, 198, 209, 193, 215, 205	204
SA 1120°C x 3hrs + Age 600°C x 8hrs	189, 183, 196, 190, 174, 170, 173, 177, 176, 179	181
SA 1120°C x 3hrs + Age 600°C x12hrs	213, 216, 230, 211, 204, 207, 208, 212, 198, 226	210
SA 1120°C x 3hrs + Age 640°C x 4hrs	206, 196, 194, 197, 211, 198, 208, 200, 218, 210,	204
SA 1120°C x 3hrs + Age 640°C x 4hrs	218, 226, 221, 244, 201, 212, 218, 217, 222, 216	220
SA 1120°C x 3hrs + Age 640°C x 12hrs	247, 263, 246, 245, 251, 244, 242, 250, 258, 262	251

The hardness of the new A-286 bar is found to be 378 HV. The average hardness of serviced turbine wheel is 340 HV. Hardness variations were also observed after different heat treatments. Hardness of 354 HV and 377 HV were observed after heat treatments of 950°C x 3hrs + 720°C x 16hrs and 1120°C x 3hrs + 720°C x 16hrs. These hardness values are close to the hardness of as new A-286 bar, which indicates that the hardness has increased after these heat treatments.

4.7 TENSILE TEST (ROOM TEMPERATURE AND HIGH TEMPERATURE)

The tensile testing was performed on the specimens of the new A-286 bar and serviced turbine wheel before and after various heat treatments at room temperature and high temperature of 450°C. The results are given in Table 4.7.

Table 4.7- Results of Room Temperature and High Temperature Tensile Test

Section	Room Temperature (RT), Tensile				High Temperature (HT)(450°C), Tensile			
	Yield Strength (YS), MPa	Ultimate Tensile Sreng th (UTS), MPa	Percentage(%) Elongation	Percentage (%) Reduction Area	Yield Strength (YS), MPa	Ultimate Tensile Strength (UTS), MPa	Percentage(%) Elongation	Percentage(%) Reduction Area
As new A-286 Bar	769	1098	23.6	39.3	690	937	17.5	45.4
Turbine Wheel - Serviced	695	950	10.8	13.7	566	862	4.5	18.8
SA 1120°C x 2hrs +Age 720°C x16hrs	675	927	20.3	22.9	575	795	15.3	16.9

Section	Room Temperature (RT), Tensile				High Temperature (HT)(450°C), Tensile			
	Yield Strength (YS), MPa	**Ultimate Tensile Sreng th (UTS), MPa**	**Percentage(%) Elongation**	**Percentage (%) Reduction Area**	**Yield Strength (YS), MPa**	**Ultimate Tensile Strength (UTS), MPa**	**Percentage(%) Elongation**	**Percentage(%) Reduction Area**
SA 950°C x 2hrs + Age 720°C x 16hrs	745	1044	24.1	35.2	656	911	17.6	28.9
SA 950°C x 3hrs + Age 720°C x 16hrs	755	1051	25.5	42.5	667	922	16.8	38.6
SA 1120°C x 3hrs + Age 720°C x 16hrs	647	923	22.2	29.7	555	776	14.8	19.1
SA 950°C x 3hrs + Age 600°C x 4hrs	381 379	808 804	48.2 49.3	55.2 57.8	307 304	633 638	52.9 56.1	54.1 55.5
SA 950°C x 3hrs + Age 600°C x 8hrs	4134 14	841 841	48.6 48.2	55.5 50.5	351 357	685 682	49.3 50.4	58.7 58.3

Section	Room Temperature (RT), Tensile				High Temperature (HT) (450°C), Tensile			
	Yield Strength (YS), MPa	**Ultimate Tensile Strength (UTS), MPa**	**Percentage(%) Elongation**	**Percentage (%) Reduction Area**	**Yield Strength (YS) MPa**	**Ultimate Tensile Strength (UTS), MPa**	**Percentage (%) Elongation**	**Percentage(%) Reduction Area RA**
SA 950°C x 3hrs + Age 600°C x 12hrs	413 415	837 840	47.6 48.8	54.1 57.3	362 369	679 684	48.4 49.3	53.4 54.1
SA 950°C x 3hrs + Age 640°C x 4hrs	452 449	895 892	42.9 42.8	54.3 51.3	380 380	710 705	45.4 44.4	52.2 49.6
SA 950°C x 3hrs + Age 640°C x 8hrs	501 496	944 941	40.1 40.3	51.8 55.0	436 435	758 767	43.6 41.7	53.4 47.5
SA 950°C x 3hrs + Age 640°C x 12hrs	538 532	971 973	38.5 37.6	48.0 47.6	464 461	799 790	38.1 42.1	51.2 48.8

Section	Room Temperature (RT), Tensile				High Temperature (HT)(450°C), Tensile			
	Yield Strength (YS), MPa	**Ultimate Tensile Strength (UTS), MPa**	**Percentage (%) Elongation**	**Percentage (%) Reudction area**	**Yield Strength (YS), MPa**	**Ultimate Tensile Strength (UTS), MPa**	**Percentage (%) Elongation**	**Percentage(%) Reduction Area**
SA 1120°C x 3hrs + Age 600°C x 4hrs	277 293	679 685	60.7 62.1	58.2 53.2	220 224	516 516	65.7 70.2	52.5 58.5
SA 1120°C x 3hrs + Age 600°C x 8hrs	308 309	691 711	62.2 62.2	49.1 50.8	250 247	546 532	55.8 60.6	48.2 58.9

The ultimate tensile strength (UTS) of the new A-286 bar at room temperature and at 450°C is found to be 1098 MPa and 937 MPa respectively. The UTS of the serviced A-286 turbine wheel at room temperature is 950 MPa and at 450°C is 852 MPa. Variations in tensile values are observed after different heat treatments. Tensile strength after heat treatments of 950°C x 3hrs + 720°C x 16hrs is 1051 MPa (room temperature) and 922 MPa (high temperature) respectively. These tensile results are close to the tensile results of the new A-286 bar, which indicates that the tensile properties has improved after this heat treatment.

4.8 CHARPY IMPACT TEST

The Charpy impact test was performed at room temperature on the A-286 bar and serviced turbine wheel before and after various heat treatments. The results are given in Table 4.8.

Table 4.8- Results of Room Temperature Charpy Impact Test

Section	Charpy Values, Joules at 20°C			
	Reading 1	Reading 2	Reading 3	Average
As new A-286 Bar	58	57	58	57.6
Turbine Wheel – Serviced	17	18	16	17
SA 1120°C x 2hrs + Age 720°C x16hrs	62	50	56	56
SA 950°C x 2hrs + Age 720°C x 16hrs	56	48	44	49.33
SA 950°C x 3hrs + Age 720°C x 16hrs	36	38	38	37.33
SA 1120°C x 3hrs + Age 720°C x 16hrs	58	57	60	58.33
SA 950°C x 3hrs + Age 600°C x 4hrs	122	107.1	120.7	116.6
SA 950°C x 3hrs + Age 600°C x 8hrs	99	97.6	97.6	98.1
SA 950°C x 3hrs + Age 600°C x 12hrs	96.3	93.6	92.2	94.0

Section	Charpy Values, Joules at 20°C			
	Reading 1	**Reading 2**	**Reading 3**	**Average**
SA 950°C x 3hrs + Age 640°C x 4hrs	93.6	90.9	94.9	93.1
SA 950°C x 3hrs + Age 640°C x 8hrs	35.93	37.96	36.61	36.83
SA 950°C x 3hrs + Age 640°C x 12hrs	35.93	35.25	35.93	35.70
SA 1120°C x 3hrs + Age 600°C x 4hrs	246.76	256.25	192.53	231.84
SA 1120°C x 3hrs + Age 600°C x 8hrs	227.78	266.42	286.08	260.09

The average Charpy impact value of new A-286 bar and serviced turbine wheel at room temperature is found to be of 57.6 Joules and 17 joules respectively. The impact value of the serviced turbine wheel is very low as compared to the new A-286 bar. Variations in impact values are observed after different heat treatments. The Charpy impact value after heat treatment of 950°C x 3hrs + 720°C x 16hrs is found to be 37.33 Joules. This means that the toughness of the serviced turbine wheel has increased after the heat treatment.

4.9 STRESS RUPTURE TEST

The stress rupture test was performed on the new A-286 bar, serviced turbine wheel before and after various heat treatments. The tests were performed at two sets of parameters; 520 MPa, 550 ^{o}C and 385 MPa, 650 ^{o}C. These test parameters were selected based on the lower and the maximum operating conditions of the turbine wheel, which also includes the material design conditions. The results are presented in Table 4.9.

Table 4.9 - Results of Stress Rupture Test

Section	**Stress Rupture**	
	Rupture Life, Hours 520 (MPa) 550(^{o}C)	**Rupture Life, Hours 385 (MPa) 650(^{o}C)**
As new A-286 Bar	993 Discontinued	993 Discontinued
Turbine Wheel – Serviced	319	207
SA 1120°C x 2hrs + Age 720°C x16hrs	350 Discontinued	350 Discontinued

Section	Stress Rupture	
	Rupture Life, Hours 520 (MPa) 550(^{o}C)	**Rupture Life, Hours 385 (MPa) 650(^{o}C)**
SA 950°C x 2hrs + Age 720°C x 16hrs	350 Discontinued	350 Discontinued
SA 950°C x 3hrs + Age 720°C x 16hrs	300 Discontinued	300 Discontinued
SA 1120°C x 3hrs + Age 720°C x 16hrs	300 Discontinued	300 Discontinued
SA 950°C x 3hrs + Age 600°C x 4hrs	100 Discontinued	100 Discontinued
SA 950°C x 3hrs + Age 600°C x 8hrs	100 Discontinued	100 Discontinued
SA 950°C x 3hrs + Age 600°C x 12hrs	100 Discontinued	100 Discontinued
SA 950°C x 3hrs + Age 640°C x 4hrs	100 Discontinued	100 Discontinued
SA 950°C x 3hrs + Age 640°C x 8hrs	100 Discontinued	100 Discontinued
SA 950°C x 3hrs + Age 640°C x 12hrs	100 Discontinued	100 Discontinued
SA 1120°C x 3hrs + Age 600°C x 4hrs	0 Ruptured as the load was applied	100 Discontinued
SA 1120°C x 3hrs + Age 600°C x 8hrs	0 Ruptured as the load was applied	100 Discontinued

The stress rupture tests at the parameters of 520 MPa, 550°C and at 385 MPa, 650 °C do not reveal any significant abnormality, for the new A-286 bar and serviced turbine wheel before and after different heat treatments. The stress rupture samples surviving for more than 100 hours indicates considerable amount of

stress rupture strength. The samples after solution annealing from 1120^0C for 3 hours and age hardening at 600°C for 4 hours and 8 hours experience failure immediately after loading the sample on to the stress rupture machine. This may be due to the machining problems or some test sample loading issues in the stress rupture machine.

4.10 COMPILED MECHANICAL TEST RESULTS

The mechanical test results performed on the new A-286 bar, serviced turbine wheel and on the sections after various heat treatments are compiled together. The combined test results of all the mechanical tests are presented in Table 4.10.

Table 4.10 - Compiled Results of Mechanical Tests

Item No.	Section Location	Heat Treatment Cycle	Carbide Dissolution	Hardness HV Min - Max	RT Tensile, Mpa	HT Tensile at 450 °C, Mpa	Stress Rupture 520 Mpa, 550 °C 385 Mpa, 650 °C	Charpy Joules
1	New A286 bar	SA – 900 °C x 2 hrs Age - 720 °C x 16 hrs	Yes	L :394, 392, 396, 386, 361, 382, 392, 394, 396, 388 T :384, 366, 363, 382, 388, 386, 390, 381, 373, 366	1098	937	993 hrs, discontinued 319 hrs, rupture	58, 57, 58
2	Serviced Wheel section	In operation for more than 200K hours	Precipitated carbides	L :340, 356, 339, 322, 331, 321, 325, 327, 340, 343 T :350, 356, 340, 322, 342, 337,334, 331, 339, 346	950	862	993 hrs, discontinued 207 hrs, rupture	17, 18, 16
3	Section 10	SA - 1120 °C x 2 hrs Age - 720 °C x 16 hrs	No	L :337, 353, 343, 366, 353, 350, 345, 342, 346, 336 T :351, 334, 333, 346, 356, 350, 348, 358, 361, 355	927	795	350 hrs Discontinued	62, 50, 56

Item No.	Section Location	Heat Treatment Cycle	Carbide Dissolution	Hardness HV Min - Max	RT Tensile, Mpa	HT Tensile at 450 °C, Mpa	Stress Rupture 520 Mpa, 550 °C 385 Mpa, 650 °C	Charpy Joules	
4	Section 2	SA - 950 °C x 2 hrs Age - 720 °C x 16 hrs	No	L :337, 325, 336, 340, 337, 339, 334, 333, 331, 330 T :356, 333, 343, 345, 342, 358, 351, 350, 355, 340	1044	911	350 hrs Discontinued	56, 48, 44	
5	Section 9A	SA - 950 °C x 3 hrs	Yes	L :174, 166, 162, 169, 171, 175, 165, 177, 164, 172 T :177, 172, 167, 169, 159, 166, 171, 174, 165, 172	530 (cal. from hardness)	Not tested	Not tested	Not tested	Tensile strength is low (less than 50%) as compared to the required; hence no further tests are done
6	Section 9B	SA - 1120 °C x 3 hrs	Yes	L :159, 160, 158, 183, 161, 174, 165, 166, 170, 171 T :158, 157, 159, 162, 165, 169, 170, 177, 157, 160	530 (cal. from hardness)	Not tested	Not tested	Not tested	

Item No.	Section Location	Heat Treatment Cycle	Carbide Dissolution	Hardness HV Min - Max	RT Tensile, Mpa	HT Tensile at 450 °C, Mpa	Stress Rupture 520 Mpa, 550 °C 385 Mpa, 650 °C	Charpy Joules
7	Section 9A	SA - 950 °C x 3 hrs Age - 720 °C x 16 hrs	Yes	L :366, 379, 370, 340, 350, 373, 356, 348, 334, 350 T :361, 363, 366, 359, 351, 343, 334, 340, 350, 368	1051	922	300 hrs Discontinued	36, 38, 38
8	Section 9B	SA - 1120 °C x 3 hrs Age - 720 °C x 16 hrs	Yes	L :370, 381, 359, 377, 373, 366, 365, 368, 356, 358 T :363, 366, 373, 336, 340, 356, 359, 351, 361, 366	923	776	300 hrs Discontinued	58, 57, 60
9	Section 8C -1	SA - 950 °C x 3 hrs Age - 600 °C x 4 hrs	Yes	L : 226, 237, 233, 231, 218, 207, 238, 230, 223, 225 T : 213, 216, 207, 218, 203, 226, 208, 223, 221, 215	808, 804	633, 638	100 hrs Discontinued	122, 107.1, 120.7

Item No.	Section Location	Heat Treatment Cycle	Carbide Dissolution	Hardness HV Min - Max	RT Tensile, Mpa	HT Tensile at 450 °C, Mpa	Stress Rupture 520 Mpa, 550 °C 385 Mpa, 650 °C	Charpy Joules
10	Section 8C - 2	SA - 950 °C x 3 hrs Age - 600 °C x 8 hrs	Yes	L : 281, 268, 286, 303, 283, 296, 279, 291, 309, 293 T: 234, 226, 232, 227, 224, 230, 237, 243, 226, 237	841, 841	685, 682	100 hrs Discontinued	99, 97.6, 97.6
11	Section 8D - 1	SA - 950 °C x 3 hrs Age - 600 °C x 12 hrs	Yes	L : 286, 283, 306, 288, 303, 307, 280, 305, 309, 313 T: 263, 268, 267, 264, 272, 269, 271, 275, 270, 266	837, 840	679, 684	100 hrs Discontinued	96.3, 93.6, 92.2
12	Section 8D - 2	SA - 950 °C x 3 hrs Age - 640 °C x 4 hrs	Yes	L: 244, 249 245, 242, 243, 230, 253, 226, 222, 231 T: 234, 249, 243, 254, 250, 241, 235, 244, 247, 242	895, 892	710, 705	100 hrs Discontinued	93.6, 90.9, 94.9

Item No.	Section Location	Heat Treatment Cycle	Carbide Dissolution	Hardness HV Min - Max	RT Tensile, Mpa	HT Tensile at 450 °C, Mpa	Stress Rupture 520 Mpa, 550 °C 385 Mpa, 650 °C	Charpy Joules
13	Section 7.1	SA - 950 °C x 3 hrs Age - 640 °C x 8 hrs	Yes	L : 273, 283, 277, 281, 287, 279, 272, 261, 266, 270 T: 250, 263, 257, 264, 253, 238, 244, 256, 262, 264	944, 941	758, 767	100 hrs Discontinued	35.93, 37.96, 36.61
14	Section 7.2	SA - 950 °C x 3 hrs Age - 640 °C x 12 hrs	Yes	L : 311, 309, 286, 298, 263, 270, 281, 288, 261, 244 T : 288, 303, 293, 283, 281, 277, 311, 275, 294, 283	971, 973	799, 790	100 hrs Discontinued	35.93, 35.25, 35.93
15	Section 6	SA - 1120 °C x 3 hrs Age - 600 °C x 4 hrs	Yes	L : 207, 203, 201, 210, 222, 215, 217, 200, 196, 194 T : 207, 206, 201, 208, 202, 198, 209, 193, 215, 205	679, 685	516, 516	0 hrs rupture 100 hrs Discontinued	246.76, 256.25, 192.53

Item No.	Section Location	Heat Treatment Cycle	Carbide Dissolution	Hardness HV Min - Max	RT Tensile, Mpa	HT Tensile at 450 °C, Mpa	Stress Rupture 520 Mpa, 550 °C 385 Mpa, 650 °C	Charpy Joules
16	Section 5.1	SA - 1120 °C x 3 hrs Age - 600 °C x 8 hrs	Yes	L : 184, 191, 186, 185, 197, 181, 180, 182, 190, 171 T : 189, 183, 196, 190, 174, 170, 173, 177, 176, 179	691, 711	546, 532	0 hrs rupture 100 hrs Discontinued	227.78, 266.42, 286.08
17	Section 5.2	SA - 1120 °C x 3 hrs Age - 600 °C x 12 hrs	Yes	L : 226, 218, 215, 203, 200, 198, 211, 217, 215, 221 T : 213, 216, 230, 211, 204, 207, 208, 212, 198, 226	722, 713	560, 565	0 hrs rupture 100 hrs Discontinued	176.3, 198.0, 184.4
18	Section 4	SA - 1120 °C x 3 hrs Age - 640 °C x 4 hrs	Yes	L : 201, 221, 207, 203, 208, 206, 204, 196, 210, 212 T: 206, 196, 194, 197, 211, 198, 208, 200, 218, 210,	753, 748	576, 573	100 hrs Discontinued	168.1, 168.1, 170.9

Item No.	Section Location	Heat Treatment Cycle	Carbide Dissolution	Hardness HV Min - Max	RT Tensile, Mpa	HT Tensile at 450 °C, Mpa	Stress Rupture 520 Mpa, 550 °C 385 Mpa, 650 °C	Charpy Joules
19	Section 3.1	SA - 1120 °C x 3 hrs Age - 640 °C x 8 hrs	Yes	L : 223, 228, 219, 218, 216, 227, 206, 210, 222, 208 T: 218, 226, 221, 244, 201, 212, 218, 217, 222, 216	782, 779	604, 601	100 hrs Discontinued	166.8, 154.6, 170.9
20	Section 3.2	SA - 1120 °C x 3 hrs Age - 640 °C x 12 hrs	Yes	L: 240, 244, 251, 263, 245, 243, 241, 262, 260, 258 T : 247, 263, 246, 245, 251, 244, 242, 250, 258, 262	797, 796	627, 632	100 hrs Discontinued	160.0, 146.4, 154.6

4.11 FRACTURE MORPHOLOGY

The fractured surfaces after the mechanical tests, such as tensile, charpy and stress rupture have been examined under scanning electron microscope to study the fracture morphology.

Scanning Electron Microscope micrographs showing the fracture surface morphology are presented in Figures 4.48 to 4.211.

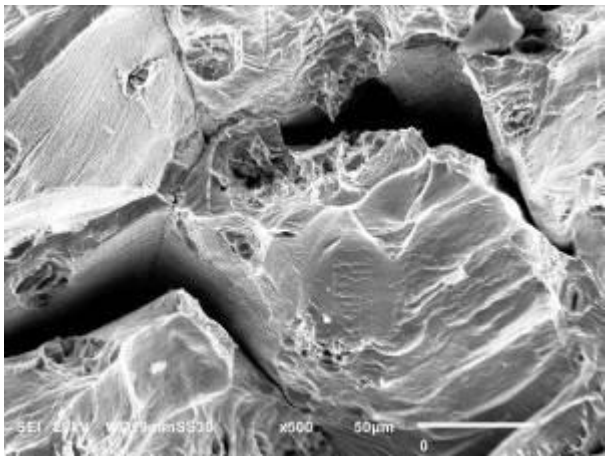

Figure 4.48: SEM micrograph of as new A-286 bar fractured tensile sample at 21^0C; Original Magnification – 500x

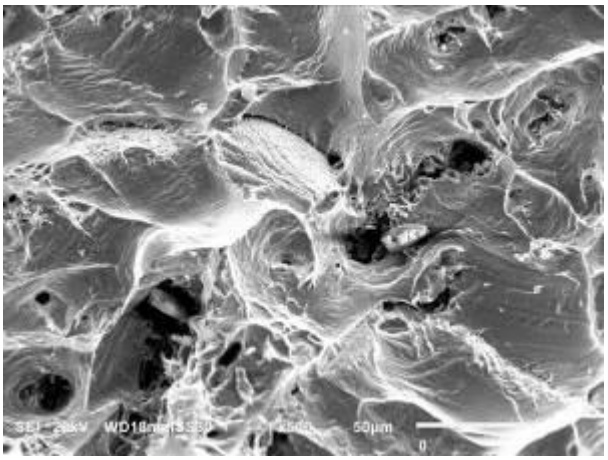

Figure 4.49: SEM micrograph of as new A-286 bar fractured tensile sample at 450^0C; Original Magnification – 500x

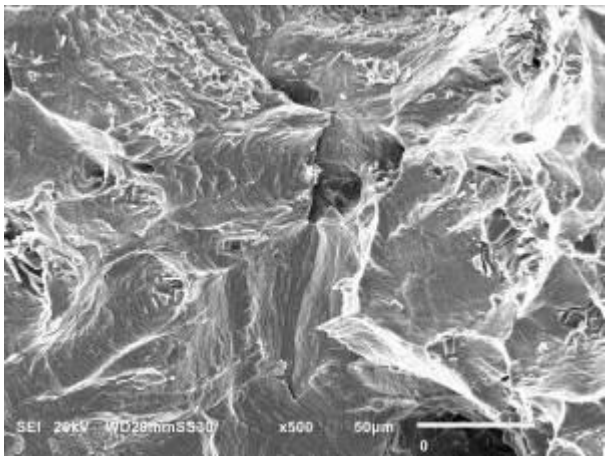

Figure 4.50: SEM micrograph of as new A-286 bar fractured Charpy sample; Original Magnification – 500x

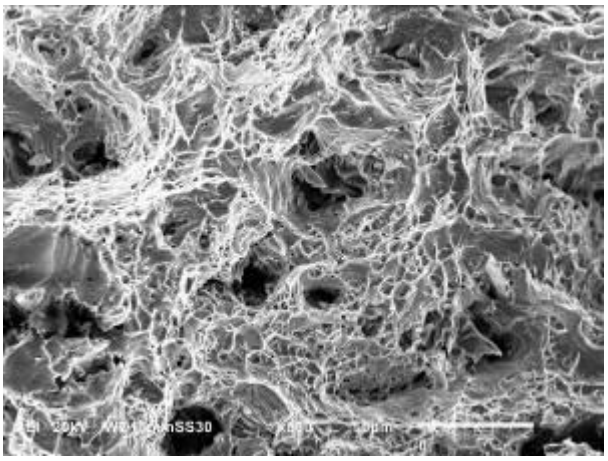

Figure 4.51: SEM micrograph of serviced A-286 wheel fractured tensile sample at 21^0C; Original Magnification – 500x

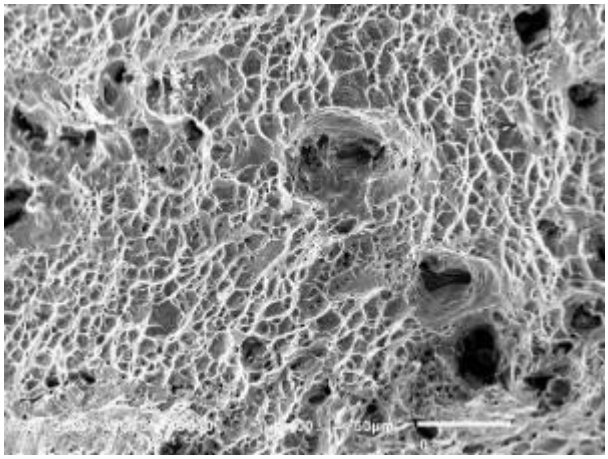

Figure 4.52: SEM micrograph of serviced A-286 wheel fractured tensile sample at 450^0C; Original Magnification – 400x

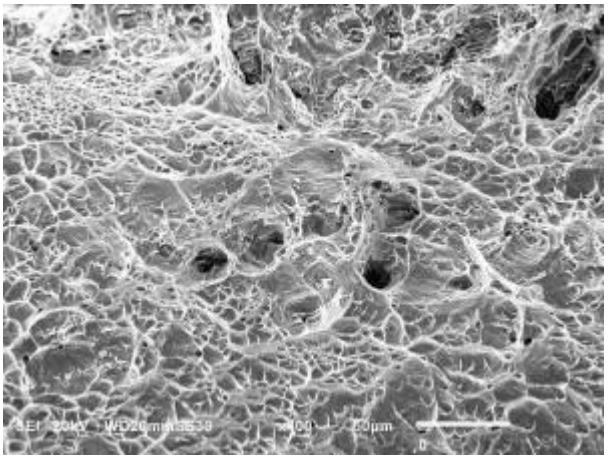

Figure 4.53: SEM micrograph of serviced A-286 wheel fractured Charpy sample; Original Magnification – 400x

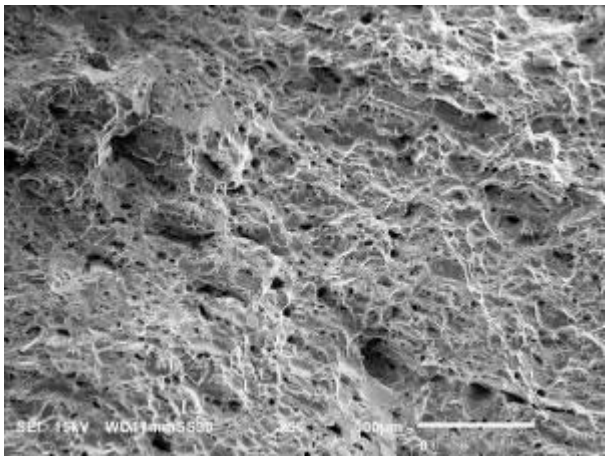

Figure 4.54: SEM micrograph of serviced A-286 wheel fractured stress rupture sample; Original Magnification – 50x

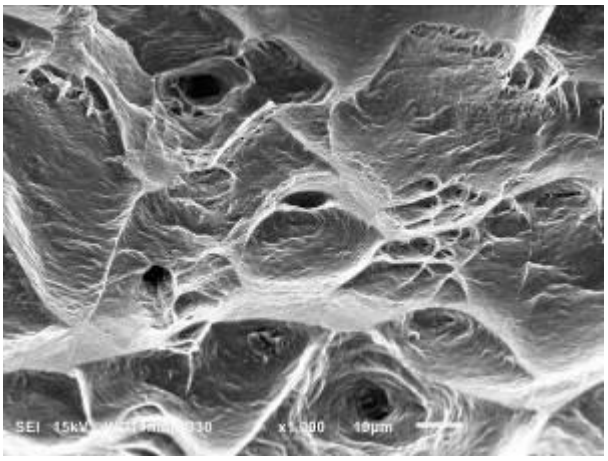

Figure 4.55: SEM micrograph of serviced A-286 wheel fractured stress rupture sample; Original Magnification – 1000x

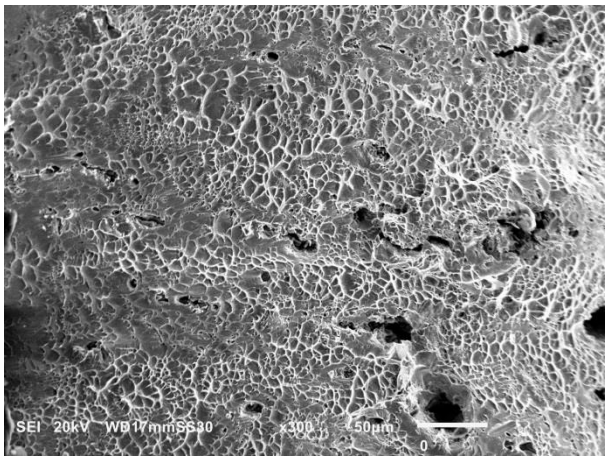

Figure 4.56: SEM micrograph of fractured tensile sample at 21 ^{0}C, (SA - 1120 ^{0}C x 2 hrs + Age – 720 ^{0}C x 16 hrs); Original Magnification – 300x

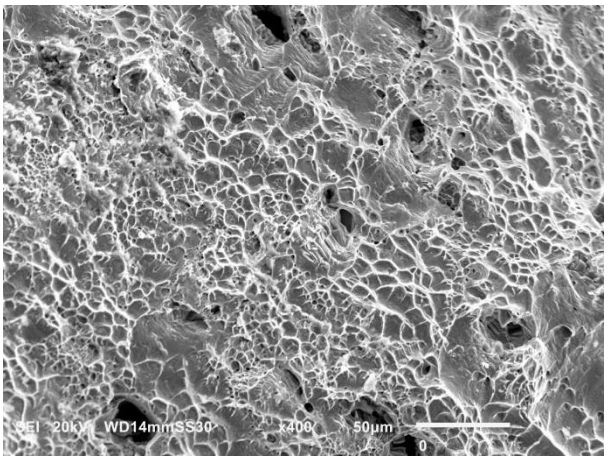

Figure 4.57: SEM micrograph of fractured tensile sample at 450 ^{0}C, (SA - 1120 ^{0}C x 2 hrs + Age – 720 ^{0}C x 16 hrs); Original Magnification – 400x

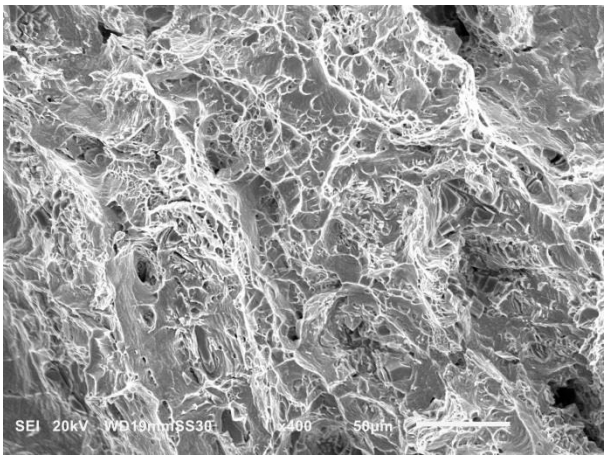

Figure 4.58: SEM micrograph of fractured charpy sample (SA - 1120 ^{0}C x 2 hrs + Age – 720 ^{0}C x 16 hrs); Original Magnification – 400x

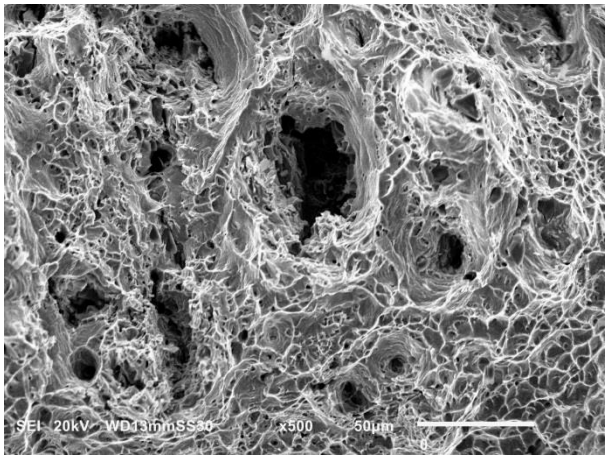

Figure 4.59: SEM micrograph of fractured tensile sample at 21 ^{0}C, (SA - 950 ^{0}C x 2 hrs + Age – 720 ^{0}C x 16 hrs); Original Magnification – 500x

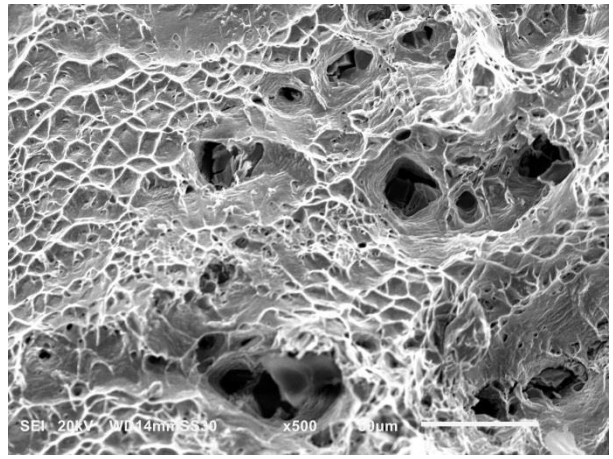

Figure 4.60: SEM micrograph of fractured tensile sample at 450 ^{0}C, (SA - 950 ^{0}C x 2 hrs + Age – 720 ^{0}C x 16 hrs); Original Magnification – 500x

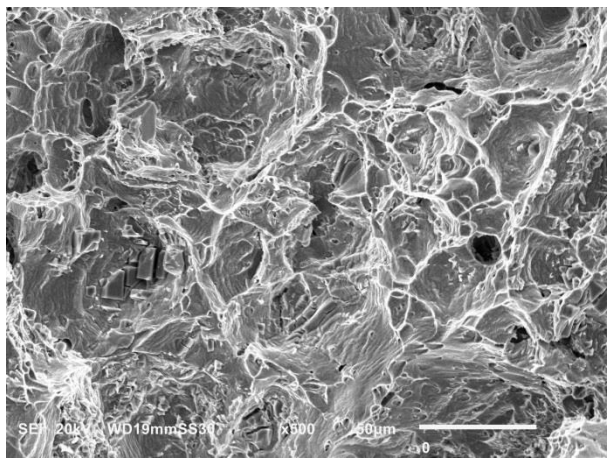

Figure 4.61: SEM micrograph of fractured charpy sample (SA - 950 ^{0}C x 2 hrs + Age – 720 ^{0}C x 16 hrs); Original Magnification – 500x

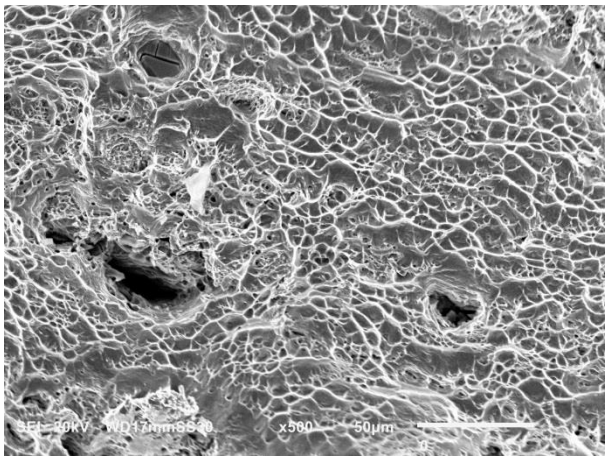

Figure 4.62: SEM micrograph of fractured tensile sample at 21 ^{0}C, (SA - 950 ^{0}C x 3 hrs + Age – 720 ^{0}C x 16 hrs); Original Magnification – 500x

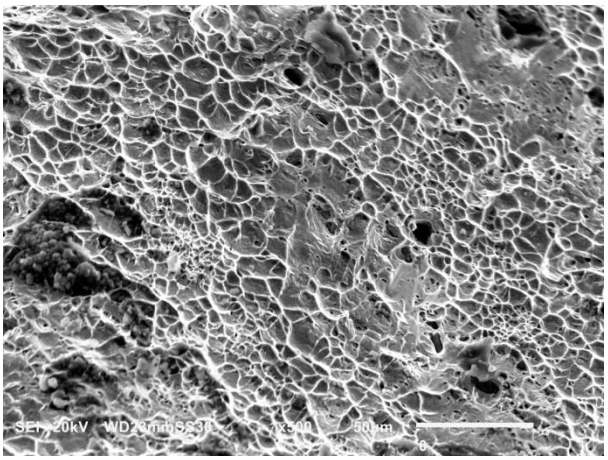

Figure 4.63: SEM micrograph of fractured tensile sample at 450 ^{0}C, (SA - 950 ^{0}C x 3 hrs + Age – 720 ^{0}C x 16 hrs); Original Magnification – 500x

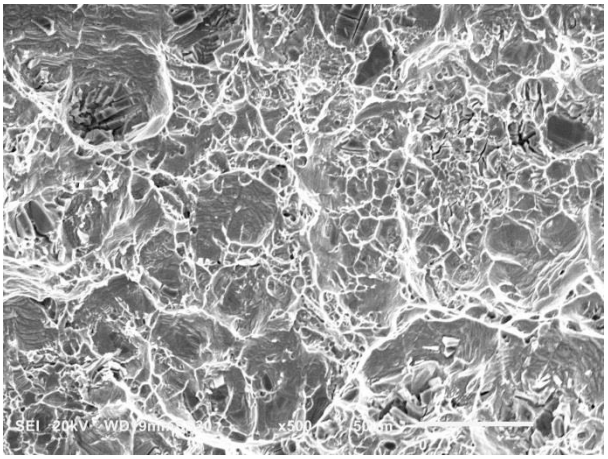

Figure 4.64: SEM micrograph of fractured charpy sample (SA - 950 ^{0}C x 3 hrs + Age – 720 ^{0}C x 16 hrs); Original Magnification – 500x

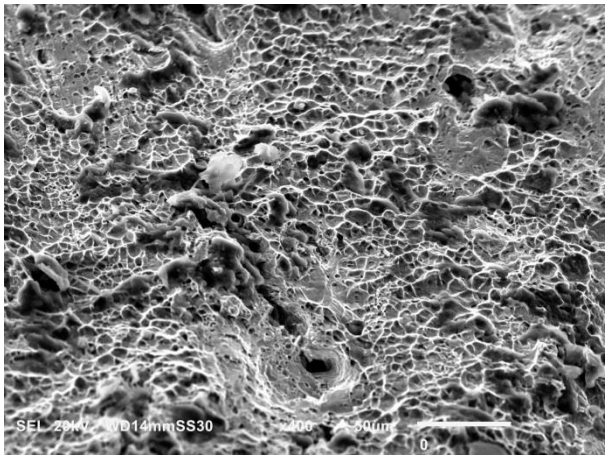

Figure 4.65: SEM micrograph of fractured tensile sample at 21 ^{0}C, (SA - 1120 ^{0}C x 3 hrs + Age – 720 ^{0}C x 16 hrs); Original Magnification – 400x

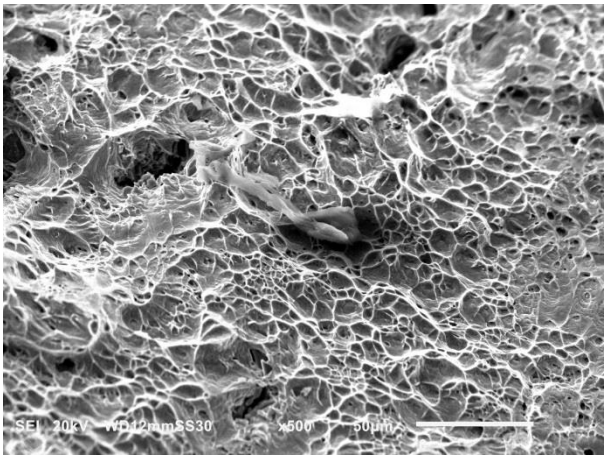

Figure 4.66: SEM micrograph of fractured tensile sample at 450 ^{0}C, (SA - 1120 ^{0}C x 3 hrs + Age – 720 ^{0}C x 16 hrs); Original Magnification – 500x

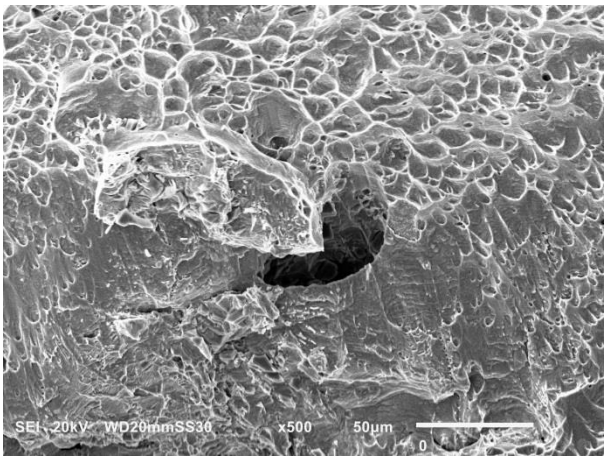

Figure 4.67: SEM micrograph of fractured charpy sample (SA - 1120 ^{0}C x 3 hrs + Age – 720 ^{0}C x 16 hrs); Original Magnification – 500x

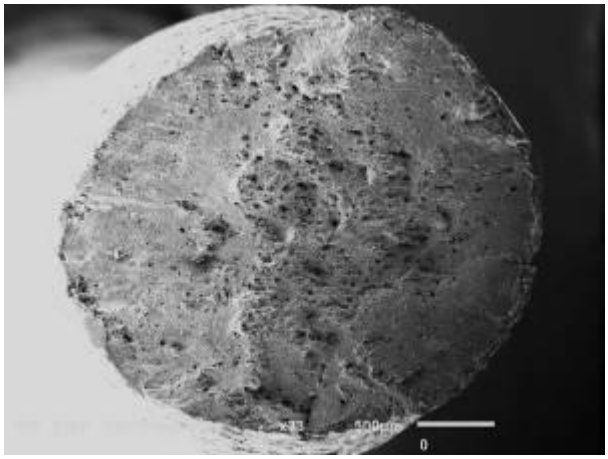

Figure 4.68: SEM micrograph of fractured tensile sample at 21 ^{0}C, (SA - 950 ^{0}C x 3 hrs + Age – 600 ^{0}C x 4 hrs); Original Magnification – 33x

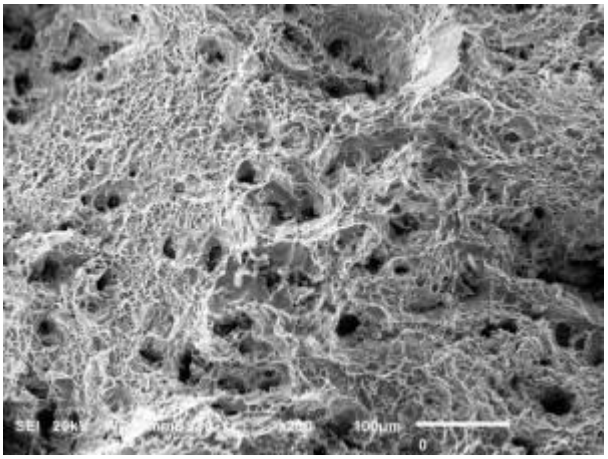

Figure 4.69: SEM micrograph of fractured tensile sample at 21 ^{0}C, (SA - 950 ^{0}C x 3 hrs + Age – 600 ^{0}C x 4 hrs); Original Magnification – 200x

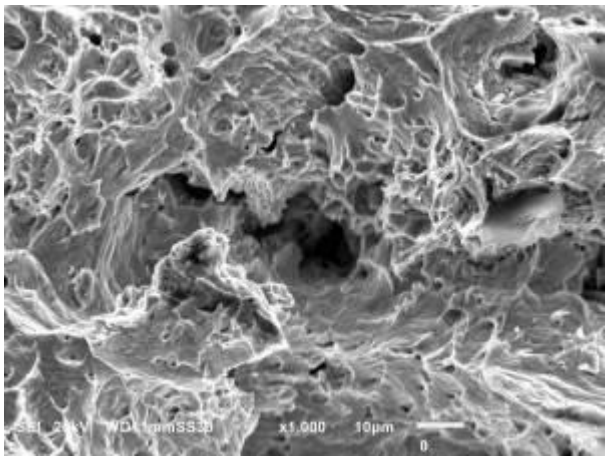

Figure 4.70: SEM micrograph of fractured tensile sample at 21 ^{0}C, (SA - 950 ^{0}C x 3 hrs + Age – 600 ^{0}C x 4 hrs); Original Magnification – 1000x

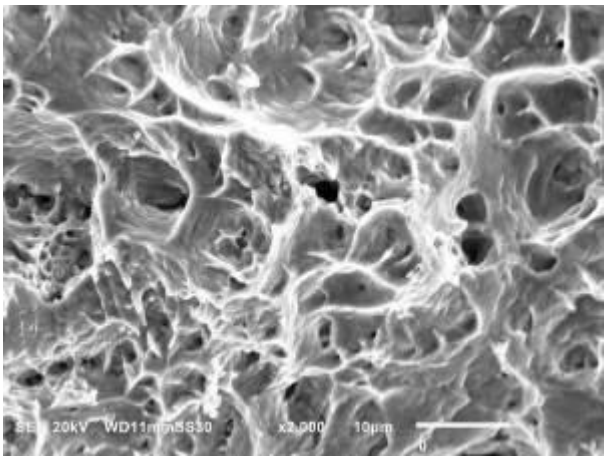

Figure 4.71: SEM micrograph of fractured tensile sample at 21 ^{0}C, (SA - 950 ^{0}C x 3 hrs + Age – 600 ^{0}C x 4 hrs); Original Magnification – 2000x

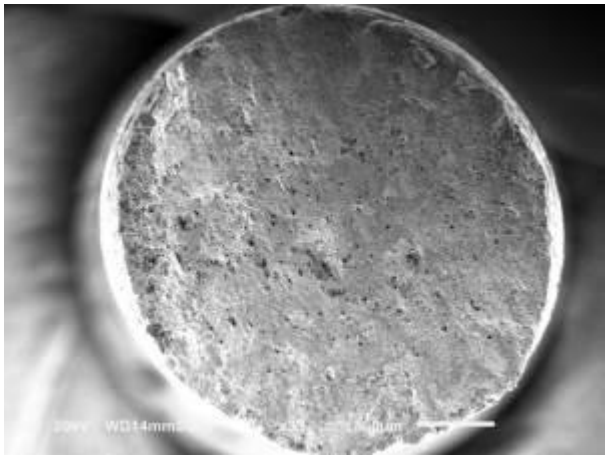

Figure 4.72: SEM micrograph of fractured tensile sample at 450 ^{0}C, (SA - 950 ^{0}C x 3 hrs + Age – 600 ^{0}C x 4 hrs); Original Magnification – 33x

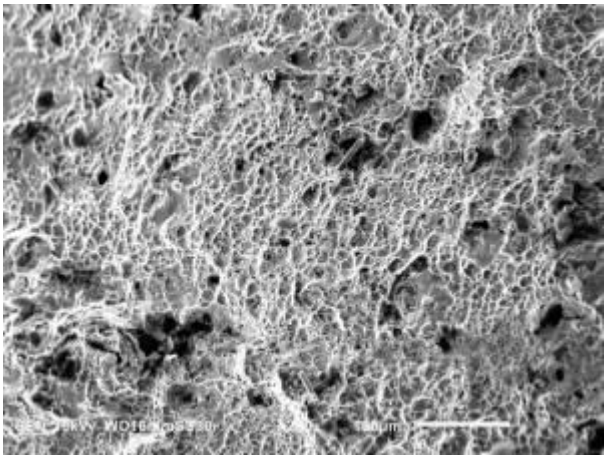

Figure 4.73: SEM micrograph of fractured tensile sample at 450 ^{0}C, (SA - 950 ^{0}C x 3 hrs + Age – 600 ^{0}C x 4 hrs); Original Magnification – 200x

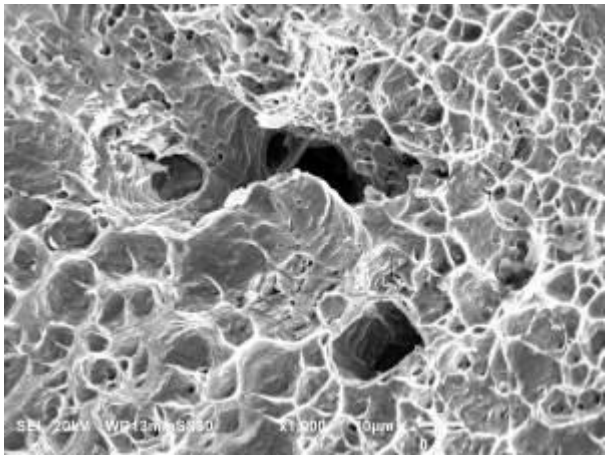

Figure 4.74: SEM micrograph of fractured tensile sample at 450 ^{0}C, (SA - 950 ^{0}C x 3 hrs + Age – 600 ^{0}C x 4 hrs); Original Magnification – 1000x

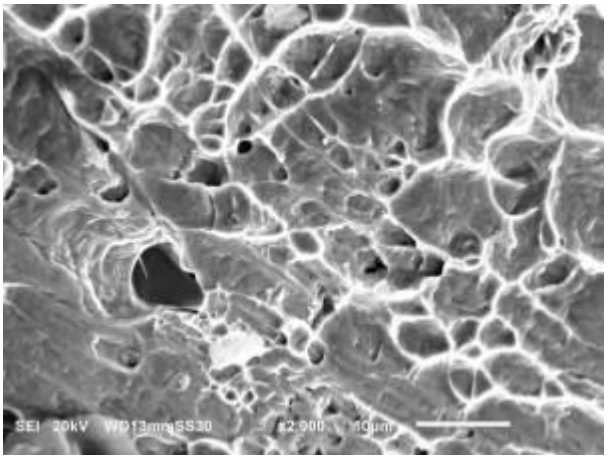

Figure 4.75: SEM micrograph of fractured tensile sample at 450 ^{0}C, (SA - 950 ^{0}C x 3 hrs + Age – 600 ^{0}C x 4 hrs); Original Magnification – 2000x

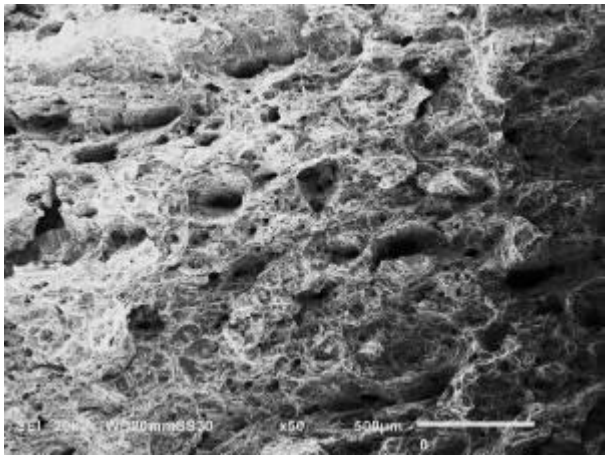

Figure 4.76: SEM micrograph of fractured charpy sample (SA - 950 ^{0}C x 3 hrs + Age – 600 ^{0}C x 4 hrs); Original Magnification – 50x

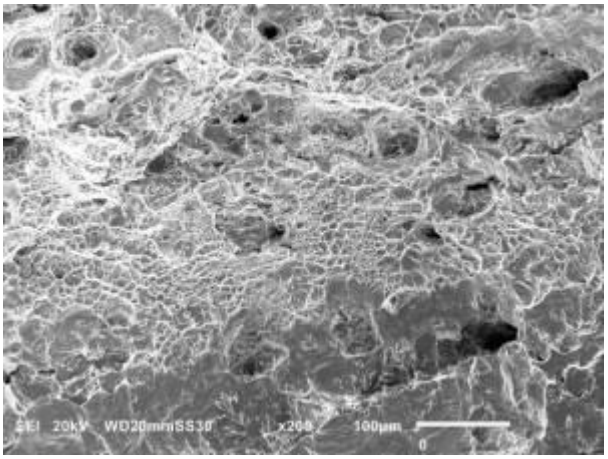

Figure 4.77: SEM micrograph of fractured charpy sample (SA - 950 ^{0}C x 3 hrs + Age – 600 ^{0}C x 4 hrs); Original Magnification – 200x

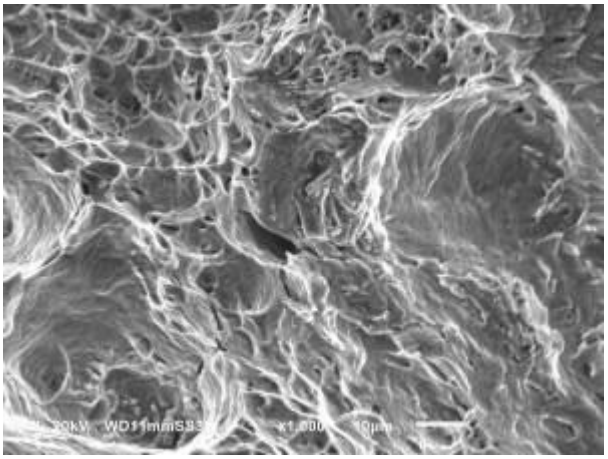

Figure 4.78: SEM micrograph of fractured charpy sample (SA - 950 ^{0}C x 3 hrs + Age – 600 ^{0}C x 4 hrs); Original Magnification – 1000x

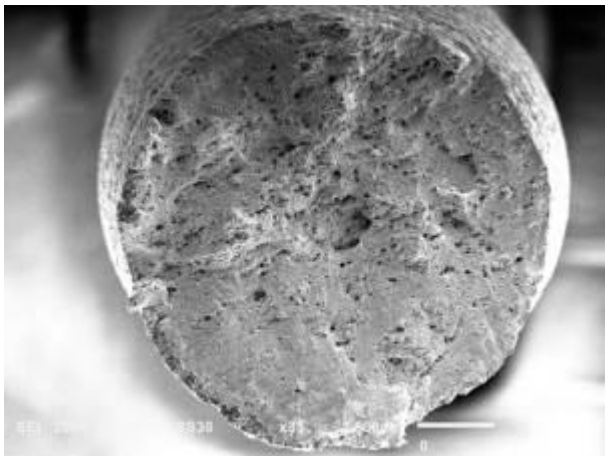

Figure 4.79: SEM micrograph of fractured tensile sample at 21 ^{0}C, (SA - 950 ^{0}C x 3 hrs + Age – 600 ^{0}C x 8 hrs); Original Magnification – 33x

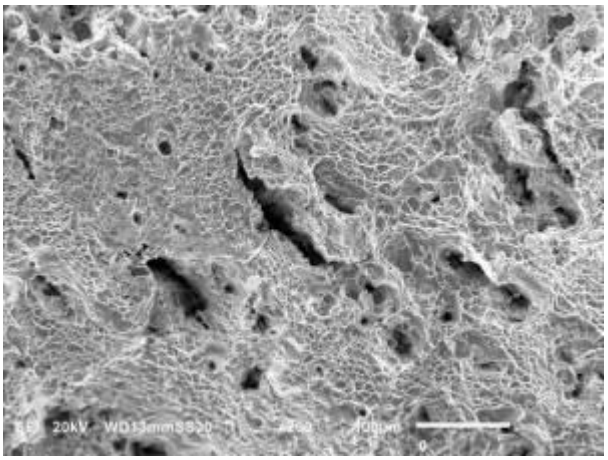

Figure 4.80: SEM micrograph of fractured tensile sample at 21 ^{0}C, (SA - 950 ^{0}C x 3 hrs + Age – 600 ^{0}C x 8 hrs); Original Magnification – 200x

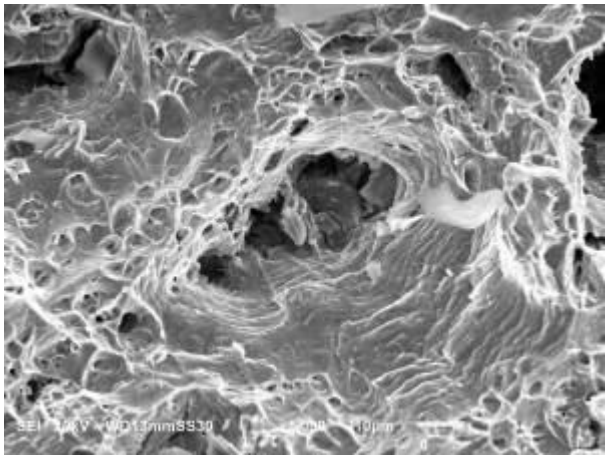

Figure 4.81: SEM micrograph of fractured tensile sample at 21 ^{0}C, (SA - 950 ^{0}C x 3 hrs + Age – 600 ^{0}C x 8 hrs); Original Magnification – 1000x

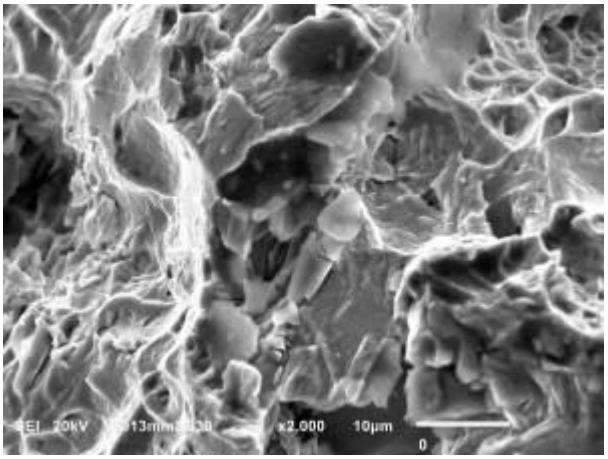

Figure 4.82: SEM micrograph of fractured tensile sample at 21 ^{0}C, (SA - 950 ^{0}C x 3 hrs + Age – 600 ^{0}C x 8 hrs); Original Magnification – 2000x

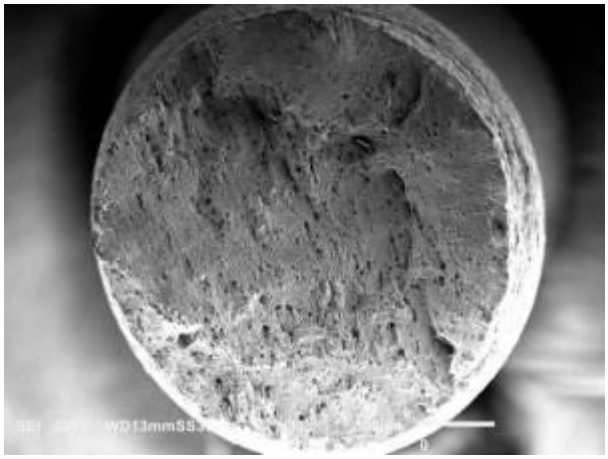

Figure 4.83: SEM micrograph of fractured tensile sample at 450 ^{0}C (SA - 950 ^{0}C x 3 hrs + Age – 600 ^{0}C x 8 hrs); Original Magnification – 33x

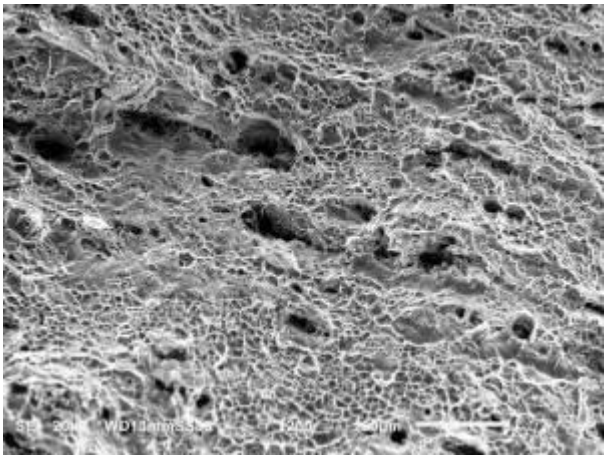

Figure 4.84: SEM micrograph of fractured tensile sample at 450 ^{0}C (SA - 950 ^{0}C x 3 hrs + Age – 600 ^{0}C x 8 hrs); Original Magnification – 200x

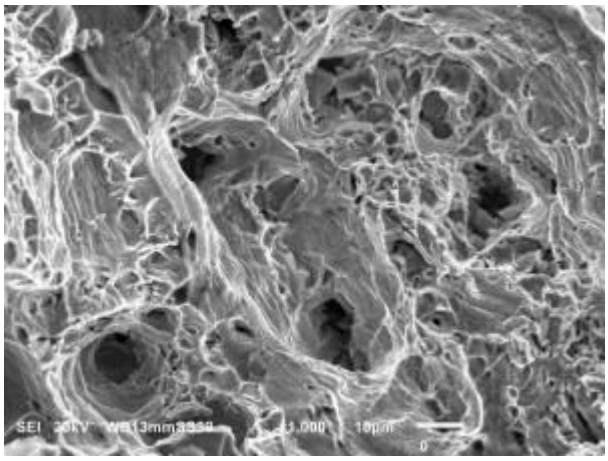

Figure 4.85: SEM micrograph of fractured tensile sample at 450 ^{0}C (SA - 950 ^{0}C x 3 hrs + Age – 600 ^{0}C x 8 hrs); Original Magnification – 1000x

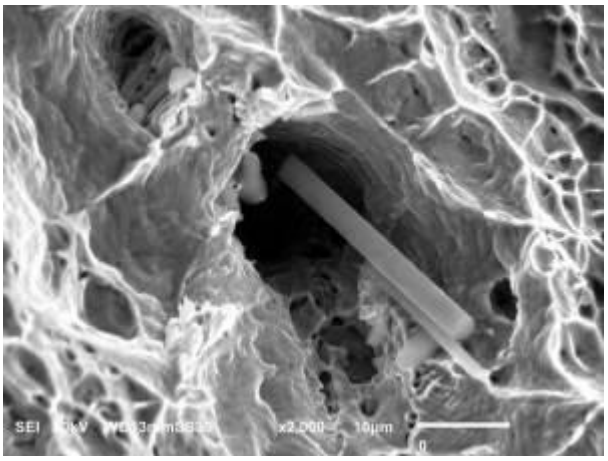

Figure 4.86: SEM micrograph of fractured tensile sample at 450 ^{0}C (SA - 950 ^{0}C x 3 hrs + Age – 600 ^{0}C x 8 hrs); Original Magnification – 2000x

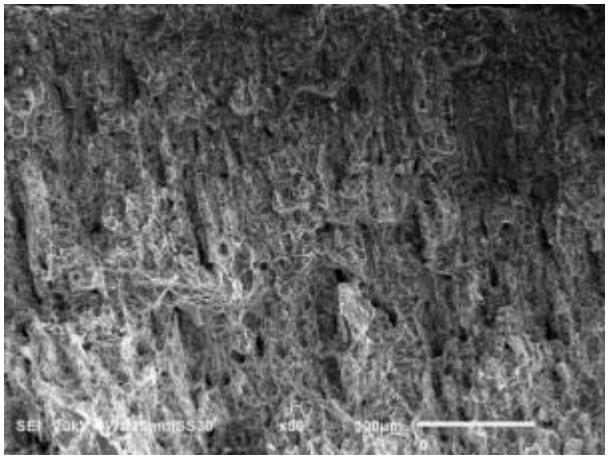

Figure 4.87: SEM micrograph of fractured charpy sample (SA - 950 ^{0}C x 3 hrs + Age – 600 ^{0}C x 4 hrs); Original Magnification – 50x

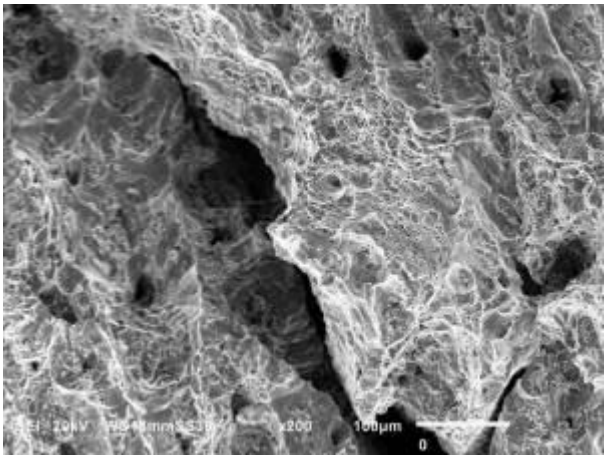

Figure 4.88: SEM micrograph of fractured charpy sample (SA - 950 ^{0}C x 3 hrs + Age – 600 ^{0}C x 4 hrs); Original Magnification – 200x

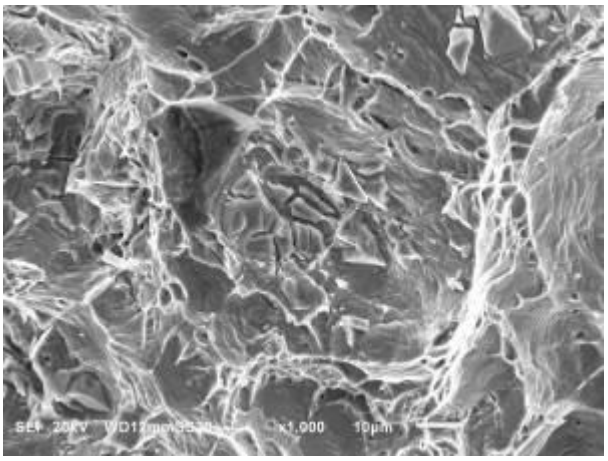

Figure 4.89: SEM micrograph of fractured charpy sample (SA - 950 ^{0}C x 3 hrs + Age – 600 ^{0}C x 4 hrs); Original Magnification – 1000x

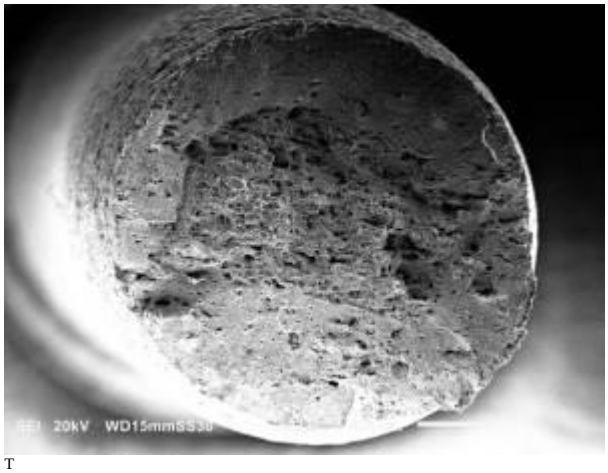

T

Figure 4.90: SEM micrograph of fractured tensile sample at 21 ^{0}C, (SA - 950 ^{0}C x 3 hrs + Age – 600 ^{0}C x 12 hrs); Original Magnification – 33x

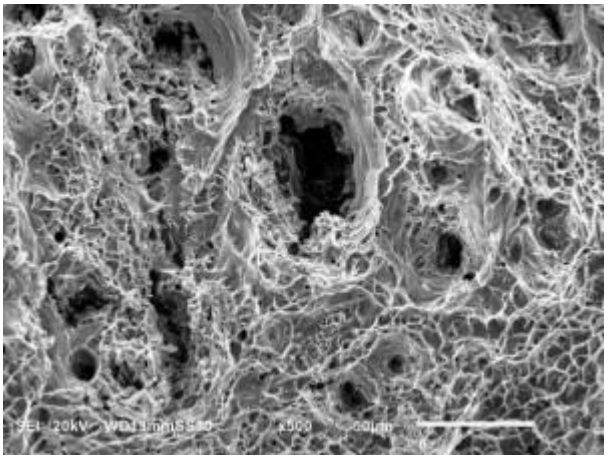

Figure 4.91: SEM micrograph of fractured tensile sample at 21 ^{0}C, (SA - 950 ^{0}C x 3 hrs + Age – 600 ^{0}C x 12 hrs); Original Magnification – 500x

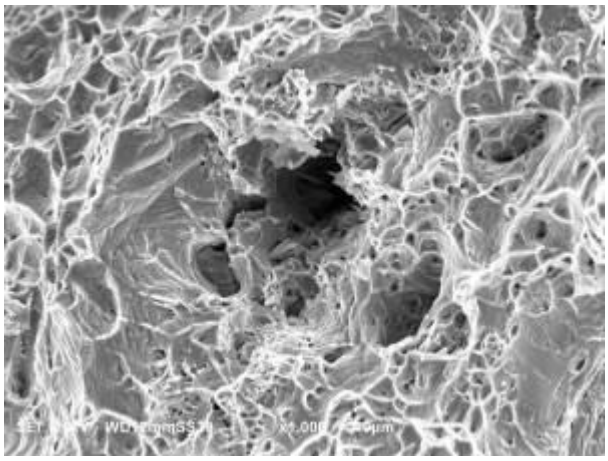

Figure 4.92: SEM micrograph of fractured tensile sample at 21 ^{0}C, (SA - 950 ^{0}C x 3 hrs + Age – 600 ^{0}C x 12 hrs); Original Magnification – 1000x

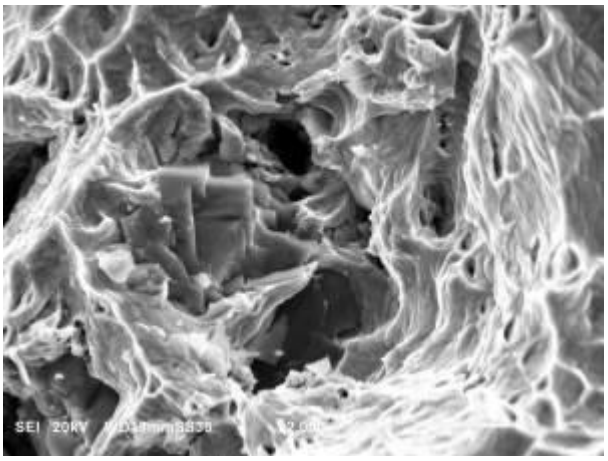

Figure 4.93: SEM micrograph of fractured tensile sample at 21 ^{0}C, (SA - 950 ^{0}C x 3 hrs + Age – 600 ^{0}C x 12 hrs); Original Magnification – 2000x

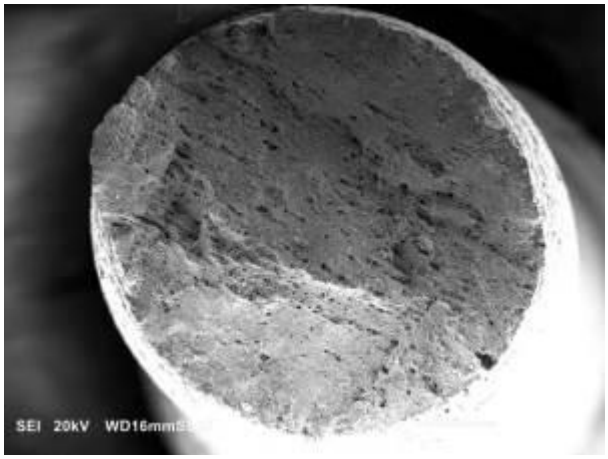

Figure 4.94: SEM micrograph of fractured tensile sample at 450 ^{0}C (SA - 950 ^{0}C x 3 hrs + Age – 600 ^{0}C x 12 hrs); Original Magnification – 33x

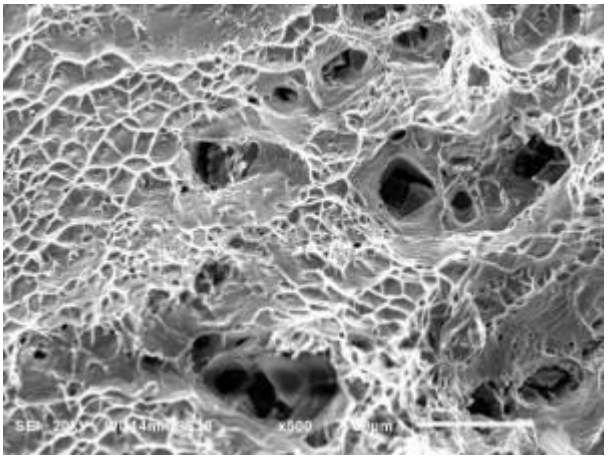

Figure 4.95: SEM micrograph of fractured tensile sample at 450 ^{0}C (SA - 950 ^{0}C x 3 hrs + Age – 600 ^{0}C x 12 hrs); Original Magnification – 500x

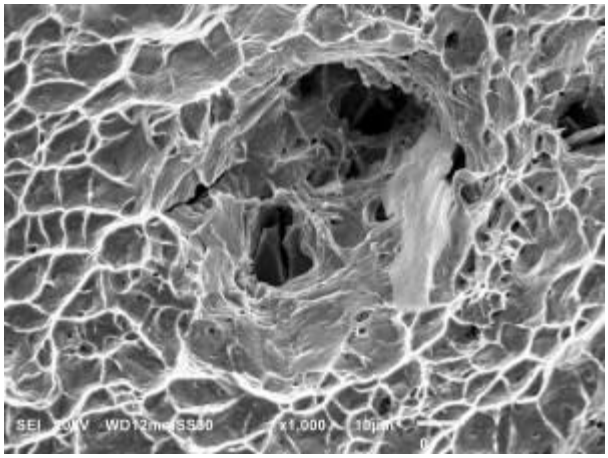

Figure 4.96: SEM micrograph of fractured tensile sample at 450 ^{0}C (SA - 950 ^{0}C x 3 hrs + Age – 600 ^{0}C x 12 hrs); Original Magnification – 1000x

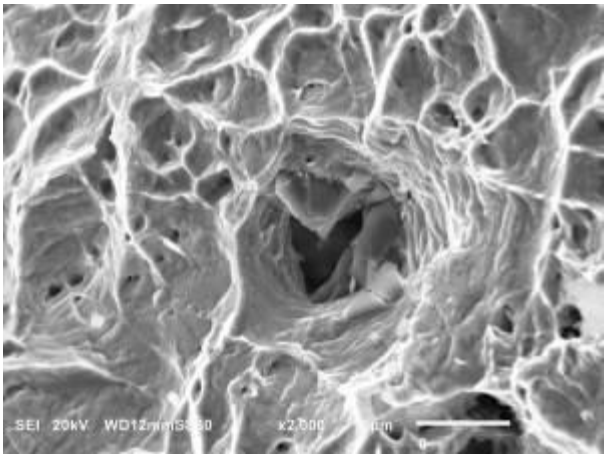

Figure 4.97: SEM micrograph of fractured tensile sample at 450 ^{0}C (SA - 950 ^{0}C x 3 hrs + Age – 600 ^{0}C x 12 hrs); Original Magnification – 2000x

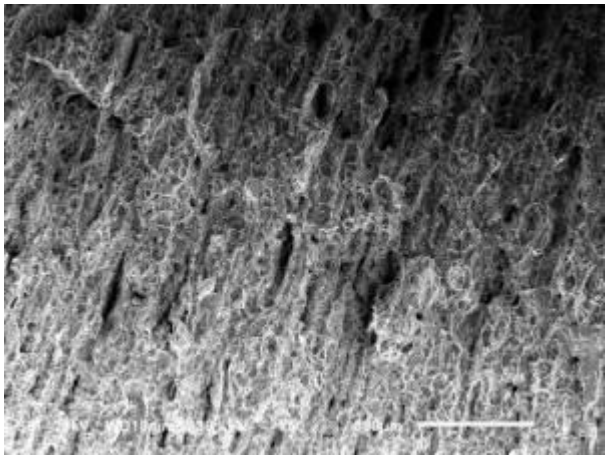

Figure 4.98: SEM micrograph of fractured charpy sample (SA - 950 ^{0}C x 3 hrs + Age – 600 ^{0}C x 12 hrs); Original Magnification – 50x

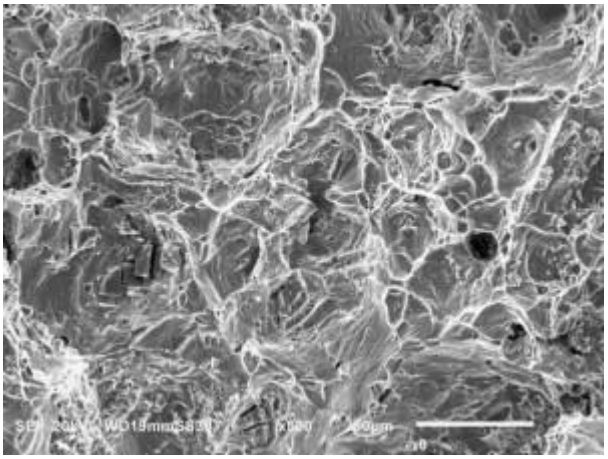

Figure 4.99: SEM micrograph of fractured charpy sample (SA - 950 ^{0}C x 3 hrs + Age – 600 ^{0}C x 12 hrs); Original Magnification – 500x

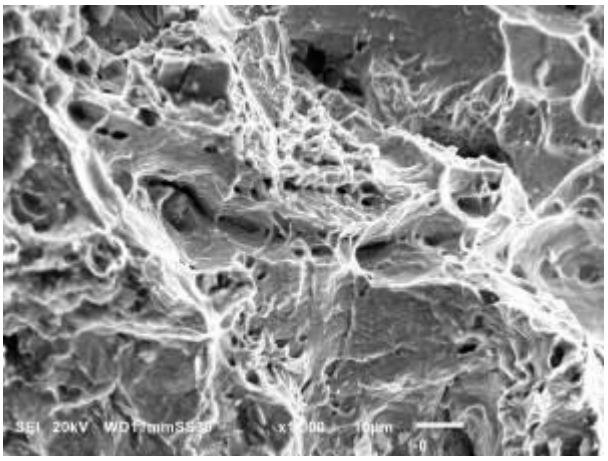

Figure 4.100: SEM micrograph of fractured charpy sample (SA - 950 ^{0}C x 3 hrs + Age – 600 ^{0}C x 12 hrs); Original Magnification – 1000x

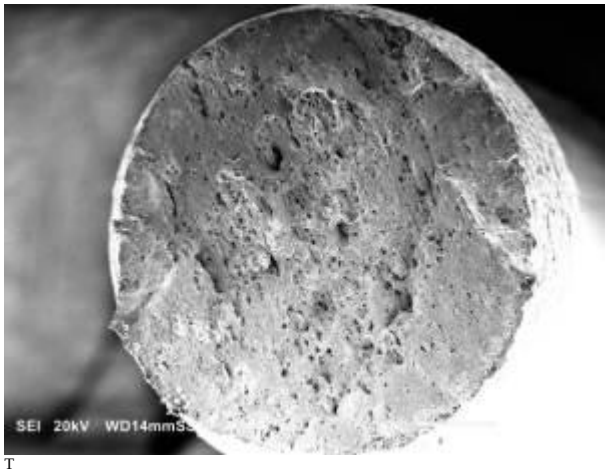

T

Figure 4.101: SEM micrograph of fractured tensile sample at 21 ^{0}C, (SA - 950 ^{0}C x 3 hrs + Age – 640 ^{0}C x 4 hrs); Original Magnification – 33x

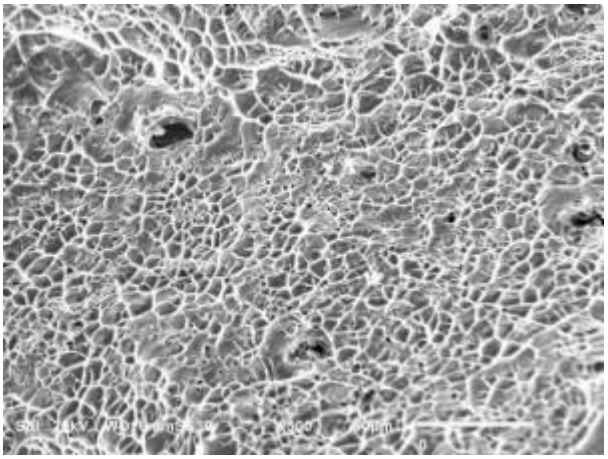

Figure 4.102: SEM micrograph of fractured tensile sample at 21 ^{0}C, (SA - 950 ^{0}C x 3 hrs + Age – 640 ^{0}C x 4 hrs); Original Magnification – 500x

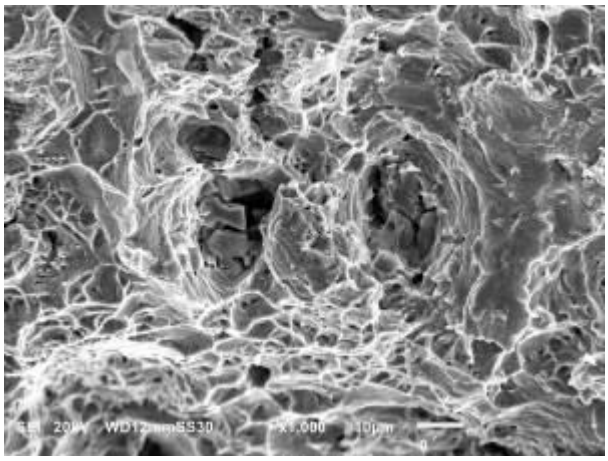

Figure 4.103: SEM micrograph of fractured tensile sample at 21 ^{0}C, (SA - 950 ^{0}C x 3 hrs + Age – 640 ^{0}C x 4 hrs); Original Magnification – 1000x

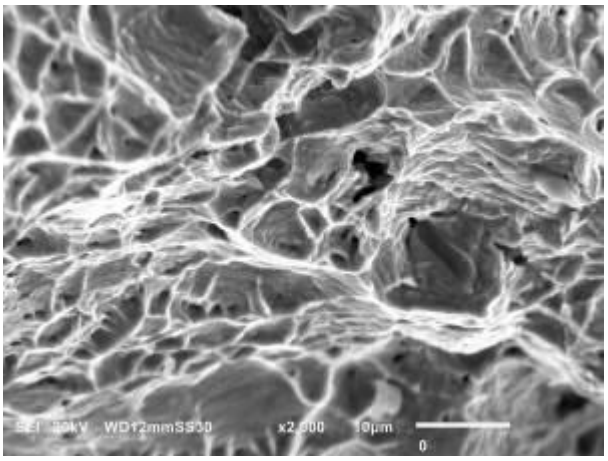

Figure 4.104: SEM micrograph of fractured tensile sample at 21 ^{0}C, (SA - 950 ^{0}C x 3 hrs + Age – 640 ^{0}C x 4 hrs); Original Magnification – 2000x

Figure 4.105: SEM micrograph of fractured tensile sample at 450 ^{0}C (SA - 950 ^{0}C x 3 hrs + Age – 640 ^{0}C x 4 hrs); Original Magnification – 33x

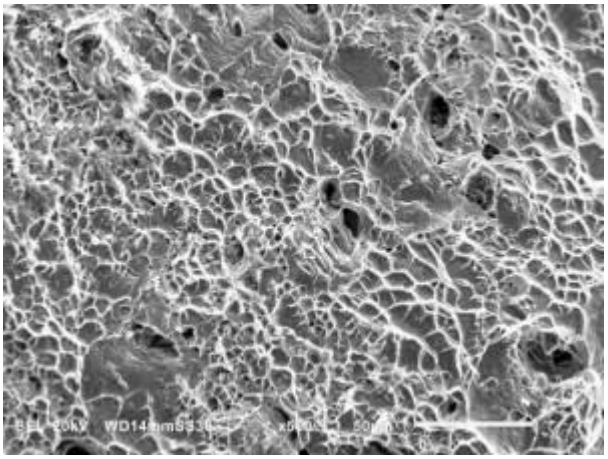

Figure 4.106: SEM micrograph of fractured tensile sample at 450 ^{0}C (SA - 950 ^{0}C x 3 hrs + Age – 640 ^{0}C x 4 hrs); Original Magnification – 500x

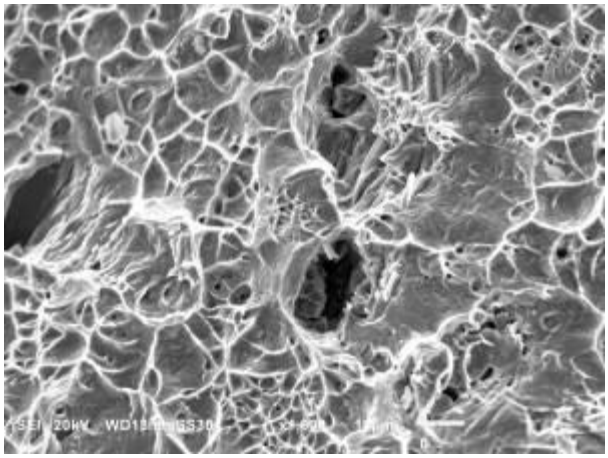

Figure 4.107: SEM micrograph of fractured tensile sample at 450 ^{0}C (SA - 950 ^{0}C x 3 hrs + Age – 640 ^{0}C x 4 hrs); Original Magnification – 1000x

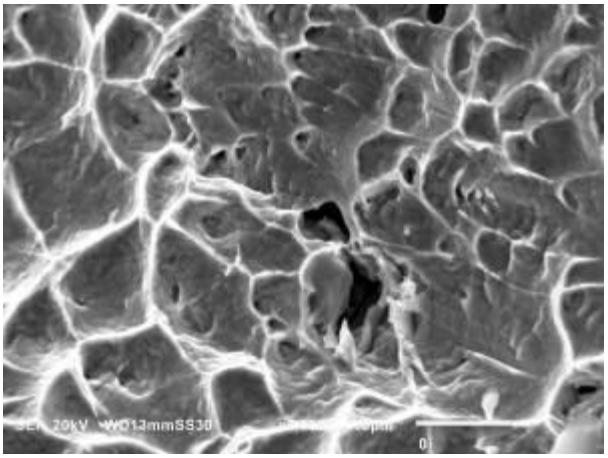

Figure 4.108: SEM micrograph of fractured tensile sample at 450 ^{0}C (SA - 950 ^{0}C x 3 hrs + Age – 640 ^{0}C x 4 hrs); Original Magnification – 2000x

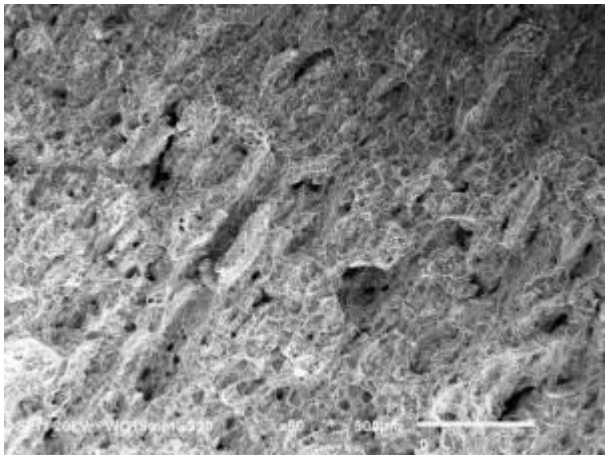

Figure 4.109: SEM micrograph of fractured charpy sample (SA - 950 ^{0}C x 3 hrs + Age – 640 ^{0}C x 4 hrs); Original Magnification – 50x

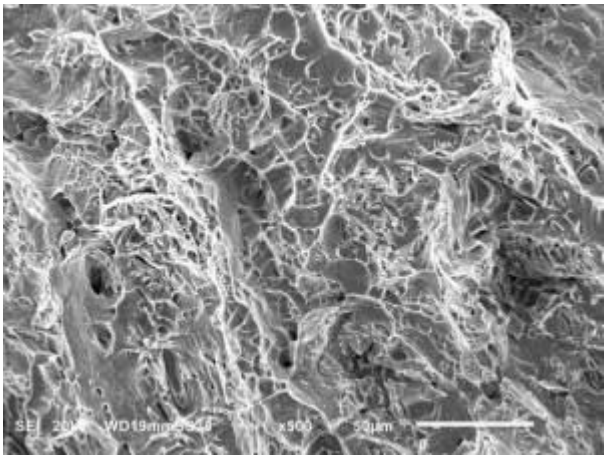

Figure 4.110: SEM micrograph of fractured charpy sample (SA - 950 ^{0}C x 3 hrs + Age – 640 ^{0}C x 4 hrs); Original Magnification – 500x

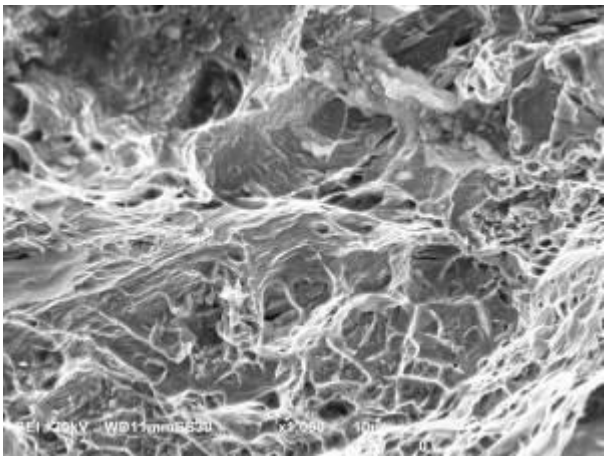

Figure 4.111: SEM micrograph of fractured charpy sample (SA - 950 ^{0}C x 3 hrs + Age – 640 ^{0}C x 4 hrs); Original Magnification – 1000x

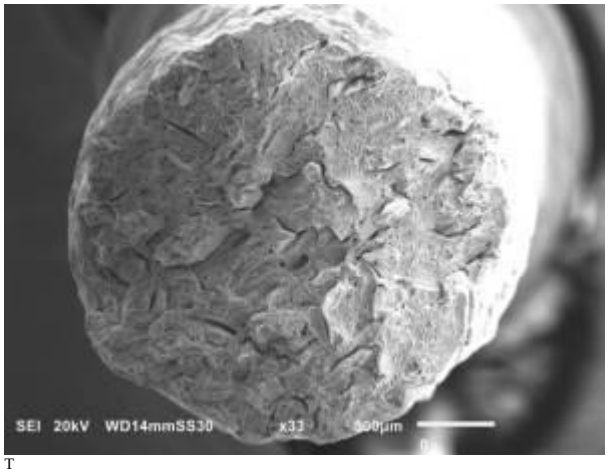

T

Figure 4.112: SEM micrograph of fractured tensile sample at 21 ^{0}C, (SA - 1120 ^{0}C x 3 hrs + Age – 640 ^{0}C x 8 hrs); Original Magnification – 33x

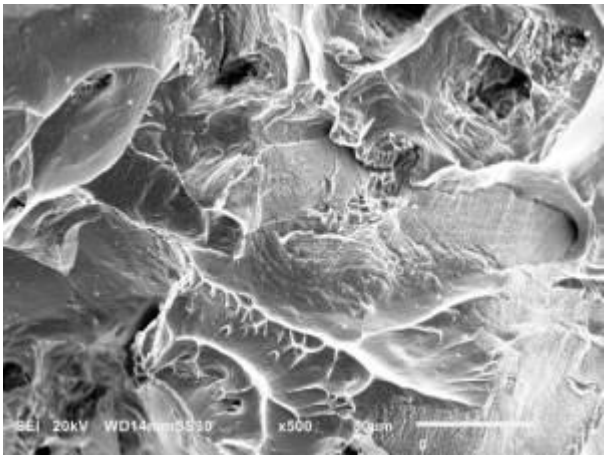

Figure 4.113:SEM micrograph of fractured tensile sample at 21 ^{0}C, (SA - 1120 ^{0}C x 3 hrs + Age – 640 ^{0}C x 8 hrs); Original Magnification – 500x

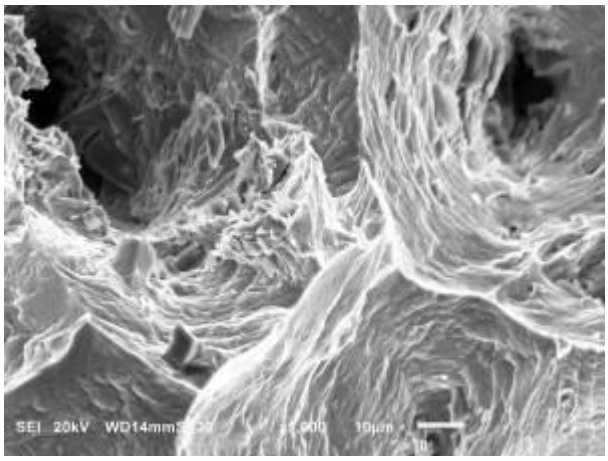

Figure 4.114: SEM micrograph of fractured tensile sample at 21 ^{0}C, (SA - 1120 ^{0}C x 3 hrs + Age – 640 ^{0}C x 8 hrs); Original Magnification – 1000x

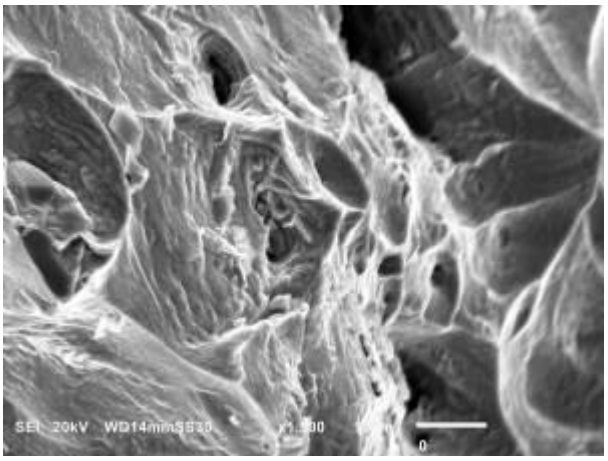

Figure 4.115: SEM micrograph of fractured tensile sample at 21 ^{0}C, (SA - 1120 ^{0}C x 3 hrs + Age – 640 ^{0}C x 8 hrs); Original Magnification – 1500x

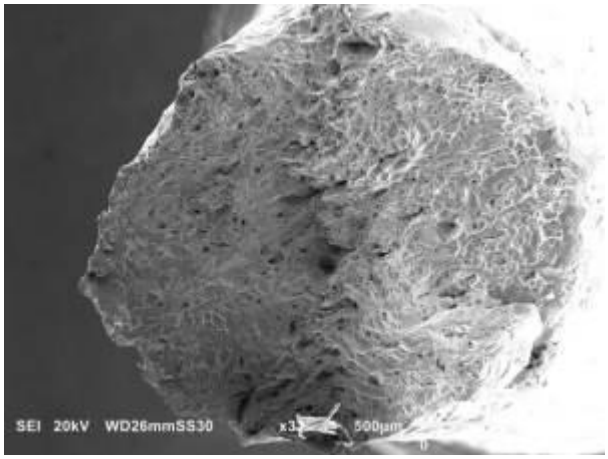

Figure 4.116: SEM micrograph of fractured tensile sample at 450 ^{0}C (SA - 1120 ^{0}C x 3 hrs + Age – 640 ^{0}C x 8 hrs); Original Magnification – 33x

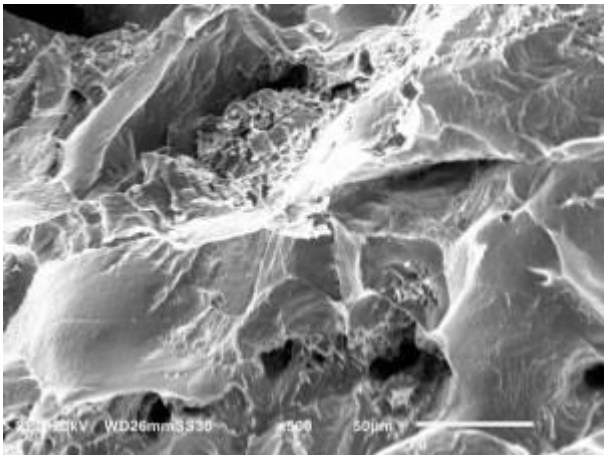

Figure 4.117: SEM micrograph of fractured tensile sample at 450 ^{0}C (SA - 1120 ^{0}C x 3 hrs + Age – 640 ^{0}C x 8 hrs); Original Magnification – 500x

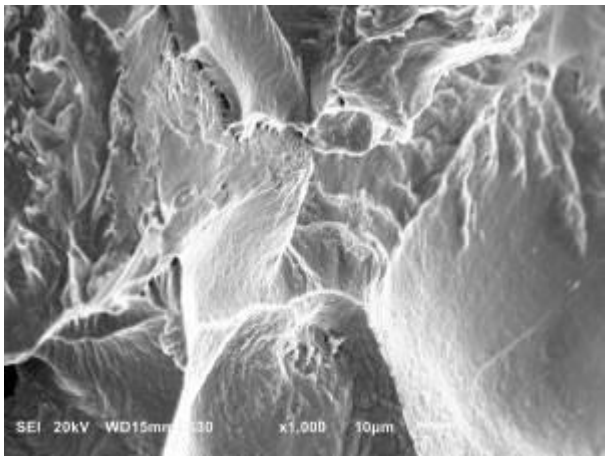

Figure 4.118: SEM micrograph of fractured tensile sample at 450 ^{0}C (SA - 1120 ^{0}C x 3 hrs + Age – 640 ^{0}C x 8 hrs); Original Magnification – 1000x

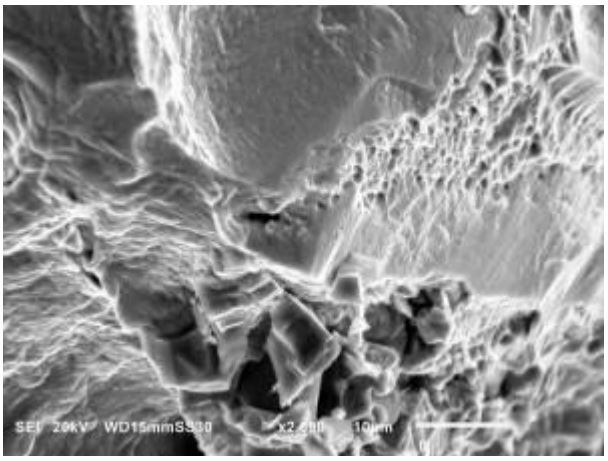

Figure 4.119: SEM micrograph of fractured tensile sample at 450 ^{0}C (SA - 1120 ^{0}C x 3 hrs + Age – 640 ^{0}C x 8 hrs); Original Magnification – 2000x

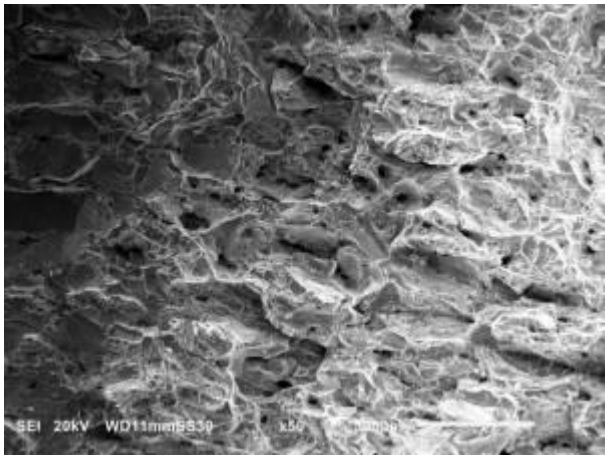

Figure 4.120: SEM micrograph of fractured charpy sample (SA - 1120 ^{0}C x 3 hrs + Age – 640 ^{0}C x 8 hrs); Original Magnification – 50x

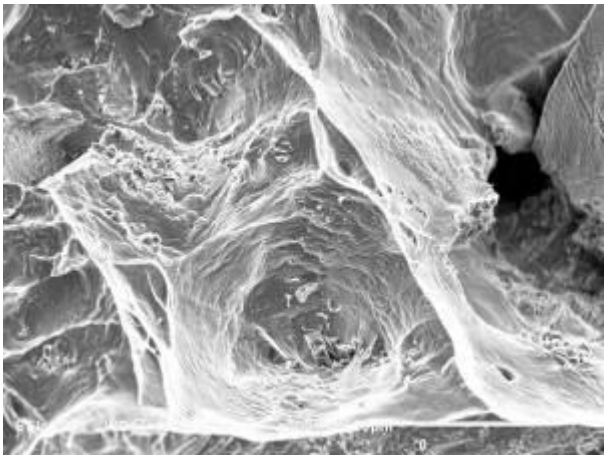

Figure 4.121: SEM micrograph of fractured charpy sample (SA - 1120 ^{0}C x 3 hrs + Age – 640 ^{0}C x 8 hrs); Original Magnification – 500x

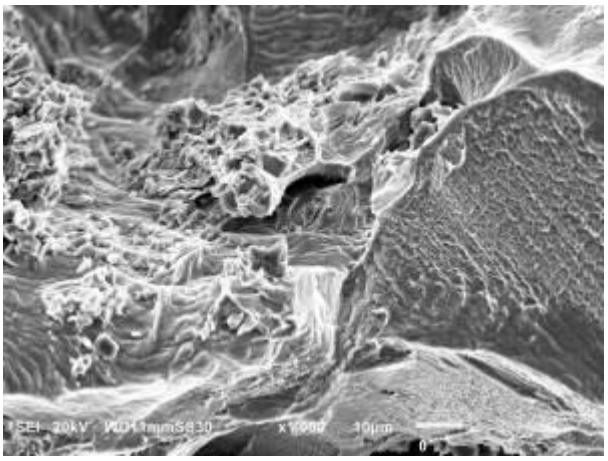

Figure 4.122: SEM micrograph of fractured charpy sample (SA - 1120 ^{0}C x 3 hrs + Age – 640 ^{0}C x 8 hrs); Original Magnification – 1000x

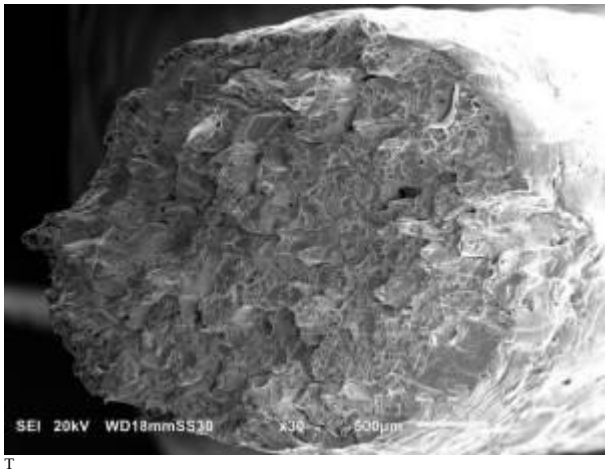

T

Figure 4.123: SEM micrograph of fractured tensile sample at 21 ^{0}C, (SA - 1120 ^{0}C x 3 hrs + Age – 640 ^{0}C x 12 hrs); Original Magnification – 30x

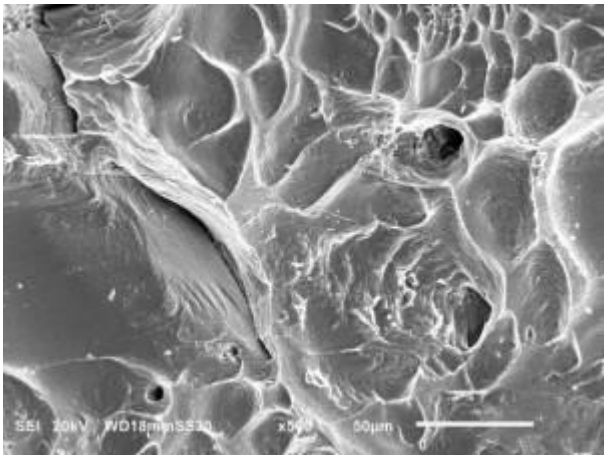

Figure 4.124: SEM micrograph of fractured tensile sample at 21 ^{0}C, (SA - 1120 ^{0}C x 3 hrs + Age – 640 ^{0}C x 12 hrs); Original Magnification – 500x

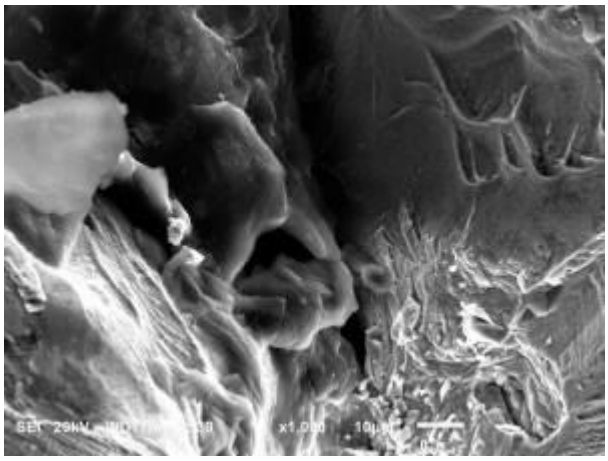

Figure 4.125: SEM micrograph of fractured tensile sample at 21 ^{0}C, (SA - 1120 ^{0}C x 3 hrs + Age – 640 ^{0}C x 12 hrs); Original Magnification – 1000x

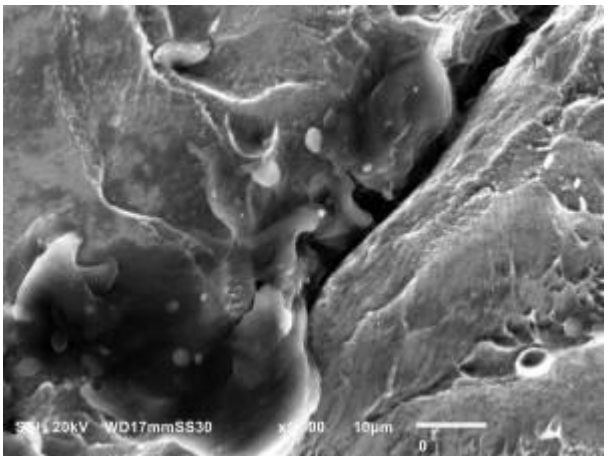

Figure 4.126: SEM micrograph of fractured tensile sample at 21 ^{0}C, (SA - 1120 ^{0}C x 3 hrs + Age – 640 ^{0}C x 12 hrs); Original Magnification – 1500x

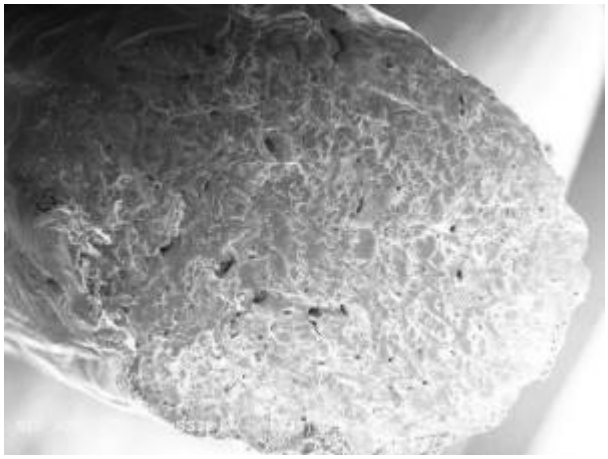

Figure 4.127: SEM micrograph of fractured tensile sample at 450 ^{0}C (SA - 1120 ^{0}C x 3 hrs + Age – 640 ^{0}C x 12 hrs); Original Magnification – 35x

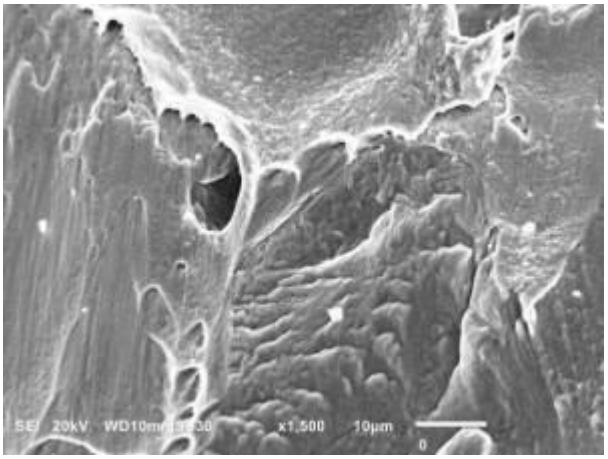

Figure 4.128: SEM micrograph of fractured tensile sample at 450 ^{0}C (SA - 1120 ^{0}C x 3 hrs + Age – 640 ^{0}C x 12 hrs); Original Magnification – 1500x

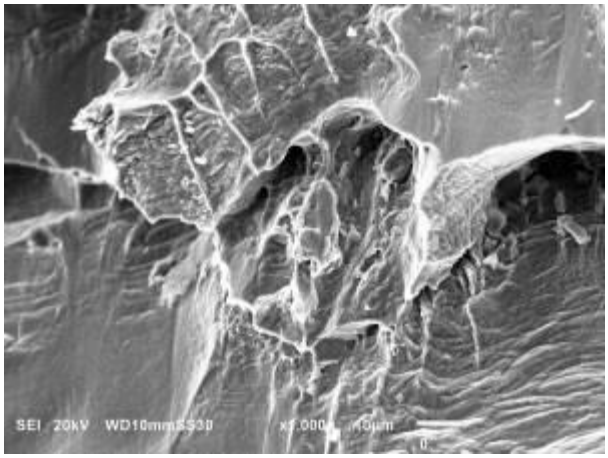

Figure 4.129: SEM micrograph of fractured tensile sample at 450 ^{0}C (SA - 1120 ^{0}C x 3 hrs + Age – 640 ^{0}C x 12 hrs); Original Magnification – 1000x

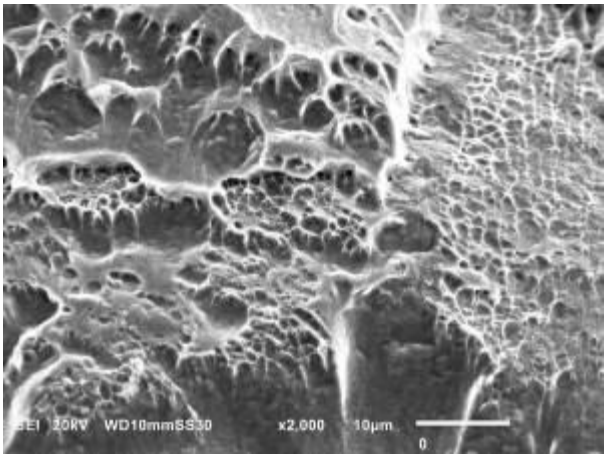

Figure 4.130: SEM micrograph of fractured tensile sample at 450 ^{0}C (SA - 1120 ^{0}C x 3 hrs + Age – 640 ^{0}C x 12 hrs); Original Magnification – 2000x

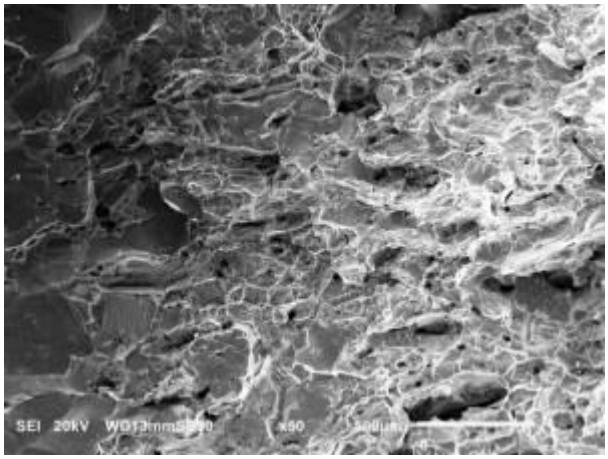

Figure 4.131: SEM micrograph of fractured charpy sample (SA - 1120 ^{0}C x 3 hrs + Age – 640 ^{0}C x 12 hrs); Original Magnification – 50x

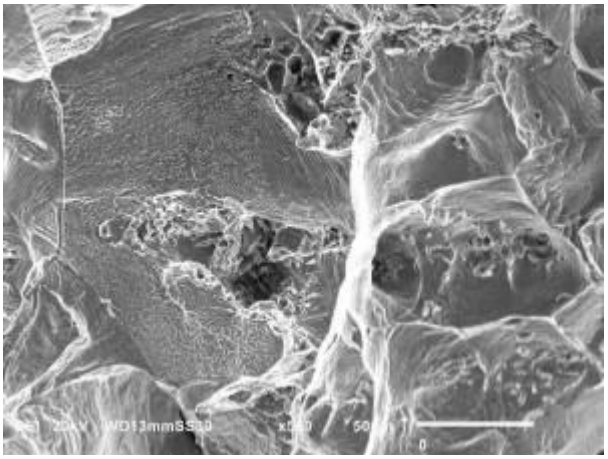

Figure 4.132: SEM micrograph of fractured charpy sample (SA - 1120 ^{0}C x 3 hrs + Age – 640 ^{0}C x 12 hrs); Original Magnification – 500x

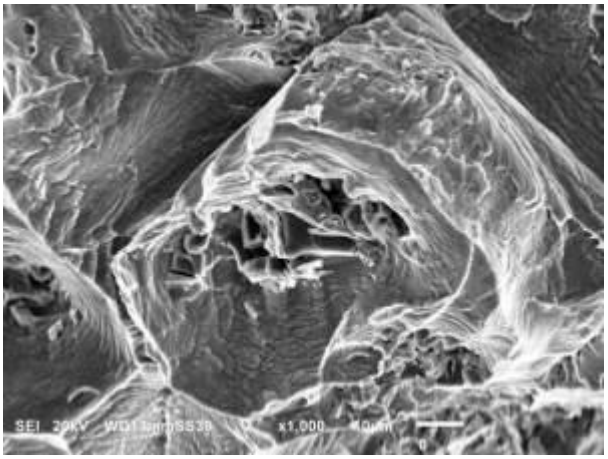

Figure 4.133: SEM micrograph of fractured charpy sample (SA - 1120 ^{0}C x 3 hrs + Age – 640 ^{0}C x 12 hrs); Original Magnification – 1000x

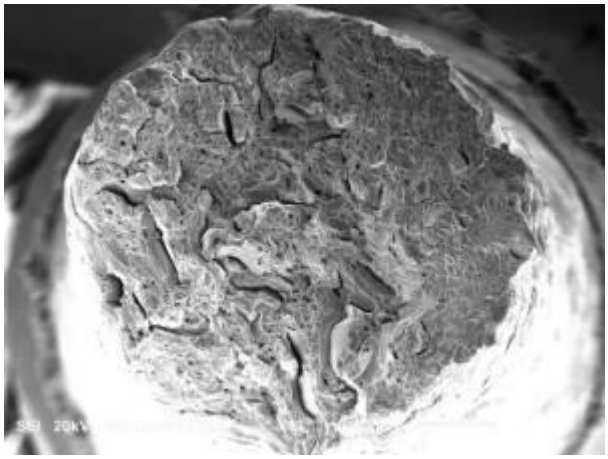

Figure 4.134: SEM micrograph of fractured tensile sample at 21 ^{0}C, (SA - 1120 ^{0}C x 3 hrs + Age – 640 ^{0}C x 4 hrs); Original Magnification – 33x

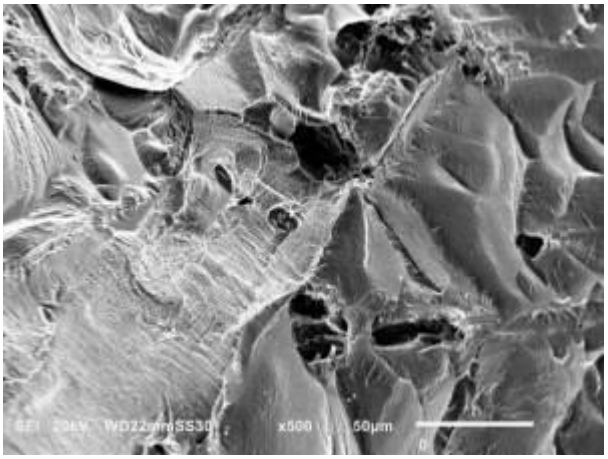

Figure 4.135: SEM micrograph of fractured tensile sample at 21 ^{0}C, (SA - 1120 ^{0}C x 3 hrs + Age – 640 ^{0}C x 4 hrs); Original Magnification – 500x

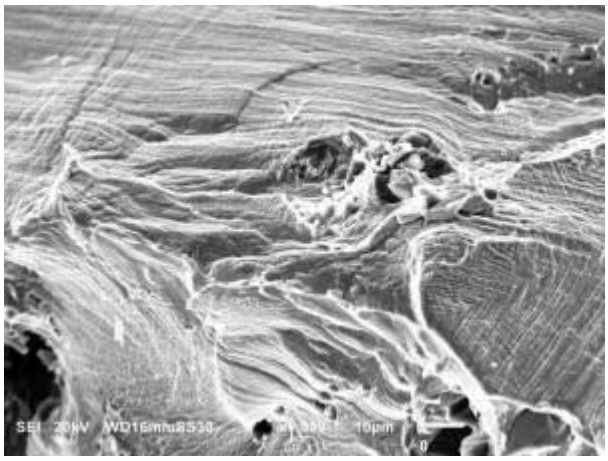

Figure 4.136: SEM micrograph of fractured tensile sample at 21 ^{0}C, (SA - 1120 ^{0}C x 3 hrs + Age – 640 ^{0}C x 4 hrs); Original Magnification – 1000x

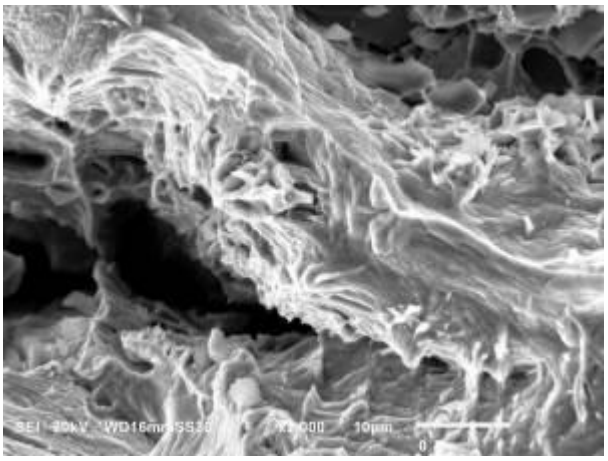

Figure 4.137: SEM micrograph of fractured tensile sample at 21 ^{0}C, (SA - 1120 ^{0}C x 3 hrs + Age – 640 ^{0}C x 4 hrs); Original Magnification – 2000x

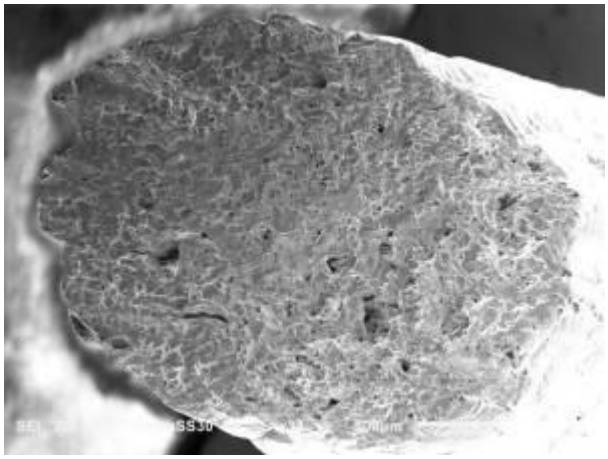

Figure 4.138: SEM micrograph of fractured tensile sample at 450 ^{0}C (SA - 1120 ^{0}C x 3 hrs + Age – 640 ^{0}C x 4 hrs); Original Magnification – 35x

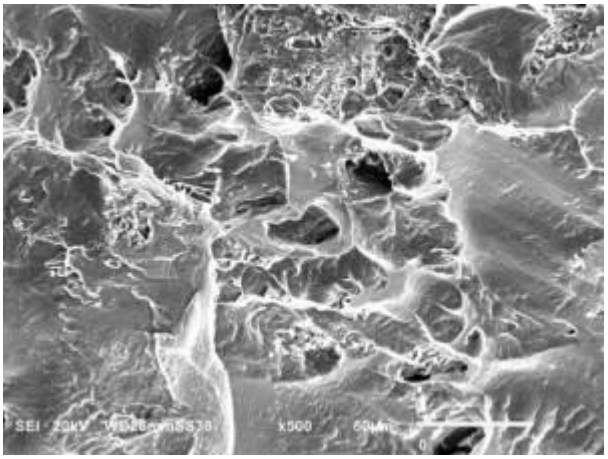

Figure 4.139: SEM micrograph of fractured tensile sample at 450 ^{0}C (SA - 1120 ^{0}C x 3 hrs + Age – 640 ^{0}C x 4 hrs); Original Magnification – 500x

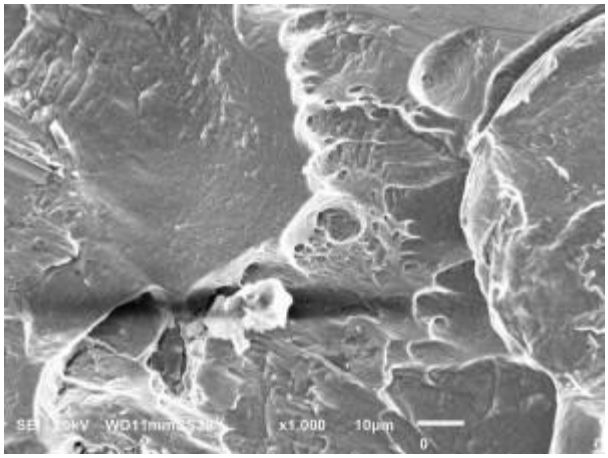

Figure 4.140: SEM micrograph of fractured tensile sample at 450 ^{0}C (SA - 1120 ^{0}C x 3 hrs + Age – 640 ^{0}C x 4 hrs); Original Magnification – 1000x

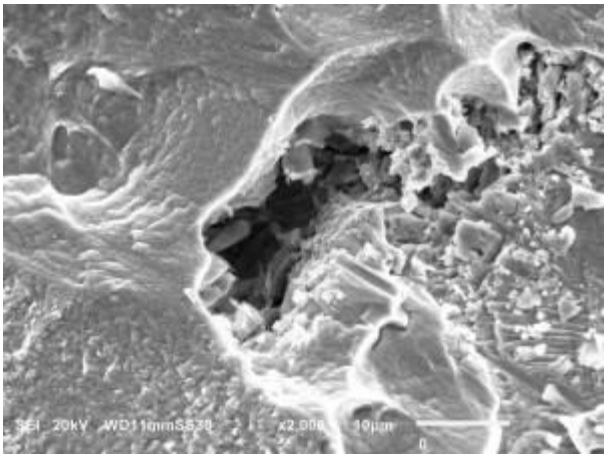

Figure 4.141: SEM micrograph of fractured tensile sample at 450 ^{0}C (SA - 1120 ^{0}C x 3 hrs + Age – 640 ^{0}C x 4 hrs); Original Magnification – 2000x

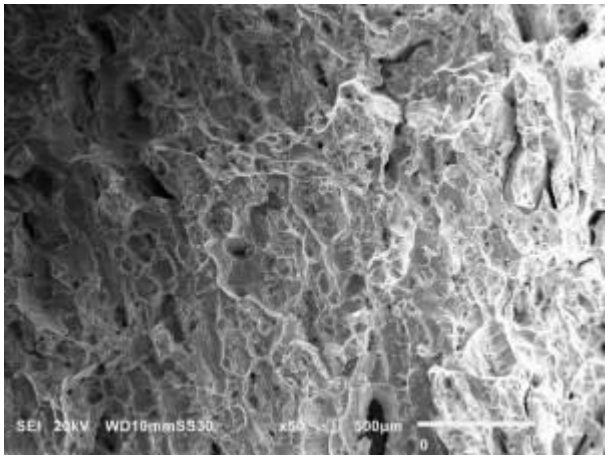

Figure 4.142: SEM micrograph of fractured charpy sample (SA - 1120 ^{0}C x 3 hrs + Age – 640 ^{0}C x 4 hrs); Original Magnification – 50x

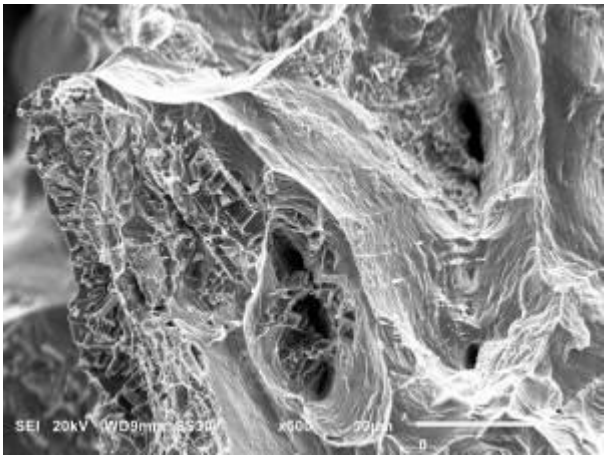

Figure 4.143: SEM micrograph of fractured charpy sample (SA - 1120 ^{0}C x 3 hrs + Age – 640 ^{0}C x 4 hrs); Original Magnification – 500x

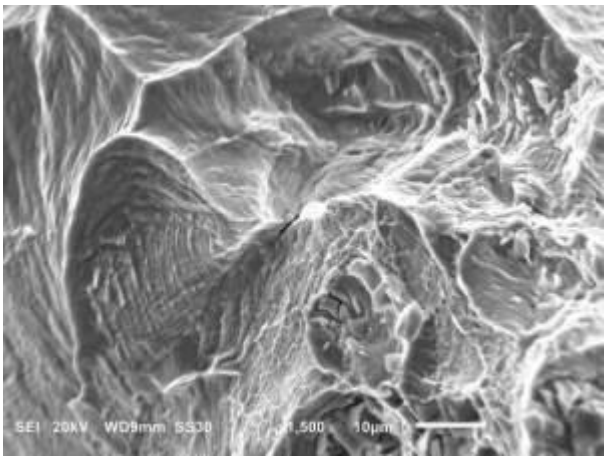

Figure 4.144: SEM micrograph of fractured charpy sample (SA - 1120 ^{0}C x 3 hrs + Age – 640 ^{0}C x 4 hrs); Original Magnification – 1500x

Figure 4.145: SEM micrograph of fractured tensile sample at 21 ^{0}C, (SA - 1120 ^{0}C x 3 hrs + Age – 600 ^{0}C x 8 hrs); Original Magnification – 33x

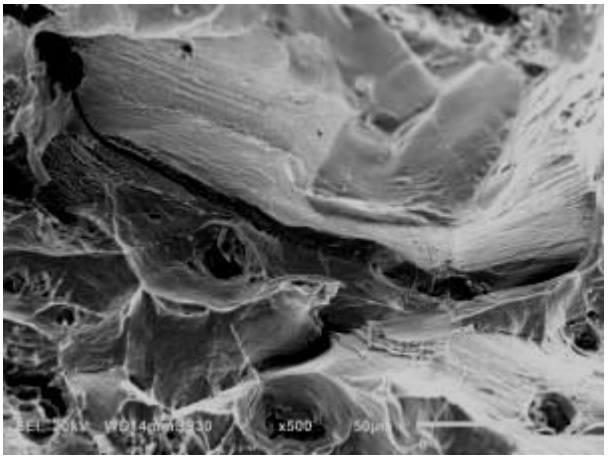

Figure 4.146: SEM micrograph of fractured tensile sample at 21 ^{0}C, (SA - 1120 ^{0}C x 3 hrs + Age – 600 ^{0}C x 8 hrs); Original Magnification – 500x

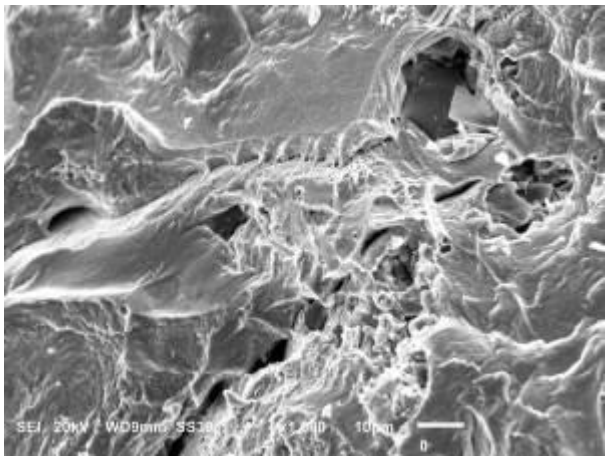

Figure 4.147: SEM micrograph of fractured tensile sample at 21 ^{0}C, (SA - 1120 ^{0}C x 3 hrs + Age – 600 ^{0}C x 8 hrs); Original Magnification – 1000x

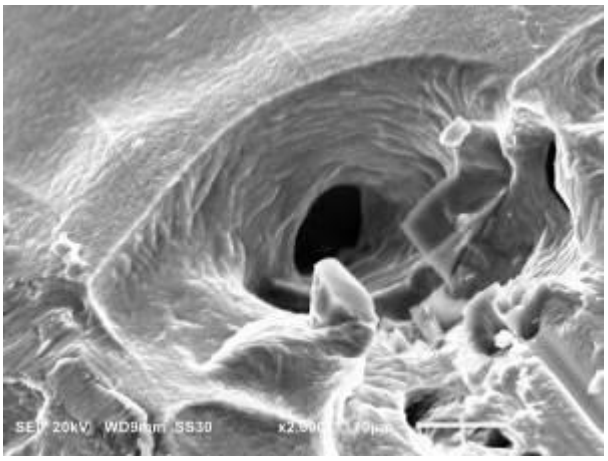

Figure 4.148: SEM micrograph of fractured tensile sample at 21 ^{0}C, (SA - 1120 ^{0}C x 3 hrs + Age – 600 ^{0}C x 8 hrs); Original Magnification – 2000x

Figure 4.149: SEM micrograph of fractured tensile sample at 450 ^{0}C (SA - 1120 ^{0}C x 3 hrs + Age – 600 ^{0}C x 8 hrs); Original Magnification – 35x

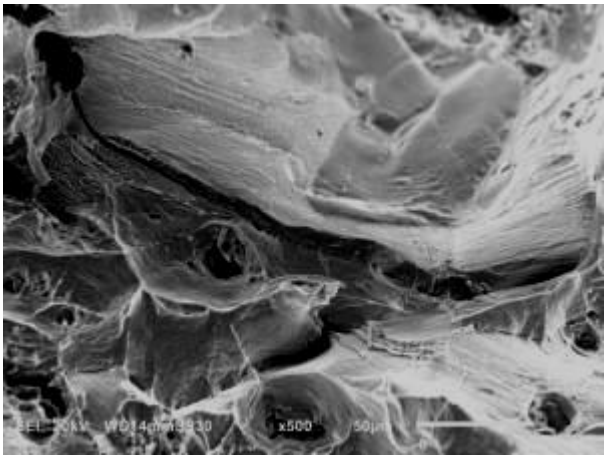

Figure 4.150: SEM micrograph of fractured tensile sample at 450 ^{0}C (SA - 1120 ^{0}C x 3 hrs + Age – 600 ^{0}C x 8 hrs); Original Magnification – 500x

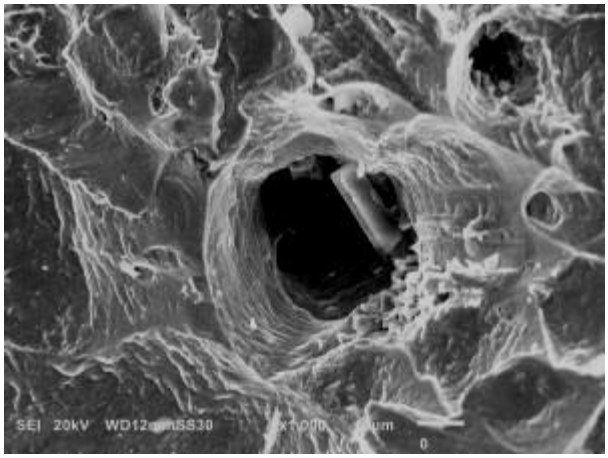

Figure 4.151: SEM micrograph of fractured tensile sample at 450 ^{0}C (SA - 1120 ^{0}C x 3 hrs + Age – 600 ^{0}C x 8 hrs); Original Magnification – 1000x

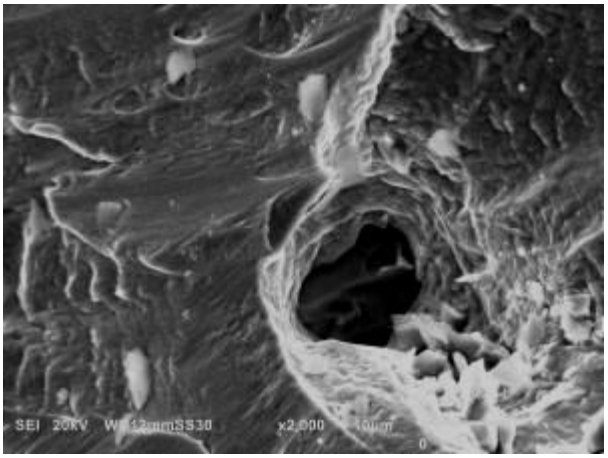

Figure 4.152: SEM micrograph of fractured tensile sample at 450 ^{0}C (SA - 1120 ^{0}C x 3 hrs + Age – 600 ^{0}C x 8 hrs); Original Magnification – 2000x

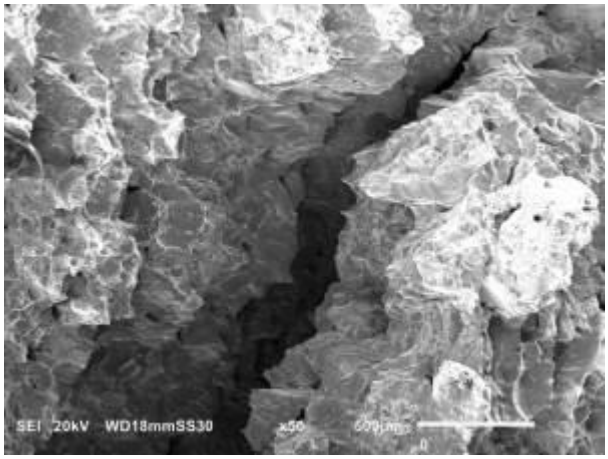

Figure 4.153: SEM micrograph of fractured charpy sample (SA - 1120 ^{0}C x 3 hrs + Age – 600 ^{0}C x 8 hrs); Original Magnification – 50x

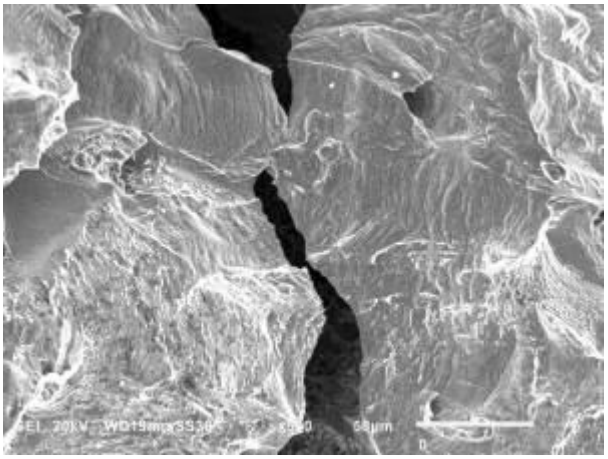

Figure 4.154: SEM micrograph of fractured charpy sample (SA - 1120 ^{0}C x 3 hrs + Age – 600 ^{0}C x 8 hrs); Original Magnification – 500x

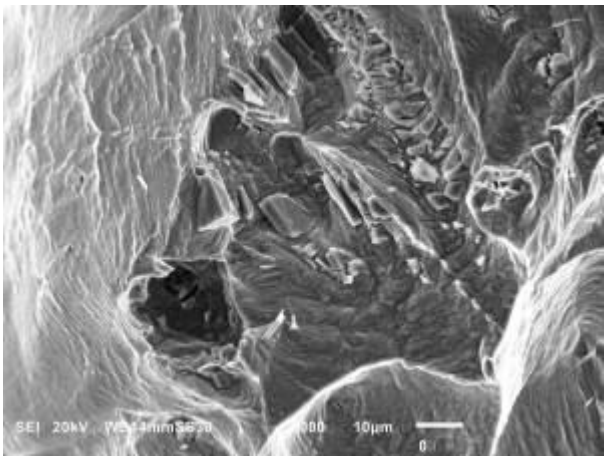

Figure 4.155: SEM micrograph of fractured charpy sample (SA - 1120 ^{0}C x 3 hrs + Age – 600 ^{0}C x 8 hrs); Original Magnification – 1000x

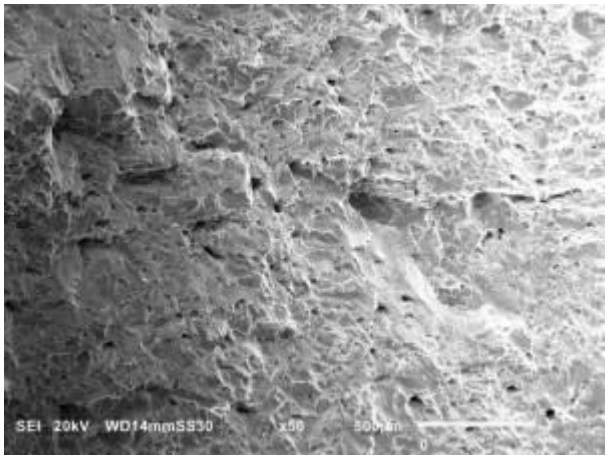

Figure 4.156: SEM micrograph of fractured stress rupture sample (SA - 1120 ^{0}C x 3 hrs + Age – 600 ^{0}C x 8 hrs); Original Magnification – 50x

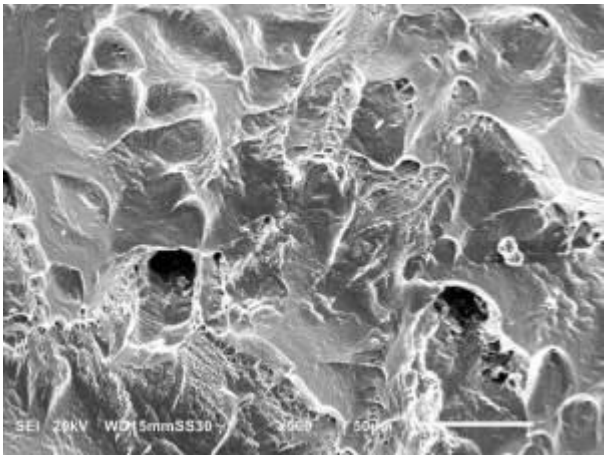

Figure 4.157: SEM micrograph of fractured stress rupture sample (SA - 1120 ^{0}C x 3 hrs + Age – 600 ^{0}C x 8 hrs); Original Magnification – 500x

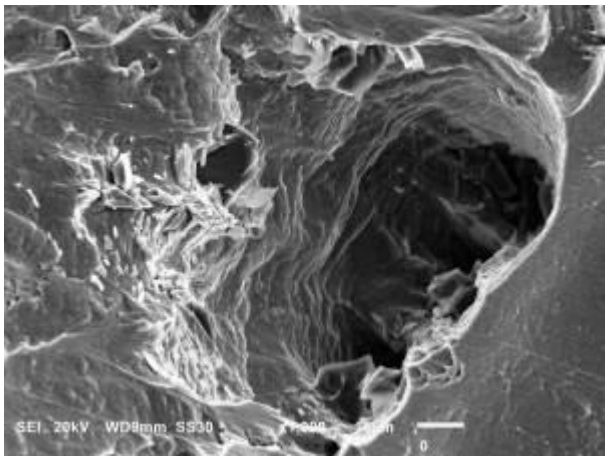

Figure 4.158: SEM micrograph of fractured stress rupture sample (SA - 1120 ^{0}C x 3 hrs + Age – 600 ^{0}C x 8 hrs); Original Magnification – 1000x

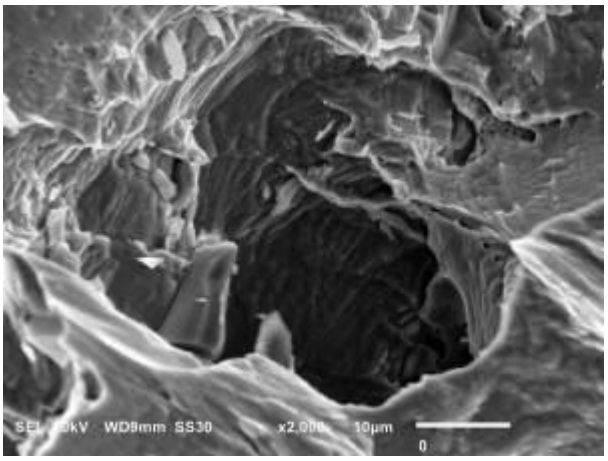

Figure 4.159: SEM micrograph of fractured stress rupture sample (SA - 1120 ^{0}C x 3 hrs + Age – 600 ^{0}C x 8 hrs); Original Magnification – 2000x

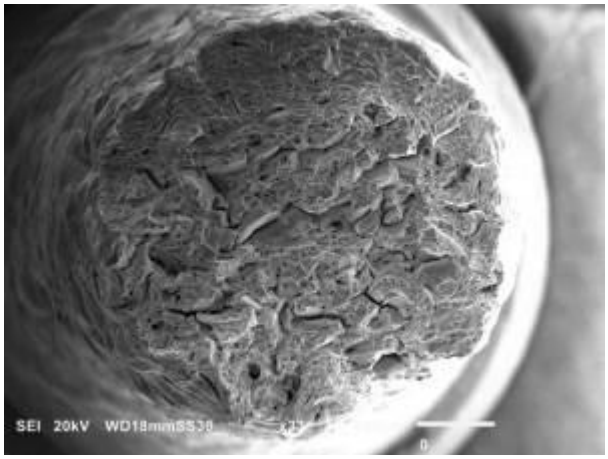

Figure 4.160: SEM micrograph of fractured tensile sample at 21 ^{0}C, (SA - 1120 ^{0}C x 3 hrs + Age – 600 ^{0}C x 12 hrs); Original Magnification – 33x

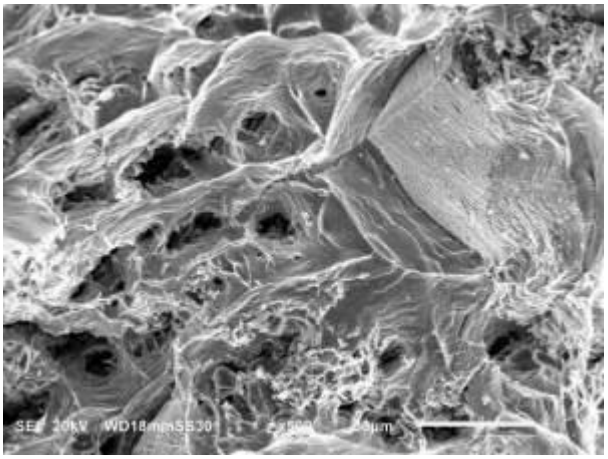

Figure 4.161: SEM micrograph of fractured tensile sample at 21 ^{0}C, (SA - 1120 ^{0}C x 3 hrs + Age – 600 ^{0}C x 12 hrs); Original Magnification – 500x

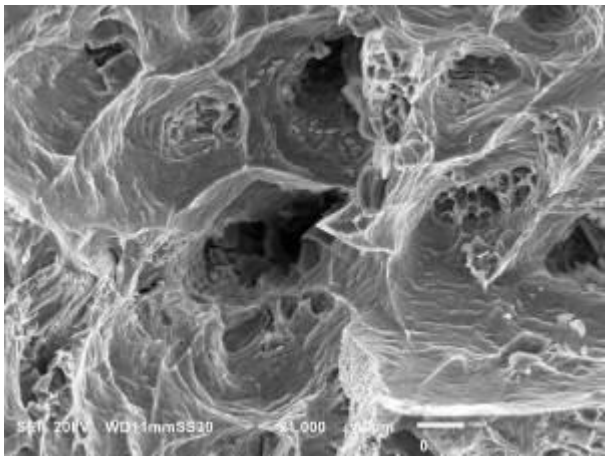

Figure 4.162: SEM micrograph of fractured tensile sample at 21 ^{0}C, (SA - 1120 ^{0}C x 3 hrs + Age – 600 ^{0}C x 12 hrs); Original Magnification – 1000x

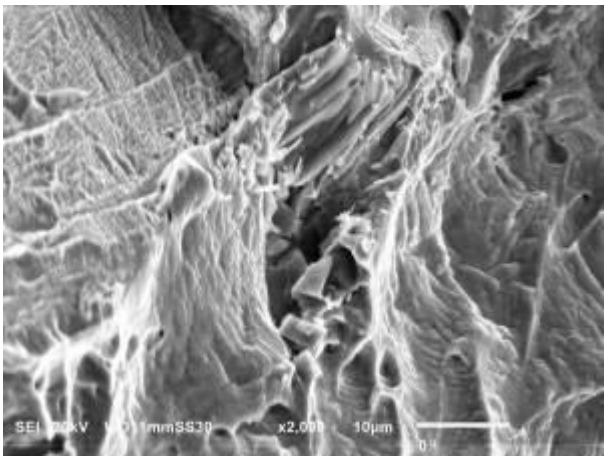

Figure 4.163: SEM micrograph of fractured tensile sample at 21 ^{0}C, (SA - 1120 ^{0}C x 3 hrs + Age – 600 ^{0}C x 12 hrs); Original Magnification – 2000x

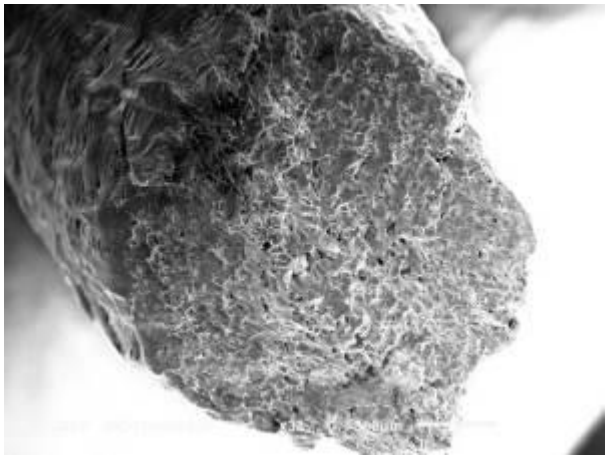

Figure 4.164: SEM micrograph of fractured tensile sample at 450 ^{0}C (SA - 1120 ^{0}C x 3 hrs + Age – 600 ^{0}C x 12 hrs); Original Magnification – 35x

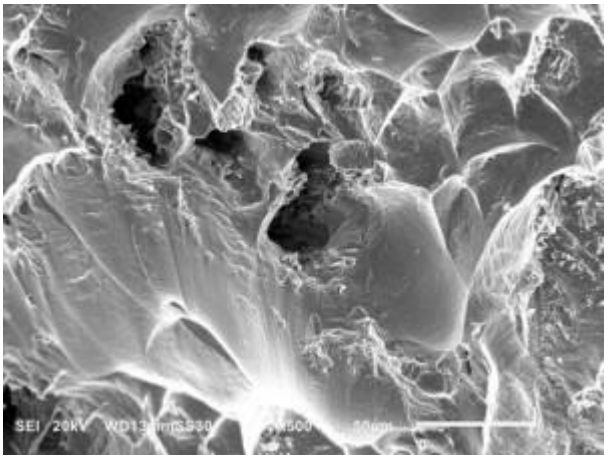

Figure 4.165: SEM micrograph of fractured tensile sample at 450 ^{0}C (SA - 1120 ^{0}C x 3 hrs + Age – 600 ^{0}C x 12 hrs); Original Magnification – 500x

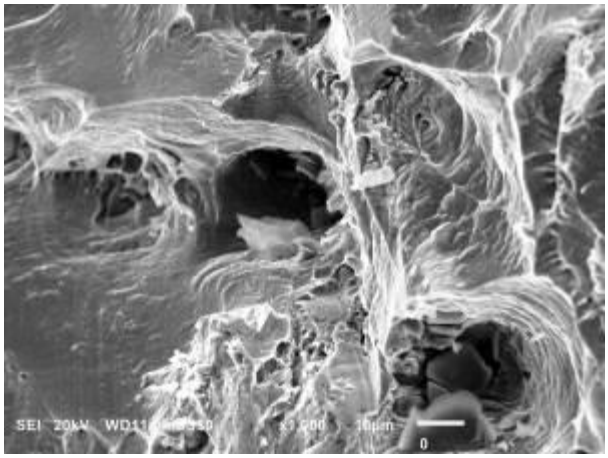

Figure 4.166: SEM micrograph of fractured tensile sample at 450 ^{0}C (SA - 1120 ^{0}C x 3 hrs + Age – 600 ^{0}C x 12 hrs); Original Magnification – 1000x

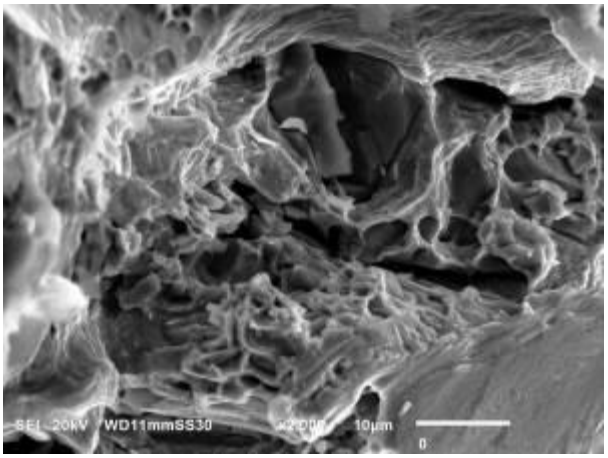

Figure 4.167: SEM micrograph of fractured tensile sample at 450 ^{0}C (SA - 1120 ^{0}C x 3 hrs + Age – 600 ^{0}C x 12 hrs); Original Magnification – 2000x

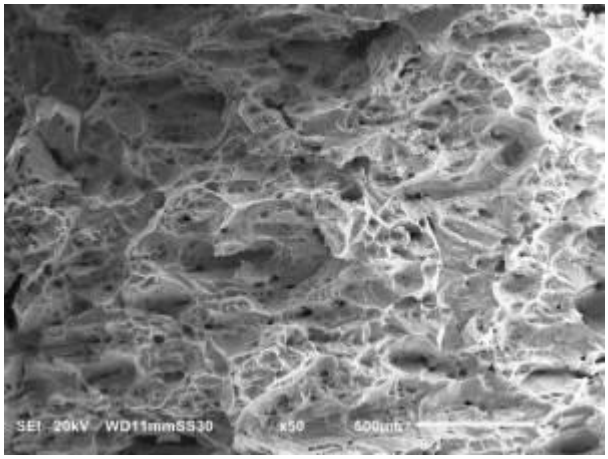

Figure 4.168: SEM micrograph of fractured charpy sample (SA - 1120 ^{0}C x 3 hrs + Age – 600 ^{0}C x 12 hrs); Original Magnification – 50x

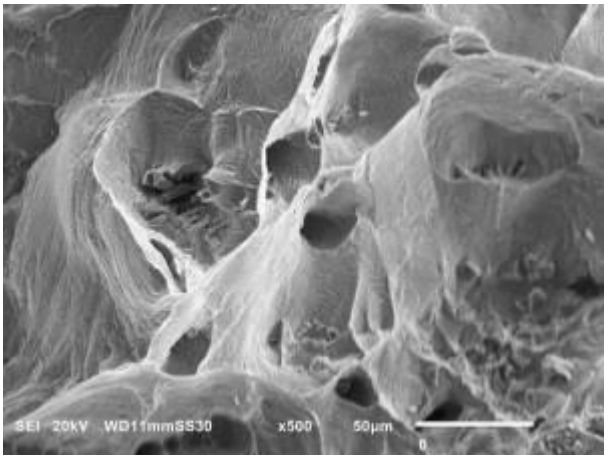

Figure 4.169: SEM micrograph of fractured charpy sample (SA - 1120 ^{0}C x 3 hrs + Age – 600 ^{0}C x 12 hrs); Original Magnification – 500x

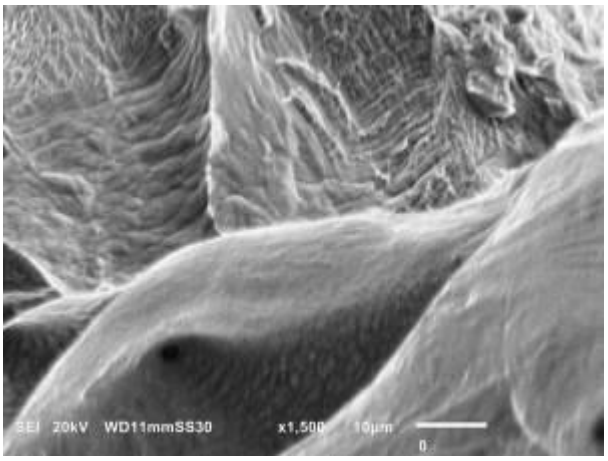

Figure 4.170: SEM micrograph of fractured charpy sample (SA - 1120 ^{0}C x 3 hrs + Age – 600 ^{0}C x 12 hrs); Original Magnification – 1500x

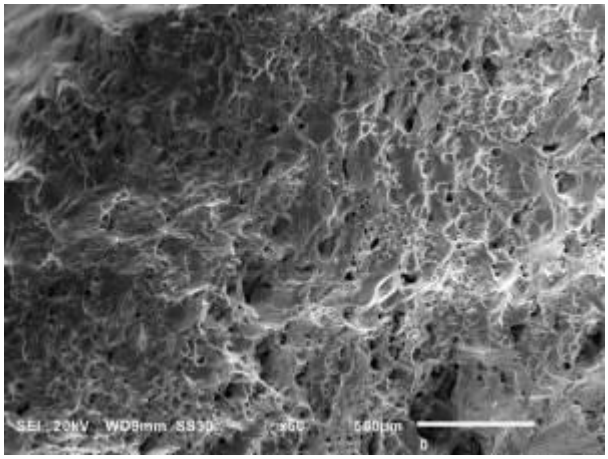

Figure 4.171: SEM micrograph of fractured stress rupture sample (SA - 1120 ^{0}C x 3 hrs + Age – 600 ^{0}C x 12 hrs); Original Magnification – 50x

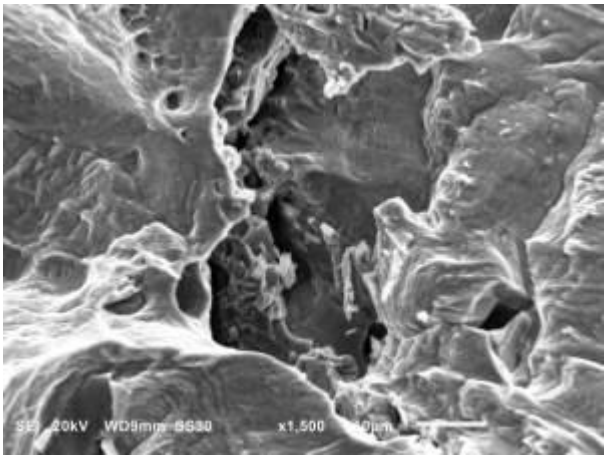

Figure 4.172: SEM micrograph of fractured stress rupture sample (SA - 1120 ^{0}C x 3 hrs + Age – 600 ^{0}C x 12 hrs); Original Magnification – 500x

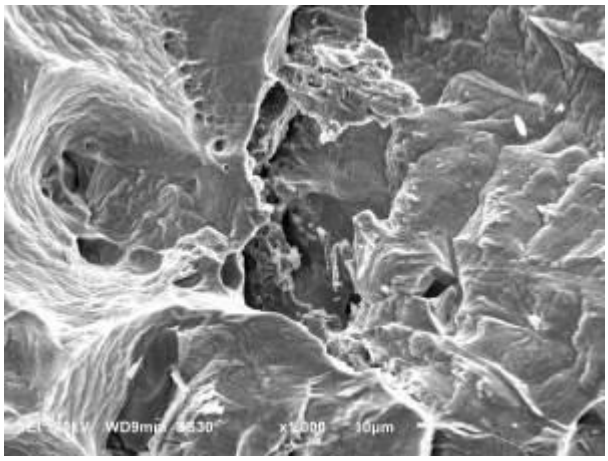

Figure 4.173: SEM micrograph of fractured stress rupture sample (SA - 1120 ^{0}C x 3 hrs + Age – 600 ^{0}C x 12 hrs); Original Magnification – 1000x

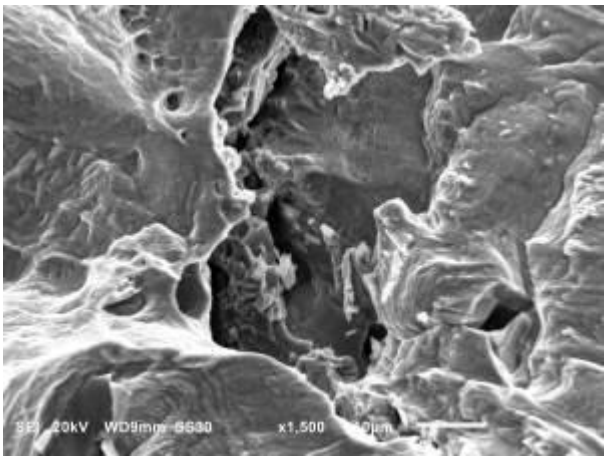

Figure 4.174: SEM micrograph of fractured stress rupture sample (SA - 1120 ^{0}C x 3 hrs + Age – 600 ^{0}C x 12 hrs); Original Magnification – 1500x

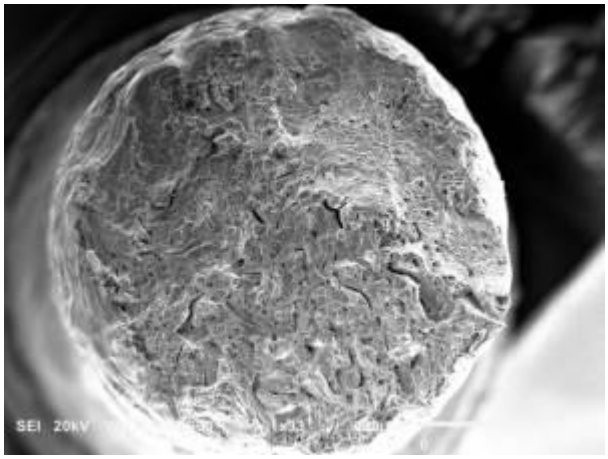

Figure 4.175: SEM micrograph of fractured tensile sample at 21 ^{0}C, (SA - 1120 ^{0}C x 3 hrs + Age – 600 ^{0}C x 4 hrs); Original Magnification – 33x

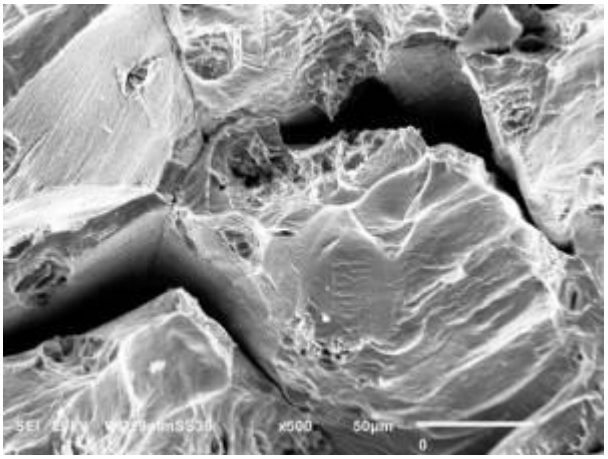

Figure 4.176: SEM micrograph of fractured tensile sample at 21 ^{0}C, (SA - 1120 ^{0}C x 3 hrs + Age – 600 ^{0}C x 4 hrs); Original Magnification – 500x

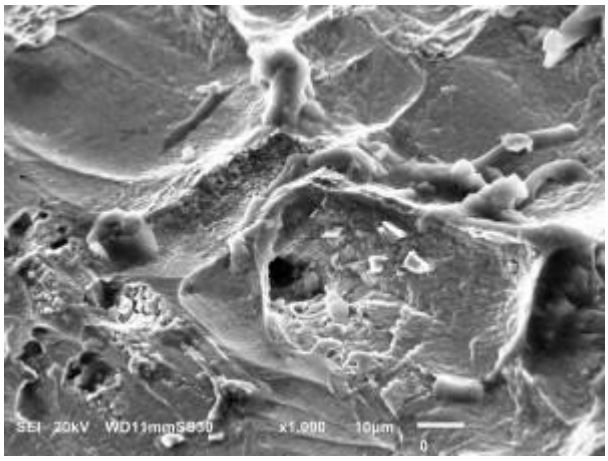

Figure 4.177: SEM micrograph of fractured tensile sample at 21 ^{0}C, (SA - 1120 ^{0}C x 3 hrs + Age – 600 ^{0}C x 4 hrs); Original Magnification – 1000x

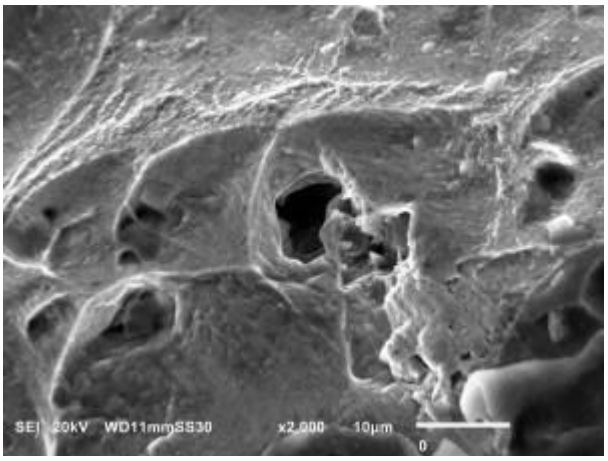

Figure 4.178: SEM micrograph of fractured tensile sample at 21 ^{0}C, (SA - 1120 ^{0}C x 3 hrs + Age – 600 ^{0}C x 4 hrs); Original Magnification – 2000x

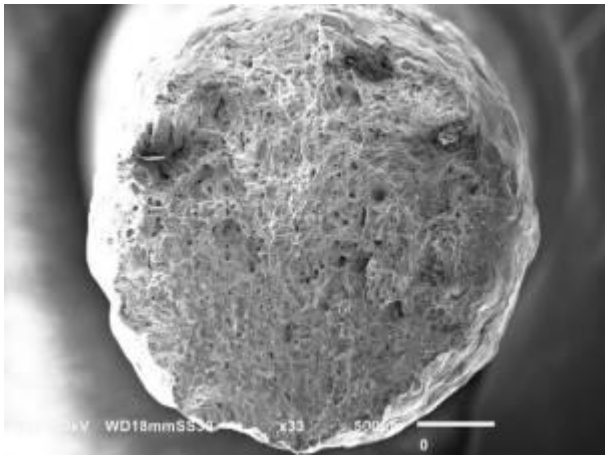

Figure 4.179: SEM micrograph of fractured tensile sample at 450 ^{0}C, (SA - 1120 ^{0}C x 3 hrs + Age – 600 ^{0}C x 4 hrs); Original Magnification – 33x

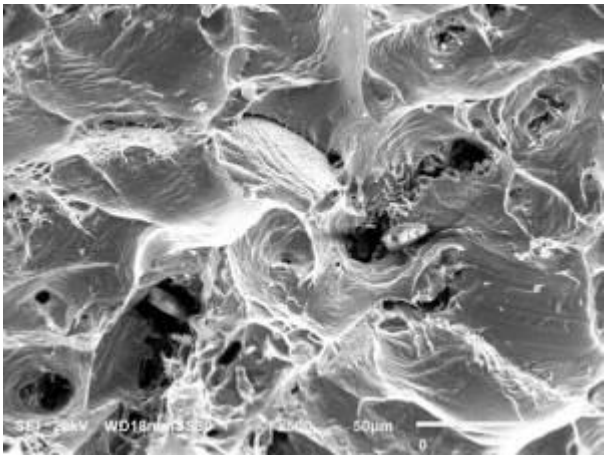

Figure 4.180: SEM micrograph of fractured tensile sample at 450 ^{0}C, (SA - 1120 ^{0}C x 3 hrs + Age – 600 ^{0}C x 4 hrs); Original Magnification – 500x

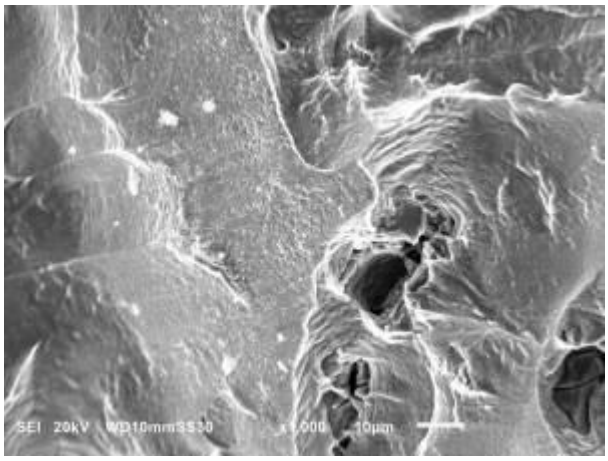

Figure 4.181: SEM micrograph of fractured tensile sample at 450 ^{0}C, (SA - 1120 ^{0}C x 3 hrs + Age – 600 ^{0}C x 4 hrs); Original Magnification – 1000x

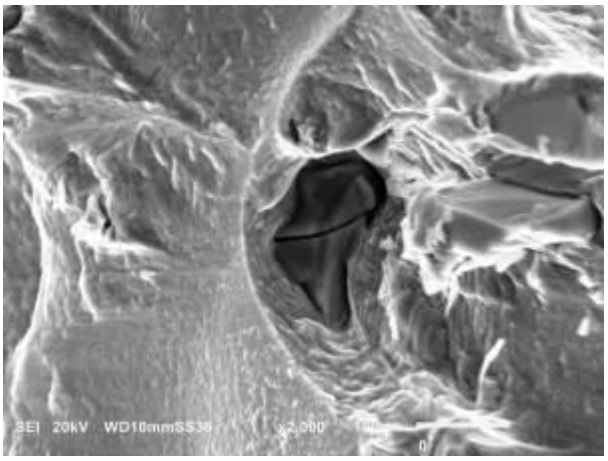

Figure 4.182: SEM micrograph of fractured tensile sample at 450 ^{0}C, (SA - 1120 ^{0}C x 3 hrs + Age – 600 ^{0}C x 4 hrs); Original Magnification – 2000x

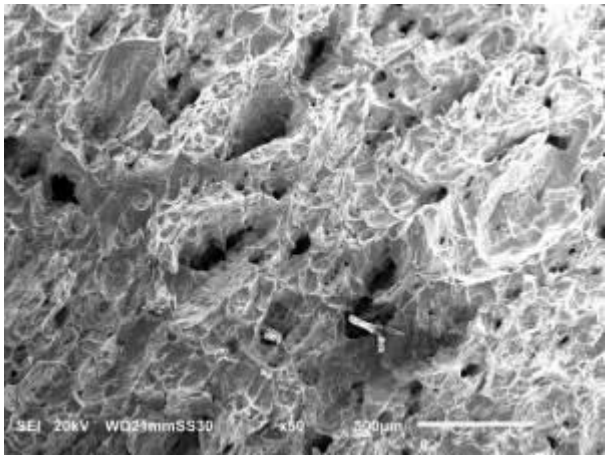

Figure 4.183: SEM micrograph of fractured charpy sample (SA - 1120 ^{0}C x 3 hrs + Age – 600 ^{0}C x 4 hrs); Original Magnification – 50x

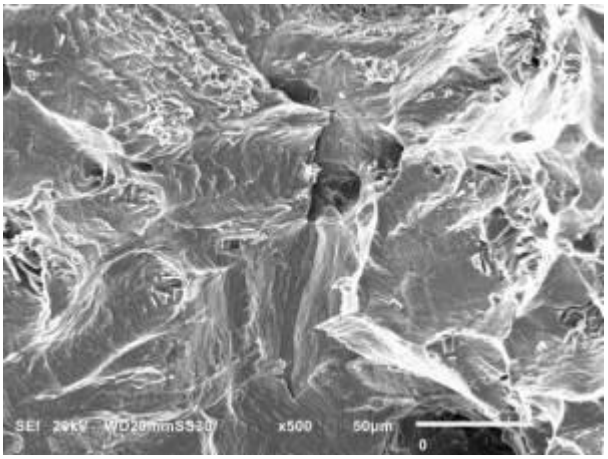

Figure 4.184: SEM micrograph of fractured charpy sample (SA - 1120 ^{0}C x 3 hrs + Age – 600 ^{0}C x 4 hrs); Original Magnification – 500x

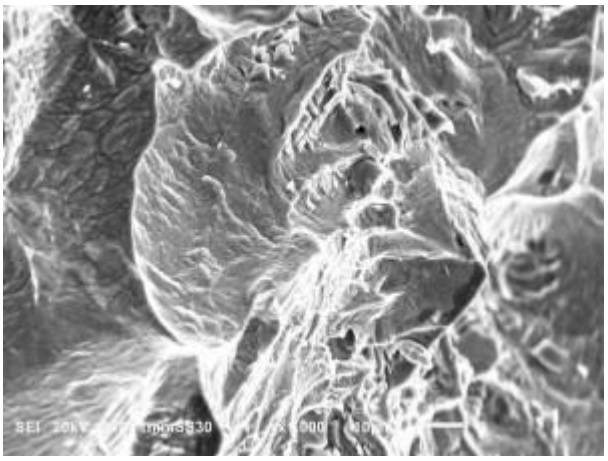

Figure 4.185: SEM micrograph of fractured charpy sample (SA - 1120 ^{0}C x 3 hrs + Age – 600 ^{0}C x 4 hrs); Original Magnification – 1000x

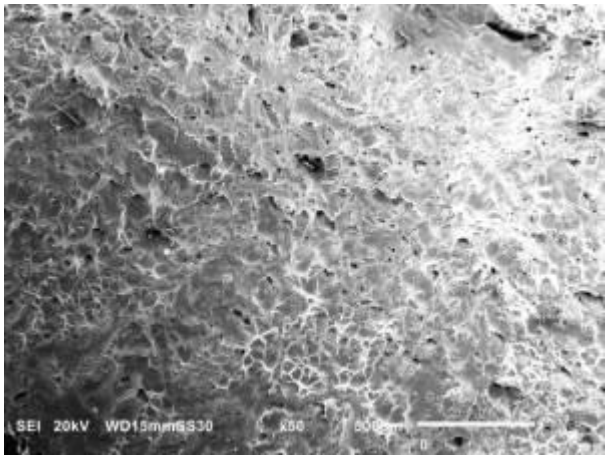

Figure 4.186: SEM micrograph of fractured stress rupture sample (SA - 1120 ^{0}C x 3 hrs + Age – 600 ^{0}C x 4 hrs); Original Magnification – 50x

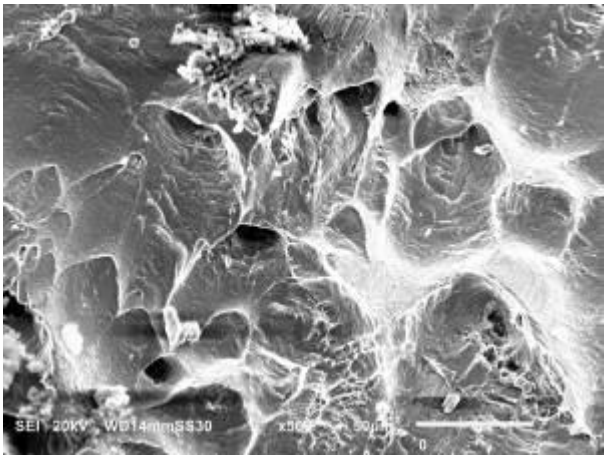

Figure 4.187: SEM micrograph of fractured stress rupture sample (SA - 1120 ^{0}C x 3 hrs + Age – 600 ^{0}C x 4 hrs); Original Magnification – 500x

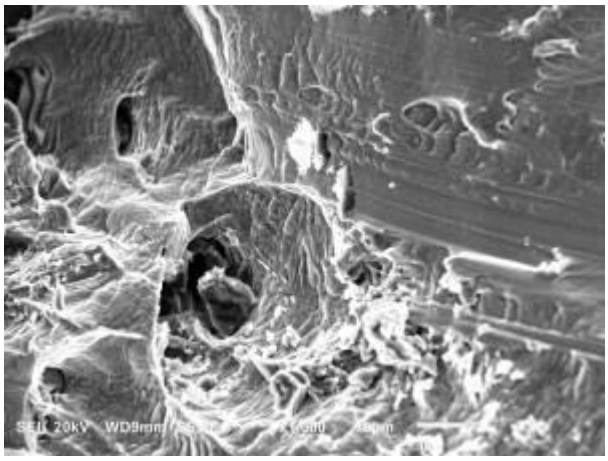

Figure 4.188: SEM micrograph of fractured stress rupture sample (SA - 1120 ^{0}C x 3 hrs + Age – 600 ^{0}C x 4 hrs); Original Magnification – 1000x

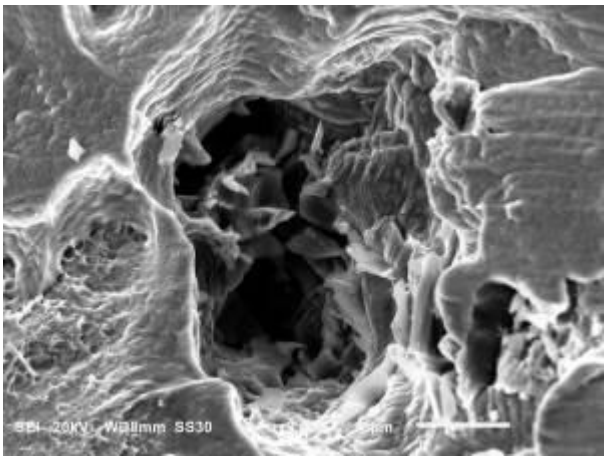

Figure 4.189: SEM micrograph of fractured stress rupture sample (SA - 1120 ^{0}C x 3 hrs + Age – 600 ^{0}C x 4 hrs); Original Magnification – 2000x

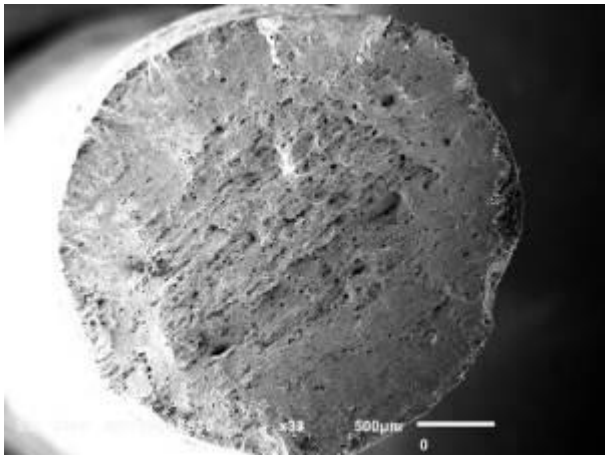

Figure 4.190: SEM micrograph of fractured tensile sample at 21 ^{0}C, (SA - 950 ^{0}C x 3 hrs + Age – 640 ^{0}C x 8 hrs); Original Magnification – 33x

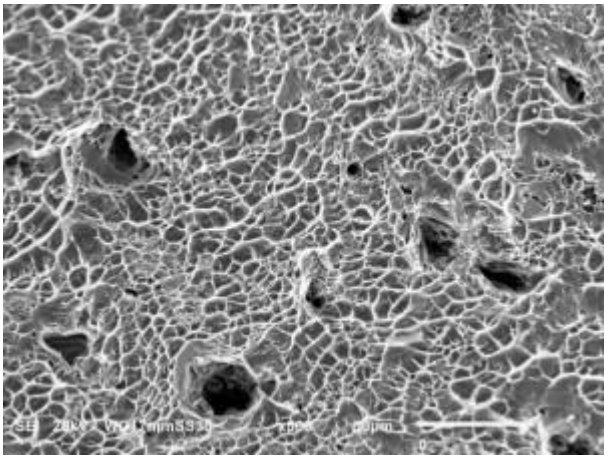

Figure 4.191: SEM micrograph of fractured tensile sample at 21 ^{0}C, (SA - 950 ^{0}C x 3 hrs + Age – 640 ^{0}C x 8 hrs); Original Magnification – 500x

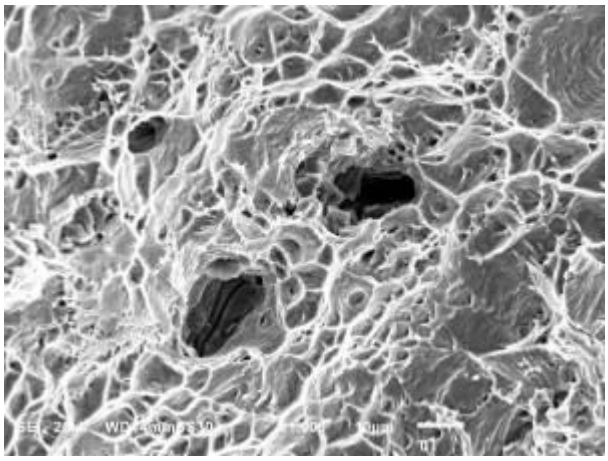

Figure 4.192: SEM micrograph of fractured tensile sample at 21 ^{0}C, (SA - 950 ^{0}C x 3 hrs + Age – 640 ^{0}C x 8 hrs); Original Magnification – 1000x

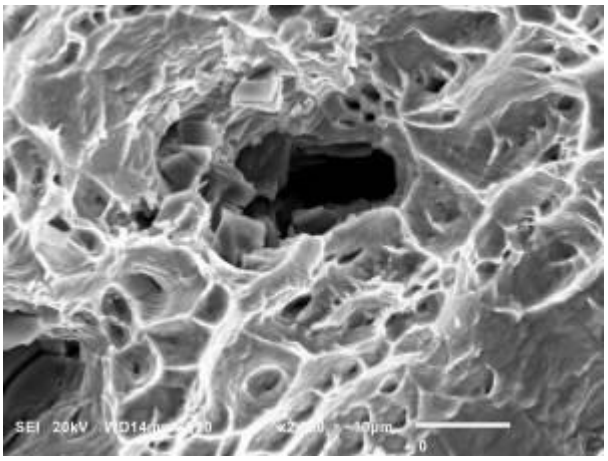

Figure 4.193: SEM micrograph of fractured tensile sample at 21 ^{0}C, (SA - 950 ^{0}C x 3 hrs + Age – 640 ^{0}C x 8 hrs); Original Magnification – 2000x

Figure 4.194: SEM micrograph of fractured tensile sample at 450 ^{0}C, (SA - 950 ^{0}C x 3 hrs + Age – 640 ^{0}C x 8 hrs); Original Magnification – 33x

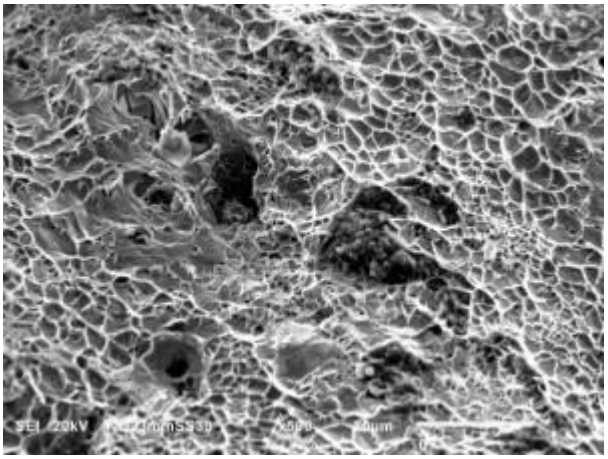

Figure 4.195: SEM micrograph of fractured tensile sample at 450 ^{0}C, (SA - 950 ^{0}C x 3 hrs + Age – 640 ^{0}C x 8 hrs); Original Magnification – 500x

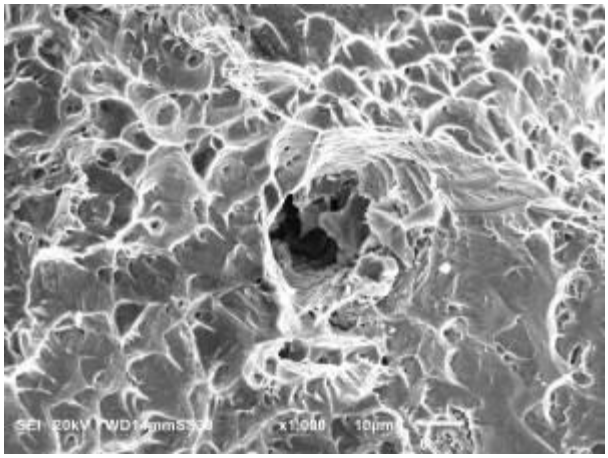

Figure 4.196: SEM micrograph of fractured tensile sample at 450 ^{0}C, (SA - 950 ^{0}C x 3 hrs + Age – 640 ^{0}C x 8 hrs); Original Magnification – 1000x

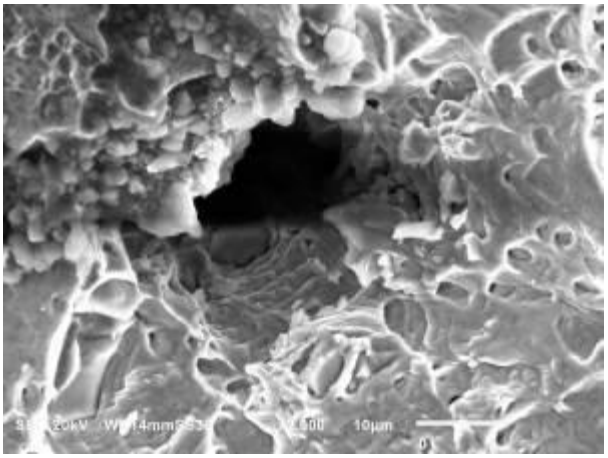

Figure 4.197: SEM micrograph of fractured tensile sample at 450 ^{0}C, (SA - 950 ^{0}C x 3 hrs + Age – 640 ^{0}C x 8 hrs); Original Magnification – 2000x

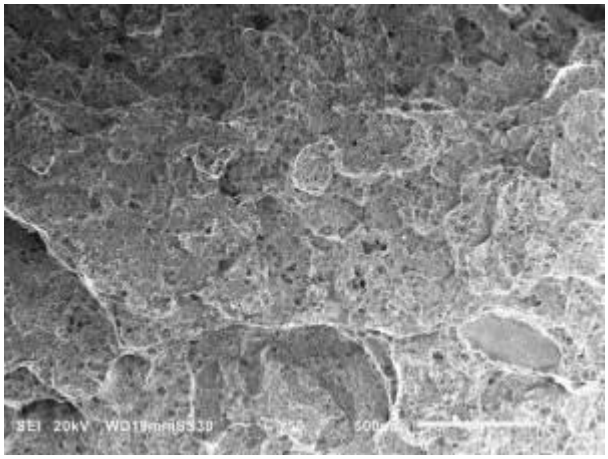

Figure 4.198: SEM micrograph of fractured charpy sample (SA - 950 ^{0}C x 3 hrs + Age – 640 ^{0}C x 8 hrs); Original Magnification – 50x

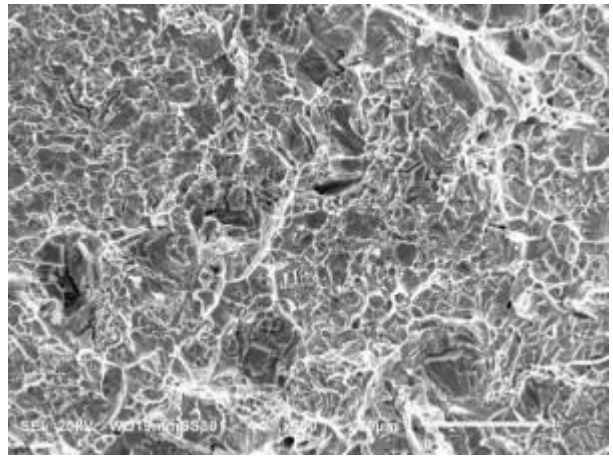

Figure 4.199: SEM micrograph of fractured charpy sample (SA - 950 ^{0}C x 3 hrs + Age – 640 ^{0}C x 8 hrs); Original Magnification – 500x

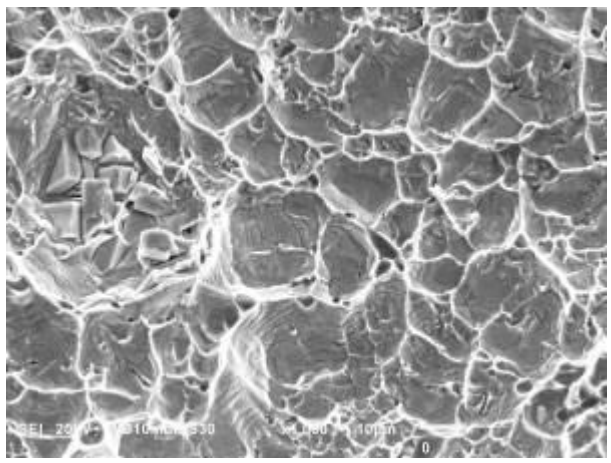

Figure 4.200: SEM micrograph of fractured charpy sample (SA - 950 ^{0}C x 3 hrs + Age – 640 ^{0}C x 8 hrs); Original Magnification – 1000x

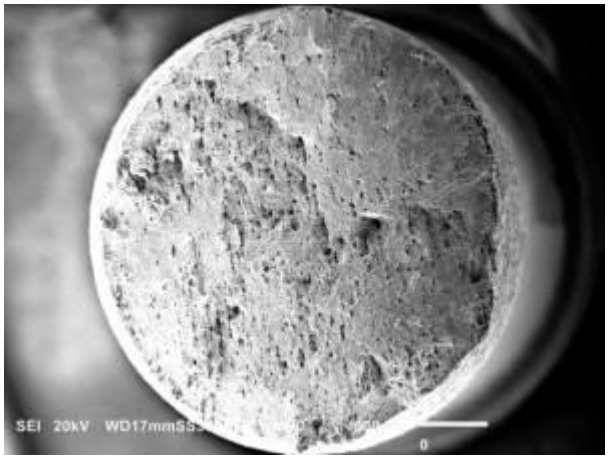

Figure 4.201: SEM micrograph of fractured tensile sample at 21 ^{0}C, (SA - 950 ^{0}C x 3 hrs + Age – 640 ^{0}C x 12 hrs); Original Magnification – 30x

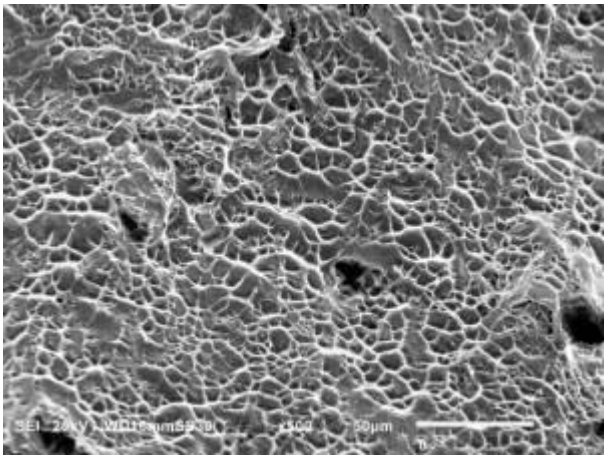

Figure 4.202: SEM micrograph of fractured tensile sample at 21 ^{0}C, (SA - 950 ^{0}C x 3 hrs + Age – 640 ^{0}C x 12 hrs); Original Magnification – 500x

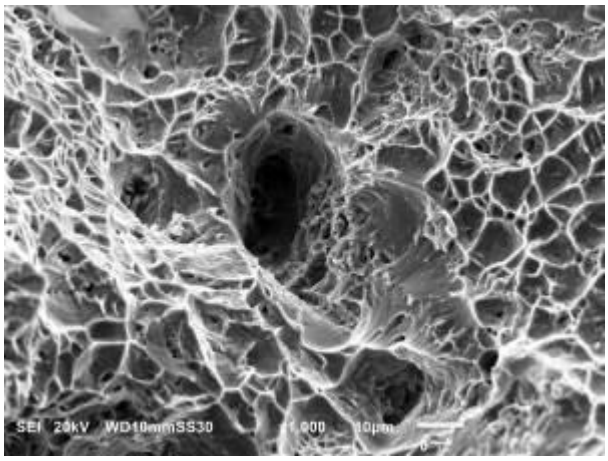

Figure 4.203: SEM micrograph of fractured tensile sample at 21 ^{0}C, (SA - 950 ^{0}C x 3 hrs + Age – 640 ^{0}C x 12 hrs); Original Magnification – 1000x

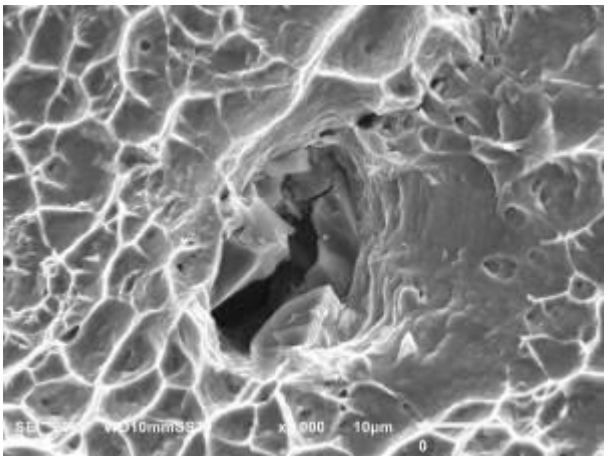

Figure 4.204: SEM micrograph of fractured tensile sample at 21 ^{0}C, (SA - 950 ^{0}C x 3 hrs + Age – 640 ^{0}C x 12 hrs); Original Magnification – 2000x

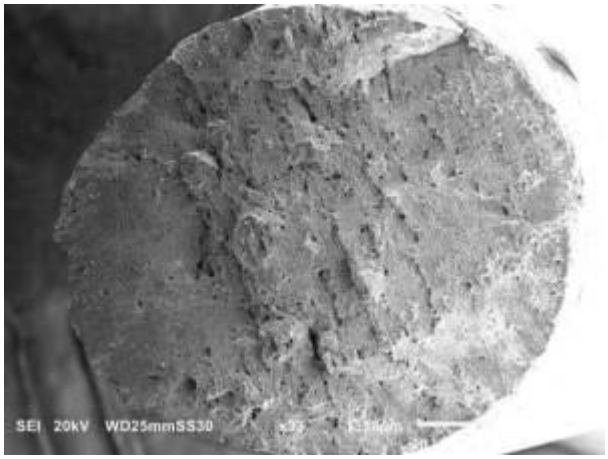

Figure 4.205: SEM micrograph of fractured tensile sample at 450 ^{0}C, (SA - 950 ^{0}C x 3 hrs + Age – 640 ^{0}C x 12 hrs); Original Magnification – 33x

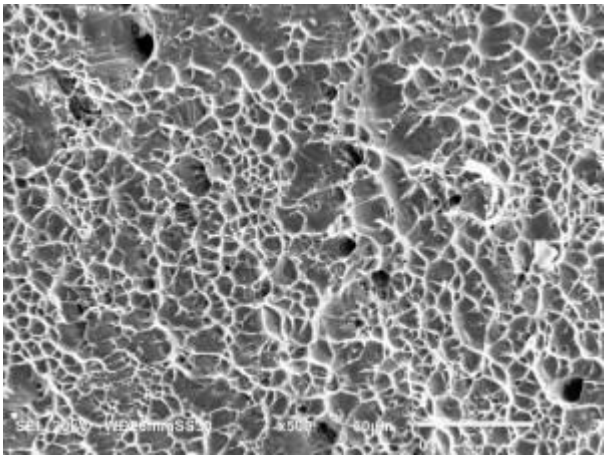

Figure 4.206: SEM micrograph of fractured tensile sample at 450 ^{0}C, (SA - 950 ^{0}C x 3 hrs + Age – 640 ^{0}C x 12 hrs); Original Magnification – 500x

Figure 4.207: SEM micrograph of fractured tensile sample at 450 ^{0}C, (SA - 950 ^{0}C x 3 hrs + Age – 640 ^{0}C x 12 hrs); Original Magnification – 1000x

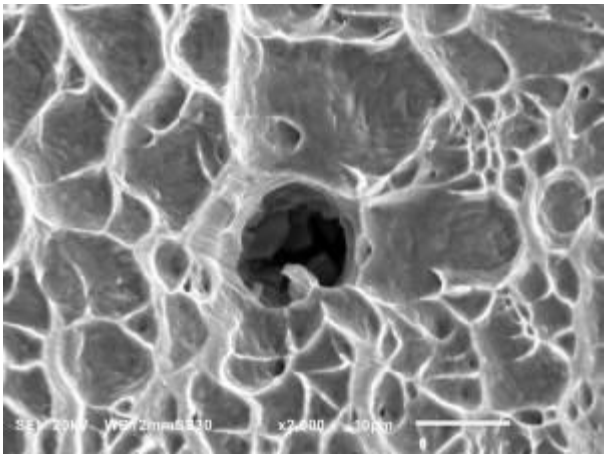

Figure 4.208: SEM micrograph of fractured tensile sample at 450 ^{0}C, (SA - 950 ^{0}C x 3 hrs + Age – 640 ^{0}C x 12 hrs); Original Magnification – 2000x

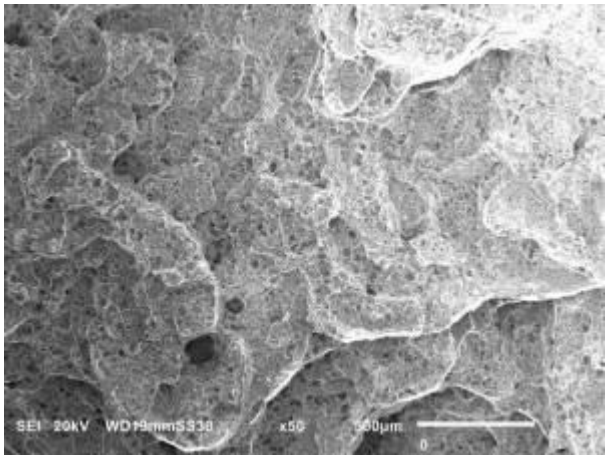

Figure 4.209: SEM micrograph of fractured charpy sample (SA - 950 ^{0}C x 3 hrs + Age – 640 ^{0}C x 12 hrs); Original Magnification – 50x

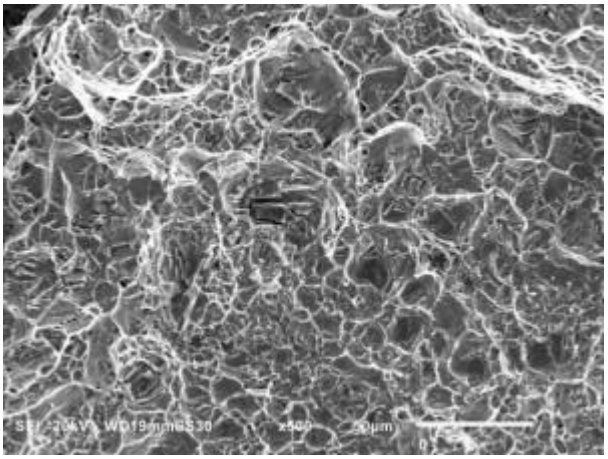

Figure 4.210: SEM micrograph of fractured charpy sample (SA - 950 ^{0}C x 3 hrs + Age – 640 ^{0}C x 12 hrs); Original Magnification – 500x

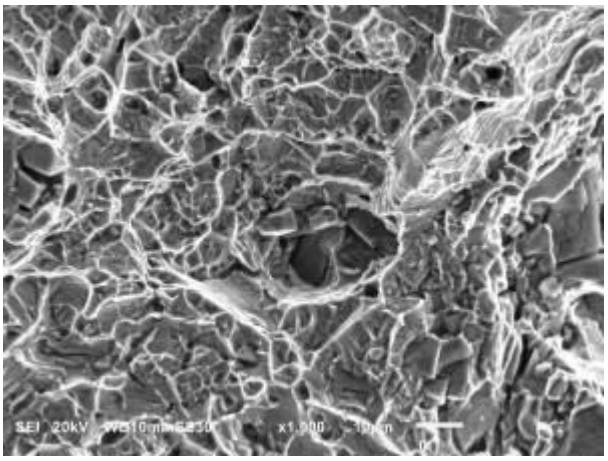

Figure 4.211: SEM micrograph of fractured charpy sample (SA - 950 ^{0}C x 3 hrs + Age – 640 ^{0}C x 12 hrs); Original Magnification – 1000x

The fracture morphology observations for the sections after heat treatments and testing are presented in Tables 4.11 and 4.12.

Table 4.11- Fracture Morphology Details for Samples in as Received Condition and after Pilot Heat Treatments

Section	**Fracture Morphology**			
	RT Tensile	**HT Tensile**	**Charpy Impact**	**Stress Rupture**
New A-286 Bar	Dimple type with microvoid coalescence	Dimple type with microvoid coalescence	Quasicleavage with microvoids	Sample did not fracture
Serviced Turbine Wheel	Dimple type with severe microvoid coalescence	Dimple type with severe microvoid coalescence	Quasicleavage with microvoids and cracks	Cleavage type with significant microvoids
PILOT SOLUTION ANNEALING (SA) HEAT TREATMENTS				
SA 750 ^{o}C x 3 hrs	Not Tested			
SA 950 ^{o}C x 3 hrs	Not Tested			
SA 1120 ^{o}C x 3 hrs	Not Tested			

Table 4.12 - Fracture Morphology Observations for Samples after Heat Treatments

Section	Fracture Morphology			
	RT Tensile	**HT Tensile**	**Charpy Impact**	**Stress Rupture**
SA 1120°C x 2hrs + Age 720°C x 16hrs	Dimple type with microvoid coalescence	Dimple type with microvoid coalescence	Quasicleavage with microvoids	Sample did not fracture
SA 950°C x 2hrs + Age 720°C x 16hrs	Dimple type with microvoid coalescence	Dimple type with microvoid coalescence	Quasicleavage with microvoids	Sample did not fracture
SA 950°C x 3hrs + Age 720°C x 16hrs	Dimple type with microvoid coalescence	Dimple type with microvoid coalescence	Quasicleavage with microvoids	Sample did not fracture
SA 1120°C x 3hrs + Age 720°C x 16hrs	Dimple type with microvoid coalescence	Dimple type with microvoid coalescence	Quasicleavage with microvoids	Sample did not fracture
SA 950°C x 3hrs + Age 600°C x 4hrs	Dimple type with microvoid coalescence	Dimple type with microvoid coalescence	Quasicleavage with microvoids	Sample did not fracture
SA 950°C x 3hrs + Age 600°C x 8hrs	Dimple type with severe microvoid coalescence	Dimple type with severe microvoid coalescence	Quasicleavage with microvoids and cracks	Sample did not fracture
SA 950°C x 3hrs + Age 600°C x 12hrs	Dimple type with microvoid coalescence	Dimple type with severe microvoid coalescence	Quasicleavage with isolated microvoids and intergranular cracks	Sample did not fracture
SA 950°C x 3hrs + Age 640°C x 4hrs	Dimple type with few microvoids	Dimple type with few isolated microvoids	Quasicleavage with isolated microvoids	Sample did not fracture
SA 950°C x 3hrs + Age 640°C x 8hrs	Dimple type with isolated microvoids	Dimple type with isolated microvoids	Quasicleavage type fracture	Sample did not fracture

Section	Fracture Morphology			
	RT Tensile	**HT Tensile**	**Charpy Impact**	**Stress Rupture**
SA 950°C x 3hrs + Age 640°C x 12hrs	Dimple type with isolated microvoids	Dimple type with isolated microvoids	Quasicleavage type fracture with intergranular cracks	Sample did not fracture
SA 1120°C x 3hrs + Age 600°C x 4hrs	Cleavage type with limited microvoids	Cleavage type with few microvoids	Cleavage with few intergranular cracks	Cleavage type with significant microvoids
SA 1120°C x 3hrs + Age 600°C x 8hrs	Cleavage type with micro cracks	Cleavage type with microcracks and voids	Cleavage type with severe intergranular cracking	Cleavage type with significant microvoids
SA 1120°C x 3hrs + Age 600°C x12hrs	Cleavage type with microvoids and cracks	Cleavage type with microvoids and cracks	Cleavage with few microvoids	Cleavage type with cracks and significant microvoids
SA 1120°C x 3hrs + Age 640°C x 4hrs	Cleavage type with micro cracks	Cleavage type with voids	Cleavage type with cracks and voids	Sample did not fracture
SA 1120°C x 3hrs + Age 640°C x 4hrs	Cleavage type with micro voids	Cleavage type with micro voids	Cleavage type with intergranular cracks and voids	Sample did not fracture
SA 1120°C x 3hrs + Age 640°C x 12hrs	Cleavage type with micro voids and crack	Cleavage type with isolated micro voids	Cleavage type with intergranular cracks and voids	Sample did not fracture

In general, most of the fractured surfaces examined reveals cleavage and dimple type of fracture morphology. The cleavage type of morphology is typical for brittle fractures and dimple type of fracture is typical for ductile fractures.

The fractured surfaces of the tensile and Charpy specimens, exhibits dimpled and quasi-cleavage fracture morphology respectively. While, the tensile fractured samples predominately exhibits dimpled fracture, the Charpy fractured surfaces exhibited a mixed mode of dimple and cleavage.

4.12 LABORATORY TEST REPORTS

The typical laboratory test reports for chemical composition, room temperature and high temperature tensile test, charpy impact test and stress rupture test are given in Appendix 1.

CHAPTER 5

DISCUSSION

The primary objective of this research was to study the feasibility of increasing the life span of the serviced turbine A-286 wheel by heat treatment. As a part of this research, several experiments were conducted on the serviced turbine wheel. These experiments consisted of various heat treatments with varying temperatures and soaking times to rejuvenate the microstructure and restoring the mechanical properties, and thereby increasing the life span. This chapter in particular covers the history and background of the serviced turbine wheel, and discusses at length the results and observations of the conducted experiments.

5.1 BACKGROUND OF THE A-286 TURBINE WHEEL

The turbine wheel on which this research was conducted, was received at Masaood John Brown, Dubai workshop for detailed inspection.

The turbine unit details and the operating history of the wheel are tabulated in Table 5.1

Table 5.1- Operating History of the A-286 Turbine Wheel

Turbine Wheel	Frame 5002, Gas Turbine
Unit Number	24KT101
Fuel Fired	Gas
Material	A-286 (Cr 14.8%, Ni: 25.1%, Mo: 1.3%, Ti: 2.4%, Mn: 1.2%)
Operating Temperature	450 to 560^{0}C
Revolutions per Minute (RPM)	4,670
Starts and Stops	Not Available
Running Hours	233,111
Wheel Dimensions	Outer Diameter (OD) - 48.05” Thickness – 14.5”

As a part of inspection, non-destructive testing such as XRF, Eddy current test, Ultrasonic flaw detection and Replica metallography were performed on the wheel to assess the condition after 233,111hrs of operation. The XRF analysis revealed that the material of the wheel was A-286 having composition of Cr 14.8%, Ni: 25.1%, Mo: 1.3%, Ti: 2.4%, Mn: 1.2%. The eddy current and ultrasonic flaw testing are widely accepted industrial practices to detect cracks [218]. We have applied these techniques on the as received serviced turbine wheel. The Eddy current inspection was performed to check for any surface cracking, and the ultrasonic flaw detection was performed to check for any internal flaws/defects. Eddy current and ultrasonic flaw detection performed on

the wheel did not reveal any flaws. Replica metallography, a widely accepted non-destructive technique to assess the life of aged components was performed on the turbine wheel in the assembled condition at four different locations to examine the microstructure [219]. The replica locations are shown in Figures 5.1 and 5.2.

Figure 5.1: Replication Locations at Dove Tail areas shown by arrows

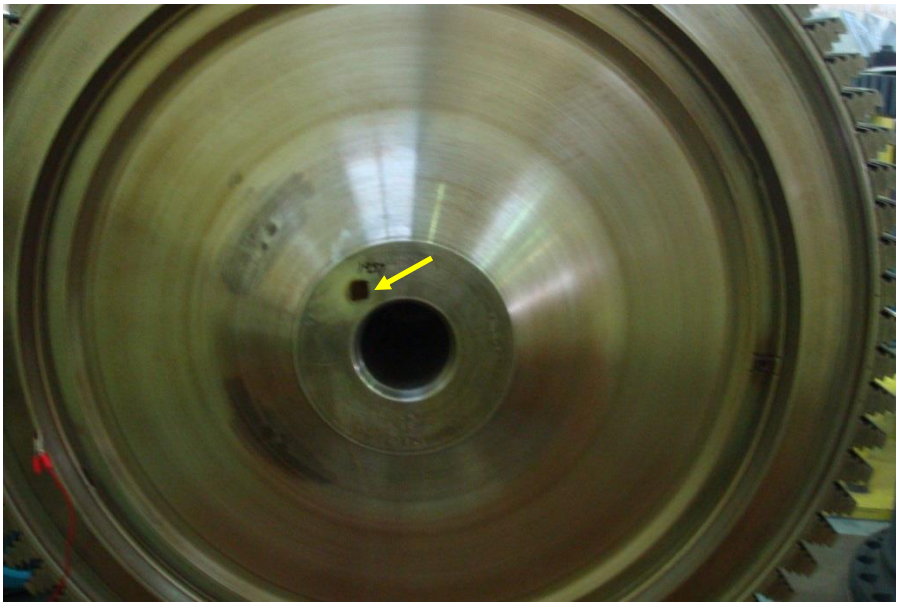

Figure 5.2: Replication Location at the Bore area shown by arrow

The replica evaluation of the A-286 turbine wheel at the dovetail area and the bore area revealed significant amounts of carbide precipitation, primarily along the grain boundaries. The representative optical microscope micrographs and scanning electron micrograph showing carbide precipitation are shown in Figure 5.3 and Figure 5.4

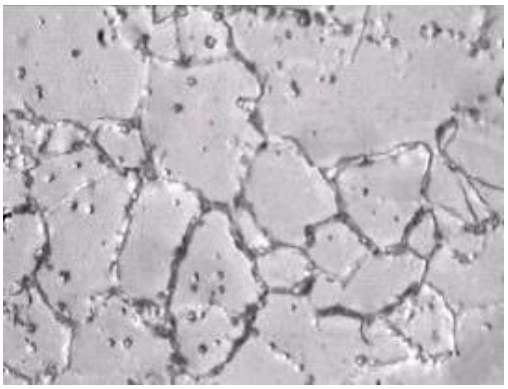

Figure 5.3: Micrograph of the replica at bore area showing carbide precipitation; Original Magnification – 500x

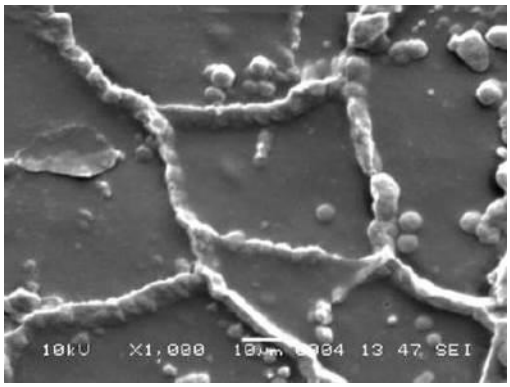

Figure 5.4: SEM micrograph of replica at the dove tail area showing significant carbide precipitation; Original Magnification – 1000x

As described earlier that carbide dissolution is possible for gas turbine components with a proper solution annealing heat treatment [101-103, 109], a portion of this wheel was retained for the purpose of this research, i.e., to check the feasibility of extending the life span of A-286 wheel.

5.2 STRESS MAPPING OF THE A-286 TURBINE WHEEL

The turbine wheel in general, rotates at a speed of 4.670 rpm in the hot zone of the turbine. Here, the turbine wheel experiences combination of loads such as surface loads, centrifugal loads and thermal loads. The surface loads acting on the turbine wheel were due to the forces resulting from the flowing of hot gases on to the surfaces of the blades. The centrifugal load on the turbine wheel is the most

critical load acting on the turbine wheel, as it can lead to deformation of the wheel. Centrifugal loads are due to the mass of the rotating disc and the turbine buckets fixed on the wheel. It is important to know that centrifugal stresses play a critical role in the turbine wheel. The distribution of centrifugal stresses across the turbine wheel should be uniform, else there are chances of bending or deflection, overloading and ultimately fracture of the turbine wheel. It was thus important to understand the stresses acting on the turbine wheel at various locations. The turbine wheel is manufactured by forging and due to the dimensional complexity of the turbine wheel, the stress distribution pattern in the wheel can vary. Through finite element analysis, it was evident that the highest stress was at the bore area (450 MPa) and at the radius areas of dovetail. High stress as expected in the bore area and radius areas of dovetail can be attributed to the forging process and temperature excursions in service. The same pattern of stress distribution can be co-related with the earlier studies performed by others [220-222].

5.3 CHEMICAL COMPOSITION

Historically, the A-286 alloy was known as modified austenitic stainless steel. With the changing times, the A-286 alloy is now called as iron-nickel based super alloy. The A-286 alloy contains major alloying elements such as Nickel (24-27%), Chromium (13.5–16%), Molybdenum (1-1.5%) and Titanium (1.9-2.35%), Vanadium (0.1-0.5%), Aluminum (0.35% maximum), Silicon (1% maximum) [223]. It is therefore important to understand the role of each alloying element in this alloy.

The carbon in the A-286 alloys is present to a maximum extent of 0.08 weight percentage. In the steel making process, iron combines with carbon and increases the hardness and strength. The variations in carbon composition renders a range of hardness and strength to the A-286 alloy. However, a very high carbon is not desired as this will form detrimental carbides, which in turn will affect the strength of the A-286 alloy.

The manganese in the A-286 alloys is present to maximum of 2.0 weight percentage. The presence of manganese improves the hot working properties and increases the strength, toughness and hardenability. Besides, manganese also stabilizes the austenite phase.

The chromium content in the A-286 alloys is in the range of 13.5 to 16.0 weight percentage. The chromium increases the resistance to oxidation at high temperatures. Additionally, chromium also imparts corrosion resistance, as it forms a self-repairing passive layer of chromium oxide on the surface. However, chromium combines with carbon to form carbides.

The nickel in the A-286 alloy is present in the range of 24.0 to 27.0 weight percentage. Nickel is an austenite phase former and stabilizes the austenite phase. Thus, addition of nickel increases the toughness, impact strength at high and low temperatures. Nickel also imparts high temperature oxidation and corrosion resistance.

The molybdenum in the A-286 alloy is present in the range of 1.0 to 1.5 weight percentage. Molybdenum in the presence of chromium and nickel imparts

resistance to high temperature corrosion and oxidation. It is thus beneficial as it adds to the strength of the A-286 alloy.

The titanium in the A-286 alloy is in the range of 1.9 to 2.35 weight percentage. The titanium stabilizes the carbides in the A-286 alloy. Titanium also combines with carbon to form hard carbides, which are difficult to dissolve in a solid solution matrix. It also increases the intergranular corrosion resistance and prevents cracking due to excessive chromium carbides.

The vanadium in the A-286 alloy is in the range of 0.1 to 0.5 weight percentage. Though the addition of vanadium is only to a small extent, it however contributes in strengthening the alloy. The addition of vanadium also resists the grain growth at high temperatures as it refines the grains.

Aluminum is present in the A-286 alloy to a maximum extent of 0.35 weight percentage. Aluminum enhances the high temperature corrosion/oxidation resistance, and is responsible for strengthening the core matrix to good extent. Aluminum also helps in re-precipitation of the carbides during the age hardening process, and in controlling the inherent grain size.

Finally, silicon is present in the A-286 alloy to maximum extent of 1.0 weight percentage. It is primarily a de-oxidizing agent used during manufacturing process. It is useful as it further contributes to the strengthening of the A-286 alloy. The silicon content was 0.17% and it enhances the tensile strength of this particular alloy [224].

The chemical composition of the new A-286 bar and the serviced turbine were in accordance to the standard A-286 alloy. It was found that the major alloying

elements such as nickel, chromium, molybdenum, and titanium were in the specified limits of an A-286 alloy. The minor alloying elements such as Aluminum, Vanadium and Silicon are as well in the specified limits of an A-286 alloy. Thus, it was confirmed that the purchased new forged bar and the serviced turbine wheel were made of A-286 alloy.

5.4 PORTABLE HARDNESS SURVEY

The portable hardness survey, performed on the dissected wheel section of the serviced turbine wheel did not reveal any significant difference throughout the wheel. In general, the hardness on the wheel was in the range of 314 to 334 HV. The hardness levels were found to be consistent with a typical A-286 serviced wheel after solution annealing and age hardening. The slight variation in the hardness levels is attributed to the variations in carbide distribution across the wheel. The A-286 serviced turbine wheel contains chromium rich and titanium rich carbides. The hardness may vary depending on the type of carbide distribution within the wheel. These carbides have different hardness due to the respective elements in that particular carbide phase. The co-relation of hardness with respect to carbide distribution has been studied earlier [225, 226].

The hardness throughout the wheel is likely to vary from manufacturing stage itself due to dimensional configuration of the wheel. With ageing of the wheel in service, there is possibility of significant hardness variation within the wheel material. In case, hardness in particular area on the wheel displays significant variations, than that particular area of the wheel would need a critical

examination. Therefore, the portable hardness survey forms a strong base for further destructive testing.

5.5 MICROSTRUCTURES OF NEW A-286 BAR AND SERVICED TURBINE WHEEL

The microstructure of the new A-286 bar was used as a reference for comparison after the heat treatments.

In order to get an idea of the initial microstructure by the chemical constituents, the Schaeffler Diagram was used. The Schaeffler diagram represents the effect of the composition of the alloy and proportion of two elements on the microstructure after heat treatments [227]. The Schaeffler diagram for an A-286 alloy is shown in Figure 5.5.

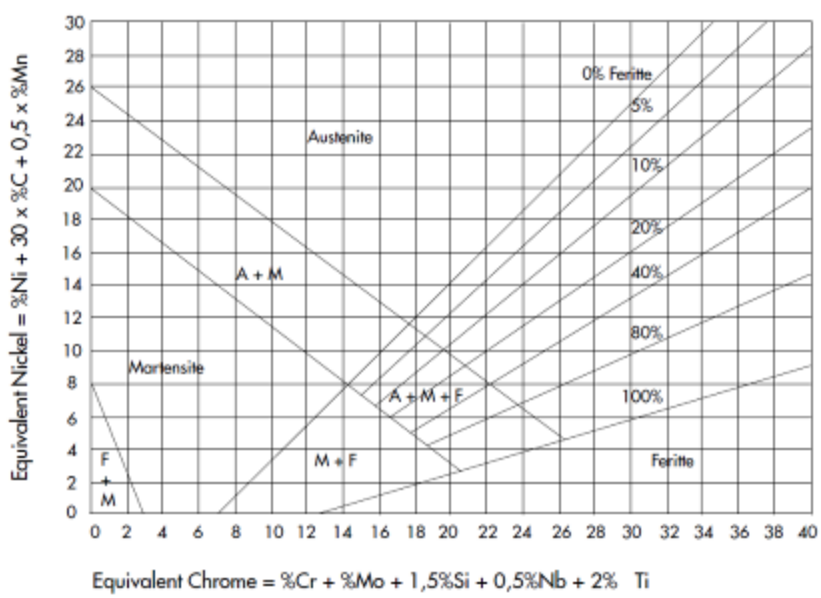

Figure 5.5: Schaeffler diagram for A-286 alloy

This particular Schaeffler diagram displays the limits of phases such as austenite, ferrite and martensite in relation to the chromium and nickel equivalent. The chromium and nickel equivalent is calculated by the equations below:

- Cr equivalent = (Cr)+2(Si)+1.5(Mo)+5(V)+5.5(Al)+1.75(Nb)+1.5(Ti)+0.75(W)
- Ni equivalent = (Ni)+(Co)+0.5(Mn)+0.3(Cu)+25(N)+30(C)

All the elements quoted are in weight percentages. The Schaeffler diagram does not determine the composition and volume of the carbide phase [228]. The chromium equivalent for an A-286 alloy material was 20.15% and the nickel equivalent was 29.40%. Thus with the aid of the Schaeffler diagram, the microstructure of the A-286 material was found to be wholly austenitic.

The microstructure of the new A-286 bar displayed austenite grains, with grain sizes in the range of 6-7. No carbide precipitation was observed. The microstructure of the serviced turbine wheel also displayed austenite grains, with grain sizes in the range of 4-5. Significant amount of carbide precipitation was evident along the grain boundaries and within the grains. In comparison to the new bar microstructure, which resembles to the microstructure of new wheel, the serviced turbine wheel displayed the following:

- Change in grain size
- Carbide precipitation within and along the grain boundaries

The carbides mapped by EDAX were of type $M_{23}C_6$, M_6C and MC. These carbides were rich in chromium and titanium. During the long-term service exposure, the primary carbides (MC) rich in titanium were reduced to secondary carbides such as $M_{23}C_6$ and M_6C.

5.6 HEAT TREATMENTS AND ROLE OF CARBIDES

The microstructure of the new A-286 turbine wheel consists of austenite grains with dissolved carbides of MC, M_6C, and $M_{23}C_6$ type and other phases within the grains and along the grain boundaries. In the representation of carbides, M represents the particular alloying element and C represents the carbon. The formation of cellular eta (η) phase is also likely to occur at higher temperatures.

In the A-286 serviced turbine wheel material, MC carbide is of predominantly titanium carbide (TiC). This type of carbide exists over a wide range of titanium within the material. The MC or TiC carbide is a globular, irregularly shaped particle, which appears grayish in color when examined under an optical microscope. These carbides normally form during the solidification processes. The MC type carbides generally are script like or blocky type in appearance and primarily form at the grain boundaries [229]. The composition of the MC carbide and its morphology depends on the solidification rate of the alloy during production.

The M_6C carbides primarily contain heavy elements such as molybdenum and tungsten, although there is some solubility for chromium, nickel, and cobalt. The M_6C type of carbides are stable at high temperatures and could be present in the as cast condition. Under the optical microscope, these carbides have no distinguished characteristics and are randomly distributed in the matrix of the as-cast alloys. M_6C type of carbides have a complex cubic structure, and usually form when the high concentration of refractory metal is present in the alloy. These

carbides may form at high temperature as discrete particles or they may also form by the reaction of MC carbides with the alloy matrix [230].

$M_{23}C_6$ are primarily rich in chromium. M represents primarily chromium, but may also contain nickel, molybdenum or iron. $M_{23}C_6$ type of carbides are known as low temperature form of carbides and these types of carbides primarily form at the grain boundaries. $M_{23}C_6$ type of carbides are dissolved in the solid solution matrix above 950^0C, but the temperature range of its existence varies with the alloy. At high temperature solution annealing, the carbon in the carbide dissolves in the solution, but is re-deposited at the grain boundaries at lower temperatures. The precipitated $M_{23}C_6$ carbides at the grain boundaries impart embrittlement and low ductility to the alloy. There are several studies, which conclude that the precipitation of $M_{23}C_6$ at the grain boundaries lowers the ductility and can lead to creep-fatigue cracking of the material. $M_{23}C_6$ can precipitate as films, globules, platelets, lamellae, and as cellular growth. The globular form of $M_{23}C_6$ is generally thought to be the "least undesirable" form as this imparts more ductility by reducing the length of micro cracking at the grain boundaries. Studies also revealed that the globular or blocky form of $M_{23}C_6$ carbides can improve stress rupture life, but the continuous precipitated films of carbides along the grain boundaries cause embrittlement resulting in cracking along the grain boundaries [231-233]. This cracking over a period of time can result in catastrophic failure of the turbine wheel. The formation of massive carbides and un-desirable phases such as $M_{23}C_6$ reduce the mechanical properties of the turbine wheel.

The heat treatment cycles consisted of solution annealing and ageing to dissolve the grain boundary carbides, the cellular eta (η) phase and to re-precipitate the carbides respectively to strengthen the mechanical properties of the wheel. The schematics in terms of microstructure and the effect of rejuvenation heat treatment is shown in Figure 5.6.

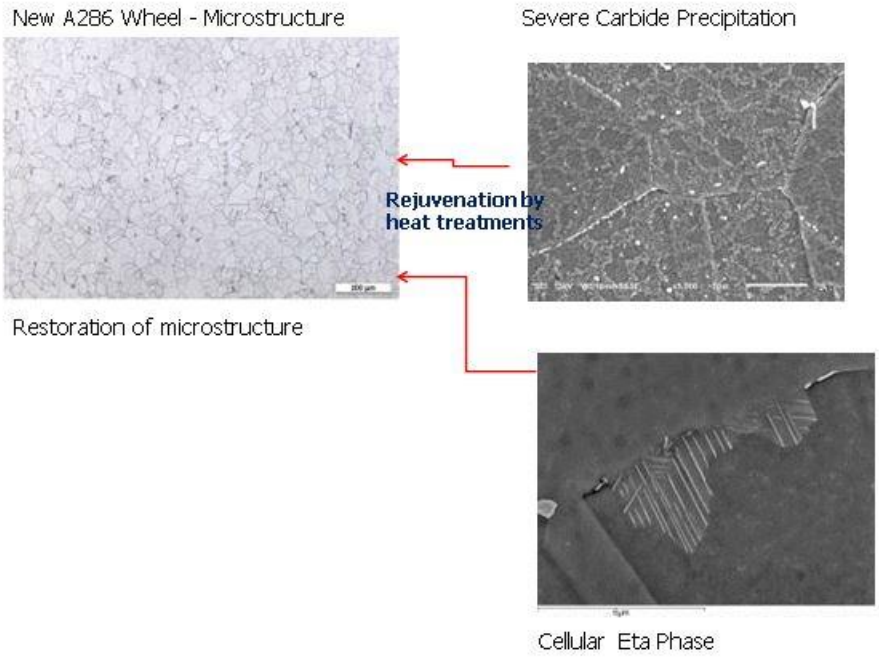

Figure 5.6: Schematic showing the carbides and restoration of microstructure after reujenation heat treatment in A-286 alloy

The solution annealing heat treatment takes the precipitated carbide back in the solution matrix. Solution annealing involves heating the material in a furnace at the specified solution annealing temperature for some hours followed by rapid quenching. Once the material is heated to a high temperature and soaked at that particular temperature, the precipitated carbides tend to dissolve in the solution

matrix. With rapid cooling, there is no chance for the carbides to precipitate, and thus the carbides remain dissolved in the solid solution matrix [234].

The initial pilot solution annealing heat treatments, at 950 ^{0}C and 1120 ^{0}C followed by rapid cooling dissolved the precipitated grain boundary carbides in the solid solution matrix. These particular solution annealing temperatures were high enough to increase the solubility of carbon in the austenite phase matrix.

The microstructures examined after solution annealing heat treatments at temperatures of 950 ^{0}C and 1120 ^{0}C exhibited carbide dissolution, but with varying differences in un-dissolved carbides with respect to the soaking period. The soaking time plays a major role in dissolution of carbides at that respective temperature. Increase in soaking period provides more time for dissolution of carbon in the austenite phase, thus leads to complete dissolution of carbides. The solution annealing at 950 ^{0}C with a soak period of 3 hours resulted in a complete carbide dissolution as compared to the solution annealing at 950 ^{0}C with a soak period of 2 hours with fine recrystallized austenite grains. The solution annealing at 1120 ^{0}C with a soak period of 2 and 3 hours resulted in complete carbide dissolution, but resulted in coarse grains. The grain size with 950 ^{0}C solution annealing was observed to be in range of 5-6 (ASTM grain size) and with 1120 ^{0}C solution annealing was observed to be in range of 1-2 (ASTM grain size). The higher solution annealing temperature leads to increase in grain size. This is due to the crystal growth, which is a part of annealing process. As the annealing temperature increases, the larger grains become bigger at the expense of smaller grains, by Oswald ripening mechanism.

Primarily it is a function of the surface area to volume ratio. In a material, the crystals will occur in varying size from very small to very large. Surface area to volume ratio will be high for the smallest crystal. As their surface area is high, it is possible that they will dissolve (melt) with increasing temperature. The dissolved mass then gradually deposited on the remaining crystals in the matrix, which are initially bigger. The larger crystals grow further at the expense of the small crystals, which keep on getting smaller (or disappearing altogether). This is how the grain growth occurs in the material with increase in solution annealing temperatures.

The solution annealing heat treatment at 950 ^{0}C dissolved the carbides and retained the required grain size of 5 -6. This can be attributed to the solubility of the carbon in the austenite matrix at 950 ^{0}C.

Age hardening is the process of precipitating coherent precipitates from a supersaturated solid solution. The prime intention in age hardening is to nucleate maximum precipitates and at the same time, avoid them from growing. The precipitates that are formed inhibit the movement of dislocations or defects in the metals crystal lattice. At the particular ageing temperature, the metal is soaked for several hours for the precipitation to occur hence, the process is called age hardening. Tensile strength and yield strength of the material are increased by the age hardening process; this increase in strength is governed by the formation of small precipitates during ageing.

The age hardening treatment with variation in temperatures from 600 ^{0}C to 640 ^{0}C and with varying soak periods of 4, 8 and 12 hours resulted in non-uniform re-

precipitation of the carbides, which is undesirable for the A-286 wheel material. The age hardening performed at 720 ^{0}C for 16 hours resulted in uniform amount of re-precipitation, which is desirable for enhancing the properties of the A-286 wheel alloy.

5.7 MECHANICAL PROPERTIES

Mechanical properties such as tensile strength, yield strength, percentage elongation and hardness are affected by the heat treatments. During heat treatments, changes in temperature and soaking period can also have an adverse effect on the mechanical properties. This is due to the changes in microstructure such as grain size and carbide dissolution [235, 236]. This is because of the movement and interaction of the dislocations along the grain boundaries. The grain boundaries obstruct the movement and gliding of dislocations along the slip planes. This results in piling up of dislocations at the grain boundaries, as they move along the same slip plane.. As the number of dislocations increase along the grain boundaries, the stress on the grain boundaries also increases. Dislocations piling will be more in the coarse or larger grains. In general, a fine grain size of the material imparts good mechanical properties, as the yield strength will increase if the grains are fine [237, 238].

The lower tensile strength and hardness after solution annealing at 1120 ^{0}C can be attributed to coarse grain microstructure. The increase in tensile and yield strength after solution annealing from 950 ^{0}C is attributed to the finer grain size.

The gamma prime (γ′) precipitate after age hardening also affects the mechanical properties such as tensile strength and yield strength. It was evident that age hardening from temperatures 600 ^{0}C to 640 ^{0}C with varying soak periods of 4, 8 and 12 hours resulted in non-uniform re-precipitation of the carbides. This leads to lower tensile and yield strength, as compared to the required strength of the new A-286 bar. The age hardening performed at 720 ^{0}C for 16 hours resulted in uniform and sufficient re-precipitation, thus increasing the tensile and yield strength of the serviced wheel, as close to that of new A-286 bar.

The room temperature ultimate tensile strength for the as new A-286 bar was 1098 MPa and the yield strength was 769 MPa. Similarly, at 450 ^{0}C the ultimate tensile strength of new A-286 bar was 937 MPa and yield strength was 690 MPa. The percentage elongation and reduction in area for the new A-286 bar at room temperature was 23.6% and 39.3% respectively. At 450 ^{0}C, the percentage elongation for new A-286 bar was 17.5% and the reduction in area was 45.4%. From this, it was quite evident that tensile properties of the new A-286 bar, which resemble the new A-286 turbine wheel, were superior at both room and at high temperatures. This fairly high ductility of new A-286 bar at 450 ^{0}C indicates that the as manufactured turbine wheel (resembling new A-286 bar) has good ductility at 450 ^{0}C.

The room temperature ultimate tensile strength for the serviced wheel was 950 MPa and the yield strength was 695 MPa. Similarly, at 450 ^{o}C the ultimate tensile strength of serviced wheel was 862 MPa and yield strength was 566 MPa.

The percentage elongation and reduction in area for the serviced turbine wheel were 10.8% and 13.7% respectively at room temperature. At 450 ^{0}C, the percentage elongation for serviced turbine wheel was 4.5% and the reduction in area was 18.8%. It is clear that the tensile strength for serviced wheel has not significantly degraded at room temperature and at high temperatures. The reduction has occurred primarily in ductility for the serviced turbine wheel at room temperature and even at high temperature, as it is evident that percentage elongation is less. A comparison of the tensile properties with the new A-286 bar suggests that the tensile strength and yield strength is moderately low, but the percentage elongation, meaning room temperature ductility and high temperature ductility is quite low. This reduction is attributed to the grain size variation and the carbide precipitation in service. The acicular type carbides M_6C, $M_{23}C_6$ and carbide envelopes/chain will lead to decrease in ductility of turbine wheel. The effect of carbide precipitation on ductility in similar alloy has been studied by other researchers [239]. Solution annealing at 1120 ^{0}C resulted in coarse grains, which resulted in lower tensile strength and hardness as compared to solution annealed samples at 950 ^{0}C.

Tensile tests were performed on various specimens after different solution annealing at 950 ^{0}C and 1120 ^{0}C, and ageing at 720 ^{0}C, 600 ^{0}C and 640 ^{0}C with variations in soaking period. The room temperature ultimate tensile strength after 950 ^{0}C x 3 hours solution annealing + 720 ^{0}C x 16 hours was 1051 MPa, yield strength was 755 MPa and at 450 ^{0}C the ultimate tensile strength was 922 MPa, yield strength was 667 MPa. The percentage elongation and reduction in area

were 25.5% and 42.5 % respectively at room temperature. At 450 ^{0}C, the percentage elongation after this particular heat treatment was 16.8% and the reduction in area was 38.6%.

The room temperature tensile and high temperature tensile properties after 950 ^{0}C x 3 hours solution annealing + 720 ^{0}C x 16 hours resulted in values very close to those of the newly forged A-286 bar. The ductility at room and at high temperatures have increased as well. The tensile properties were lower as compared to the new A-286 bar for the other specimens, solution annealed at 950 ^{0}C and 1120 ^{0}C, and aged at 720 ^{0}C, 600 ^{0}C and 640 ^{0}C with varying soaking period. The increase and decrease in tensile properties is attributed to the variation in re-precipitated carbides after age hardening.

The fractured surfaces of the new A-286 bar and of heat treated specimens after tensile test (room and high temperature) exhibited dimple type fracture with microvoid coalescence. This is consistent with a ductile mode of failure. The dimple type rupture is associated with microvoid coalescence. Dimple type fracture/rupture occurs primarily due to overload on the material. A particular steel or alloy when no longer can withstand the loading capacity due to stress, fracture occurs. The overload fracture is due to microvoid coalescence. Microvoids start nucleating at the localized regions of strains within the material. The regions of localized strain could be inclusions, grain boundaries, and dislocations in a line or second phase particles. Due to overload, such as in tensile testing the strain in the material begins to increase. With increasing strain in the material, the microvoids grow and coalesce. Further, the microvoid coalescence

results in formation of micro crack resulting in macro crack and a continuous fracture surface. Due to the microvoid coalescence, this type of fracture exhibits numerous cuplike depressions known as dimples. The resultant fracture mode is thus, known as dimple type rupture.

5.7.1 CHARPY IMPACT TEST

The Charpy impact test measures the toughness of a particular material. The average Charpy impact value for the new bar was 57.6 Joules and for the serviced turbine wheel was 17 Joules respectively. A comparison clearly shows that the impact values were very less for the serviced turbine wheel as compared to the new A-286 wheel in the same heat-treated condition. This means that the toughness has decreased a lot for the serviced turbine wheel after operating hours of more than 200K hours. The decrease in toughness can thus, be attributed to the microstructural transformations such as grain size variation and significant carbide precipitation, which occurred during the extended service period of the wheel. The co-relation between toughness and various microstructural transformations within various steels and alloys have been studied by other researchers [240, 241]. The increase or decrease in Charpy values is related to the grain size. Fine or small grain size will obstruct the dislocation movement more as compared to the coarse or large grains. This is due to large number of grain boundaries per unit area. Internal stresses are developed due to the piling up of dislocations at the grain boundaries. As the internal stresses increases, a large

force has to be applied to cause the material flow i.e. to overcome dislocation pile-up stresses and because of this, the material toughness increases.

The heat treatment cycle of 950 ^{0}C x 3 hours solution annealing + 720 ^{0}C x 16 hours resulted in an average Charpy value of 37.33 Joules. It was found that the toughness increased after this particular heat treatment and was close to the toughness of the new A-286 bar. There is an increase or decrease in the Charpy values for the other specimens of the serviced wheel which were solution annealed at 950 ^{0}C and 1120 ^{0}C followed by ageing at 720 ^{0}C, 600 ^{0}C and 640 ^{0}C . The low temperature ageing at 600 ^{0}C resulted in a very high Charpy value but with decrement in the tensile values.

The fractured surfaces of the new A-286 bar and serviced turbine wheel after Charpy impact test revealed quasi-cleavage mode of fracture, which is typical of a mixed mode of ductile and brittle fracture. The fractured surfaces of heat treated specimens after Charpy impact test displayed quasi-cleavage mode with microvoids or intergranular cracks.

Fracture surfaces that display morphology or features of both dimple and cleavage type are called as quasi-cleavage fractures. In general, the quasi-cleavage fracture surface will have a combination of severe plastic deformation and brittle mode. This type of fracture often initiates at the central cleavage facets, and as the crack radiates, the cleavage facets blend to dimple rupture and the cleavage steps appear to be as tear ridges [242].

5.7.2 STRESS RUPTURE TEST

The stress rupture test was to determine the rupture time at higher stress than the actual service stress at particular temperatures. The stress rupture test results; primarily the time to rupture depends on the applied stress and temperature during the testing. Stress rupture testing is much similar to creep testing, but the stresses are higher in stress rupture test, and are used in remaining life analysis [243].

The parameters for stress rupture were 520 MPa, 385 MPa stress and 550 ^{0}C and 650 ^{0}C temperatures. The stress rupture hours for the new A-286 bar and the serviced turbine wheel lasted for more than 100 hours. From this, it could be concluded that the microstructural changes such as carbide precipitation did not have any adverse effect on the stress rupture strength of the A-286 wheel. The stress rupture results after different solution annealing and age hardening heat treatments did not reveal any significant difference. The samples sustained the minimum requirement of 100 hours.

Literature suggests that A-286 alloy may have problem of notch sensitivity. This can have an effect on the stress rupture property [244]. The other factors which can affect the stress rupture properties are microcracks or crack growth, deformation due to slip band both homogeneous and non-homogeneous, ductility, environment, intergranular oxidation, chromium content, incipient melting of phases and carbides, microstructure and grain boundary morphology [245, 246]. All these could form a weak link within the material, leading to early stress rupture failure. All the stress rupture samples survived the minimum requirement of 100 hours. This suggests that the A-286 turbine wheel material do not have any

direct effect of the carbide precipitation on the stress rupture property. The stress rupture fractures after solution annealing at 1120 ^{0}C x 3 hours and ageing at 600 ^{0}C for 4, 8 and 12 hours displayed cleavage type mode of failure with microvoids.

5.7.3 VICKERS HARDNESS SURVEY

The average Vickers hardness of the new A-286 forged bar was 388 HV. The average Vickers hardness of the serviced A-286 turbine wheel was 334 HV. It was evident that for the serviced turbine wheel the hardness has reduced approximately by 50 HV, as compared to the new A-286 bar which was solution annealed and age hardened. The reduction of hardness in the serviced wheel can be attributed to the changes in microstructure and reduction in tensile properties. The pilot solution annealing heat treatments at 750 ^{0}C, 950 ^{0}C, and 1120 ^{0}C, resulted in low hardness values of 181 HV, 170 HV and 167 HV respectively. This is due to the dissolution of the carbides and material softening and in agreement with the result of earlier studies on nickel base alloys by other researchers [247].

Experiments revealed variations in microhardness after various heat treatments. The variation in hardness is primarily due to age hardening treatment, which tends to increase or decrease the re-precipitates depending on the temperature and soaking time. The solution annealing heat treatment at 950 ^{0}C with a soak period of 3 hours followed by age hardening heat treatment cycle at 720 ^{0}C resulted in a hardness of 357 HV. The hardness after this particular heat treatment was most near to the hardness of the new A-286 bar, amongst all the heat treatments

performed. It was evident that the age hardening temperatures of 600 ^{0}C and 640 ^{0}C did not impart hardness more than 298 HV. The age hardening heat treatments at 720 ^{0}C resulted in hardness value of more than 300 HV. This can be attributed to the uniform re-precipitation of the carbides at 720 ^{0}C as compared to ageing at 600 ^{0}C and 640 ^{0}C.

5.8 SELECTION OF OPTIMIZED HEAT TREATMENT

The various heat treatments consisted of the pilot solution annealing heat treatments at 750 ^{0}C, 950 ^{0}C and 1120 ^{0}C with a soak period of 3 hours. The microstructural evidence displayed carbide dissolution at 950 ^{0}C and 1120 ^{0}C, but the microstructure revealed coarse grains (ASTM 1-2) for solution annealing at 1120 ^{0}C as compared to the desirable grain size (ASTM 5-6) achieved by solution annealing at 950 ^{0}C. There is concrete evidence that solution annealing at 950 ^{0}C for 3 hours resulted in total dissolution of carbides and resulted in the desired grain size, hence this solution annealing temperature was selected. A similar evidence regarding dissolution of carbides was observed in a study conducted on Alloy 718 by other researchers [248].

On finalization of the solution annealing temperature, it was essential to select the desirable age hardening heat treatment. Age hardening at temperature 720 ^{0}C for 16 hours produced optimum desired results. A complete cycle consisting of solution annealing and age hardening was selected. Microstructure displayed dissolution of grain boundary carbides after the heat treatment 950 ^{0}C x 3 hours solution annealing + 720 ^{0}C x 16 hours. The mechanical properties with this

particular heat treatment were significantly better as compared to the mechanical properties with other heat treatments performed. With the observed results, this particular heat treatment will definitely increase the life of the wheel for another cycle of 48,000 hours. The experimental work has successfully demonstrated that the detrimental carbides in the long-term serviced A-286 gas turbine wheels can be dissolved in solid solution matrix with 950 ^{0}C x 3 hours solution annealing heat treatment. The age hardening heat treatment at 720 ^{0}C x 16 hours serves to impart the necessary re-precipitates to restore the required properties. Thus, this particular heat treatment comprising of solution annealing and age hardening restores the microstructure back to a near new microstructural state.

CHAPTER 6

CONCLUSION

The present study was started with several objectives, primarily to develop a rejuvenation heat treatment for life extension of A-286 turbine wheel beyond its designed life of 200k hours as recommended by OEM.

The research work comprises the study of the microstructural transformations in the A-286 turbine wheel, which had been in service over a period of 200k hours. Further, the research focusses on rejuvenating the degraded microstructure and restoring the mechanical properties as close to the new turbine wheel. The rejuvenation was done with particular set of heat treatments, which consist of solution annealing and age hardening. The objectives of the research work were accomplished as the microstructure could be rejuvenated with improved mechanical properties. This chapter outlines the conclusions drawn from the present research study. The main conclusions drawn are as follows:

1. Stress mapping using Finite Element Analysis reveals a complex distribution of radial stress across the wheel with stress variation in the range of 300- 450 MPa. Highest stress of 450 MPa is at the bore area and at the radius areas of dovetail. High stress in the bore area and radius areas of dovetail can be attributed to the surface loads due to flowing of hot gases over the blades, centrifugal force due to mass of blades and wheel

rotating at high speed, forging process and temperature excursions in service.

2. No significant variation is observed in hardness as the hardness values vary in the range of 314 to 334 HV across the wheel. The slight variation in the hardness levels is attributed to the type of carbide distribution across the wheel as carbides have different hardness due to the respective elements in that particular carbide phase.
3. Schaeffler diagram indicates the microstructure of A-286 alloy to be wholly austenitic. The microstructure of the new A-286 bar, which resembles a new A-286 turbine wheel exhibits carbide free fine austenite grains with grain size in the range of 6 to 7 ASTM No. whereas the microstructure of serviced A-286 turbine wheel exhibits slightly coarser austenite grains of 4 to 5 ASTM No. with significant amount of carbide precipitates within the grains and along the grain boundaries. Grain coarsening and presence of carbides may be attributed to long-term high temperature exposure during service.
4. EDAX analysis confirms that the carbides present in the microstructure of serviced turbine wheel are a combination of MC, MC_6 and $M_{23}C_6$ type carbides rich in titanium and chromium. During high temperature exposure over long period, primary carbides (MC) rich in titanium get reduced to form secondary carbides (MC_6 and $M_{23}C_6$) through morphological transformations.

5. Carbide dissolution is found to be dependent on solution annealing temperature and soaking period. Higher solution annealing temperature and long soaking period help in dissolution of carbides as solution annealing at 1120 ^{0}C x 3 hours and at 950 ^{0}C x 3 hours results in complete carbide dissolution whereas solution annealing at 720 ^{0}C x 3 hours does not dissolve any carbide. At the same time, solution annealing at 1120 ^{0}C x 2 hours and at 950 ^{0}C x 2 hours results in partial dissolution of carbides. The carbide dissolution at high temperature and long soaking period may be attributed to increase in solubility of carbon in austenite with increase in temperature and availability of more time to dissolve carbon respectively,
6. The solution annealing heat treatment at 950 ^{0}C x 3 hours and at 1120 ^{0}C x 3 hours results in complete dissolution of detrimental carbides in serviced turbine wheel but with varying grain size. Solution annealing at 950 ^{0}C x 3 hours produces desirable ASTM Grain size of 5 to 6, which is close to the new A-286 bar whereas solution annealing at 1120 ^{0}C x 3 hours produces coarse ASTM Grain size of 1 to 2. It was hence concluded that solution annealing from 950 ^{0}C is satisfactory as compared to solution annealing from 1120 ^{0}C. The higher solution annealing temperature provides higher crystal growth rate to produce coarse grains as the larger grains become bigger at the expense of smaller grains by Oswald ripening mechanism.
7. Size, distribution and coherency of re-precipitated carbides in the recrystallized microstructure is found to be dependent on ageing

temperature and time. Lower ageing temperature of 600 ^{0}C and short ageing time of 4 & 8 hours do not support the re-precipitation. Medium ageing temperature of 640 ^{0}C and moderate ageing time of 12 hours results in non-uniform re-precipitation of very fine coherent carbide particles whereas higher ageing temperature of 720 ^{0}C and long ageing time of 16 hours results in precipitation of uniformly distributed but slightly larger and semi-coherent carbide particles. Uniform distribution of re-precipitated carbide particles may be attributed to increase in nucleation sites with increasing temperature.

8. The average Vicker's hardness of serviced A-286 material is found to be 10% less than that of new A-286 material primarily due to change in microstructure and precipitation of detrimental massive carbide particles after long-term high temperature exposure during service. The average Vicker's hardness shows small variation with annealing temperature and soaking period. Hardness decreases with increasing annealing temperature for same soaking period due to the dissolution of the carbides and material softening but increases with increase in soaking time at same temperature. Hardness shows variation with ageing temperature and time. It increases with ageing temperature and ageing time. Average hardness of serviced A-286 material increases after heat treatments at higher annealing and ageing temperature. Hardness varies in the range of 347 to 377 HV (close to 378 HV of new A-286 material) with annealing at 1150 ^{0}C or 950 ^{0}C for 2 hours or 3 hours followed by ageing at 720 ^{0}C for 16 hours. Hardness of

serviced A-286 material gets reduced after all other heat treatments conducted. The increase in hardness values after these treatments may be attributed to more uniform re-precipitation of the carbides at 720 ^{0}C as compared to ageing at 600 ^{0}C and 640 ^{0}C.

9. Long-term exposure to high temperature during service imparts reduction in tensile properties of A-286 material. Room temperature yield strength and ultimate tensile strength reduce to 695 MPa from 769 MPa and 950 MPa from 1098 MPa respectively. High temperature (450 ^{0}C) yield strength and ultimate tensile strength reduce to 566 MPa from 690 MPa and 862 from 937 MPa respectively. Decrease in strength values at room temperature and high temperature after long term exposure to high temperature may be attributed to grain coarsening and presence of incoherent and massive carbide particles within the grains and along the grain boundaries, The detrimental effect of coarse grains and carbide particles is evident from the fractured surface morphology as the fractured surface of serviced A-286 material exhibits severe micro-void coalescence while fractured surface of new A-286 material exhibits normal micro-void coalescence.
10. Room temperature and high temperature strength values are found to vary with annealing temperature, soaking time, ageing temperature and ageing time. In general, room temperature and high temperature strength increase with increase in soaking period when annealed at lower temperature but decrease with increase in soaking period for higher annealing temperature

followed by same ageing process in all cases. Strength values increase with increase in ageing temperature and ageing time after same annealing process. The room temperature and high temperature strength of serviced turbine wheel are increased after heat treatments consisting of "Solution Annealing at 950 ^{0}C x 2 hours + Age Hardening at 720 ^{0}C x 16 hours" and "Solution Annealing at 950 ^{0}C x 3 hours + Age Hardening at 720 ^{0}C x 16 hours" whereas these are decreased after all other heat treatments conducted in the present study. The high strength values at lower annealing temperature and higher ageing temperature may be attributed to fine recrystallized grains with complete dissolution of carbides and uniform distribution of coherent re-precipitated carbide particles.

11. Other tensile properties like percentage elongation and percentage reduction in area are greatly affected by the long-term high temperature exposure during service as the values decrease from 23.6% to 10.8% & 39.3% to 13.7% at room temperature respectively whereas these decrease from 17.5% to 4.5% & 45.4% to 18.8% respectively at high temperature. This reduction in properties may be attributed to the grain size variation and the carbide precipitation during service and their effect is evident from the severe micro-void coalescence exhibited by the fractured surface.
12. All the heat treatments conducted in the present study brings significant improvement in percentage elongation and percentage reduction in area. The effect of annealing temperature, soaking time and ageing time is marginal but effect of ageing temperature is very significant. Though the

ageing treatment at lower temperature improves these properties drastically however, the values obtained after heat treatment consisting of "Solution Annealing at 950 ^{0}C x 3 hours + Age Hardening at 720 ^{0}C x 16 hours" are closest to that of new A-286 material. The improvement in these properties after heat treatment is attributed to grain refining, dissolution of carbides and re-precipitation of coherent carbide particles.

13. Long-term exposure to high temperature during service affects the toughness of the material to a great extent due to coarsening of the grains and precipitation of incoherent carbide particles within the grains and along the grain boundaries. The average Charpy impact strength decreases to 17.0 Joules for serviced A-286 material against 57.6 Joules for new A-286 material. The detrimental effect of grain coarsening and presence of incoherent carbide particles is evident from the quasi-cleavage type fracture with presence of micro-voids and cracks under tri-axial stress condition in Charpy impact test as exhibited by the fractured surface.
14. All the heat treatments conducted in the present study brings significant improvement in Charpy impact strength. Average impact values decrease with increase in soaking period when annealed at lower temperature but increase with increase in soaking period for higher annealing temperature followed by same ageing process in all cases. Average impact values increase with increase in ageing temperature and ageing time after same annealing process at lower temperature. The increase or decrease in Charpy values primarily depends on the grain size. Fine or small grains

leads to high Charpy values. Highest values are obtained at higher annealing temperature with lower ageing temperature and short ageing time. It is very unusual and needs further study since higher annealing temperature results in coarser grain.

15. The stress rupture tests at two different sets of stress and temperature combination i.e. 520 MPa, 550°C and 385 MPa, 650 ^{o}C do not reveal any significant abnormality for the new A-286 bar and serviced turbine wheel before and after different heat treatments. None of the samples fails after 100 hours duration in stress rupture tests (except samples after solution annealing at 1120^{0}C for 3 hours and age hardening at 600^{0}C for 4 hours and 8 hours which fail immediately after loading due to the machining problems or some test sample loading issues) indicating considerable amount of stress rupture strength. The microstructural changes such as grain coarsening and carbide precipitation do not have any adverse effect on the stress rupture strength of the A-286 wheel.
16. Comparison of the microstructures and mechanical properties reveals that the heat treatment consisting of "Solution Annealing at 950 ^{0}C x 3 hours + Age Hardening at 720 ^{0}C x 16 hours" results in most desirable combination of microstructure and mechanical properties (close to new A-286 material) among all the heat treatments conducted in the present study. It is therefore, concluded that the life of serviced turbine wheel may surely be extended to a reasonable extent after above-mentioned rejuvenation heat treatment.

17. Based on improvement in the mechanical properties, the present research work suggests a life extension of further 48k hours to the A-286 turbine wheel after the rejuvenation heat treatment. The gas turbine users have a scheduled major outage after 48,000 hours. During the major outage, there is an opportunity to check the microstructure of the same rejuvenated turbine wheel, primarily for any carbide precipitation. The microstructure evaluation can be done by replica metallography, which is non-destructive method. If there is any alarming situation, found in microstructure after 48k hours, it can be communicated to the end users and appropriate measures to run or replace the wheel can be taken. . Thus, a detailed life cycle management plan can be established for the continuation of A-286 gas turbine wheels after 200k hours.

6.1 LIFE CYCLE MANAGEMENT OF TURBINE WHEELS

A life cycle management plan is essential for the long-term performance of the A-286 turbine wheels. From, the experimental research it is concluded that the life of A-286 turbine wheels can be increased by rejuvenation heat treatment. Replacement of the turbine wheel is not economical but heat-treating the turbine wheel is certainly an economical option. The rejuvenation heat treatment of turbine wheel will serve as a cost effective solution to utilize heat treatment approach for life extension and reliable operation of gas turbines after 200k hours of operation. The research data will serve as a guideline or model for similar fleet

of A-286 turbine wheels for estimating the remaining life, which will lead to considerable amount of cost savings.

The rejuvenated turbine wheel can be continued in service for 48k hours. Microstructure can be monitored for any further transformations during the outage by replica metallography.

The life cycle management plan for the turbine wheels based on the research observations and results follow:

1. Data collection in terms of turbine operational history needs to be collected. The operational history will provide an overview of the temperatures experienced by the turbine wheel in service, number of starts and stops, and any other modification if done in the turbine unit.
2. Examine the turbine wheel after removal from turbine non-destructively. The non-destructive tests shall include replica metallography to evaluate the microstructure, eddy current testing for surface and subsurface cracks. If required, a dimensional check can also be performed depending on the integrity of the turbine wheel.
3. The replica metallography evaluation will provide vital information regarding any microstructural transformations. Microstructure should be examined for grain boundary carbide precipitation, microvoids and microcracks, detrimental phases such as eta phase. Microstructure should be checked by replica metallography at different locations on the turbine wheel for carbide dissolution.

4. In case, the microstructure displays evidence of significant grain boundary carbide precipitation, solution annealing and ageing heat treatment should be performed on the turbine wheel. To assure, the carbides have dissolved in solid solution matrix replica metallography needs to be performed on the turbine wheel after solution annealing and heat treatment.
5. If carbide dissolution is to satisfactory extent after rejuvenation heat treatment, the wheel can be continued further in service.
6. The turbine wheel can be in service until another inspection cycle, which is normally 48,000 hours.
7. On completion of the 48,000 hours, the turbine wheel needs to be inspected for any cracks and carbide precipitation.

The life cycle management flow chart for the turbine wheel is presented in Figure 6.1.

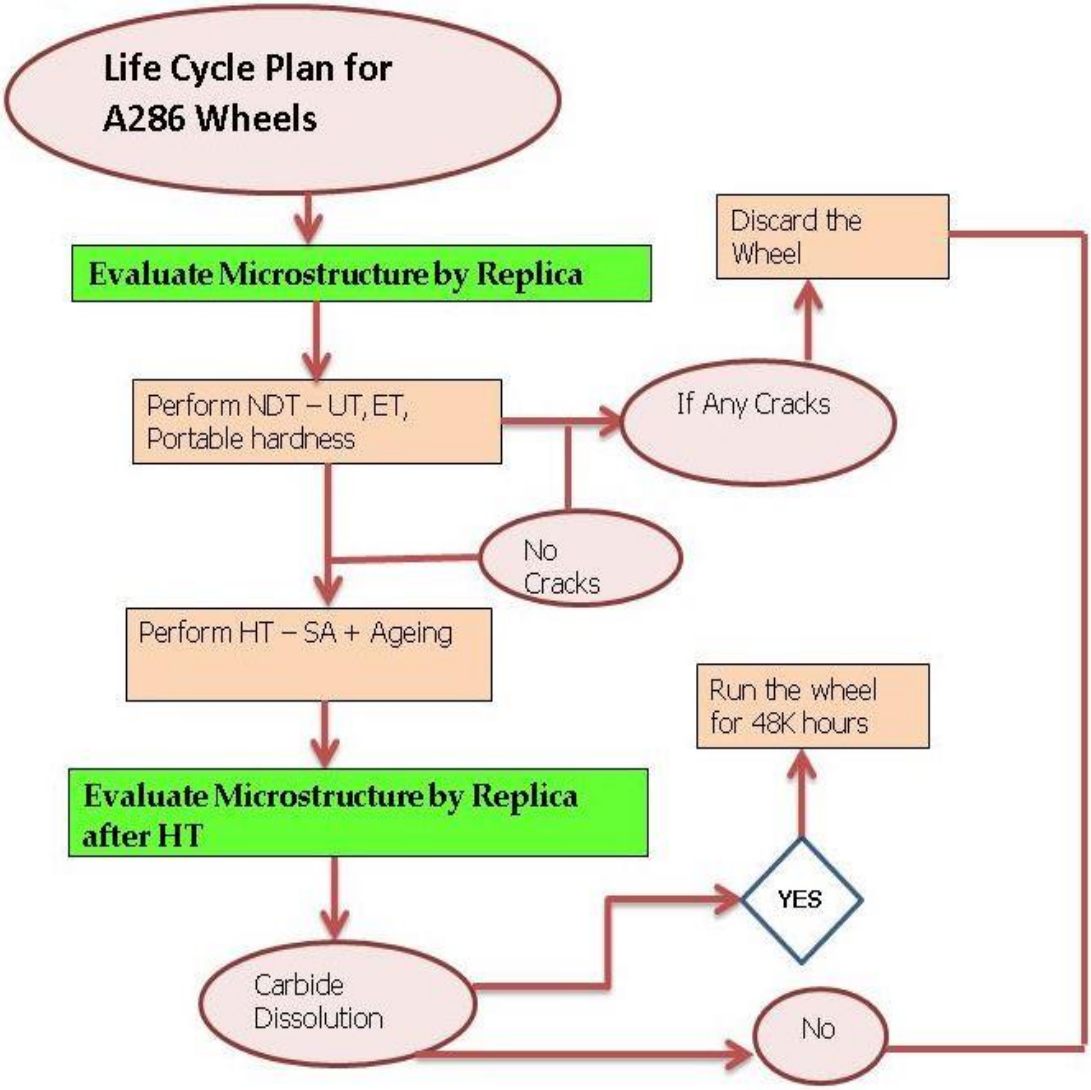

Figure 6.1: Life Cycle Management of Turbine Wheel - Flow Chart

6.2 FUTURE SCOPE OF WORK

The present research concluded that it is possible to extend the life of A-286 gas turbine wheels by rejuvenation heat treatment. Various experimental heat treatments and the evaluation of microstructure and mechanical properties suggest that the properties are improved. Further work on this research is outlined below:

1. Determination of creep and fatigue properties on the A-286 serviced wheel after rejuvenation heat treatment.
2. Study of carbide precipitation mechanism in A-286 serviced turbine wheel.
3. Microstructural and mechanical property evaluation of Cr-Mo-V turbine wheels.
4. Development of a similar rejuvenation heat treatment for Cr-Mo-V steel turbine wheels, which has crossed 200k hours of service.

REFERENCES

[1] www.bath.ac.uk/en9bg/gas%20turbine.htm, Jan 2001.

[2] www.marketsandmarkets.com/Market-Reports/gas-turbines-market-94641697.html, Report Code EP3998, Oct 2017.

[3] www.gminsights.com/industry-analysis/gas-turbine-market, March 2017.

[4] www.technavio.com/report/global-unit-operations-gas-turbine-market, May 2016.

[5] "Gas Turbines A Handbook of Air, Land, Sea and Applications", Claire Soares, Chapter 1.

[6] M. Cocca, N. Marcucci, "Performance and Reliability Improvements for MS5002 Gas Turbines", GER4171, July 2009, pp. 3-5.

[7] K.J. Pallos, "Gas Turbine Repair Technology", GER3957B, March 2001, pp. 7-9.

[8] SWRI & EPRI, "Gas Turbine Blade Life Assessment and Repair Guide", EPRI GS-6544, Project 2775-6, Final Report, Nov 1989, pp. 4-8.

[9] J. Joannides, L.Cooke, "Practical Experience with The Development of Superalloy Rejuvenation", Liburdi Turbine Services, Frame 6 Users Group Conference, Cincinnati, June 2009.

[10] "Rotor Life Management GE Learning Session", GE Energy Customer Solutions Conference", Year 2010, pp. 2-11.

[11] W. Abbasi, S. Rahman, “NDE Inspections and Lifetime Assessment of Turbine Equipment”, PowerGen International Conference, Orlando, Florida, Dec 2008, pp.3-8.

[12] P.W.Schilke, “Advanced Gas Turbine Materials and Coatings”, GER3569F, 1996, pp. 17.

[13] D. Grace, T. Christiansen, “Quantifying the Cost of Unplanned Outage Events for Combined-Cycle Plants” Energy-Tech Magazine, Aug 2012.

[14] J. Liburdi, “Enabling Technologies for Turbine Component Life Extension”, RTO-AVTP Workshop on Qualification of Life Extension Schemes for Engine Components, Greece, Oct 1998

[15] A. Koul, R. Thamburaj, M. Raizenne, W. Wallace, “"Practical Experience with Damage Tolerance Based Life Extension of Turbine Engine Components", AGARD Conference Proceedings, SMP Panel, San Antonio, Texas, U.S.A., April 1985, AGARD-CP-393, pp 22-23.

[16] Outage Handbook, “Rotor Life Extension”, Combined Cycle Journal, Year 2011. www.ccj-online.com/archives/special-issue-outage-handbook/rotor-life-extension.

[17] GE Energy, “Gas Turbine Rotor Inspections”, Technical Information Letter No. 1576, June 2007.

[18]www.geoilandgas.com/pipeline-storage/gas-processing-compression/heavy-duty-gas-turbines

[19] P.W.Schilke, “Advanced Gas Turbine Materials and Coatings”, GER3569G, Aug 2004, pp. 20.

[20] P. Sisto, D. Benericetti, “Risk Assessment of Gas Turbines Rotors That Have Exceeded Their Design End of Life”, ASME Turbo Expo 2015, Paper No. GT2015-42865, V)&AT28A007.

[21] G. Shejale, R. Garg, G. Subrahmanyam, A. Schnell, “Condition Assessment Study of A-286 Alloy Gas Turbine Wheel”, Journal of Failure Analysis and Prevention, Vol 16, Issue 5, Oct 2016, pp. 712-717.

[22] B. Michael “Microstructural Characterization and Heat Treatment of A-286 Turbine Buckets"; Year 2009, ETD Collection for University of Texas, El Paso, AA11468288, pp. 5-7.

[23] www.industrialinfo.com

[24] H. Saravanamuttoo, G. Rogers, and H. Cohen, “Gas Turbine Theory 50 years”; Publisher Prentice Hall, 2001.

[25]www.gepower.com/resources/knowledge-base/combined-cycle-power-plant-how-it-works

[26] R. Viswanathan, “Life Assessment Techniques for Combustion Turbines”, Chapter 9, Damage Mechanisms and Life Assessment of High Temperature Components”, ASM International, pp. 416-417, Jan 2006.

[27] R. Chaplin, “Condition Assessment and Life Extension”, Encyclopedia of Life Support Systems, Thermal Power Plants – Vol. I, Chapter 1, Year 2008.

[28] T. Sakurai, S. Sugai, M. Aoki, “Life Assessment of High-Temperature Components of Thermal Power Plants in Japan”, Journal of Nuclear Engineering and Design, Issue 3, Vol 139, March 1993, pp. 311-317.

[29] M. Warren, J. Roderick, “Extending Useful Life of a Cobalt-Based Gas Turbine Component”, United States Patent Application 20120084980, Application No 12/902902, Dec 2012.

[30] T. Maccagno, A. Koul, J. Immarigeon, G. Leoperance, “Microstructure, Creep properties, and Rejuvenation of Service-exposed alloy 713C Turbine Blades”, Metallurgical and Materials Transactions, A 21(12):3115-3125, Jan 1990.

[31] R. Viswanathan, “Residual Life Techniques for Plant Life Extension”, Materials Science and Engineering Journal, Vol 103, Issue 1, Aug 1988, pp.131-139.

[32] L. Zhimin, D. Mavris, N. Volovoi, “Creep Life Prediction of Gas Turbine Components Under Varying Operating Conditions", ASME International Joint Power Generation Conference, June 2001, New Orleands, Louisiana, USA

[33] G. Webster and R.A. Ainsworth, “High Temperature Component Life Assessment”, SpringerScience+Business Media, 1994, pp.5-7.

[34] C. Dinh, B. Marriner, R. Tadros, S. Yoongeu and T. Farineau, “Design and Operation of Large Fossil-Fueled Steam Turbines in Cyclic Duty”, GER4933, July 2016, pp. 4-6.

[35] R. Viswanathan and S.T. Scheirer, “Materials Advances in Land-based Gas Turbines”, Power Gen, Orlando, Dec 9-11, 1998.

[36] Y.L. George, “High Temperature Corrosion and Materials Applications”, ASM International, USA, Year 2007.

[37] T. Carter, “Common Failures in Gas Turbine Blades", Engineering Failure Analysis, Vol. 12, No. 2, pp. 237-247.

[38] Hot Section: High Temperature Coating System, EPRI, report 1000432, 2000, Palo Alto, CA, USA.

[39] R. Kurz, and K. Brun, "Degradation in Gas Turbine Systems", Journal of Engineering for Gas Turbines and Power, Vol. 123, No. 70, Year 2001, pp. 70-77.

[40] GE FA First Stage Blade Analysis, EPRI, Report 1000318, 2000, Palo Alto, CA, USA.

[41] M. Kemppainen, J. Scheibel, R. Vishwanathan, “Combustion Turbine Hot Section Life Management”; OMMI, Volume I, Issue-2, Aug 2002.

[42] W. Abbasi, S. Rahman, and J. Metala, “NDE Inspections and Lifetime Assessment of Turbine Equipment” Siemens Technology and Inspection Services, PowerGen International, Orlando, Florida, Dec 2008.

[43] A.I. Zwebek, and P. Pilidis, "Degradation Effects on Combined Cycle Power Plant Performance-Part III: Gas and Steam Turbine Component Degradation Effects", Journal of Engineering for Gas Turbines and Power, Vol. 126, No. 2, Year 2004, pp. 306-315.

[44] R. Viswanahan and J. Stringer, "Failure Mechanisms of High Temperature Components in Power Plants", Journal of Engineering Materials and Technology, Vol. 122, No. 3, Year 2000, pp. 246-255.

[45] N. Eliaz, G. Shemesh, and R. Latanision, “Hot Corrosion in Gas Turbine Components", Engineering Failure Analysis, Vol. 9, No. 1, Year 2002, pp. 31-43.

[46] G. Holcomb, “Hot Corrosion in a Temperature Gradient", Materials and Corrosion, Vol. 51, No. 8, Year 2000, pp. 564-569.

[47] J. Li, and A. Dasgupta, “Failure-Mechanism Models for Creep and Creep-Rupture", Reliability IEEE Transactions, Vol. 42, No. 3, Year 1993, pp. 339-353.

[48] De. Ridder, and R. Noel, “Deformation Processing of Superalloy Gas Turbine Components," SAE Technical Paper, 690101, 1969.

[49] S. Eshati, F. M. Ghafir, P. Laskaridis, and G. Li, “Impact of Operating Conditions and Design Parameters on Gas Turbine Hot Section Creep Life", Proceedings of ASME Turbo Expo 2010: Power for Land, Sea and Air, GT2010-22334, June 14-18, 2010, Glasgow, UK.

[50]M. Siegel, “Remaining Life Analysis of Highly Stressed Steam Turbine Components and Total Operating Enhancement,” Power-Gen Europe 2007, Madrid, Spain, June 26-28, 2007.

[51] R.Viswanathan, "Residual Life Techniques for Plant Life Extension", Materials Science and Engineering, A, Vol. 103, No. 1, Year 1988, pp. 131-139.

[52] D. J. Gooch, "Plant Life Extension Remnant Life Assessment of High Temperature Components", Power Engineering Journal, Vol. 2, No. 6, Year 1988, pp. 323-331.

[53] V. Cuffaro, F. Cura, R. Sesana, P. Torino, C. Duca, “Advanced Life Assessment Methods for Gas Turbine Engine Components”, XVII International Colloquium on Mechanical Fatigue of Metals, Procedia Engineering 74, 2014, pp. 129-134.

[54] R. Timmins, “Verified Approaches to Life Assessment and Improved Design of Elevated Turbine Equipment” Synthesis Report for Publication, Project BE-4285, June 1992.

[55]E. Benvenuti, “Innovative Gas Turbine Performance Diagnostics and Hot Parts Life Assessment Techniques”, Proceedings of the 30th Turbo Machinery Symposium, 2003.

[56] M. I. Wood, “Gas Turbine Hot Section Components: The Challenge of Residual Life Assessment", Journal of Power and Energy, Vol. 214, No. 3, Year 1999, pp. 193-201.

[57] C.Giovanni, M. Gazzino, F. Botta, and C. Salvini, “Production Planning with Hot Section Life Prediction for Optimum Gas Turbine Management”, International Journal of Gas Turbine Propulsion and Power Systems, Vol 2, No. 1, Dec 2008.

[58] Y. Assoul, S. Benbelaid, V. Zeravcic, G. Bakic, and M. Dukic, “Life Estimation of First Stage High Pressure Gas Turbine Blades", Scientific Technical Review, Vol. LVIII, No. 2, Year 2008, pp. 8-13.

[59] D. Sheperd, T. Ward, A. Wisbey, B. Vermeulen, and A. Lee, “Life Extension Methods in Aero-Engines", Operation Maintenance and Materials Issues-OMMI, Vol. 3, No. 1, Year 2004, pp.1-15.

[60] C. Rinaldi, V. Bicego, and P. Colombo, “Validation of CESI Blade Life Management System by Case Histories and in Site NDT", Journal of Engineering for Gas Turbines and Power, Vol. 128, No. 1, Year 2006, pp. 73-80.

[61] R. Prasad, K. Singh, “Remaining Life Analysis of Gas Based Units”, Transactions of the Indian Institute of Metals, April 2010, Volume 63, Issue 2, pp:349-356.

[62] P. Dowson, W. Wang, A. Aliga, “Remaining Life Assessment of Steam Turbine and Hot Gas Expander Componnets”, Proceedings of the 34th Turbomachinery Symposium, 2005.

[63] A.K. Koul, A. Tiku, S. Shankar, and J. Zhao, “Probabilistic Creep Life Prediction of Turbine Disc, Paper GT2010-22169", Proceeding of ASME Turbo Expo 2010, Glasgow, UK.

[64] S. Cheruvu, R. Malmfeldt, “Metallurgical Characterization of a High-Pressure Rotor for Remaining Service Life Assessment After 26 Years of Service” Journal of Engg. Gas Turbines & Power, April 2008, pp:543-549.

[65] H. Jin, P. Lowden, and R. Pistor, “Remaining Life Assessment of Power Turbine Disks”, ASME Turbo Expo Conference 2008; Power for Land Sea & Air, Volume 7, June 2008.

[66] V. Iyengar, S. James and H. Simmons, “On Remaining Life Analysis of Turbine disks Subjected to High Thermal Stresses”, ASME 2011 Turbo Expo-Turbine Technical Conference and Exposition, Paper No GT 2011-45082, June 2011, pp:959-967.

[67] V. Cuffaro, and R. Sesana, “Advanced Life Assessment Methods for Gas Turbine Engine Components”, Procedia Engineering, Volume 74, 2014, pp. 129-134.

[68] G. Asquith, and A. C. Pickard, “Fatigue Testing of Gas Turbine Components,” in: K. J. Marsh (Ed.), Full-Scale Fatigue Testing of Components and Structures, Butterworth, 1994, pp. 210–234.

[69] D. Karimbaev and N. Servetnik, “Low-cycle Fatigue Life Assessment for Gas Turbine Engine Disks under Flight Cycle Conditions”, Journal of Strength of Materials, Volume 41, Issue 1, Jan 2009, pp. 102-105.

[70] Z. Liu, N. Mavris, and V. Volovoi, “Creep Life Prediction of a Gas Turbine Components under Varying Operating Conditions”, Proceedings of 2001 ASME International Joint Power Generation Conference, June 4–7, 2001, New Orleans, Louisiana, USA.

[71] Z. Liu, N. Mavris, and V. Volovoi, “ Creep Life Prediction of a Gas Turbine Components under Varying Operating Conditions”, Proceedings of 2001 ASME International Joint Power Generation Conference, June 4–7, 2001, New Orleans, Louisiana, USA.

[72] J. Cunha, T. Dahmer, and K. Chyu, “Thermal-Mechanical Life Prediction System for Anisotropic Turbine Components”, ASME Paper GT2005-68107, June 6-9, 2005, Reno-Tahoe, Nevada.

[73] M. Wallace, D. Mavris, “ Creep Life Uncertainty Assessment of a Gas Turbine Airfoil”, Proceedings of 5th AIAA Non-Deterministic Approaches Forum, Norfolk, VA, April 7-10, 2003.

[74] G. Cerri, S. Borghetti, C. Salvini, “Models for Simulation and Diagnosis of Energy Plant Components, ASME Paper PWR2006-88146, ASME Power, Atlanta, Georgia, USA, 2-4 May, 2006.

[75] W.Z. Zhuang, and N.S. Swansson, “Thermo-Mechanical Fatigue Life Prediction -A Critical Review, DSTO-RR-0609, Year 1998.

[76] C. Monkman, and J. Grant, 1965, “An Empirical Relationship between Rupture Life and Minimum Creep Rate", Deformation and Fracture at Elevated Temperatures, MIT Press, Year 1965.

[77] B. J. Cane, “Remaining Creep Life Estimation by Strain Assessment on Plant", International Journal of Pressure Vessels and Piping, Vol. 10, No. 1, Year 1982, pp. 11-30.

[78] G. Cerri, M. Gazzino, and S. Borghetti, “Hot Section Life Assessment by a Creep Model to Plan Gas Turbine Based Power Plant Electricity Production", 3rd International Conference, The Future of Gas Turbine Technology, Year 2006, Brussels, Belgium.

[79] D. A. Rosario, "Life Assessment of Critical Boiler and Turbine Components Using EPRI's Creep-Fatigue Pro Software", EPRI International Conference on Advances in Power Plant Life Assessment, March 11-13, 2002, Orlando, Florida.

[80] H. Kaftelen, A. Baldan, “Comparative Creep Damage Assessments Using the Various Models", Journal of Materials Science, Vol 39, No. 13, Year 2004, pp. 4199-2461.

[81] M. Evans, “A Comparative Assessment of Creep Property Predictions for a 1Cr-Mo-V Rotor Steel Using the CRISPEN, CDM, Omega and Theta Projection Techniques", Journal of Materials Science, Vol. 39, No. 6, Year 2004, pp. 2053-2071.

[82] F. Cunha, T. Dahmer, and M. Chyu, “Thermal-Mechanical Life Prediction System for Anisotropic Turbine Components”, Transactions - American Society of Mechanical Engineers, Journal of Turbomachinery, Vol. 128, No. 2, Year 2006, pp. 240-250.

[83] J. Zhao, S. Han, H. Gao, and l. Wang, “Remaining Life Assessment of a Cr-Mo-V Steel Using the Z-Parameter Method", International Journal of Pressure Vessels and Piping, Vol. 81, Year 2004, pp. 757-760.

[84] S. Zhu, and H. Zhong, “A Generalized Energy-Based Fatigue-Creep Damage Parameter for Life Prediction of Turbine Disk Alloys”, Journal of Engineering Fracture Mechanics; Elsevier Volume -90; Aug 2012, pp. 89-100.

[85] T. Tiedo, J. Kampen, B. Jager, J. Kok, “Gas Turbine Combustor Liner Life Assessment Using a Combined Fluid/Structural Approach”, Journal of Engineering for Gas Turbines and Power, 129(1), 2007, pp. 69-79.

[86] A. Dibbert, "Extending Gas Turbine Life", Turbomachinery International, Vol. 47, No. 2, Year 2006, pp. 36-37.

[87] J. Hepworth, J. Wilson, J. Alein, and G. Touchton “Life Assessment of Gas Turbine Blades and Vanes”, International Gas Turbine & Aeroengine Congress & Exhibition”, Orlando, Florida, June 1997.

[88] P. Lowden, B. Weber, R. Grant, H. Jin and R. Pistor, “Prediction of Gas Turbine Blade Life: An Interdisciplinary Engineering Approach for Condition-Based Maintenance”, ASME Paper GT2006-90037, May 8-11, 2006, Barcelona, Spain.

[89] S. Chan, S. Cheruvu, R. Leverant, and R. Vishwanathan, “ Life Prediction Strategies for Land-Based Gas Turbine Blades”, Proceedings of the 2003 TMS Annual Meeting & Exhibition, San Diego, California, March 2-6, 2003, pp. 191-209.

[90] G. Marahleh, I. Kheder, and F. Hamad, “Creep-Life Prediction of Service-Exposed Turbine Blades", Journal of Materials Science, Vol. 42, No. 4, Year 2006, pp. 476-481.

[91] M. Vaezi, and M. Soleymani, “Creep Life Prediction of Inconel 738 Gas Turbine Blade”, Journal of Applied Sciences, Vol. 9, No. 10, Year 2009, pp. 1950-1955.

[92] M. Khalifa, F. Khan, and M. Thorp, “Risk-based Maintenance and Remaining Life Assessment for Gas Turbines”, Journal of Quality in Maintenance Engineering, 21(1), March 2015, pp. 100-111.

[93] R. Viswanathan, and A.C. Dolbec, “Life Assessment Technology for Combustion Turbine Blades”, Journal of Engineering Gas Turbines Power, 109(1), Jan 1987, pp. 115-123.

[94] Y. Yoshioka, D. Saito, I. Murakami, K. Fujiyama, N. Okabe, “Life Assessment of Gas Turbine Bucket Coating Based on Degradation Analysis”, Journal of the Society of Materials Science Japan, Vol. 41, No. 471, 1992, pp. 1724-1728.

[95] Sh. Zangench, H. Farhangi, R. Lashgari, “Rejuvenation of Degraded First Stage Gas Turbine Nozzle by Heat Treatment” Journal of Alloys and Compounds, Vol. 497, Issue 1-2, May 2010, pp. 360-368.

[96] J. Brown, R. Freer and A. Rowley, “Reconditioning of Gas Turbine Components by Heat Treatment” Journal of engineering and Gas Turbines Power, Vol. 123, Issue 1, May 2000, pp. 57-61.

[97] M. Konter, and M. Thumann, “Materials and Manufacturing of Advanced Industrial Gas Turbine Components”, Journal of Materials Processing Technology, Vol. 117, Year 2001, pp. 386-390.

[98] D.J. Tillack, M. Manning, and R. Hensley, “Heat-Treating of Nickel and Nickel Alloys”, ASM Handbook, Volume. 4, pp. 907 – 912.

[99] A. Baldan, “Materials Aging and Component Life Extension”, Conference Proceeding, Engineering Materials Advisory Services Ltd., Milan, Italy, Vol. 2. Oct 1995, pp. 943–50.

[100] S. Ingistov, R. Bhargava, G. Doerksen, “Repair and Rejuvenation of a Severely Damaged 16-Stage Steam Turbine Rotor” Paper No. GT2009-6000, ASME Turbo Expo 2009: Power for Land, Sea, and Air, Volume 4, June 8-12, 2009, pp. 677-684.

[101] W. Kurt and W. Greaves, “Life Assessment of Gas Turbine Components using Non-Destructive Inspection Techniques,” GT-373, International Gas Turbine and Aero-engine Congress and Exhibition, Orlando, Florida, June 1997.

[102] J. Wortmann, “Improving Reliability and Life-time of Rejuvenated Turbine Blades,” Materials Science and Technology, Vol. 1, No. 8, 1985, pp. 644–650.

[103] V. Krongtong, P. Tuengsoook, W. Homkrajai, E. Nisaratanaporn, and P. Wangyao, “The Effect of Re-heat Treatments on Microstructural Restoration in Cast Nickel Superalloy Turbine GTD-111, Acta Metallurgica Slovaca; Volume 11, 2; 2005, pp; 171-182.

[104] J. Daleo, “Metallurgical Considerations for Life Assessment and the Safe Refurbishment and Re-Qualification of Gas Turbine Blades,” Journal of Engineering Gas Turbine Power, Vol. 124, Issue 3, June 2002, pp. 571-579.

[105] J. Liburdi, J.Stephens, “Experience in Extending the Life of Gas Turbine Blades”, ASME presented at Gas Turbine Conference & Products Show, ASME, Year 1980, New Orleans, USA.

[106] H. M. Tawancy, L Hadhrami L., “On the Service Performance of Refurbished Turbine Blades in a Power Station,” ASME Paper No. GT2008-50057, Year 2008.

[107] A. K. Koul, R. Castillo, “Assessment of Service Induced Microstructural Damage and its Rejuvenation in Turbine Blades”, Volume 19, Issue 8August 1988, pp 2049–2066.

[108] A. Motallebi, Y. Sahebi, “Presentation of Rejuvenation and Optimization Method and an Analysis of the Metallurgical Effect on Gas Turbine Blades Lifetime Estimation”, Middle-East Journal of Scientific Research, Vol. 9 (2), Year 2011, pp. 149-152.

[109] J. Liburdi and G. VanDrunen, “Rejuvenation of Used Turbine Blades by Hot Isostatic Processing” Proceedings of the Sixth Turbomachinery Symposium, Year 1977.

[110] P. Wangyao, N. Chuankrerkkul, S. Polsilapa, P. Sopon, and W. Homkrajai, “Gamma Prime Phase Stability after Long-Term Thermal Exposure in Cast Nickel Based Superalloy IN-738”, Chiang Mai Journal of Science, Volume 36, Issue 3, pp. 312-319.

[111] A. Stevens, and J. Flewitt, “Intermediate Regenerative Heat Treatments for Extending the Creep Life of the Superalloy IN-738”; Material Science and Engineering Journal, Volume 50, Issue 2, Oct 1981, pp. 271-284.

[112] W. M. Miglietti, “Rejuvenation Heat Treatments and Their Role in the Repair of IN738 Turbine Components,” ASME Paper No. GT-30536, Year 2002.

[113] S. Polisilapai, P. Soponi, N. Panich, N. Chuankrekkul, and A. Thueploy, “Reheat Treated Microstructures and Gamma Prime Particle Coarsening Behaviour at 900˚C of Cast Nickel Based Superalloy IN-738”, Journal of Metals, Materials and Minerals,. Vol.16, No.2, 2006, pp.7-13.

[114] T. Maccagno, A. Koul, J. Immarigeon, “Microstrcuture, Creep Properties, and Rejuvenation of service Exposed Alloy 713C Turbine Blades”, Metallurgical Transactions, Volume 21, Issue 12, pp. 3115-3125.

[115] J. Liburdi, P. Lowden, D. Nagy, T. Priamus, S. Shaw, “Practical Experience with the Development of Superalloy Rejuvenation”, ASME TurboExpo 2009, Paper GT#59444, Gas Turbine Congress and Exposition, Orlando, Florida, USA.

[116] K. J. Ducki, “Effect of Heat Treatment on the Structure and Creep Resistance of Austenitic Fe-Ni Alloy”, Archives of Materials Science and Engineering, International Scientific Journal, Vol 47, Issue 1, Jan 2011, pp. 33-40.

[117] K.J. Ducki, and M. CieGla, “Effect of Heat Treatment on the Structure and Fatigue Behavior of Austenitic Fe-Ni Alloy, “Journal of Achievements in Materials and Manufacturing Engineering” Volume 30, Issue, Year 2008, pp. 19-26.

[118] P. Bala, “Influence of Solution Heat Treatment on the Microstructure and Hardness of the new Ni-based Alloy with a High Carbon Content”, Archives of Materials Science and Engineering, Volume 45, Issue 1, Year 2010, pp. 40-47.

[119] K.J. Ducki, and M. Hetmanczyk, “The Influence of Prolonged Aging on the Structure and Properties of Precipitation Hardened Austenitic Alloy, Journal of Materials Engineering, Volume 4, Year2001, pp. 290-293.

[120] Dr. Nripjit, S. Kumar, “A Case Study on Ni based Super Alloys Ageing for Improvement of its Properties”, International Advanced Research Journal in Science Engineering and Technology Vol. 2, Issue 9, Sept. 2015.

[121] D. Muzyka, and G. Maniar, “Microstructure Approach to Property Optimization in Wrought Superalloys,” Metallography - A Practical Tool for Correlating the Structure and Properties of Materials, ASTM STP 557, American Society for Testing and Materials, 1974, pp.198-219.

[122] J. Moll, G. Maniar, and D. Muzyka, “The Microstructure of 706, a New Fe-Ni Base Superalloy,” Metallurgical Transactions, Vol. 2, Issue 8, Aug 1971, pp. 2143-2151.

[123] A. Johnson, and K.Fritz, “Properties and Microstructure of a Large Forged Superalloy Turbine Wheel,” Superalloys - Metallurgy and Manufacture, AIME, 1976, pp. 25-35.

[124] C. Sullivan, and M. Donachie, “Microstructures and Mechanical Properties of Iron Base (Containing) Superalloys,” Metals Engineering Quarterly, Nov. 1971, pp. l-11.

[125] X. Qin, J. Guo, C. Yuan, C. Chen, J. Hou, H. Ye, “Decomposition of Primary MC Carbide and its Effects on the Fracture Behaviors of a Cast Ni-Base Superalloy” Materials Science and Engineering, A 485, Year 2008, pp. 74–79.

[126] A. Baldan, “Progress in Ostwald Ripening Theories and their Applications to Nickel-base Superalloys. Part I: Ostwald Ripening Theories,” Journal of Materials Science, Vol. 37, No. 11, Year 2002, pp. 2171–2202.

[127] J. Wasson and G.E. Fuchs, “The Effect of Carbide Morphologies on Elevated Temperature Tensile and Fatigue Behavior of a Modified Single Crystal Ni-Base Superalloy”, The Minerals, Metals and Materials Society, Year 2008.

[128] Sh. Zangeneh, and H. Farhangi, “Influence of Service Induced Microstructural Changes on the Failure of a Cobalt-based Superalloy First Stage Nozzle”, Materials & Design,

Volume 31, Issue 7, Aug 2010, pp. 3504–3511.

[129] C. Walker, J. Cosart, “Innovations in Refurbishing Gas Turbine Components”, ASME Gas Turbine and Aeroengine Congress and Exposition, 90-GT-202, June 11-14, 1990, Brussels, Belgium.

[130] L. Cooke, “Life Extending Advanced Component Repairs — Field Operating Experience”, ASME Turbo Expo 2000: Power for Land, Sea, and Air, Paper No. 2000-GT-0609, Munich, Germany, May 8–11, 2000, pp: 3-15.

[131] G. Shejale, “Metallurgical Evaluation and Condition Assessment of FSX 414 Nozzle Segments in Gas Turbines by Metallographic Methods”, ASME Journal of Enginnering Gas Turbines Power, Vol. 133, Issue 7, March 2011.

[132] G. Lvov, V.I. Levit, and M.J. Kaufman, “Mechanism of Primary MC Carbide Decomposition in Ni-base Superalloys”, Metallurgical and Materials Transactions A, June 2004, Volume 35, Issue 6, pp 1669–1679.

[133] L. Cooke, “Component Management Programs for Reliable Life Extension”, ASME Turbo Expo 2001: Power for Land, Sea, and Air, Paper No. 2001-GT-0431, June 2001, pp: 3-11.

[134] “ATI Allvac Technical Data Sheet for ATI A-286 Alloy”, March 2008.

[135] “Metallic Materials Properties Development and Standardization (MMPDS-01), DOT/FAA/AR-MMPDS-01, Jan 2003.

[136] Heat Resistant Materials “ASM Specialty Handbook, 1997, ISBN 0-87170-596-6, Page 294.

[137] “Special Metals Technical Data Sheet for Incoloy Alloy A-286”, March 2008.

[138] A. R. Salehi, S. Serajzadeh, and N. Yazdipour, “A Study on Flow Behaviour of A-286 Superalloy during Hot deformation” Materials, Chemistry and Physics Journal, Volume 101, Issue 1, Jan 2007, pp:153-157.

[139] T. Sakurai, H. Yamada, K. Kazuo, “Conditions for the Formation of “A” Segregation and Precipitating Phases in iron Based Superalloy A286”; Journal Stage- The Iron & Steel institute of Japan, Vol. 74, No.12; Dec 1988, pp: 2286-2293.

[140] H. De Cicco, M.I. Luppo, H. Raffaeli, J. Di Gaetano, L.M. Gribaudo; “Creep Behaviour of an A286 type Stainless Steel”;, Materials Characterization; Volume 55, Issue 2, Aug 2005, pp:97-105.

[141] H.De Cicco, M.I. Luppo, L.M. Gribaudo, Overajo Garcia; "Microstructural Development and Creep Behaviour in A286 Super Alloy"; Materials Characterization; Volume 52, Issue 2, May 2004; pp:85-92.

[142] K. Kusabiraki, Y. Takasawai, and T. OOka, "Precipitation Alloy and Growth of ɣ' and n Phases in 53Fe-26Ni-15Cr Alloy" ISIJ International, Vol. 35, Issue 5, Year 1995, pp. 542-547.

[143] D. Raynor, and J. Silcock, "Strengthening Mechanisms in γ′ Precipitating Alloys", Metal Science Journal, Volume 4, Issue 1, 1970, pp. 121-130.

[144] I. L. W. Wilson, T. R. Mager, "Stress Corrosion of Age-Hardenable NiFeCr Alloys, Corrosion Journal, Volume 42, Issue 6, 1986, pp. 352-361.

[145] M. Savoie, C. Esnouf, L. Fournier and D. Delafosse, " Influence of Ageing Heat Treatment on Alloy A-286 Microstructure and Stress Corrosion Cracking Behaviour in PWR Primary Water", Journal of Nuclear Materials 360:3, March 2007, pp. 222-230.

[146] K.J. Ducki, "Structure and Precipitation Strengthening in a High-Temperature Fe–Ni Alloy", Archives of Materials Science and Engineering, Volume 28, Issue 4, April 2007, pp. 203-210.

[147] T. Hasegawai, and F. Terasaki, "Effect of Heat Treatment on High-Temperature Strength of A286 Alloy", Journal of Iron and Steel Institute Japan, Vol. 49, Issue 2, 2011, pp. 160-165.e

[148] B. Michael "Microstructural Characterization and Heat Treatment of A-286 Turbine Buckets"; Year 2009, ETD Collection for University of Texas, El Paso, AA11468288.

[149] K. Kobayashi, K. Yamaguchi, M. Hayakawa, M. Kimura, "High-Temperature Fatigue Properties of Austenitic Superalloys 718, A286 and 304L", International Journal of Fatigue, Volume 30, Year 2008, pp. 1978–1984.

[150] H. Wua, Y. Oshidab, S. Hamadac and H. Noguchic, “Fatigue Strength Properties of Precipitation Strengthening Stainless Steel A286 Focused Attention on Small Fatigue Crack Behaviour”, Procedia Engineering, Vol. 10, Year 2011, pp.1973-1978.

[151] R. Natole, “Gas Turbine Components Determining Repairability and Innovations to Refurbish Parts”, Paper 87-GT-66, ASME, 1987.

[152] J. Gayda, T. Gabb, P. Kantzos, “The Effect of Dual Microstructure Heat Treatment on an Advanced Nickel-base Disk Alloy”, Superalloys The Minerals, Metals & Materials Society, Year 2004.

[153] M. Jackson, “Heat Treatment of Udimet 720Li: the Effect of Microstructure on Properties”, Journal of Materials Science and Engineering, Volume 259, Issue 1, 15 January 1999, pp. 85-87.

[154] A. Brooks, and W. Thompson, “Microstructure and Hydrogen Effects on Fracture in the Alloy A-286”, Journal of Metallurgical Transactions (Physical Metallurgy and Materials Science), Vol.24, Issue 9, Sept 1993, pp 1983–1991.

[155] Z. Mei, J. Morris, “The Growth of Small Fatigue Cracks in A-286 Steel”, Metallurgical Transactions, Volume 24, Issue 3, March 1993, pp. 689–700.

[156] l. James, “Effect of Temperature on the Fatigue-Crack Propagation Behavior of A-286 Steel”, Technical Report, HEDL-TME, Year 1976, pp. 75-82.

[157] M. Ohnami, M. Sakane, “A Study on Creep-Fatigue Interaction of Super Alloy Steel A286 Specially, Notch Effect in Creep-Fatigue Interaction at Elevated Temperature” Journal of the Society of Materials Science, Japan, Vol. 24, No. 261, 1975, pp. 545-550.

[158] A. Sinha, and J. Moore, “Precipitation of M23C6 Carbides in an Aged Inconel X-750”, Metallography, Volume 19, Issue 1, Feb 1986, pp. 87-98.

[159] V. Ratna, and D.Sarma, “Influence of Thermal Fatigue on the Microstructure of a Ni-base Super Alloy”, Scripta METALLURGICA, Vol. 29, 1993, pp. 467-472.

[160] H. Dehghan, S. Abbasi, A. Momeni, C. Karimi, A. Taheri “On the Constitutive Modeling and Microstructural Evolution of Hot Compressed A-286 Iron-base Super Alloy” Journal of Alloys and Compounds, Vol. 564, Year 2013, pp. 13-19.

[161] M. Miglin, H. Domian, “Microstructure and Stress Corrosion Resistance of Alloys X750, 718, and A286 in Light Water Reactor Environments”, Journal of Materials Engineering, Volume 9, Issue 2, June 1987, pp. 113–132.

[162] B.Rho, S. Nam, “Fatigue-Induced Precipitates at Grain Boundary of Nb-A286 Alloy in High Temperature Low Cycle Fatigue”, Materials Science and Engineering, A291, Year 2000, pp. 54–59.

[163] B. Rho, S. Woo Nam, “ The Effect of Applied Strain Range on the Fatigue Cracking in Nb-A286 Iron-base Superalloy” Materials Letters, Vol. 48, Issue 1, March 2001, pp. 49-55.

[164] D. Satayanarayana, G. Malakondaiah, D. Sarma, “Characterization of the Age-Hardening Behavior of a Precipitation-Hardenable Austenitic Steel” Materials Characterization, Volume 47, Issue 1, July 2001, pp. 61–65.

[165] O. Martina, P. Tiedrab, and M. San-Juana, “Study of Influence of Gamma Prime and Eta Phases on Corrosion Behaviour of A286 Superalloy by Using Electrochemical Potentiokinetic Techniques”, Materials & Design, Volume 87, 15 Dec 2015, pp. 266–271.

[166] J. Janawitz, J. Masso, and C. Childs, “Heavy-Duty Gas Turbine Operating and Maintenance Considerations”, GER-3620M, February 2015, pp. 5-15.

[167] C. Jaw, N. Dong, and D. Bryg, “Tracking and Control of Gas Turbine Engine Component Damage/Life”, "Symposium on Ageing Mechanisms and Control: Part B - Monitoring and Management of Gas Turbine Fleets for Extended Life and Reduced Costs”, Manchester, UK, 8-11 Oct 2001, pp. 1-4.

[168] M. Clerico, L. Giroletti and C. Marelli, “NDT Techniques For Diagnosis and Life Extension of Industrial Plants”, “Trends in NDE Science & Technology”, Proceedings of the 14th World Conference on Non-Destructive Testing, New Delhi, 8-13 December 1996.Vol. 2, pp. 1197 – 1200.

[169] A. Meguid, S. Kanth, “Finite Element Analysis of Fir-Tree Region in Turbine Discs”, Finite Elements in Analysis and Design, Volume 35, Issue 4, July 2000, pp. 305-317.

[170] R. Claudio, C. Branco, E. Gomes, J. Byrne, G. Harrison, M. Winstone, “Fatigue Life Prediction and Failure Analysis of a Gas Turbine Disc Using the Finite-Element Method”, Journal of Fatigue and Fracture of Engineering Materials & Structure”, Volume 27, Issue 9, September 2004, pp. 849-860.

[171] X. Ling, S. Tung Tu and J. Ming Gong, “Damage Mechanics Considerations for Life Extension of High-Temperature Components”, Journal of Pressure Vessel Technology, Volume 122, Issue 2, Dec 15, 1999.

[172] D. Moon, F. Wall, “ The Effect of Phase Instability on the High Temperature Stress-Rupture Properties of Representative Nickel Base Superalloys”, Scientific Paper 68-ID4-STABL-P1, Westinghouse Research Laboratories, Pittsburgh, August 1968.

[173] A. Pard, “Long Time Aging Studies of Some Nickel Base Alloys”, Final Report on project RP2775-1, Electric Power Research Institute, Palo Alto, CA, 1988.

[174] D. Klarstrom, G. Hoback, V. Ishwar and J. Qureshi, “Rejuvenation Heat Treatment and Weld Repairability Studies of HAYNES® 230® Alloy”, ASME Turbo Expo 2000: Power for Land, Sea, and Air; Paper No. 2000-GT-0629,

Manufacturing Materials and Metallurgy; Ceramics; Structures and Dynamics; Controls, Diagnostics and Instrumentation, Germany, May 8-11.

[175] I. Storey, D. Klarstrom, G. Hoback, V. Ishwar and J. Qureshi, "The Metallurgical Background to Rejuvenation Heat Treatments and Weld Reparability Procedures for Gas Turbine Sheet Metal Components", Journal of Materials at High Temperatures, Volume 18, Issue 4, pp. 241-247.

[176] Z. Zhang, Z. Zhao, Z. Zhong, Q. Peng, "Development of Rejuvenation Process for Creep Damage of Turbine Blades", Transactions of Materials and Heat Treatment, Volume 33, Issue 12, Year 2012.

[177] A. Baldan, "Rejuvenation Procedures to Recover Creep Properties of Nickel-base Superalloys by Heat Treatment and Hot Isostatic Pressing Techniques", Journal of Materials Science, Volume 26, Issue 13, January 1991, pp. 3409-3421.

[178] S. Bell, "Repair and Rejuvenation Procedures for Aero Gas-Turbine Hot-Section Components", Journal of Materials Science and Technology, Volume 1, Issue 8, 1985; pp. 629-634.

[179] P. Norman, S. Michael, "Heat Treatment and Repair of Cobalt Base Superalloy Articles", United States Patent, United Technologies Corporation, ID 25373275, July 26, 1994.

[180] V. Fassel, R. Kniseley, "Inductively Coupled Plasma – Optical Emission Spectroscopy", Journal of Analytical Chemistry, Volume 46, Issue 13, Nov 1974, pp. 1110-1120.

[181] S. Hufner, "Photoelectron Spectroscopy: Principles and Applications", 3rd Edition, Springer Publication, Year 2003.

[182] A. Glen, S. Brooks, "A New Method for Measuring Optical Scattering Properties of Atmospherically Relevant Dusts Using the Cloud and Aerosol

Spectrometer with Polarization (CASPOL), Journal of Atmospheric Chemistry and Physics, Volume 13, Feb 2013, pp. 1345-1356.

[183] J. Potts, "X-ray Fluorescence Analysis-Principles and Practice of Wavelength Dispersive Spectrometry", A Handbook of Silicate Rock Analysis, Springer, Boston, MA, Year 1987.

[184] V. Thomsen, "Basic Fundamental Parameters in X-Ray Fluorescence", Journal of Spectroscopy, Volume 22, Issue 5, May 2007.

[185] K. Bathe, "Finite Element Procedures", Publisher Klaus-Jurgen Bathe, Chapter 1, Year 2006.

[186] J. Hughes, "The Finite Element Method: Linear Static and Dynamic Finite Element Analysis", Courier Corporation, Technology & Engineering, May 23, 2012.

[187] J. Reddy, "An Introduction to Nonlinear Finite Element Analysis: With Applications to Heat Transfer, Fluid Mechanics, and Solid Mechanics, OUP Oxford, Oct 23, 2014.

[188] S. Reh, J. DanielBeley, S. Mukherjee, "Probabilistic Finite Element Analysis Using ANSYS", Journal of Structural Safety, Volume 28, Issue 1-2, Jan-Apr 2006, pp. 17-43.

[189] M. Kompatscher, "Equotip Rebound Hardness Testing After D. Leeb", Hardness Measurements Theory and Application in Laboratories and Industries, Washington D.C, USA, 11-12 November, 2004.

[190] H. Modin, S. Modin, "Metallurgical Microscopy", Elsevier, Technology & Engineering, Jan 22, 2016.

[191]W. Rosenhain, "The Metallurgical Microscope", Journal of Microscopy, Volume 40, Issue 4, Dec 1920, pp. 128-134.

[192] “Construction and Function of Optical Microscope”, www.wikilectures.eu/index.php/Construction_and_function_of_optical_microscope.

[193] D. McMullan, “Scanning Electron Microscopy 1928-1965” Volume 17, Issue 3, Year 2006, pp. 175-185.

[194] Stokes, J. Debbie, “Principles and Practice of Variable Pressure Environmental Scanning Electron Microscopy (VP-ESEM)” John Wiley & Sons, Year 2008. ISBN 978-0470758748.

[195] K. Smith, CW. Oatley, “The Scanning Electron Microscope and its Fields of Application", British Journal of Applied Physics, Volume 6, Issue 11, 1955, pp. 391–399.

[196] B. Rad, Leili, “Computational Scanning Electron Microscopy", International Conference on Frontiers of Characterization and Metrology, Year 2007.

[197] C. Oatley, W. Nixon, R. Pease, “Scanning Electron Microscopy” Advances in Electronics and Electron Physics, Volume 21, Year 1966, pp. 181-247.

[198] J. Venables, C. Harland, “Electron Back-Scattering Patterns – A New Technique For Obtaining Crystallographic Information in the Scanning Electron Microscope”, Journal of Philosophical Magazine, Volume 27, Issue 5, Aug 2006, pp. 1193-1200.

[199] Joseph Goldstein et al. “Scanning Electron Microscopy and X-Ray Microanalysis”.

[200] http://www.microscopy.ethz.ch/aed.htm

[201] J. Friel, “X-ray and Image Analysis in Electron Microscopy”, Princeton Gamma-Tech.

[202] D.Williams and B. Carter, “Transmission Electron Microscopy: A Textbook for Materials Science”. Plenum.

[203] “Casino” Monte Carlo Simulation, http://www.gel.usherbrooke.ca/casino/download2.html

[204] Images and much of text from: “Energy Dispersive X-ray Microanalysis Hardware Explained”, Oxford Instruments Analytical Technical Briefing.

[205] C. Hays, E. Kendall, “An Analysis of Knoop Microhardness”, Journal of Metallography, Volume 6, Issue 4, Aug 1973, pp. 275-282.

[206] J. Antunes, A. Cavaleiro, L. Menezes, M. Simoes, J. Fernandes, “Ultra-Microhardness Testing Procedure with Vickers Indenter”, Journal of Surface and Coatings Technology, Volume 149, Issue 1, Jan 2002, pp. 27-35.

[207] R. Smith, G. Sandland, "An Accurate Method of Determining the Hardness of Metals, with Particular Reference to Those of a High Degree of Hardness," Proceedings of the Institution of Mechanical Engineers, Vol. I, Year 1922, pp. 623–641.

[208] F. Frohlich, P. Grau, W. Grellmann, “Performance and Analysis of Recording Microhardness Tests”, Journal of Applications and Material Science, Volume 42, Issue 1, July 1977.

[209] R. Fabian, “Vacuum Technology – Practical Heat Treating and Brazing”, ASM International, Jan 1993, Chapter 2 & 6.

[210] vacaero.com/information-resources/the-heat-treat-doctor/1496-the-fundamentals-of-vacuum-theory-part-1.html

[211] T. Rajan, C. Sharma, A. Sharma, “Heat Treatment: Principles and Techniques”, Heat Engineering, Year 2011, Chapter 1 to 3.

[212] www.independencetube.com/downloads/Processing/CharpyVNotch.pdf

[213] T. Siewert, A. Manahan, M. McCowan, C. Holt, J. Marsh, R. Ruth, " Pendulum Impact Testing: A Century of Progress", ASTM STP 1380. ASTM, Year 1999.

[214] D. Sun, W. Brocks, W. Schmitt, "Fracture Toughness Evaluation by Tensile and Charpy-type Tests Based on Micromechanical Models of Materials", Material Science, Volume 30, Issue 2, March 1995, pp 223–229.

[215] https://web.statler.wvu.edu/rliang/creeptest.pdf

[216] W. Pridemore, "Stress-Rupture Characterization in Nickel-Based Superalloy Gas Turbine Engine Components", Journal of Failure Analysis and Prevention, Volume 8, Issue 3, June 2008, pp 281–288

[217] T.Langdon, "Grain Boundary Sliding as a Deformation Mechanism During Creep", Journal of Philosophical Magazine, Volume 22, Issue 178, Aug 2006, pp. 689-700.

[218] J. Rose, S. Winwood, "A Novel Approach for Improving Turbine Wheel Quality Using Eddy Current Inspection" Cummins Turbo Technologies (CTT), Huddersfield, UK June 2015

[219] A. Marder, "Replication Microscopy Techniques for NDE", ASM Handbook, Volume 17: Nondestructive Evaluation and Quality Control, Year 1989, pp. 52-56.

[220] M. Naidu1, D. SanthaRao, J. KanthaRao, "Stress Analysis of Gas Turbine Wheel", International Journal of Engineering Research & Technology (IJERT), Volume 2, Issue 2, February 2013.

[221] R. Haigh, M. Murdoch, "Analysis of Centrifugal Stresses in Turbine Wheels", Journal of Mechanical Engineering and Science, Volume 5, Issue 1, March 1963.

[222] W. Kearton, “The Calculation of the Stresses in a Turbine Wheel by the Method of Superposition”, Proceedings of the Institution of Mechanical Engineers, Volume 155, Issue 1, Year 1946.

[223] https://www.aircraftmaterials.com/data/alstst/A286.html

[224] R. Higgins, “Engineering Metallurgy: Part 1 Applied Physical Metallurgy”, Year 1993.

[225] J.Kameda, R.Ranjan, “Nondestructive Evaluation of Steels using Acoustic and Magnetic Barkhausen Signals -Effect of Carbide Precipitation and Hardness”, Acta Metallurgica, Volume 35, Issue 7, July 1987, pp. 1515-1526.

[226] P. Villars, L. Calvert, “Pearson’s Handbook of Crystallographic Data for Intermetallic Phases”, American Society for Metals, Ohio, 1985.

[227] A. David, M. Vitek, W. Reed, L. Hebble, “Effect of Rapid Solidification on Stainless Steel Weld Metal Microstructures and its Implications on the Schaeffler Diagram”, Technical Report No ORNL/TM-10487 ON: DE88001489, Oak Ridge National Lab., TN-USA, Year 1987.

[228] D. Olson, “Prediction of Austenitic Weld Metal Microstructure and Properties” Welding Research Supplement, Oct 1985, pp. 281-294.

[229] C. Sims, “A Contemporary View of Nickel-Base Superalloys”, The Journal of The Minerals, Metals & Materials Society (TMS), Volume 18, Issue 10, Jan 2017, pp 1119–1130.

[230] L. Liu, T. Jin, N. Zhao, H. Guan, “Formation of Carbides and their Effects on Stress Rupture of a Ni-base Single Crystal Superalloy”, Materials Science and Engineering: Volume 361, Issues 1–2, November 2003, pp. 191-197.

[231] J. Chen, J. Lee, C. Jo, Y. Lee, “MC Carbide Formation in Directionally Solidified MAR-M247 LC Superalloy”, Materials Science and Engineering, Volume 247, Issues 1–2, June 1998, pp. 113-125.

[232] F. Furillo, J. Davidson, J. Tien, “The Effects of Grain Boundary Carbides on the Creep and Back Stress of a Nickel-Base Superalloy”, Materials Science and Engineering, Volume 39, Issue 2, August 1979, pp. 267-273.

[233] Y. Jinxia, Q. Zheng, S. Xiaofeng, G. Hengrong, H. Zhuanggi, “Morphological Evolution of MC Carbide in K465 Superalloy”, Journal of Materials Science, Volume 41, Issue 19, Oct 2006, pp 6476–6478.

[234] J. Agren, “Kinetics of Carbide Dissolution”, Scandavian Journal of Metallurgy, Volume 19, Year 1990, pp. 2-8.

[235] G.AppaRao, M. Kumar, M.Srinivas, D.Sarmab, “Effect of Standard Heat Treatment on the Microstructure and Mechanical Properties of Hot Isostatically Pressed Superalloy- Inconel 718”, Materials Science and Engineering, Volume 355, Issues 1–2, August 2003, pp. 114-125.

[236] J.Otubo, F. Nascimento, P. Lisandro, M.Kaufman, A. Brooks, A.Thompson; “Influence of Austenite Grain Size on Mechanical Properties of Stainless SMA”; Materials Transactions, Volume 43, No. 5, 2002, pp:916-919.

[237] O.Bouaziz, S.Allain, C.Scott, “Effect of Grain and Twin Boundaries on the Hardening Mechanisms of Twinning-induced Plasticity Steels”, Scripta Materialia, Volume 58, Issue 6, March 2008, pp. 484-487.

[238]www.doitpoms.ac.uk/tlplib/mechanical-testing/grainsize.php.

[239] “Failure Analysis and Prevention”, ASM Handbook, Volume 11, Year 2002, pp 730-736.

[240] D. Curry, J.Knott, “The Relationship Between Fracture Toughness and Microstructure in the Cleavage Fracture of Mild Steel”, Journal of Metal Science, Volume 10, Issue 1, Year 1976, pp. 1-6.

[241] Y. Tomita, K. Okabayashi, “Effect of Microstructure on Strength and Toughness of Heat-Treated Low Alloy Structural Steels”, Metallurgical Transactions, Volume 17, Issue 7, July 1986, pp. 1203-1209.

[242] M. Martin, J. Fenske, I. Robertson, “On the Formation and Nature of Quasi-Cleavage Fracture Surfaces in Hydrogen Embrittled Steels”, Acta Materialia, Volume 59, Issue 4, Feb 2011, pp. 1601-1606.

[243] R. Hart, “Assessment of Remaining Creep Life Using Accelerated Stress-Rupture Tests”, Journal of Metals and Technology, Volume 3, Issue 1, Year 1976, pp. 1-7.

[244] H. Voorhees, J. Freeman, “Notch Sensitivity of Aircraft Structural and Engine Alloys”, Part-I Preliminary Studies with A-286 and 17-7 PH Alloy, WADC Technical Report 57-58, Materials Laboratory, Project No 7360, Ohio, Dec 1956.

[245] Y. Zhao, M. Chen, S. Wang, “ Stress Rupture Properties of alloy 783”, Journal of Energy Materials, Year 2017, pp. 289-294.

[246] J. Larson, S. Floreen, “ Metallurgical Factors Affecting the Crack Growth Resistance of a Superalloy”, Metallurgical Transactions, Volume 8, Issue 1, January 1977, pp. 51-55.

[247] J. Oblak, W. Owczarski, “Thermomechanical Strengthening of a γ′ Precipitation-Hardened Nickel-Base Alloy” Volume 3, Issue 3, March 1972, pp. 617-626.

[248] M. Qian, J. Lippold, “Investigation of Grain Refinement During a Rejuvenation Heat Treatment of wrought Alloy 718”, Materials Science and Engineering, Volume 456, Issue 1-2, May 207, pp. 147-155.

APPENDIX - 1

1. Chemical Composition Report for New A-286 Bar

Lonestar Technical Services (L.L.C.)

P.O.Box 8817, Building # DY34
Inside Dubai Ship Docking Yard
Al Jadaf, Dubai
United Arab Emirates

Tel: +971 4 324 3888
Fax: +971 4 324 3682
Email: testing@lonestar-lab.com
Website: www.lonestar-lab.com

Analytical Chemistry Section
Material Analysis Report

SAMPLE#	300 - 16-02417	***REPORT#***	CR44273S1	***REVISION#***	0	***JOB#***	70868

CLIENT	Masaood John Brown	***ATTENTION***	Mr. Girish Shejale
	PO BOX: 11931	***CLIENT ORDER #***	PO # JB-060361
	DUBAI	***ANALYST***	BDG
	UNITED ARAB EMIRATES	***ANALYSIS DATE***	18-FEB-2016
		DATE RECEIVED	15-FEB-2016
		TEST METHOD	As Below

Sample Description	Material Sample. Description: A-286 New Bar. PO # JB-060361 dated 14-Feb-2016

TEST	TEST METHOD	RESULT
Carbon, wt. %	CHM-SOP-210 / ASTM E 1019	0.036
Sulfur, wt. %	CHM-SOP-210 / ASTM E 1019	< 0.002
Phosphorus, wt. %	CHM-SOP-006 / ASTM E 353	0.020
Manganese, wt. %	CHM-SOP-265 / ASTM E 353	1.2
Chromium, wt. %	CHM-SOP-265 / ASTM E 353	14.9
Nickel, wt. %	CHM-SOP-265 / ASTM E 353	25.1
Molybdenum, wt. %	CHM-SOP-265 / ASTM E 353	1.2
Silicon, wt. %	CHM-SOP-265 / ASTM E 353	0.17
Iron, wt. %	CHM-SOP-265 / ASTM E 353	56.0
Aluminum, wt. %	CHM-SOP-265 / ASTM E 353	0.23
Vanadium, wt. %	CHM-SOP-265 / ASTM E 353	0.40
Titanium, wt. %	CHM-SOP-265 / ASTM E 353	2.4
Boron, wt. %	ASTM E 415	0.0027

NOTE: The chemistry of the sample meets the requirements of 'Alloy A286' for the elements analyzed.

QC CHECKED

	Approved by		Checked by
Name	**M.Mubin Shaikh**	Name	**Arun Tom Mathew**
Designation	**Deputy Manager**	Designation	**Assistant Manager**
Signature		Signature	

QC SEAL MANDATORY

Page 1 of 1

The Terms and Conditions mentioned on the back of this report are an integral part of this report.

Locations : Dubai • Abu Dhabi • Oman • Iraq • Kuwait

2. Chemical Composition Report for A-286 Turbine Wheel Section

Lonestar Technical Services (L.L.C.)

P.O.Box 8817, Building # DY34
Inside Dubai Ship Docking Yard
Al Jadaf, Dubai
United Arab Emirates

Tel: +971 4 324 3888
Fax: +971 4 324 3682
Email: testing@lonestar-lab.com
Website: www.lonestar-lab.com

Analytical Chemistry Section
Material Analysis Report

SAMPLE#	300 - 16-02418	REPORT#	CR44273S2	REVISION#	0	JOB#	70868

CLIENT	Masaood John Brown PO BOX: 11931 DUBAI UNITED ARAB EMIRATES	ATTENTION	Mr. Girish Shejale
		CLIENT ORDER #	PO # JB-060361
		ANALYST	BDG
		ANALYSIS DATE	18-FEB-2016
		DATE RECEIVED	15-FEB-2016
		TEST METHOD	As Below

Sample Description	Material Sample. Description: A-286 Turbine Wheel Section. PO # JB-060361 dated 14-Feb-2016

TEST	TEST METHOD	RESULT
Carbon, wt. %	CHM-SOP-210 / ASTM E 1019	0.039
Sulfur, wt. %	CHM-SOP-210 / ASTM E 1019	< 0.002
Phosphorus, wt. %	CHM-SOP-006 / ASTM E 353	0.022
Manganese, wt. %	CHM-SOP-265 / ASTM E 353	1.2
Chromium, wt. %	CHM-SOP-265 / ASTM E 353	14.8
Nickel, wt. %	CHM-SOP-265 / ASTM E 353	25.1
Molybdenum, wt. %	CHM-SOP-265 / ASTM E 353	1.3
Silicon, wt. %	CHM-SOP-265 / ASTM E 353	0.17
Iron, wt. %	CHM-SOP-265 / ASTM E 353	56.2
Aluminum, wt. %	CHM-SOP-265 / ASTM E 353	0.23
Vanadium, wt. %	CHM-SOP-265 / ASTM E 353	0.39
Titanium, wt. %	CHM-SOP-265 / ASTM E 353	2.4
Boron, wt. %	ASTM E 415	0.0030

NOTE: The chemistry of the sample meets the requirements of 'Alloy A286' for the elements analyzed.

QC CHECKED

	Approved by		Checked by
Name	M.Mubin Shaikh	Name	Arun Tom Mathew
Designation	Deputy Manager	Designation	Assistant Manager
Signature		Signature	

QC SEAL MANDATORY

Page 1 of 1

The Terms and Conditions mentioned on the back of this report are an integral part of this report.
Locations: • Dubai • Abu Dhabi • Oman • Iraq • Kuwait

3. TENSILE, CHARPY IMPACT AND STRESS RUPTURE TEST REPORTS

SPECIAL METALS **IncoTest**

Holmer Road, Hereford, England HR4 9SL
Tel: + 44 (0)1432 352230
Fax: + 44 (0)1432 353545
Email: info@incotest.co.uk
www.incotest.co.uk
A Division of Special Metals Wiggin Limited
Registered in England at the above address under number 36721

Accredited Nadcap Materials Testing Laboratory

CERTIFIED LABORATORY TEST REPORT
UKAS Testing Laboratory no. 0281

UKAS TESTING 0281

CUSTOMER BY E-MAIL

Customer
MASAOOD JOHN BROWN
B54 OILFIELDS SUPPLY CENTRE
JEBEL ALI FREE ZONE
PO BOX 11931
DUBAI
UNITED ARAB EMIRATES
FAO: **Girish Shejale**

Certificate No.	**LT 0303731/02**
Dated	26 04 2016
Page No.	1 of 1
Customer Order Number	JB-060394
Date Received	19/02/2016
Laboratory Reference Number	J39692 1

Specification	Description of Samples	Test piece nom. dim. (mm)
+ customer amendments	Bar and Wheel Section	10H ROUND 6.35 14K ROUND 6.25 28A V NOTCH 10.00x10.00

Number of Samples 1

HEAT TREATMENT ON TEST PIECES

As Supplied

MECHANICAL TEST RESULTS

Specimen identity	T/P Type	Temp. C	0.2% PS MPa	UTS MPa	%Elong. on 4D	R. of A. (%)
NEW A-286 BAR	10H	20	769	1096	23.6	39.3
A-286 TURBINE WHEEL	10H	20	695	950	10.8	13.7
Test Method ASTM E8/E8M MAY 15 (0.5/ 5.0)						
NEW A-286 BAR	14K	450	690	937	17.5	45.4
A-286 TURBINE WHEEL	14K	450	566	662	4.5	16.8
Test Method ASTM E21 MAY 09 (0.5/5.0)						
Specification Requirement		20	Info.	Info.	Info.	Info.
		450	Info.	Info.	Info.	Info.

OTHER TESTS

Specimen identity	T/P Type	
NEW A-286 BAR	28A	CHARPY 'KV2' notch = 58 Joules at 20 C
	28A	CHARPY 'KV2' notch = 57 Joules at 20 C
	28A	CHARPY 'KV2' notch = 58 Joules at 20 C
A-286 TURBINE WHEEL	28A	CHARPY 'KV2' notch = 17 Joules at 20 C
	28A	CHARPY 'KV2' notch = 18 Joules at 20 C
	28A	CHARPY 'KV2' notch = 16 Joules at 20 C
Test Method ASTM E23-12C NOV12 (300J)		
Specification Requirement		CHARPY Charpy : information only Joules at 20 C

OTHER REMARKS/ENDORSEMENTS

Tested in compliance with ISO/IEC 17025.
Test results meet Specification Requirements unless otherwise stated.

End of test results

Q3103 Rev01 03/06

Certified that the above mentioned specimens/parts/materials/systems have been tested/examined in accordance with the terms of the contract order applicable thereto. This Certificate does not relate to the standard or quality of manufacture of the item/material except as may be specified in test contract/order. This certificate shall not be reproduced, except in full without the written approval of the laboratory.

Signed

for and on behalf of IncoTest
Authorised Laboratory Signature
J.SKERRATT
Sales Manager

Date 26/04/2016

SPECIAL METALS
IncoTest
Holmer Road, Hereford, England HR4 9SL
Tel: + 44 (0)1432 352230
Fax: + 44 (0)1432 353545
Email: info@incotest.co.uk
www.incotest.co.uk
A Division of Special Metals Wiggin Limited
Registered in England at the above address under number 36721

Accredited Nadcap Materials Testing Laboratory

CERTIFIED LABORATORY TEST REPORT

UKAS Testing Laboratory no. 0251

UKAS TESTING 0251

Certificate No.	LT 0303957/01
Dated	08 04 2016
Page No.	1 of 1
Customer Order Number	JB-060394
Date Received	19/02/2016
Laboratory Reference Number	J39692 2

CUSTOMER BY E-MAIL

Customer
MASAOOD JOHN BROWN
B54 OILFIELDS SUPPLY CENTRE
JEBEL ALI FREE ZONE
PO BOX 11931
DUBAI
UNITED ARAB EMIRATES
FAO: Girish Shejale

Specification	Description of Samples	Test piece nom. dim. (mm)
+ customer amendments	Bar and Wheel Section Number of Samples 1	12F ROUND 4.51

HEAT TREATMENT ON TEST PIECES

As Supplied

STRESS RUPTURE & CREEP TEST RESULTS

Specimen Identity	T/P Type	Stress MPa	Temp. C	Life h Rupture	Life h Discont.	%Elong. on 4D	R. of A. (%)
NEW A-266 BAR	12F	520	550		993		
A-266 TURBINE WHEEL	12F	520	550		993		
NEW A-266 BAR	12F	365	650	319		23.2	26.2
A-266 TURBINE WHEEL	12F	365	650	207		14.9	14.3
Test Method ASTM E139 JUN 11							
Specification Requirement		520	550	Info.	Info.	Info.	Info.
		365	650	Info.	Info.	Info.	Info.

OTHER REMARKS/ENDORSEMENTS

Tested in compliance with ISO/IEC 17025.
Test results meet Specification Requirements unless otherwise stated.

End of test results

08/03 Rev01. 03/04

Certified that the above mentioned specimens/parts/materials/systems have been tested/examined in accordance with the terms of the contract order applicable thereto. This Certificate does not relate to the standard or quality of manufacture of the item/material except as may be specified in test contract/order. This certificate shall not be reproduced, except in full without the written approval of the laboratory.

Signed

for and on behalf of IncoTest
Authorised Laboratory Signature
J.SKIRRATT
Sales Manager

Date 08/04/2016

Westmoreland Mechanical Testing & Research, Ltd.
19 Wildmere Road, Banbury
Oxfordshire OX16 3JU, U.K.
Telephone: +44 (0) 1295 261211
Fax: +44 (0) 1295 263096
Website: www.wmtr.co.uk

Accredited Nadcap Materials Testing Laboratory

UKAS TESTING 2616

Tensile & Charpy Test Report
Tests Conform to: ASTM E8-15a, ASTM E21-09 & ASTM E23-12C

Masaood John Brown International
Building #61 10th Roundabout
P.O Box 11931
Dubai
United Arab Emirates

Attn: Girish Shejale

Report Number:	**UK-16001152 (Tensile & Charpy)**
Section No:	**8C-1**
Report Date:	4th August 2016
WMTR Quote No:	QB161107 - Rev 2
Purchase Order No:	JB-062145
Material:	A-286 Turbine Wheel
Specimen Orientation:	As Supplied
Tensile 1st Test Rate:	0.005 strain/min
Tensile 2nd Test Rate:	0.050 strain/min (over Lc)
Test Date:	29th July – 2nd August 2016
Operator Initials:	M.P, O.F. & T.F.

Tensile Tests

The specimens were of nominal diameter 4.0mm and parallel length (Lc) 25.0mm, marked with a 4D gauge length for the determination of plastic elongation.

Specimens 45048C & 45049C were instrumented with a single channel extensometer and tested at ambient temperature.

Specimens 45056C & 45057C were instrumented with a single channel extensometer and tested at an elevated temperature of 450°C (Heat up time approx.: 60 mins, Soak Time: 30 mins).

All specimens were tested in strain rate control at the first rate to beyond yield at which point the second rate was adopted and the extensometry was removed.

Full details of the testing and equipment used are contained in the laboratory customer folder.

The results in this report relate only to the items tested.

Testlog	Sample Id	Temp (°C)	0.2% PS (MPa)	UTS (MPa)	Plastic Elong. (%)	R/A (%)
45048C	8C-1 SA - 950°C x 3hrs + Age - 600°C x 4 hrs	21	381	808	48.2	55.2
45049C		21	379	804	49.3	57.8
45056C		450	307	633	52.9	54.1
45057C		450	304	638	56.1	55.5

THIS CERTIFICATE OR REPORT SHALL NOT BE REPRODUCED EXCEPT IN FULL WITHOUT THE WRITTEN APPROVAL OF WMT&R LTD. KNOWINGLY OR WILFULLY FALSIFYING OR CONCEALING A MATERIAL FACT ON THIS FORM OR MAKING FALSE, FICTITIOUS OR FRAUDULENT STATEMENTS OR REPRESENTATIONS HEREIN COULD CONSTITUTE A CRIMINAL OFFENCE, PUNISHABLE UNDER UK LAW.

Westmoreland Mechanical Testing & Research, Ltd.
Telephone: +44 (0) 1295 261211 Fax: +44 (0) 1295 263096

Report No: UK-16001152
Tensile & Charpy 8C-1

Full Stress-Strain Plot

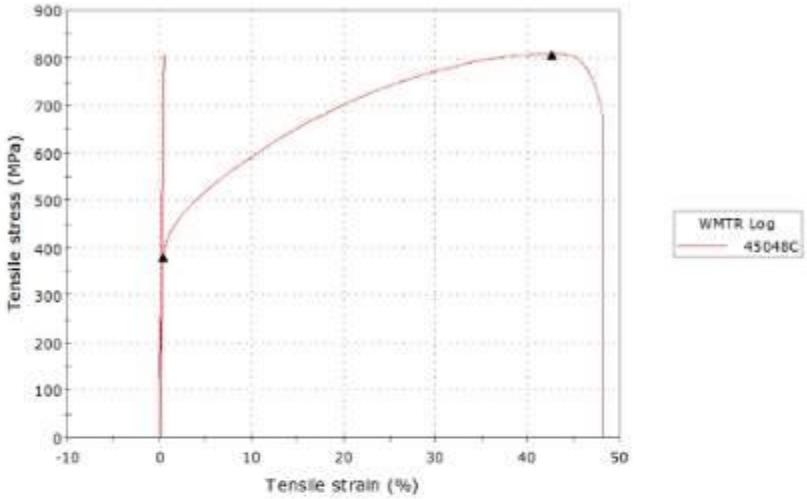

Full Stress-Strain Plot

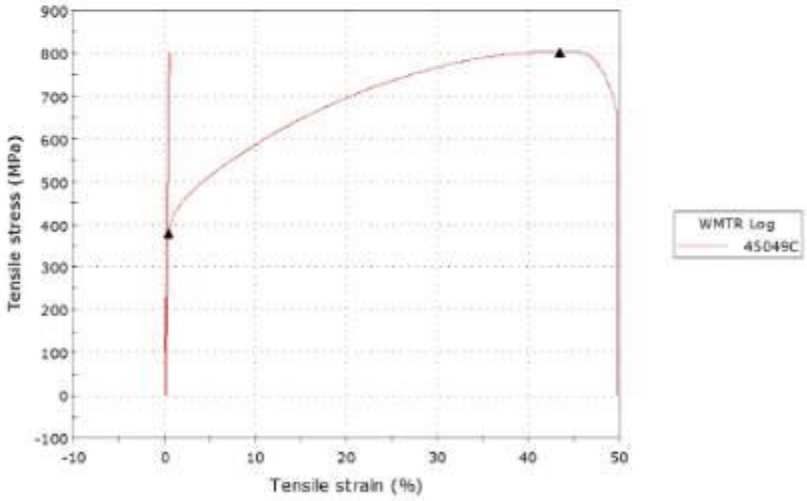

THIS CERTIFICATE OR REPORT SHALL NOT BE REPRODUCED EXCEPT IN FULL WITHOUT THE WRITTEN APPROVAL OF WMT&R LTD. KNOWINGLY OR WILFULLY FALSIFYING OR CONCEALING A MATERIAL FACT IN THIS FORM OR MAKING FALSE, FICTITIOUS OR FRAUDULENT STATEMENTS OR REPRESENTATIONS HEREIN COULD CONSTITUTE A CRIMINAL OFFENCE, PUNISHABLE UNDER UK LAW.

Westmoreland Mechanical Testing & Research, Ltd.
Telephone: +44 (0) 1295 261211 Fax: +44 (0) 1295 263096

Report No: UK-16001152
Tensile & Charpy 8C-1

Full Stress-Strain Plot

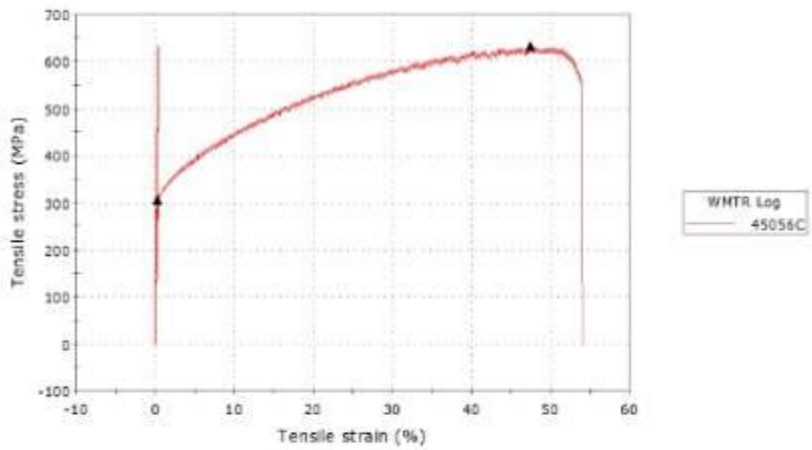

Full Stress-Strain Plot

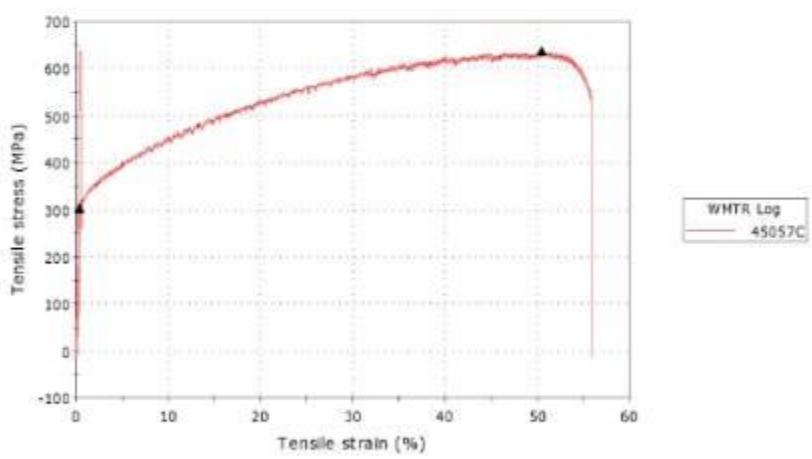

THIS CERTIFICATE OR REPORT SHALL NOT BE REPRODUCED EXCEPT IN FULL WITHOUT THE WRITTEN APPROVAL OF WMTAR LTD. KNOWINGLY OR WILFULLY FALSIFYING OR CONCEALING A MATERIAL FACT IN THIS FORM OR MAKING FALSE, FICTITIOUS OR FRAUDULENT STATEMENTS OR REPRESENTATIONS HEREIN COULD CONSTITUTE A CRIMINAL OFFENCE, PUNISHABLE UNDER UK LAW.

Westmoreland Mechanical Testing & Research, Ltd.
Telephone: +44 (0) 1295 261211 Fax: +44 (0) 1295 263096

Report No: UK-16001152
Tensile & Charpy 8C-1

Charpy Tests

Charpy impact samples were machined for testing in accordance to ASTM E23-12c, at room temperature (20°C). The machine striking energy is 240 ftlb. The NIST calibrated range of the impact test machine is 6.3ftlb to 108.0ftlb. Any results acquired that failed to meet the NIST calibration requirements are for information purposes only. The results in this report relate only to the items tested.

Testlog	Sample ID	Absorbed Energy (Joules)	Average Absorbed Energy (Joules)	% Shear Fracture	Lateral Expansion (mils)
45064C	8C-1 SA - 950°C x 3hrs + Age - 600°C x 4 hrs	122.0	116.6	20	68
45065C		107.1		20	67
45066C		120.7		20	74

Approved Signatory: _____

Terry Cook – Operations Manager
For and on behalf of WMT& R Limited

THIS CERTIFICATE OR REPORT SHALL NOT BE REPRODUCED EXCEPT IN FULL WITHOUT THE WRITTEN APPROVAL OF WMT&R LTD. KNOWINGLY OR WILFULLY FALSIFYING OR CONCEALING A MATERIAL FACT ON THIS FORM OR MAKING FALSE, FICTITIOUS OR FRAUDULENT STATEMENTS OR REPRESENTATIONS HEREIN COULD CONSTITUTE A CRIMINAL OFFENCE, PUNISHABLE UNDER UK LAW.

PROFILE OF THE SCHOLAR

Girish Shejale

Inspection and Laboratory Services Manager

Masaood John Brown, Dubai, U.A.E

Mobile: +971 50 3408005

E-mail: girish.shejale@gmail.com

Girish Shejale is pursuing PhD (Engineering) from University of Petroleum and Energy Studies. He is holding Bachelors of Engineering (Metallurgy) from College of Engineering, Pune University.

He has rich experience of more than 23 years in power generation industries such as boilers and gas turbines. Girish has got experience in process developments related to repairs of gas turbine components such as welding, brazing, heat treatments, plasma coatings, metallurgical evaluation/testing, and non-destructive testing. He has vast experience on remaining life analysis of high temperature gas turbine and boiler components.

The publications of Girish Shejale are mentioned below:

- "In-situ Metallography of High Temperature Components"; Energy Conservation Conference, Stuggart, Germany, October, 2002.
- "Metallurgical Evaluation and Condition Assessment of FSX 414 Nozzle Segments in Gas Turbines by Metallographic Methods", GT2010-22542, ASME TurboExpo Conference, June 2010, Glasgow, United Kingdom.
- "Failure Investigation of 1st Stage Buckets from Frame 3002, 10 MW Gas Turbine Unit", GT20111-46863, Jan 2011, Vancouver, Canada.

- "Application of Metallographic Evaluation for Repair of FSX 414-1st Stage Nozzle Segments", GT2012-68042, June 2012, Copenhagen, Denmark.
- "Condition Assessment Study of A-286 Alloy Gas Turbine Wheel", ASTM Journal of Failure Analysis and Prevention, June 2016.
- "Replica Metallography: An NDT Technique for Condition Assessment of Gas Turbine Components", ASNT Journal "Materials Evaluation", May 2017.

Work Experience

- Masaood John Brown, Dubai, U.A.E
  From May 2006 to Present
  Designation: Inspection & Laboratory Services Manager
- Lonestar Techanical Services, Dubai, U.A.E
  From Jan 2003 to April 2006
  Designation: Senior Metallurgy Engineer
- Thermax Limited, Pune, India
  From Aug 1995 to Dec 2002
  Designation: Assistant Manager

Trainings

- Six Sigma Green Belt from Motorola University, Year 2008.
- Internal Auditors course from Vincette, Year 2009.
- ASNT NDT Level III in Eddy Current Testing, Dye Penetrant Testing and Magnetic Particle Testing, Year 2012.
- Remaining Life Analysis of Gas Turbine Components from ERA, United Kingdom, Year 2014.

PUBLISHED PAPERS

- "Condition Assessment Study of A-286 Alloy Gas Turbine Wheel", ASTM Journal of Failure Analysis and Prevention, June 2016.

- "Replica Metallography: An NDT Technique for Condition Assessment of Gas Turbine Components", ASNT Journal "Materials Evaluation", May 2017.